

# **Metal-free heterogeneous photocatalysts for solar energy harvesting**

*A thesis submitted for the partial fulfillment of the degree of  
Doctor of Philosophy*

by

*Sanjit Mondal*



Department of Chemical Sciences

Indian Institute of Science Education and Research  
Sector-81, Knowledge City, Mohali, Punjab-140306

June 2021



# CERTIFICATE

The work presented in this thesis has been carried out by me under the supervision of Dr. Ujjal K. Gautam at the Department of Chemical Sciences, Indian Institute of Science Education and Research (IISER) Mohali.

This work has not been submitted in part or full for a degree, a diploma, or a fellowship to any other university or institute.

Whenever contributions of others are involved, every effort is made to indicate this clearly, with due acknowledgement of collaborative research and discussions. This thesis is a bonafide record of original work done by me and all sources listed within have been detailed in the bibliography.

17-06-2021

Mohali

**Date**

**Place**

**Sanjit Mondal**

In my capacity as supervisor of the candidate's thesis work, I certify that above statements made by the candidate are true to the best of my knowledge.

**Dr. Ujjal K. Gautam**  
**(Supervisor)**



*Dedicated to  
my beloved family*



## Acknowledgements

*First and foremost, I wish to express my deepest gratitude to my supervisor Dr. Ujjal K. Gautam for his constant support and guidance throughout the journey of my PhD. He always encouraged me to be professional and provided me confidence. Each and every conversation (whether scientific or non-scientific), I had with him was stimulating and captivating. He was always there motivating and guiding me during the bad phases of my PhD tenure. I am grateful to him for introducing me in the field of nanomaterials. I sincerely acknowledge the suggestions and advice he provided me during my research. I feel extremely fortunate to be a part of his esteemed research team and consider it as one of the finest experiences of my life. I am thankful to him for his help in writing of this thesis. Thank you, Sir!*

*I would like to thank to Prof. J. Gourisankar (Director, IISERM), Prof. N. Sathyamurthy and Prof. Debiprasad (Former Director, IISERM), Prof. Sanjay Singh (Head, Dept. of Chemical Sciences, IISERM) for providing excellent research facilities in IISER-Mohali.*

*I express thanks to my doctoral committee members Dr. Angshuman Roy Choudhury and Prof. Sugumar Venkataramani for their annual evaluation of my thesis work and giving valuable comments and suggestions on my research work.*

*I would like to thank my course instructors Prof. Sanjay Mondal, Dr. Sanjay Singh, Dr. Arijit De for their instructive and enjoyable courses, and stimulating scientific interactions.*

*I am thankful to all my collaborators, Dr. Arijit De, Dr. Sudipta and Mr. Soumya from IISER Tirupati, Dr. Vinod from NCL Pune and Dr. M. Satish from CECRI, Karaikudi, for their help and fruitful discussions.*

*I believe research is always a collaborative and collective effort from multiple minds. I was fortunate, having a bunch of talented and helpful people in the lab, who not only helped me in my work but also provided an excellent working environment in lab. I would like to acknowledge all my present (Lipi, Reeya, Maqsuma, Raj, Komal, Yuvraj, Kiran, Jaspreet) and past (Dr. Moumita, Dr. Arabinda, Dr. Karthik, Kaustav, Vikram, Neeru, Nayana, Nihal, Sandita, Parmeet, Utkarsh,*

*and Antik) lab members for their supports and contributions. A special credit goes to Lipi for being there and helping me in a countless way from the day one to the end of my PhD. It wouldn't have been possible without you guys.*

*I would like to thank my friends (Lipi, Uttam, Raju, Yogita, Sourav, Chandan, Pranab, Deba, Rahul) for being there for me whenever I needed. I extend my sincere thanks to Dr. Mrinmoyee Basu, Dr. Surojit Pande, Dr. Kasinath, Dr. Aparna, Dr. Debashree, Dr. Sharmila, and Dr. Manu Sharma.*

*I would like to acknowledge IISER Mohali for providing my scholarship.*

*Special thanks to Dr. Monikankana Sharma and Mr. Anuraj Gautam (Reon) for their kind hospitality, affection and care.*

*Last, but not the least, my heartfelt gratitude goes to my Ma, Baba and my entire family for their constant support and love. I am very thankful to god for giving me this beautiful life, a supportive family, some amazing friends and few great teachers. I am highly grateful to the god for all the wonderful things that I have received in my life. It's his blessing which has given me the required strength and insight to complete this thesis work.*



## Thesis Synopsis

The thesis entitled “*Metal-free heterogeneous photocatalysts for solar energy harvesting*” comprises two major parts. **Part 1**, which is extended to 4 sub-chapters, describes the syntheses of graphitic carbon quantum dots (CQDs) from waste polyethylene, its unique properties such as oxygen-harvesting, light-induced hypoxia, and self-sensitized photo-oxidation (autophagy), and further their applications in photocatalytic oxidation reactions. **Part 2**, containing 4 sub-chapters, presents the development of new strategies for the synthesis of g-C<sub>3</sub>N<sub>4</sub> nanosheets and strategies to enhance their photocatalytic activities for various organic transformation and water splitting reactions. A brief description of each part is given below:

**Chapter 1.1** describes the novel large-scale synthesis strategy of CQDs from waste-polyethylene (PE). This is a unique example of chemical transformation from an alkane to graphene where acid-mediated dehydrogenation of a PE backbone results in the formation of alkenes, which then undergoes cyclization reaction forming benzene derivatives and finally tiny functionalized graphene chunks (PE-CQDs). Furthermore, it was found that in the presence of these PE-CQDs, the ability of water to dissolve and diffuse molecular oxygen significantly increases. Therein, the PE-CQDs adsorbs molecular O<sub>2</sub> from the air with more than 1% of its weight under ambient conditions which is higher than the same expected from conventional materials such as zeolites, etc. Such O<sub>2</sub> enrichment is very useful in photocatalytic oxidation reactions because it offers the possibility of doing such reactions in the air, without the need of creating an oxygen-rich environment. Therefore, it was observed that when the CQDs were used to catalyze photo-oxidation of aromatic alcohols by sunlight, the efficiency was higher than in previous instances despite those employing high O<sub>2</sub> pressure and temperature.

**Chapter 1.2** describes that surface-adsorbed oxygen molecules on CQDs are extremely high, aided by specific combinations of its surface functional groups that lead to profound photocatalytic efficiency for oxidative chemical transformations. Due to oxygen enrichment, the apparent quantum efficiency for selective oxidation of benzylamine was found to be ~35% along with a reaction rate that is significantly faster than the existing photocatalysts, including those using expensive noble metals, an oxygenated atmosphere, and harsh reaction conditions. It was also established that the concentration of adsorbed O<sub>2</sub> on CQDs surface can be controlled by using an

external light source so that a CQDs solution can have different oxygen contents at different portions of the solution. The effect arises due to the modulation of charge-transfer between the CQDs and the adsorbed O<sub>2</sub> molecules in the presence of light that generates excitons in the CQDs and can make them behave as charged particles. Moreover, the use of light and distance from the air-interface offers an unusual possibility of creating a landscape of varied oxygen contents in a solution that may offer new opportunities in chemical reactions.

**Chapter 1.3** narrates the complete conversion of waste polyethylene into CQDs in a greener way by a simple acid-mediated heat treatment method. In doing so, the nature of surface functional groups on PE-CQDs and their sizes can be controlled by tuning the oxidation step of the carbon material derived from polyethylene to realize improved oxygen enrichment properties and therefore enhanced photocatalytic benzyl alcohol oxidation efficiency at ambient conditions. Also, the rate of pollutant dye degradation is at least five times better than any other photocatalyst reported to date. Importantly, we observed that in the absence of the reactants, the PE-CQDs undergo self-sensitized photo-oxidation forming CO<sub>2</sub> and leading to its complete removal from the system. The extinction process that is unlike any other photocatalyst known to date, maybe termed as ‘*carbon-dot autophagy*’ and is deemed advantageous as no separation process for the PE-CQDs is required.

**Chapter 1.4** summarizes the key observations and the prospects of the above studies discussed findings in chapter 1.

**Chapter 2.1** describes the development of new g-C<sub>3</sub>N<sub>4</sub> nanosheets (NS) exhibiting highly blue-shifted, excitation-energy independent photoluminescence (PL) centered at ~425 nm. When the g-C<sub>3</sub>N<sub>4</sub> nanosheets are loaded with Au nanoparticles (NP), the composite retains the PL characteristics but results in alteration of its exciton decay kinetics due to transfer of the long-lived photoexcited electrons in g-C<sub>3</sub>N<sub>4</sub> to the adjacent Au NPs. The Au/g-C<sub>3</sub>N<sub>4</sub> nanosheets exhibited excellent light-harvesting in the extended solar spectrum and photocatalytic efficiency for benzylamine oxidation, emanating not only from a typical Surface Plasmon induced ‘hot-electron injection’ mechanism but also from a less-cared-for, pronounced co-catalytic effect by the Au NPs. The surface plasmon resonance of the Au NPs are responsible for the high visible-light response and assisting the reaction by the ‘hot-electron injection’ mechanism, while an uncharacteristic, pronounced co-catalytic effect by them further improves the efficiency.

**Chapter 2.2** demonstrates the engineering of an effective g-C<sub>3</sub>N<sub>4</sub>-based photocatalyst system (Pd/g-C<sub>3</sub>N<sub>4</sub> nanosheets) for the efficient Suzuki-Miyaura cross-coupling reactions under visible light. Pd NPs loaded onto g-C<sub>3</sub>N<sub>4</sub> NSs become electron-rich under visible light irradiation due to generation of excited electrons which get transferred to the Pd NPs and thereby accelerate the rate-determining step by facilitating the oxidative addition of aryl halides. The Suzuki-Miyaura cross-coupling reaction was carried out in environmentally friendly aqueous media at room temperature. As synthesized Pd/g-C<sub>3</sub>N<sub>4</sub> NSs exhibited a very high turnover frequency of 1700 h<sup>-1</sup> for photocatalytic cross-coupling reactions among previously reported photocatalysts. This material also demonstrated high recyclability for Suzuki cross-coupling reactions. This provides an efficient photocatalytic route for the preparation of biaryl compounds and a facile strategy to design novel photocatalysts for various organic transformation reactions driven by visible light.

**Chapter 2.3** describes the strategy for one-step synthesis of highly red-shifted visible light active, high surface-area g-C<sub>3</sub>N<sub>4</sub> NSs. The NSs were synthesized by simple calcination of melamine and diethyleneglycol mixture at 520 °C for 4 h under Ar atmosphere. The specific surface area of the synthesized sample was found to be ~3 times higher than the bulk g-C<sub>3</sub>N<sub>4</sub>, thereby offering more active sites for the catalytic reactions and eliminating the need for an extra, low-yield preparation step involving the high temperature or chemical exfoliation. The synthesized g-C<sub>3</sub>N<sub>4</sub> NSs showed an enhanced H<sub>2</sub> evolution rate (530 μmol h<sup>-1</sup> g<sup>-1</sup>) under visible light irradiation compared to the as-synthesized conventional g-C<sub>3</sub>N<sub>4</sub> (87 μmol h<sup>-1</sup> g<sup>-1</sup>).

**Chapter 2.4** summarizes the key observations and the future prospects of the studies described in chapter 2.



# Contents

Certificate	i
Acknowledgements	v
Thesis synopsis	vii
Table of content	xi

## Chapter 1: General introduction

1.1 Photocatalysis	1
1.2 Energy problem and its relation to photocatalysis	2
1.3 Type of photocatalytic reactions	4
1.3.1 Photocatalytic organic transformation reactions	4
1.3.2 Photocatalytic fuel generation reactions	6
1.4 Types of the photocatalytic systems	8
1.4.1 Homogeneous photocatalysis	8
1.4.2 Heterogeneous photocatalysis	9
1.5 Reaction mechanisms in heterogeneous photocatalysis	10
1.6 Recently developed heterogeneous semiconductor photocatalysts	12
1.7 Concluding remarks	15
Bibliography	17

## Chapter 2: Materials and characterization techniques

2.1.1 Materials	21
2.1.2 Characterization techniques	22

# Part 1: Carbon quantum dots; synthesis, unique properties and application in photocatalysis

## Chapter 3.1: Introduction

3.1.1	Carbon quantum dots	27
3.1.2	Composition and structure	28
3.1.3	Synthesis of carbon quantum dots (CQDs)	29
3.1.3.1	Top-down synthetic routes	30
3.1.3.2	Bottom-up synthetic routes	32
3.1.4	Surface passivation and functionalization	35
3.1.5	Optoelectronic properties of CQDs	36
3.1.5.1	Photoluminescence	38
3.1.5.2	Bandgap transitions originated from conjugated $\pi$ -domain	39
3.1.5.3	Fluorescence emissions originated via surface defects	39
3.1.6	Applications of CQDs	42
3.1.6.1	Chemical sensing	42
3.1.6.2	Bio-sensing and bio-imaging	42
3.1.6.3	Photocatalytic application	44
3.1.7	Concluding remarks	48
	Bibliography	49

## **Chapter 3.2: High and reversible oxygen uptake in carbon dot solutions generated from polyethylene**

Summary	53
3.2.1 Introduction	54
3.2.2 Scope of the present investigation	54
3.2.3 Methods	56
3.2.4 Results and discussion	59
3.2.4.1 Mechanism of CQDs formation	59
3.2.4.2 Oxygen adsorption of PE-CQDs	66
3.2.4.2 Photocatalytic performance	70
3.2.5 Concluding remarks	83
Bibliography	84

## **Chapter 3.3: Light-induced hypoxia in carbon quantum dots and ultrahigh photocatalytic efficiency**

Summary	87
3.3.1 Introduction	88
3.3.2 Scope of the present investigation	88
3.3.3 Methods	90
3.3.4 Results and discussion	92
3.3.4.1 Origin of high oxygen adsorption and light induced desorption (hypoxia) (Experimental and theoretical studies)	96
3.3.4.2 Photocatalytic oxidation of benzylamine	100
3.3.4.3 Mechanistic investigations	105
3.3.5 Conclusions	107

## **Chapter 3.4: ‘Autophagy’ and unique aerial O<sub>2</sub> harvesting properties exhibited by highly photocatalytic CQDs**

Summary	111
3.4.1 Introduction	112
3.4.2 Scope of the present investigation	112
3.4.3 Methods	114
3.4.4 Results and discussion	116
3.4.4.1 Total oxygen content in PE-CQDs	120
3.4.4.2 Photocatalytic oxidation of benzyl alcohol by PE-CQDs	122
3.4.4.3 Mechanistic investigations	126
3.4.4.4 Of stability, light-induced oxidative-elimination, or autophagy of CQDs	127
3.4.5 Conclusions	133
Bibliography	135

## **Chapter 3.5: Conclusions of Part 1 & future directions** 137



## **Part 2: Novel syntheses of g-C<sub>3</sub>N<sub>4</sub> based highly active photocatalysts**

### **Chapter 4.1: Introduction**

4.1.1	Graphitic C <sub>3</sub> N <sub>4</sub>	143
4.1.2	History of Carbon Nitrides	143
4.1.3	Structure of carbon nitride	144
4.1.4	Optical properties of g-C <sub>3</sub> N <sub>4</sub>	145
4.1.5	Synthesis of g-C <sub>3</sub> N <sub>4</sub>	148
4.1.6	Applications of g-C <sub>3</sub> N <sub>4</sub>	151
4.1.7	Concluding remarks	157
	Bibliography	158

### **Chapter 4.2: Wavelength-dependent luminescence decay kinetics in g-C<sub>3</sub>N<sub>4</sub> NSs; plasmonic enhancement**

	Summary	161
4.2.1	Introduction	162
4.2.2	Scope of the present investigation	163
4.2.3	Methods	164
4.2.4	Results and discussion	166
	4.2.4.1 The unusual optical properties of the nanosheets	170
	4.2.4.2 Photocatalytic oxidation of benzylamine and its derivatives	177
	4.2.4.3 Co-catalytic vs. plasmonic enhancement of the activity	181
	4.2.4.4 Mechanistic investigations	182
4.2.5	Conclusions	185
	Bibliography	186

## **Chapter 4.3: Enhanced catalytic activity of Pd NPs towards Suzuki Cross-Coupling by g-C<sub>3</sub>N<sub>4</sub> photosensitization**

Summary	189
4.3.1 Introduction	190
4.3.2 Scope of the present investigation	190
4.3.3 Methods	192
4.3.4 Results and discussion	193
4.3.4.1 Photocatalytic Suzuki cross-coupling reaction	198
4.3.4.2 Mechanistic investigation	200
4.3.5 Conclusions and further studies	203
Bibliography	204

## **Chapter 4.4: One-step high-yield synthesis of high surface-area g-C<sub>3</sub>N<sub>4</sub> NSs for enhanced light absorption & solar H<sub>2</sub>-evolution**

Summary	207
4.4.1 Introduction	208
4.4.2 Scope of the present investigation	208
4.4.3 Methods	209
4.4.4 Results and discussion	210
4.4.5 Application	215
4.4.6 Conclusions and further studies	217
Bibliography	218

## **Chapter 4.5: Conclusions of part 2 & future directions** 220





# CHAPTER 1

## General Introduction

### 1.1 Photocatalysis

Photocatalysis is a process that produces useful chemical energy by utilizing light energy.<sup>1,2</sup> Sunlight is a sustainable, renewable, and globally available energy source. One strategy to store solar energy is to utilize that energy for the synthesis of chemicals (“solar chemicals”) and fuel molecules (“solar fuels”), via artificial photosynthesis.<sup>3</sup> The essential requirement to carry out the artificial photosynthesis is the use of a light-harvesting catalyst suspended with electron donor and acceptor substrates in an aqueous medium and sunlight as a source of energy, sometimes directly and sometimes with the assistance of an external electrical source as shown in **Figure 1.1**.<sup>4</sup> This idea was inspired by natural photosynthesis, where plants convert carbon dioxide and water into carbohydrates using sunlight.

Key goals of solar chemical synthesis are the photocatalytic conversion through oxidation or reduction of one chemical into other useful chemicals such as the synthesis of amines, aldehydes, ketones, and many more using solar energy in the presence of a photocatalyst.<sup>5-10</sup> On the other hand, a similar process can also be used to generate H<sub>2</sub> from H<sub>2</sub>O and conversion of CO<sub>2</sub> to CO, hydrocarbons such as CH<sub>4</sub>, C<sub>2</sub>H<sub>6</sub>, acids (HCO<sub>2</sub>H) or alcohols (CH<sub>3</sub>OH) under sunlight illumination in the presence of a photocatalyst.<sup>11-18</sup> The photocatalytic process has several advantages over conventional catalysis that uses high temperatures and pressures, tedious steps, and the use of expensive/toxic catalysts. Investigations on photocatalysis have grown tremendously since the discovery of photocatalytic water-splitting on TiO<sub>2</sub> by Honda and Fujishima in 1972.<sup>4,19</sup> Particularly, designing a metal-free visible-light responsive photocatalyst is intriguing due to the increasing demand for global energy as they are inexpensive and usually non-toxic. Therefore, a great deal of effort has been put in by many scientists at present to develop scalable and eco-friendly photocatalytic systems with high conversion efficiencies.

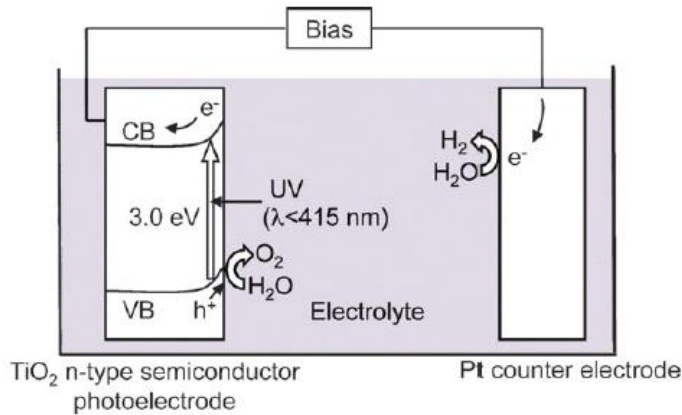


**Figure 1.1** Honda-Fujishima effect on water-splitting using a  $\text{TiO}_2$  photoelectrode. Herein, light is shined on a  $\text{TiO}_2$  anode to generate excited electrons. Due to the extra energy possessed by the electron, water oxidation occurs at the electrode with minimal use of electricity. As a counter-reaction,  $\text{H}_2$  fuel is generated at the Pt cathode. Adapted with permission from [19].

## 1.2 Energy problem and its relation to photo-catalysis

Both environmental protection and sustainable energy supply are the two prime concerns for the sustainable development of the present society. Meeting the growing energy demand is one of the most important challenges of the 21<sup>st</sup> century.<sup>20</sup> Currently, our society depends highly on fossil fuels for the supply of energy. However, the burning of fossil fuel produces a large quantity of  $\text{CO}_2$ , which significantly increases the greenhouse effect, and also the nitrogen and sulphur containing impurities that eventually convert to  $\text{NO}_x$  and  $\text{SO}_x$  respectively during the combustion process, which causes environmental pollution. Also due to the high consumption rate, the fuel supply will not meet the fuel demand by the next century and therefore replacement of fossil-fuels with other alternative renewable energies is highly important. Solar energy is attractive among all alternative energy resources due to its high abundance, cleanliness, and easy accessibility. Each year, approximately 3850000 exajoules (EJ) of solar power is received by the Earth and only 1% of this total energy is sufficient to meet the energy demand of human beings at the present rate of energy consumption. To date, globally per year, humans expend only 539 EJ, which is nearly 0.014% of the total solar energy available on the Earth surface. The global utilization of solar energy by developing new approaches such as photocatalysis, solar heating, solar thermal electricity, and solar photovoltaics, may increase the world's energy security by reducing

pollution, enhancing sustainability, and reducing fossil fuel dependency. **Figure 1.2** shows the total energy produced by different sources including solar sources.<sup>21</sup>

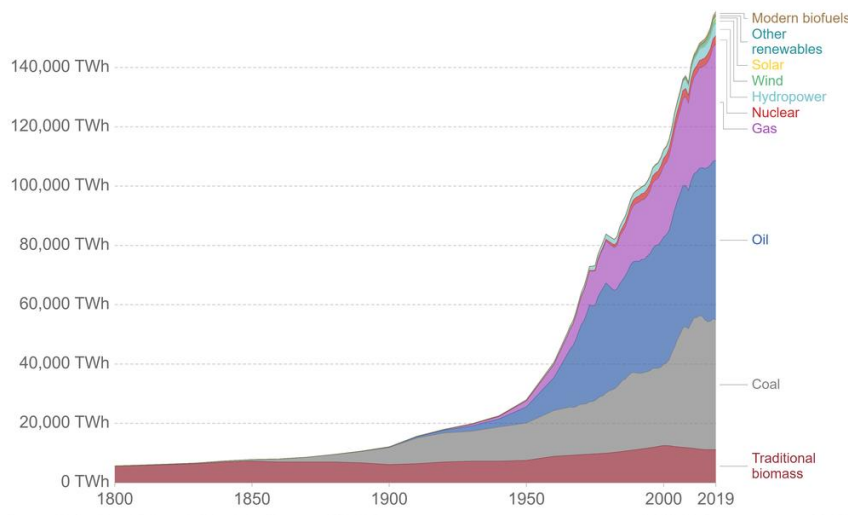


**Figure 1.2** The trends in total world energy consumption split on various sources from 1800 to 2019. Adapted with permission from [21].

Recently, the direct utilization of solar energy has gained considerable attention and it is necessary to develop new approaches where solar energy can be directly used with improved efficiency.<sup>22,23</sup> Yang and co-workers designed core-shell nanostructure of CdS-Cu<sub>2</sub>S and used them as photovoltaic devices which show 3.8% of power conversion efficiencies and also stable up to one month when stored inside the desiccator.<sup>24</sup> Among various routes, photocatalysis is one of the most promising approaches for the direct utilization of solar energy. The photocatalytic application includes the evolution of hydrogen from the splitting of water, conversion of CO<sub>2</sub> into hydrocarbon fuels, organic transformations, and pollutant degradation.<sup>5,8,12,16-18,25-32</sup> The photocatalytic efficiency of a catalyst depends on several factors such as light absorption-capacity and the extent of exciton separation within the photocatalyst. In recent days, many excellent photocatalysts have been developed to improve the hydrogen production efficiency from water electrolysis and organic reactions.<sup>20</sup> Hydrogen gas is energetically dense by weight and storable which makes it attractive as a fuel for the storage of solar energy. Besides, H<sub>2</sub> is a feedstock for

various catalytic processes and thus can be used to convert carbon dioxide and nitrogen into liquid fuels for easy handling.

A typical photocatalytic reaction is the degradation of toxic dye molecules used in coloring and textile industries.<sup>33-36</sup> Therein, oxygen molecules adsorbed on the surface of a photocatalyst get reduced to superoxide radicals in the presence of photogenerated electrons in the conduction band of the catalyst while the holes in the valence band react with water to form hydroxyl radicals. Thus, simultaneous oxidation and reduction reactions take place with the involvement of photogenerated holes and electrons in the valence and conduction band respectively. The produced superoxide radicals and together with the hydroxyl radicals decompose organic pollutant molecules in the wastewater to small molecules such as water and carbon dioxide.

### **1.3 Type of photocatalytic reactions**

Photocatalytic reactions can be classified into two different major categories depending upon the nature of the reaction. (i) Photocatalytic organic-transformations, and (ii) photocatalytic fuel generation reactions.

#### **1.3.1 Photocatalytic organic-transformation reactions**

Many organic chemicals are crucial intermediates for the manufacturing of a large number of commodities and various other useful chemicals including pesticides, pharmaceuticals, and food additives. Though many organic synthesis routes and manufacturing processes have been established by chemical industries, the environmental impact of those processes has not yet changed greatly over the years. However, with the increasing use of some of the catalysts, reagents, waste solvents, and toxicity of by-products, environmental concerns have become more stringent. Besides, the safety issues related to the handling of highly reactive and toxic reagents and the energy costs also need additional consideration. Therefore, improvements in each step of the manufacturing processes by including alternative green processing method and green synthesis route is highly required. The conventional methods for the synthesis of many important organic chemicals require harsh reaction conditions, such as high pressure and temperature. Therefore, the development of the photocatalytic route, a greener approach that employs light as an energy source



to drive the chemical reaction with milder experimental conditions is highly desirable. These photocatalytic routes may be heterogeneous or homogeneous in nature. The homogeneous systems utilize reaction-media soluble photosensitive molecules such as photoactive dyes whereas the heterogeneous system employs particulates or films of semiconductor photocatalysts.

Many photocatalytic organic transformation reactions have been known to date such as oxidation of benzyl alcohol to benzaldehyde, benzylamine to imine, cyclohexane to cyclohexanone, and many more.<sup>37-51</sup> These organic transformation reactions are important because of the use of the product in pharmaceutical, bio-medicinal chemistry as well as fine chemical synthesis. Apart from the greener approach, the photocatalytic reactions also give higher selectivity to the products in many occasions due to special geometrical formulations of the catalyst-reactant adducts, which is crucial. However, the desired product selectivity remains unsatisfactory under UV-induced chemical reactions due to the formation of free radical species during the reaction. This issue becomes more prominent during the selective oxidation of organic compounds using molecular O<sub>2</sub> as an oxidant.<sup>52,53</sup> O<sub>2</sub> molecule can be easily coupled to the produced free radical species, leading to uncontrolled oxidation of the reactant or the product molecules. Therefore, visible-light-induced organic transformation reactions are favoured to obtain higher selectivity of the product. Li et al. reported a plasmonic Au supported BiOCl with oxygen vacancies by a simple hydrothermal method, which exhibited selective and controlled oxidation of benzyl alcohol into benzaldehyde under visible light and O<sub>2</sub> atmosphere (**Figure 1.3 a-b**).<sup>54</sup> It has been proposed that the oxygen vacancies present on BiOCl primarily facilitate the trapping and transfer of plasmonic hot-electron to adsorbed O<sub>2</sub>, producing superoxide radical anion, while the holes (plasmonic) on the Au surface oxidize benzyl alcohol into carbon-centered radicals. Next, the concerted additions of both the radical species result in the product (benzaldehyde) formation as shown in **Figure 1.3c**. The synergistic effect of both plasmonic electrons and holes is responsible for the highly selective and improved benzyl alcohol photo-oxidation.

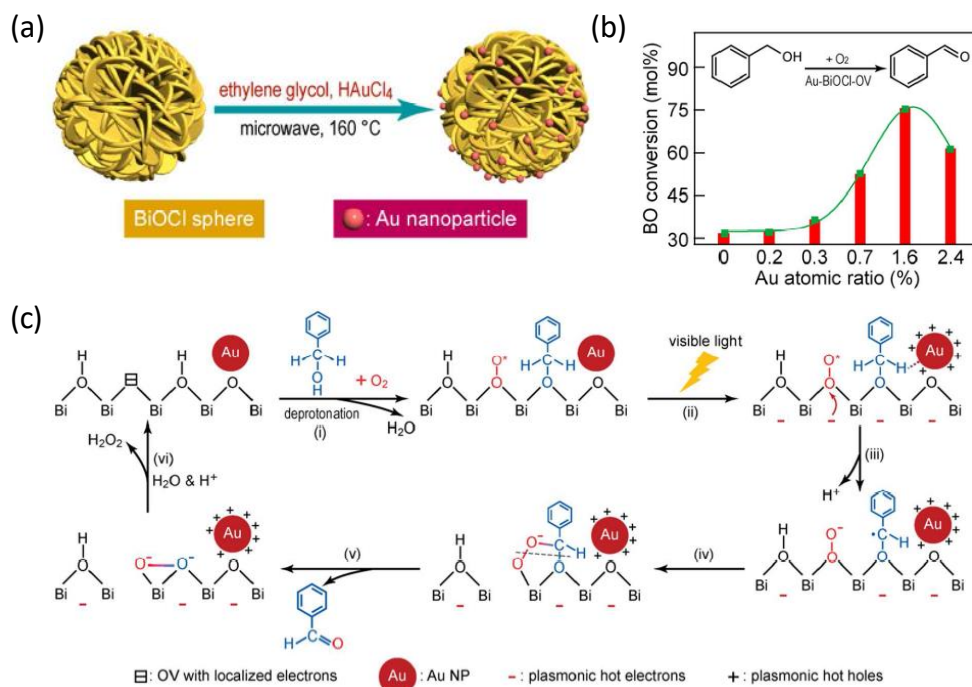
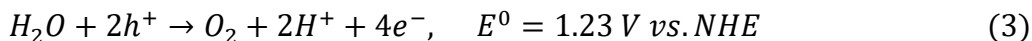
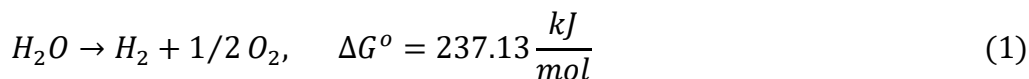


**Figure 1.3** (a) The schematic representation of the synthesis of Au-BiOCl-OV. (b) Photocatalytic BA oxidation activities of Au-BiOCl-OV with various Au loading amounts. (c) Proposed reaction mechanism of selective BA oxidation over Au-BiOCl-OV Adapted with permission from [54].

### 1.3.2 Photocatalytic fuel generation reactions

Significant attention has been given to explore novel routes for developing renewable energies. The transformation of solar energy into chemical energy in the form of solar fuels (such as H<sub>2</sub>, CH<sub>4</sub>, CH<sub>3</sub>OH, etc.) is deemed as one of the most promising strategies to solve environmental and energy problems in the future. The photocatalytic solar fuel generation has been mainly divided into two reactions; (a) photocatalytic water-splitting and (b) photocatalytic conversion of CO<sub>2</sub>.

**(a) Photocatalytic water-splitting:** Hydrogen has an energy content of 120–142 MJ kg<sup>-1</sup> which is higher than hydrocarbon fuels.<sup>55-57</sup> It has been predicted that up to 2080, it will be the major source of energy production (90%). At present, worldwide per year more than 44.5 million tons of H<sub>2</sub> are produced.<sup>58,59</sup> However, the splitting of water into hydrogen and oxygen is thermodynamically unfavourable which requires an energy input to overcome an energy barrier, based on Gibbs free energy values, as shown in equation 1.<sup>60</sup>



To drive the above chemical reactions, a semiconductor photocatalyst is required which is activated by photons having energy equal to or greater than its bandgap. In such a scenario, electrons go to the conduction band (CB) from the valence band (VB), while holes remain in the VB. These holes and electrons are capable of H<sub>2</sub>O oxidation and H<sup>+</sup> reduction respectively, only if the top of the VB is located at a more positive potential than the oxidation potential of H<sub>2</sub>O to O<sub>2</sub> (1.23 V vs. NHE at pH = 0, equation 3) and bottom of the CB is located at a value more negative potential than the reduction potential of H<sup>+</sup> to H<sub>2</sub> (0 V vs. NHE at pH = 0, equation 2).

Therefore, the transformation of solar energy into hydrogen energy has been considered as promising approach for utilizing solar energy and meeting the energy needs of the future. Among all different strategies applied for solar energy storage, photochemical and photo-electrochemical (PEC) water splitting approaches have gained tremendous attention due to their high efficiency and simplicity.<sup>61</sup> For such approaches, an ideal photocatalyst is highly necessary which should fulfil the following conditions: i) it should be of low cost, (ii) it should absorb a wide range of visible light energy, and iii) it should also have high catalytic efficiency and excellent stability. Along with a suitable photocatalyst and light source, an external circuit and a voltage bias are also used in PEC cells to generate H<sub>2</sub>. In contrast, in the photochemical process, simply irradiating a photocatalyst dispersed in an aqueous medium produces H<sub>2</sub> and therefore can be advantageous for its simplicity, ease of scale-up, and low cost.

**(b) Photocatalytic conversion of CO<sub>2</sub> into fuels:** The level of CO<sub>2</sub> in the atmosphere has risen significantly in the last few decades leading to global warming. There have been increasing research activities in finding ways to reduce atmospheric CO<sub>2</sub> leading to, in principle, two possible strategies: (i) reduction of CO<sub>2</sub> to value-added products or (ii) it's capturing and storage, probably in the deep sea. Since storage does not lead to a permanent solution, conversion of CO<sub>2</sub> to fuels, which can be carried out by direct use of sunlight or by electrochemical means or by a combination of both is one of the most promising processes.<sup>62-65</sup> However, this has appeared to be an extremely

challenging process due to the highly stable nature of the CO<sub>2</sub> molecule that does not easily undergo a chemical reaction, which inspired a surge in research activities recently. Researchers in the field have carried out CO<sub>2</sub> reduction reaction (CO<sub>2</sub>RR) in (i) a homogenous manner using metal complexes or (ii) by heterogeneous processes using solids, often having nanoscale dimensions, as active catalysts. The homogeneous CO<sub>2</sub>RR is inherently difficult due to the multi-electron requirement of reduction limited by single-photon, single-electron-transfer reactions. Besides, the stability of the metal complexes is poor too. Therefore, many believe that the heterogeneous catalytic approach is advantageous for the reduction of CO<sub>2</sub>.

## **1.4 Types of the photocatalytic systems**

Depending upon the physical nature of the catalysts, the photocatalytic reactions can be classified into two types (i) homogeneous and (ii) heterogeneous photocatalytic systems.

### **1.4.1 Homogeneous photocatalysis**

In a homogeneous photocatalytic system, the photocatalyst is soluble in the reaction medium leading to only one reaction phase. Upon light absorption or sensitization by chemical compounds, the electronic configuration changes due to electronic excitation.<sup>66-69</sup> Therefore, the reactivity of such chemical compounds remarkably changes with respect to the ground state of the molecules. Homogeneous photocatalysis by soluble metal complex as photocatalysts has been used for several years for various types of reactions such as carbonylation, hydrogenation, polymerization, and oxidation. The most unique feature of this catalytic system is a very high catalytic activity with higher selectivity under mild reaction conditions. It also can activate commercially available substrates such as hydrogen, CO, alcohols, and olefins. However, homogeneous catalysis was perceived industrial importance several decades ago with the development of hydroformylation technology (oxo-process), carbonylation of methanol to acetic acid, Wacker process, and ethylene polymerization by Zeigler-Natta catalysts. The activity performances of homogeneous photocatalysts depend on a few factors such as the type of metal, ligands, co-catalysts, and promoters. Several transition metal complexes highlighting metal to ligand charge transfer (MLCT) excited states complexes based on Ir(III), Ru(II), Cu(I) and Re(I), etc. have been extensively investigated for solar-driven H<sub>2</sub> generation. However, these photocatalysts are limited by their inherent poor photo-stability. Yang et al reported a cyclometalated Ir(III) diimine complex

which exhibited high photostability for the homogeneous aqueous photocatalytic hydrogen production for 90 h under visible-light irradiation (**Figure 1.4**).<sup>70</sup> The major drawback in homogeneous catalysis is the separation of products and most importantly catalyst from the reaction mixture. It is noteworthy that 80% of the industrial catalytic reactions involve heterogeneous catalysis consisting of supported metal catalysts.

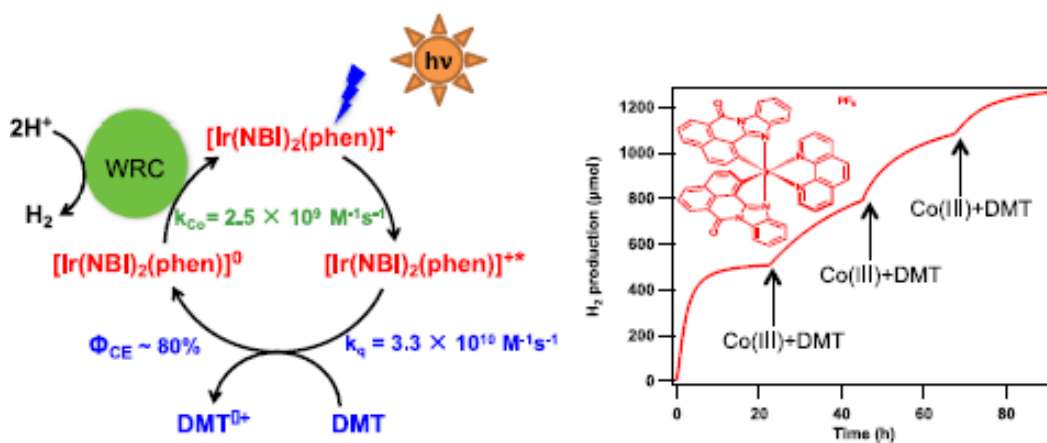


**Figure 1.4** (a) Proposed photocatalytic  $H_2$  evolution reaction using cyclometalated Ir(III) diimine complex. (b) The regeneration of  $H_2$  resumed after addition of fresh Co(III) catalyst and DMT at the end of each cycle, suggesting that the Co(III) catalyst and/or DMT degraded prior to the Ir(III) PS that remained active during visible light irradiation (90 h). Adapted with permission from [70].

## 1.4.2 Heterogeneous photocatalysis

In this system, the photocatalyst is immiscible in the reaction medium, making a separate phase. Various chemicals that are industrially important can be easily synthesized by using heterogeneous photocatalytic systems. Significant efforts have been made to develop new, highly active catalysts with the industrially achievable strategy of separation. Also, many research groups have attempted to explore the heterogeneous Pd catalysts for the olefins carbonylation. Several photocatalytic reactions have also been executed by depositing various metal NPs onto semiconductor oxide supports such as  $TiO_2$ ,  $ZrO_2$ ,  $ZnO$ , etc., polymer supports, and carbon-based supports.<sup>71-77</sup> Heterogeneous catalysis has few major advantages over homogeneous catalysis as discussed below:

(i) *Ease of separation of the photocatalysts:* Catalyst removal from the reaction vessel is highly challenging in the case of homogeneous catalysis. Due to the heterogeneous nature of the semiconductor photocatalyst, separation of the catalyst particles becomes easy after the completion of the reaction, such as by simple precipitation or filtering. However, there are certain limitations related to these photocatalytic systems from a fundamental understanding point of view as there are multiple, interdependent factors that influence their efficiencies as compared to well-defined molecular catalysts.

(ii) *High recyclability:* The heterogeneous nature and high stability of the photocatalysts enable multiple cycles of reactions with the same catalyst, which is desirable for any photocatalytic applications.

(iii) *Comparable catalytic activity:* Apart from the easy separation and stability of the catalysts, the activities obtained by the heterogeneous photocatalytic systems are also becoming comparable with the homogeneous photocatalytic systems, brightening their prospects in industrial applications.

### **1.5 Reaction mechanisms in heterogeneous photocatalysis**

In the case of heterogeneous photocatalysis, the catalysis reaction is primarily mediated by a photocatalyst. Each semiconductor photocatalyst has an electronic structure characterized by a VB (electron filled) and CB (empty) and the energy gap between them is called the bandgap of the semiconductor material. Upon light irradiation with equal or more than the bandgap energy of the semiconductor, an electron in VB gets excited and goes to the CB and at the same time, a hole is generated in the VB. Next, the excited electrons and holes in CB and VB respectively undergo charge-transfer to species adsorbed on the surface of the semiconductor from a gas-phase or the solution. The semiconductor surface can donate an electron to reduce an electron acceptor (e. g. molecular O<sub>2</sub>) (pathway C, **Figure 1.5**), and the surface migrated hole combines with an electron from the donor species and oxidizes the species (pathway D). The rate and the probability of the charge (photo-excited electrons and holes) transfer processes depend on the positions of the band edges for the CB and VB and also on the adsorbate species redox potential levels. In competition, recombination of the photogenerated electron and hole can occur in the volume of the

semiconductor material (pathway B) or on the surface (pathway A) with the released energy in the form of heat or luminescence.

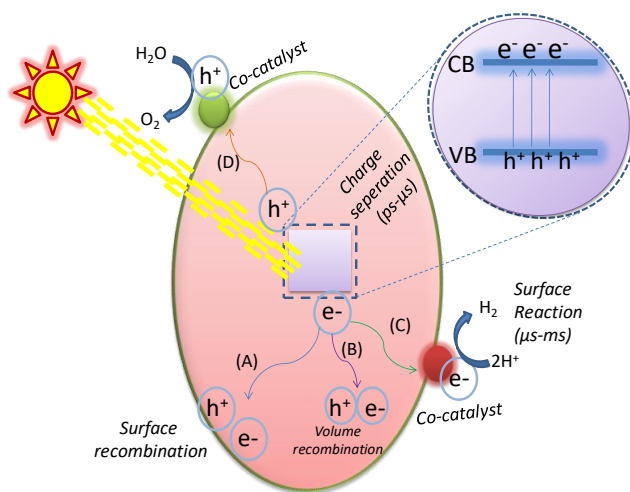


**Figure 1.5** Schematic of photo-excitation in a heterogeneous photocatalyst system. Pathway A and B represent the surface and volume recombination of exciton pairs that limit photocatalytic efficiency. Pathway C and D show the oxidation and reduction reactions carried out by excitons generated in a photocatalyst system.

Generally, in the case of a heterogeneous photocatalytic system, the catalytic reaction takes place in the adsorbed phase and the overall reaction process can be broken down into the following steps:

- 1) At least one of the reactants gets adsorbed.
- 2) Reactants transfer from the bulk of fluid to the catalyst surface.
- 3) Reactants transfer from the external catalyst surface to a catalytically active centre.
- 4) The catalytic reaction takes place in the adsorbed phase.
- 5) The desorption of the product molecule occurs.
- 6) Transfer of the product molecule from the vicinity of the active site to the bulk of the fluid.

Therefore, for improving the efficiency of the heterogenous photocatalysts, multiple factors have to be addressed. However, one factor may not be independent of another, giving rise to the need for complex manoeuvring all of them simultaneously.

## 1.6 Recently developed heterogeneous semiconductor photocatalysts

To date, various metal-based semiconductor photocatalysts such as TiO<sub>2</sub>, Fe<sub>2</sub>O<sub>3</sub>, ZnO, Cu<sub>2</sub>O, CdS, Ag<sub>3</sub>PO<sub>4</sub>, WO<sub>3</sub>, SrTiO<sub>3</sub>, and BiVO<sub>4</sub>, etc. have shown exciting prospects for many photocatalytic applications such as water-splitting, organic pollutant removal, CO<sub>2</sub> reduction, organic transformation reactions, etc.<sup>78</sup> The band positions of these semiconductors are displayed in **Figure 1.6**.<sup>79</sup> Over the past few decades, though these semiconductor materials have exhibited high catalytic performance in extensive studies by many research groups, there are still limitations associated with them that might restrict their practical applications. Among the afore-mentioned photocatalysts, TiO<sub>2</sub>, SrTiO<sub>3</sub>, and ZnO are active in the UV region, corresponding to only ~4% in the solar spectrum and limiting applications under natural sunlight while CdS, Cu<sub>2</sub>O, and Ag<sub>3</sub>PO<sub>4</sub> suffer due to their toxic and photo-corrosive nature. In addition, in many cases the most of the photo-generated electron-hole pairs tend to recombine in the photocatalysts, leading to a depletion of the catalytic activity. To date, many strategies have been developed to overcome such drawbacks. Besides, the high cost and limited source of the metallic precursor confine their practical applications.

Carbon-based semiconductors such as carbon quantum dots (CQDs), graphene oxide (GO), and graphitic carbon nitride (g-C<sub>3</sub>N<sub>4</sub>) have showed promise in enhancing the photocatalytic performance, by increasing surface-area, active sites and adsorption efficiency, and as co-catalysts and electron acceptors during photosensitization, etc.<sup>80-83</sup> Apart from the low cost, CQDs and g-C<sub>3</sub>N<sub>4</sub> are also visible light active photocatalysts and hence used for many catalytic applications such as water-splitting, CO<sub>2</sub> reduction, organic transformation, and so forth. However, low light absorption co-efficient and a higher rate of recombination further limit their application in catalysis. Therefore, numerous strategies have been developed to further improve their light absorption properties and to decrease the rate of exciton recombination.

In general, visible light-harvesting carbon-based metal-free semiconductors are very few. In them, exciton recombination is a major reason for efficiency drop. Besides, their absorption in the visible range is very less. In this context, surface plasmon-generated hot electrons in metal nanoparticles (NPs) can extraordinarily increase the absorption in the visible range and hence increase the photocatalytic activity for various reactions. In 2005, Tatsuma and co-workers elegantly illustrated the phenomenon of hot electron injection using Au nanocrystals and TiO<sub>2</sub>.<sup>84</sup>



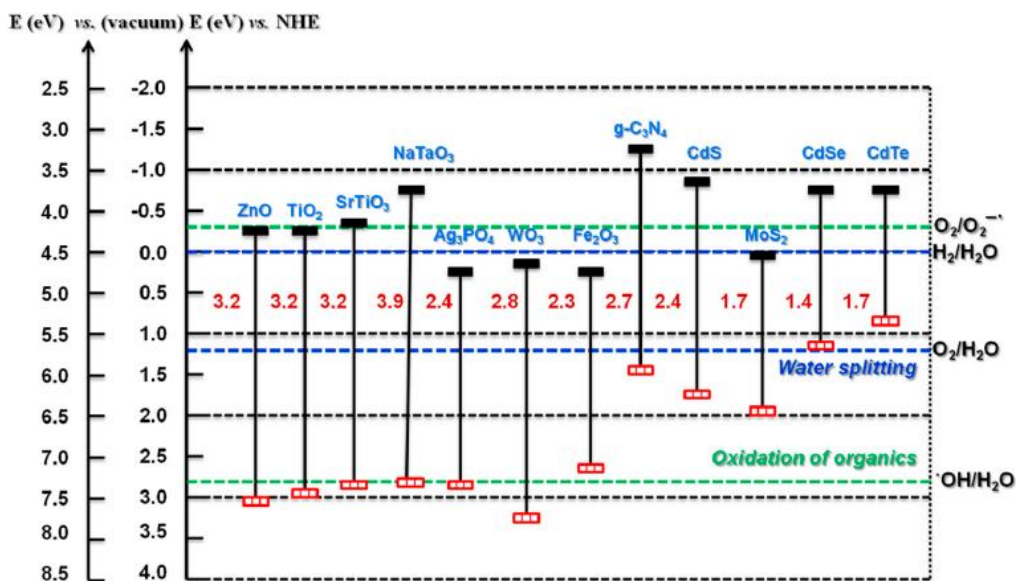


**Figure 1.6** Schematic representation of the band-gap energy ( $E_g$ ), positions of VB and CB of several widely used heterogeneous semiconductor photocatalysts. Adapted with permission from [79].

Mie's theory defines the localized surface plasmon resonance (LSPR) as the coherent oscillation of charges induced by the resonant photon established at the interface of metal-dielectric when the photon frequency matches with the frequency of metal surface electrons which oscillates against restoring force of their positive nuclei. Simply stated, LSPR is the collective oscillation of free- electrons on the surface of metal NPs which is driven through the electromagnetic field generated by the incident light.<sup>85</sup> For example, Ag, Au, and Cu NPs exhibit a strong photo-absorption in the visible energy range because of their surface plasmon that shows maxima at nearly 400, 550, and 580 nm, respectively. However, Ag and Cu nanostructures easily get oxidized, while Au nanoparticles are chemically more stable. The energy accumulated in the LSPR process may decay by two pathways: i) radiative pathway via the re-emission of a photon, and ii) non-radiative pathway through the production of hot charge carriers as displayed in **Figure 1.7**.<sup>86,71</sup>

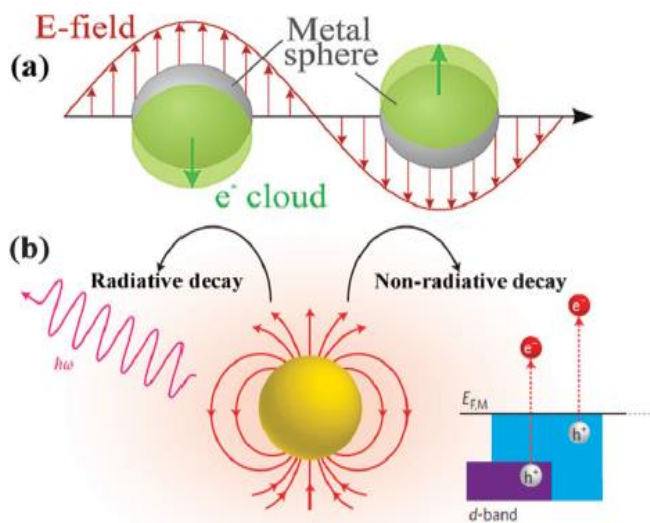


**Figure 1.7** A schematic of LSPR in a spherical metal NP that is irradiated by light. Adapted with permission from [86]. (b) surface-plasmon decay processes: localized surface plasmons can decay non-radiatively via excitation of hot electrons (right), or radiatively via re-emitted photons (left). Adapted with permission from [71].

Excellent light absorption via LSPR and production of hot carriers extended the use of plasmonically active metal NPs as an efficient photocatalyst -assist. Earlier the photocatalytic studies were primarily influenced by improving both light-absorption and charge-separation efficiency by the use of metal NPs as a plasmonic antenna in a metal/semiconductor hybrid system. Recently, Jain and co-workers have demonstrated the capability of multielectron transfer in plasmonic AuNP, where, Au NPs reduce  $\text{CO}_2$  to  $\text{CH}_4$  and  $\text{C}_2\text{H}_6$ , under visible light illumination (**Figure 1.8a**).<sup>87</sup> The  $\text{CO}_2$  to  $\text{CH}_4$  reduction involves an  $8\text{e}^-$ - $8\text{H}^+$  transfer while the reduction into  $\text{C}_2\text{H}_6$  requires a  $12\text{e}^-$ - $12\text{H}^+$  transfer step. Moreover, the formation of  $\text{CH}_4$  and  $\text{C}_2\text{H}_6$  was also controlled by tuning the light-intensity, which successively controls the formation of hot charge-carriers (**Figure 1.8b-c**). The presence of a suitable hole scavenger (to reduce recombination rate) and higher photon flux (to increase the electron excitation rate), were found to be pivotal for the accumulation and multiple charge carriers transfer on the NPs surface. Similarly, one of the photocatalytic studies using Ag/AgBr/g- $\text{C}_3\text{N}_4$  ternary system was reported by Wang and co-workers (**Figure 1.8d**).<sup>88</sup> The enhancement of light absorption is primarily due to the LSPR effect

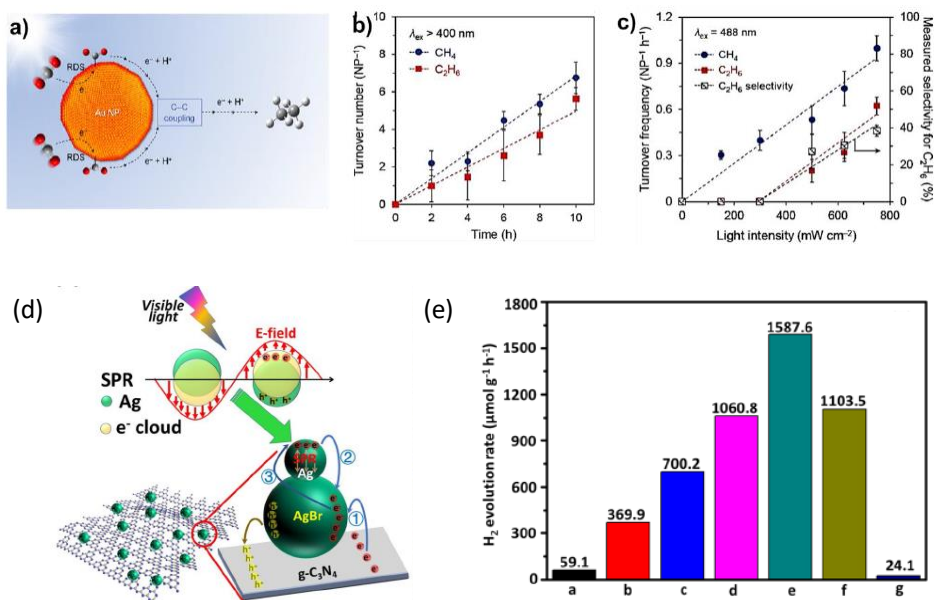


**Figure 1.8** (a) Schematic illustration for photocatalytic reduction of CO<sub>2</sub> on plasmonic AuNP. (b) Time dependent CH<sub>4</sub> and C<sub>2</sub>H<sub>6</sub> formation under visible light (> 400 nm). (c) Intensity-dependent CH<sub>4</sub> and C<sub>2</sub>H<sub>6</sub> formation under 488 nm laser irradiation. Adapted with permission from [87]. (d) Schematic of the charge separation in ternary hybrid photocatalyst of Ag/AgBr/g-C<sub>3</sub>N<sub>4</sub> photocatalysts under visible-light. (e) The plot of average rate of H<sub>2</sub> production: (a) g-C<sub>3</sub>N<sub>4</sub>, (b) 5% Ag/AgBr/g-C<sub>3</sub>N<sub>4</sub>, (c) 10% Ag/AgBr/g-C<sub>3</sub>N<sub>4</sub>, (d) 15% Ag/AgBr/g-C<sub>3</sub>N<sub>4</sub>, (e) 18% Ag/AgBr/g-C<sub>3</sub>N<sub>4</sub>, (f) 21% Ag/AgBr/g-C<sub>3</sub>N<sub>4</sub> and (g) Ag/AgBr under visible-light. Adapted with permission from [88].

of Ag NPs in the ternary system. The synergistic effect between g-C<sub>3</sub>N<sub>4</sub> and Ag/AgBr leads to an improved photocatalytic H<sub>2</sub> evolution activity and long-term stability (**Figure 1.8e**). Hou et al. reported plasmonic Au/TiO<sub>2</sub> photocatalyst used for the generation of hydrocarbon fuels from CO<sub>2</sub> under visible illumination, leading to 24-fold enhancement in activity due to the intense electromagnetic fields produced by the surface plasmons of the Au NPs.<sup>89</sup>

## 1.7 Concluding remarks

It can be seen from the above discussion that to improve photocatalytic efficiency, suitable modification or design of photocatalyst is necessary. Besides, the choice of material with respect to band position is another key parameter which plays an important role for various photocatalytic reactions. Several strategies such as loading of plasmonic metal nanoparticles for extra light-

harvesting, other noble metal nanoparticles as co-catalysts, formation of Z-scheme heterojunctions with other semiconductors etc. for superior charge separation, etc. have been adopted to enhance the overall photocatalytic performance of a material. Among various semiconductors, carbon-based semiconductors (such as g-C<sub>3</sub>N<sub>4</sub>, CQDs etc.) have gained significant research attention in photocatalytic applications due to their unique and tunable optical properties and ease to synthesis.

However, for sustainable application, improvement in several areas is still needed. In this regard, the synthesis strategies for the functional materials that are easy, inexpensive and scalable is needed to be developed. More attention should be given for achieving long-term stability of the photocatalysts. It will be advantageous to understand charge-transfer dynamics in the catalyst for designing the photocatalyst. As most of them are heterostructures, interfacial characterization for efficient charge transfer is very important and needed to be understood in detail. By successfully addressing them, it will be possible to use solar energy efficiently and move towards a greener future.

## Bibliography

1. H. Wang, L. Zhang, Z. Chen, J. Hu, S. Li, Z. Wang, J. Liu and X. Wang, *Chem. Soc. Rev.*, 2014, **43**, 5234–5244.
2. Y. Wang, H. Suzuki, J. Xie, O. Tomita, D. J. Martin, M. Higashi, D. Kong, R. Abe and J. Tang, *Chem. Rev.*, 2018, **118**, 5201–5241.
3. G. A. M. Hutton, B. C. M. Martindale and E. Reisner, *Chem. Soc. Rev.*, 2017, **46**, 6111–6123.
4. A. FUJISHIMA and K. HONDA, *Nature*, 1972, **238**, 37–38.
5. X. Lang, X. Chen and J. Zhao, *Chem. Soc. Rev.*, 2014, **43**, 473–486.
6. J. Kou, C. Lu, J. Wang, Y. Chen, Z. Xu and R. S. Varma, *Chem. Rev.*, 2017, **117**, 1445–1514.
7. A. Savateev, I. Ghosh, B. König and M. Antonietti, *Angew. Chemie Int. Ed.*, 2018, **57**, 15936–15947.
8. L. Chen, J. Tang, L.-N. Song, P. Chen, J. He, C.-T. Au and S.-F. Yin, *Appl. Catal. B Environ.*, 2019, **242**, 379–388.
9. D. Friedmann, A. Hakki, H. Kim, W. Choi and D. Bahnemann, *Green Chem.*, 2016, **18**, 5391–5411.
10. H. Hao, L. Zhang, W. Wang and S. Zeng, *Catal. Sci. Technol.*, 2018, **8**, 1229–1250.
11. Q. Wang and K. Domen, *Chem. Rev.*, 2020, **120**, 919–985.
12. J. Ran, J. Zhang, J. Yu, M. Jaroniec and S. Z. Qiao, *Chem. Soc. Rev.*, 2014, **43**, 7787–7812.
13. K. Maeda and K. Domen, *J. Phys. Chem. Lett.*, 2010, **1**, 2655–2661.
14. M. Ni, M. K. H. Leung, D. Y. C. Leung and K. Sumathy, *Renew. Sustain. Energy Rev.*, 2007, **11**, 401–425.
15. J. Ran, M. Jaroniec and S.-Z. Qiao, *Adv. Mater.*, 2018, **30**, 1704649.
16. J. Albero, Y. Peng and H. García, *ACS Catal.*, 2020, **10**, 5734–5749.
17. Y.-X. Pan, Y. You, S. Xin, Y. Li, G. Fu, Z. Cui, Y.-L. Men, F.-F. Cao, S.-H. Yu and J. B. Goodenough, *J. Am. Chem. Soc.*, 2017, **139**, 4123–4129.
18. Y.-F. Xu, M.-Z. Yang, B.-X. Chen, X.-D. Wang, H.-Y. Chen, D.-B. Kuang and C.-Y. Su, *J. Am. Chem. Soc.*, 2017, **139**, 5660–5663.
19. A. Kudo and Y. Miseki, *Chem. Soc. Rev.*, 2009, **38**, 253–278.
20. W. Wang, M. O. Tadé and Z. Shao, *Chem. Soc. Rev.*, 2015, **44**, 5371–5408.
21. "Wind energy generation by region". *Our World in Data*. Retrieved 5 March 2020.
22. N. S. Lewis, *Science (80-. )*, 2016, **351**, aad1920.
23. Y. Kuang, Y. Zhang, B. Zhou, C. Li, Y. Cao, L. Li and L. Zeng, *Renew. Sustain. Energy Rev.*, 2016, **59**, 504–513.
24. A. B. Wong, S. Brittman, Y. Yu, N. P. Dasgupta and P. Yang, *Nano Lett.*, 2015, **15**, 4096–4101.
25. T. Takata, J. Jiang, Y. Sakata, M. Nakabayashi, N. Shibata, V. Nandal, K. Seki, T. Hisatomi and K. Domen, *Nature*, 2020, **581**, 411–414.
26. K. Takanabe, *ACS Catal.*, 2017, **7**, 8006–8022.
27. Z. Liu, W. Hou, P. Pavaskar, M. Aykol and S. B. Cronin, *Nano Lett.*, 2011, **11**, 1111–1116.
28. I. K. Konstantinou and T. A. Albanis, *Appl. Catal. B Environ.*, 2004, **49**, 1–14.
29. S. Veziroglu, A.-L. Obermann, M. Ullrich, M. Hussain, M. Kamp, L. Kienle, T. Leißner,

- H.-G. Rubahn, O. Polonskyi, T. Strunskus, J. Fiutowski, M. Es-Souni, J. Adam, F. Faupel and O. C. Aktas, *ACS Appl. Mater. Interfaces*, 2020, **12**, 14983–14992.
30. S. Sakthivel, B. Neppolian, M. V Shankar, B. Arabindoo, M. Palanichamy and V. Murugesan, *Sol. Energy Mater. Sol. Cells*, 2003, **77**, 65–82.
  31. S. Wang, D. Li, C. Sun, S. Yang, Y. Guan and H. He, *Appl. Catal. B Environ.*, 2014, **144**, 885–892.
  32. N. M. Mahmoodi, M. Arami, N. Y. Limaee and N. S. Tabrizi, *J. Colloid Interface Sci.*, 2006, **295**, 159–164.
  33. M. A. Basith, R. Ahsan, I. Zarin and M. A. Jalil, *Sci. Rep.*, 2018, **8**, 11090.
  34. F. Liu, Y. H. Leung, A. B. Djurišić, A. M. C. Ng and W. K. Chan, *J. Phys. Chem. C*, 2013, **117**, 12218–12228.
  35. R. Pelegrini, P. Peralta-Zamora, A. R. de Andrade, J. Reyes and N. Durán, *Appl. Catal. B Environ.*, 1999, **22**, 83–90.
  36. S. Kampouri, T. N. Nguyen, M. Spodaryk, R. G. Palgrave, A. Züttel, B. Smit and K. C. Stylianou, *Adv. Funct. Mater.*, 2018, **28**, 1806368.
  37. C. Meng, K. Yang, X. Fu and R. Yuan, *ACS Catal.*, 2015, **5**, 3760–3766.
  38. Y. Markushyna, P. Lamagni, J. Catalano, N. Lock, G. Zhang, M. Antonietti and A. Savateev, *ACS Catal.*, 2020, **10**, 7336–7342.
  39. Z. Liu, Q. Su, P. Ju, X. Li, G. Li, Q. Wu and B. Yang, *Chem. Commun.*, 2020, **56**, 766–769.
  40. J. Shi, J. Zhang, T. Liang, D. Tan, X. Tan, Q. Wan, X. Cheng, B. Zhang, B. Han, L. Liu, F. Zhang and G. Chen, *ACS Appl. Mater. Interfaces*, 2019, **11**, 30953–30958.
  41. C. Zheng, G. He, X. Xiao, M. Lu, H. Zhong, X. Zuo and J. Nan, *Appl. Catal. B Environ.*, 2017, **205**, 201–210.
  42. H. Liu, C. Xu, D. Li and H.-L. Jiang, *Angew. Chemie Int. Ed.*, 2018, **57**, 5379–5383.
  43. W. Feng, G. Wu, L. Li and N. Guan, *Green Chem.*, 2011, **13**, 3265–3272.
  44. H. Tsunoyama, N. Ichikuni, H. Sakurai and T. Tsukuda, *J. Am. Chem. Soc.*, 2009, **131**, 7086–7093.
  45. S. Yurdakal, G. Palmisano, V. Loddo, V. Augugliaro and L. Palmisano, *J. Am. Chem. Soc.*, 2008, **130**, 1568–1569.
  46. A. Abad, P. Concepción, A. Corma and H. García, *Angew. Chemie Int. Ed.*, 2005, **44**, 4066–4069.
  47. J. A. Mueller, C. P. Goller and M. S. Sigman, *J. Am. Chem. Soc.*, 2004, **126**, 9724–9734.
  48. H. Hattori, Y. Ide, S. Ogo, K. Inumaru, M. Sadakane and T. Sano, *ACS Catal.*, 2012, **2**, 1910–1915.
  49. D. Peng, Y. Zhang, G. Xu, Y. Tian, D. Ma, Y. Zhang and P. Qiu, *ACS Sustain. Chem. Eng.*, 2020, **8**, 6622–6633.
  50. J. Liu, Y. Yang, N. Liu, Y. Liu, H. Huang and Z. Kang, *Green Chem.*, 2014, **16**, 4559–4565.
  51. J. T. Carneiro, J. A. Moulijn and G. Mul, *J. Catal.*, 2010, **273**, 199–210.
  52. F. Su, S. C. Mathew, G. Lipner, X. Fu, M. Antonietti, S. Blechert and X. Wang, *J. Am. Chem. Soc.*, 2010, **132**, 16299–16301.
  53. M. Zhang, C. Chen, W. Ma and J. Zhao, *Angew. Chemie*, 2008, **120**, 9876–9879.
  54. H. Li, F. Qin, Z. Yang, X. Cui, J. Wang and L. Zhang, *J. Am. Chem. Soc.*, 2017, **139**, 3513–3521.
  55. T. da Silva Veras, T. S. Mozer and A. da Silva César, *Int. J. Hydrogen Energy*, 2017, **42**,

- 2018–2033.
56. A. Naseri, M. Samadi, A. Pourjavadi, A. Z. Moshfegh and S. Ramakrishna, *J. Mater. Chem. A*, 2017, **5**, 23406–23433.
  57. X. Zou and Y. Zhang, *Chem. Soc. Rev.*, 2015, **44**, 5148–5180.
  58. S. J. A. Moniz, S. A. Shevlin, D. J. Martin, Z.-X. Guo and J. Tang, *Energy Environ. Sci.*, 2015, **8**, 731–759.
  59. T. Hisatomi and K. Domen, *Nat. Catal.*, 2019, **2**, 387–399.
  60. Z. Wang, C. Li and K. Domen, *Chem. Soc. Rev.*, 2019, **48**, 2109–2125.
  61. H. Yu, R. Shi, Y. Zhao, G. I. N. Waterhouse, L.-Z. Wu, C.-H. Tung and T. Zhang, *Adv. Mater.*, 2016, **28**, 9454–9477.
  62. Ž. Kovačič, B. Likozar and M. Huš, *ACS Catal.*, 2020, **10**, 14984–15007.
  63. X. Liu, S. Inagaki and J. Gong, *Angew. Chemie Int. Ed.*, 2016, **55**, 14924–14950.
  64. O. Ola and M. M. Maroto-Valer, *J. Photochem. Photobiol. C Photochem. Rev.*, 2015, **24**, 16–42.
  65. D. Li, M. Kassymova, X. Cai, S.-Q. Zang and H.-L. Jiang, *Coord. Chem. Rev.*, 2020, **412**, 213262.
  66. J. Bonin, M. Robert and M. Routier, *J. Am. Chem. Soc.*, 2014, **136**, 16768–16771.
  67. C. Bachmann, B. Probst, M. Oberholzer, T. Fox and R. Alberto, *Chem. Sci.*, 2016, **7**, 436–445.
  68. I. Krivtsov, D. Mitoraj, C. Adler, M. Ilkaeva, M. Sardo, L. Mafra, C. Neumann, A. Turchanin, C. Li and B. Dietzek, *Angew. Chemie*, 2020, **132**, 495–503.
  69. H. Jun, S. Choi, M. Y. Yang and Y. S. Nam, *J. Mater. Chem. A*, 2019, **7**, 17254–17260.
  70. M. Yang, J. E. Yarnell, K. El Roz and F. N. Castellano, *ACS Appl. Energy Mater.*, 2020, **3**, 1842–1853.
  71. C. Clavero, *Nat. Photonics*, 2014, **8**, 95–103.
  72. S. Mukherjee, F. Libisch, N. Large, O. Neumann, L. V Brown, J. Cheng, J. B. Lassiter, E. A. Carter, P. Nordlander and N. J. Halas, *Nano Lett.*, 2013, **13**, 240–247.
  73. J. A. Lopez-Sanchez, N. Dimitratos, C. Hammond, G. L. Brett, L. Kesavan, S. White, P. Miedziak, R. Tiruvalam, R. L. Jenkins and A. F. Carley, *Nat. Chem.*, 2011, **3**, 551–556.
  74. B. Liu, H. Yao, W. Song, L. Jin, I. M. Mosa, J. F. Rusling, S. L. Suib and J. He, *J. Am. Chem. Soc.*, 2016, **138**, 4718–4721.
  75. I. V Lightcap, T. H. Kosel and P. V Kamat, *Nano Lett.*, 2010, **10**, 577–583.
  76. P. Munnik, P. E. de Jongh and K. P. de Jong, *Chem. Rev.*, 2015, **115**, 6687–6718.
  77. S. Wunder, Y. Lu, M. Albrecht and M. Ballauff, *Acs Catal.*, 2011, **1**, 908–916.
  78. S. Cao and J. Yu, *J. Photochem. Photobiol. C Photochem. Rev.*, 2016, **27**, 72–99.
  79. S. Kumar, S. Karthikeyan and A. F. Lee, *Catalysts*, 2018, **8**, 74.
  80. A. Mishra, A. Mehta, S. Basu, N. P. Shetti, K. R. Reddy and T. M. Aminabhavi, *Carbon N. Y.*, 2019, **149**, 693–721.
  81. J. Liu, Y. Liu, N. Liu, Y. Han, X. Zhang, H. Huang, Y. Lifshitz, S.-T. Lee, J. Zhong and Z. Kang, *Science (80-. )*, 2015, **347**, 970 LP – 974.
  82. F. Su, S. C. Mathew, L. Möhlmann, M. Antonietti, X. Wang and S. Blechert, *Angew. Chemie Int. Ed.*, 2011, **50**, 657–660.
  83. K. A. S. Fernando, S. Sahu, Y. Liu, W. K. Lewis, E. A. Gulians, A. Jafariyan, P. Wang, C. E. Bunker and Y.-P. Sun, *ACS Appl. Mater. Interfaces*, 2015, **7**, 8363–8376.
  84. Y. Tian and T. Tatsuma, *J. Am. Chem. Soc.*, 2005, **127**, 7632–7637.
  85. S. Sarina, E. R. Waclawik and H. Zhu, *Green Chem.*, 2013, **15**, 1814–1833.

86. K. L. Kelly, E. Coronado, L. L. Zhao and G. C. Schatz, 2003.
87. S. Yu, A. J. Wilson, J. Heo and P. K. Jain, *Nano Lett.*, 2018, **18**, 2189–2194.
88. Y. Che, Q. Liu, B. Lu, J. Zhai, K. Wang and Z. Liu, *Sci. Rep.*, 2020, **10**, 721.
89. W. Hou, Z. Liu, P. Pavaskar, W. H. Hung and S. B. Cronin, *J. Catal.*, 2011, **277**, 149–153.



## CHAPTER 2

### 2.1 Materials and characterization techniques

#### 2.1.1 Materials

Polyethylene sheets (HDPE) were collected from IISER-Mohali campus. Sulphuric acid ( $\text{H}_2\text{SO}_4$ , 98%, Merck), Hydrogen peroxide ( $\text{H}_2\text{O}_2$ , Merck), Sodium sulphate ( $\text{Na}_2\text{SO}_4$ , Rankem, 99%), Acetonitrile ( $\text{CH}_3\text{CN}$ , AR, 99.5%), Benzylalcohol (99%, Sigma), 4-chlorobenzylalcohol ( $\text{C}_7\text{H}_8\text{NCl}$ , Alfa Aesar, >97%), 4-fluorobenzylalcohol ( $\text{C}_7\text{H}_8\text{FN}$ , Alfa Aesar, >98%), Ammonium oxalate ( $\text{C}_2\text{H}_8\text{N}_2\text{O}_4$ , Sigma Aldrich, >99 %), Potassium persulfate ( $\text{K}_2\text{S}_2\text{O}_8$ , Sigma Aldrich, 99%), (Benzoquinone ( $\text{C}_6\text{H}_4\text{O}_2$ , Alfa Aesar, 98%), ((2,2,6,6 -Tetramethylpiperidine-1-yl)oxyl)) (TEMPO, Sigma-Aldrich, 98%), melamine (Alfa Aesar, 99%), gold(III) chloride trihydrate (Sigma Aldrich, 99.9%), ethyl acetate, (Rankem, 99%), benzylamine ( $\text{C}_7\text{H}_9\text{N}$ , Alfa Aesar, 98%), methanol ( $\text{CH}_3\text{OH}$ , Rankem, 99%), isopropanol ( $\text{C}_3\text{H}_8\text{O}$ , Merck, 99%), ammonium oxalate ( $\text{C}_2\text{H}_8\text{N}_2\text{O}_4$ , Sigma Aldrich, >99%), potassium persulfate ( $\text{K}_2\text{S}_2\text{O}_8$ , Sigma Aldrich, 99%), benzoquinone ( $\text{C}_6\text{H}_4\text{O}_2$ , Alfa Aesar, 98%), acetonitrile ( $\text{CH}_3\text{CN}$ , AR, 99.5%), absolute ethanol ( $\text{C}_2\text{H}_5\text{OH}$ , Merck, 99.9%), 4-chlorobenzylamine ( $\text{C}_7\text{H}_8\text{NCl}$ , Alfa Aesar, >97%), 4-trifluoromethylbenzylamine ( $\text{C}_8\text{H}_8\text{F}_3\text{N}$ , Alfa Aesar, 98%), 4-fluorobenzylamine ( $\text{C}_7\text{H}_8\text{FN}$ , Alfa Aesar, >98%), 4-methylbenzylamine ( $\text{C}_8\text{H}_{11}\text{N}$ , Alfa Aesar, 98%), 4-tert-butylbenzylamine ( $\text{C}_{11}\text{H}_{17}\text{N}$ , Alfa Aesar, 98%), 4-methoxybenzylamine ( $\text{C}_8\text{H}_{11}\text{NO}$ , Alfa Aesar, >98%), Nafion solution (Sigma-Aldrich, 99%), ((2,2,6,6- tetramethylpiperidine-1-yl)oxyl) (TEMPO, Sigma-Aldrich, 98%), and sodium sulphate ( $\text{Na}_2\text{SO}_4$ , Rankem, 99%), Melamine ( $\text{C}_3\text{H}_6\text{N}_6$ , Alfa Aesar, 99%), Hydrochloric Acid (Conc. HCl, Himedia, 35% pure, Hi-AR), Palladium (II) Chloride ( $\text{PdCl}_2$ , 99.9% metals basis), Potassium carbonate anhydrous (anhy.  $\text{K}_2\text{CO}_3$ , 99%, Loba Chemie, Extra pure), Phenyl boronic acid ( $\text{C}_6\text{H}_7\text{BO}_2$ , Alfa Aesar, >98%), Iodobenzene ( $\text{C}_6\text{H}_5\text{I}$ , Aldrich Chemistry, 98%), 1-Iodo-4-nitrobenzene ( $\text{IC}_6\text{H}_4\text{NO}_2$ , Alfa Aesar, >98%), 4-Iodoanisole ( $\text{IC}_6\text{H}_4\text{OCH}_3$ , Alfa Aesar, >98%), 4-Iodotoluene ( $\text{CH}_3\text{C}_6\text{H}_4\text{I}$ , Alfa Aesar, 98%), 4-Iodobenzonitrile ( $\text{CNC}_6\text{H}_4\text{I}$ , Alfa Aesar, 98%), 4-methoxy Benzeneboronic acid ( $\text{C}_7\text{H}_9\text{BO}_3$ , Alfa Aesar, 97%), 4-Acetyl Benzeneboronic acid ( $\text{C}_8\text{H}_9\text{BO}_3$ , Alfa Aesar, 98%), Hexane ( $\text{C}_6\text{H}_{14}$ , Rankem LR, >98%), Chloroform ( $\text{CHCl}_3$ , Himedia, AR), Triethanolamine (Sigma Aldrich, 99.9%), Hexachloro platinumic acid ( $\text{H}_2\text{PtCl}_6$ , Sigma Aldrich, 99.99%), Chloroform D +0.03% Tetramethyl silane (Euriso-top,

CDCl<sub>3</sub>+0.03% C<sub>4</sub>H<sub>12</sub>Si), Dichloromethane (CH<sub>2</sub>Cl<sub>2</sub>, Rankem, LR), Silica gel (SiO<sub>2</sub>, Merck, 100-200 mesh) were used without further purification. Milli-Q water was used for all the experiments.

### 2.1.2 Characterization techniques

Powder X-ray diffraction (PXRD) studies were carried out on a Rigaku Ultima IV diffractometer equipped with Cu-K $\alpha$  radiation (40 kV and 40 mA) with a DTex Ultra detector using parallel beam geometry with a scan speed of 2° per minute and scan step of 0.02° (2 $\theta$  range 10-80°). The samples were grounded into a fine powder by using a mortar and pestle before recording the data.

Field emission scanning electron microscopy (FESEM, JSM-7600F) and Transmission Electron Microscopy (TEM, JEOL JEM-F200) were used to investigate the morphology and size of the prepared samples. The FESEM was operated with an accelerating voltage of 20-30 kV. SEM samples were prepared by drop-casting ethanolic solution of the sample on the silicon wafer substrate and allowing the solvent to evaporate at room temperature in a vacuum desiccator. TEM specimens were prepared by dispersing the samples in ethanol and adding onto a porous holey carbon-coated copper grid. The chemical composition of the synthesized samples were investigated by EDS (Energy Dispersive X-ray Spectroscopy, Oxford Instruments) operating at 10 kV.

Fourier Transform Infrared Spectroscopy (FT-IR, PerkinElmer) studies were carried out to find out the functional groups present in the prepared samples. Samples were grounded with KBr powder using mortar and a pestle, and then the mixed powder was pressed into a pellet using a hydraulic press to record the data. Data were recorded in the range of 400–4000 cm<sup>-1</sup>.

UV-Vis absorption spectroscopy studies of all the samples were recorded using a Agilent Cary 60-UV-Vis spectrometer at room temperature. The range of the measurement was 200-800 nm with a step of 1 nm.

Diffuse-reflectance spectra (DRS) were recorded on Shimadzu UV-2450 spectrophotometer where the baseline was fixed using barium sulfate as reference. The samples were grounded into fine powder and transferred into the solid holder uniformly. .

Photoluminescence spectroscopy (PL) studies of the aqueous dispersion samples were carried out using Spectrofluorometer (Horiba Scientific) using a quartz cuvette. Quantum yield (QY) of the PE-CQDs was calculated by taking quinine sulphate as the standard (QY of 54%) in 0.1 M H<sub>2</sub>SO<sub>4</sub>. Time-Correlated Single Photon Counting (TCSPC, Fluorocube, Horiba Jobin Yvon, NJ) data were collected by using laser diode head of 375 nm (NanoLED, Horiba Scientific) as an

excitation source and all decay traces are recorded at different emission wavelength range. The instrument response function (IRF) was collected by using colloidal solution of silica particles (Ludox, Sigma Aldrich) at 375 nm and found to be 310 ps. All data were collected by fixing peak preset at 10,000 counts and keeping the polarization at the magic angle ( $54.5^\circ$ ). DAS6 (Horiba Scientific) software was used to analyze the lifetime (maintaining best-fitting parameters).

Composition and electronic structure of the samples was examined by X-ray photoelectron spectroscopy (XPS, Omicron Nanotechnology spectrometer with monochromatic Al K $\alpha$  X-radiation). The measurements were carried out by a Thermo K alpha+ spectrometer using micro-focused and monochromated Al K $\alpha$  radiation (1486.6 eV).

Nitrogen adsorption–desorption isotherms were recorded at liquid nitrogen temperature (77 K) using Quantachrome Autosorb-iQ-CXR. The samples were degassed at 180 °C for 12 h prior to the surface area measurements. The specific surface area was calculated by the Brunauer-Emmett-Teller (BET) method.

High resolution mass spectra (HRMS) were recorded on a Waters Synapt G2-Si Q-TOF Mass Spectrometer. The measurements were performed in electron spray ionization (ESI) mode with a Q-TOF mass analyser.

The concentration of metal loaded on the surface of catalysts was monitored using Atomic Absorption Spectroscopy (AAS). The AAS analysis of the samples was carried out on Lab India AA7000 Spectrophotometer with flame as atomizer.

Raman spectrum of the synthesized samples was recorded using Renishaw Raman Spectrometer equipped with the 514 nm laser as the excitation source.

Gas Chromatography (GC-2014 SCHIMAZHU) was used for the detection of H<sub>2</sub> gas during the period of photocatalytic water-splitting reaction. The gaseous sample was collected by using 5 ml syringe.

***Electrochemical study:*** Electrochemical measurements of all the samples were performed in a three electrode experimental system using a CHI760E Electrochemical Workstation. The catalyst ink was prepared by taking 3 mg catalyst in 300 microliters of Nafion solution (Nafion solution contains 2 ml water, 1 ml isopropyl alcohol (IPA) and 50 microliters 5% Nafion). The solution

was then sonicated to make a homogeneous suspension. An ITO glass (16 mm X 10 mm) was cleaned with water and then washed with IPA. One edge of the ITO glass was covered with scotch tape and the remaining area (5 mm X 10 mm) was spin-coated with 0.020 ml of the catalyst ink. The ITO glass was kept as such for a night and then dried under an IR-lamp. The scotch tape on the edge of the ITO glass was removed and a Cu-wire was connected on the ITO glass using conductive silver paste. The ITO glass was again kept for 4-6 h to get the silver paste dry. Once the silver paste dried completely, a certain quantity of epoxy glue (non-conductive) was used to cover the silver paste and air dried for overnight. The prepared electrode on ITO glass was used as the working electrode and Ag/AgCl and a Pt wire were used as the reference and counter electrode, respectively. The electrolyte was 10 ml of a 0.5M Na<sub>2</sub>SO<sub>4</sub> aqueous solution. Mott–Schottky measurements were performed in the potential range of 0 V to 0.8 V (vs. RHE) and at frequencies of 500, 1000 and 1500 Hz with an amplitude of 10 mV and the frequency of 10 Hz. For electrochemical impedance spectroscopy (EIS), the same catalyst ink (10 microliters) was drop-cast on an RDE (rotating disk electrode, 5 mm diameter). The EIS tests were performed at open circuit potential (OCP) over the frequency range between 1000 and 100 KHz, with an AC voltage magnitude of 10 mV. The photocurrent measurements were performed at +0.25 V (vs. Ag/AgCl) with illumination of 400 W Xe-lamp with the 10 seconds of light on-off interval for many cycles. As the cycles progressed, there was a decrease in the dark current. The data for different samples were compared for the same repeat cycles after dark current subtraction. The conversion of potential vs. Ag/AgCl to potential vs. RHE was done by using the following equation:

$$E_{\text{RHE}} = E_{\text{observed}} + 0.0591 \times \text{p}^{\text{H}} + E_{\text{Ag/AgCl}}^0$$

*E<sub>observed</sub>* = experimentally observed potential using Ag/AgCl reference electrode

*E<sub>Ag/AgCl</sub><sup>0</sup>* = 0.2 V for 3M KCl filling

*pH* = 6.5 for 0.5 M aqueous Na<sub>2</sub>SO<sub>4</sub>

## Part 1

*Carbon quantum dots; synthesis, unique properties and application in photocatalysis.*



# CHAPTER 3.1

## Introduction

### 3.1.1 Carbon quantum dots

Carbon-based nanomaterials such as fullerenes, nanodiamonds, graphene sheets, carbon nanotubes, and carbon quantum dots (CQDs) or fluorescent carbon nanoparticles have been extensively used in a wide range of applications due to their unique and attractive properties.<sup>1-10</sup> The term “quantum dots” is usually associated with the tiny semiconductor nanoparticles having different optical and electronic properties than the larger particles due to the quantum confinement effect. CQDs are carbon particles with few nanometers in size (less than 10 nm), containing various surface functional groups.<sup>8</sup> Among all the electronic and physical properties, the optical properties of CQDs, in particular, have attracted tremendous recent interest as they are unique among the carbon-nanomaterials, and give rise to many novel applications that are otherwise possible using metal-containing nanomaterials only. For example, metal-based semiconductor quantum dots such as CdS, CdSe, etc. have been massively investigated in the past few years for their strong fluorescence emission properties, enabling their application in bio-imaging and bio-sensing.<sup>11-14</sup> However, these possess certain limitations such as a high toxicity due to the presence of heavy metals. In general, heavy metals are toxic even in relatively trace levels, prohibiting the application in clinical studies. CQDs have been shown to be non-toxic and can replace metal-based semiconductor quantum dots because of their biocompatibility, chemical inertness, good water solubility, and low-cost besides having tunable fluorescence emission properties.<sup>15-18</sup> CQDs have gained significant importance due to their high solubility in water and strong luminescence and hence referred to as ‘carbon nanolight’.<sup>19</sup> The CQDs have been accidentally discovered by Xu et al. in 2004, during the separation and purification of single-walled carbon nanotubes and explored the fluorescence properties creating a new class of fluorescent nanomaterials.<sup>20</sup> In 2006, they were given the name “carbon quantum dots” by Sun et al. who discovered a new route to synthesize surface passivated CQDs with high fluorescence emission intensity.<sup>21</sup>

### 3.1.2 Composition and structure

The composition of CQDs depends on the precursor material and the method of synthesis. Liu et al. prepared CQDs from the raw candle soot which contains 91.7% C, 1.8% N, 1.8% H, and 4.4% O, whereas the synthesis of CQDs from glucose as starting material only contains C, O, and H. Characteristically, CQDs are quasi-spherical carbon nanoparticles composed of amorphous to crystalline carbon core.<sup>22</sup> Primarily, it is made up of  $sp^2$  graphitic carbon (or) graphene-oxide sheets combined through the insertion of  $sp^3$  hybridized carbon. It was observed that the CQDs prepared by the electrochemical oxidation of multi-wall carbon nanotubes are graphitic in nature, confirmed from Raman spectroscopy which shows the presence of both graphitic and defective bands.<sup>23</sup> Hu et al. have reported that the selected area electron diffraction (SAED) results in a ring pattern of 3 nm CQDs obtained by a laser passivation/ablation method as shown in **Figure 3.1.1a**.<sup>24</sup> The calculated ratio of the squares of the ring radius is 3 : 8 : 11 : 16 : 19, suggesting the diamond-like structure of CQDs and the ring corresponding to (111), (220), (311), (400), and (331) respectively. The lattice spacing value is in the range of 0.2 to 0.23 nm, indicating the presence of the graphite (100) plane. CQDs synthesized by alkali-assisted electrochemical route revealed 0.32 nm lattice spacing, implying the (002) graphitic planes. Raman spectra of pristine graphite and CQDs synthesized by Ming et al. are shown in **Figure 3.1.1b** for comparison of their structure.<sup>25</sup> In the case of pristine graphite, three peaks appear at 1345, 1570, and 2696  $cm^{-1}$ , corresponding to the D, G, and 2D bands respectively. On the other hand, CQDs only consist of D and G bands. The ratio of the D and G band intensity i.e  $I_D/I_G$ , measures the extent of the disorder and the  $sp^3/sp^2$  carbon ratio. The  $I_D/I_G$  ratio for pristine graphite and CQDs are 0.365 and 1.234 respectively. The noticeable increase in the value is due to the more disorder in the structure, which arises from the generation of oxygenated groups (C-O, C=O, O-C=O) in the  $sp^2$  carbon site after the electrochemical oxidation and thereby the  $sp^3$  carbon sites get produced. The different types of functional groups produced on CQD surfaces were analyzed extensively by X-ray photoelectron spectroscopy (XPS) technique as shown in **Figure 3.1.1c**. Peak appeared at 288 eV in C1s spectra of C-dots, indicating more oxidized groups (C-O, C=O), which is consistent with the Raman results. Thus, even though CQDs can be crystalline, like graphene, they have high  $sp^3$  defect density and a large number of surface functional groups, making them distinct from graphene or graphene oxide.



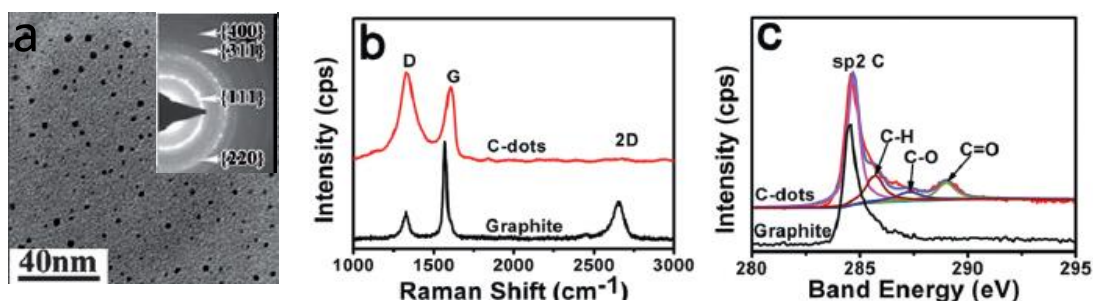
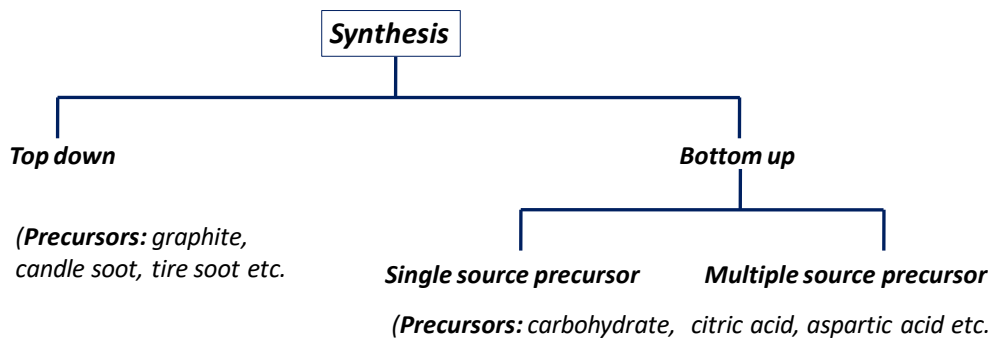


**Figure 3.1.1** (a) TEM image and SAED pattern of C-dots. (b) Raman spectra of graphite and C-dots ( $\lambda_{ex} = 633 \text{ nm}$ ), (i) C1s XPS spectra of graphite and C-dots. Adapted with permission from [24,25].

### 3.1.3 Synthesis of carbon quantum dots (CQDs)

Unlike other carbon-based nonmaterial, several simple methods have been developed to synthesize CQDs. The common method used for the synthesis is the exfoliation of graphite materials by the means of physical or chemical process. The challenges associated with CQDs synthesis are: (i) their aggregation during carbonization, which can be minimized by doing confined pyrolysis and electrochemical synthesis method, (ii) controlling the size and the particle size distribution, which can be optimized by post-treatments, such as centrifugation, dialysis, column chromatography, and gel electrophoresis, and (iii) surface properties of CQDs which is important for solubility and some selected applications, and can be tuned during the synthesis or post-treatment. The synthesis procedures can be roughly classified into two different approaches: (i) top-down and (ii) bottom-up synthetic routes, as discussed below:



### 3.1.3.1 Top-down synthetic routes

The method involves breaking down bigger carbon structures, such as carbon nanotubes, graphite, graphite oxide, nanodiamonds, carbon fibers, carbon soot and activated carbon, by employing methods like laser ablation, arc discharge, chemical, and electrochemical oxidation.<sup>26-33</sup> The entire CQD formation mechanism involves the breakage of carbon-carbon bonds. The first example of CQDs was also using top-down route by Xu et al during the separation and purification of SWCNTs obtained by arc discharge.<sup>20</sup> In the greener approaches, researchers have shown the use of waste carbon-based precursors such as candle soot, natural gas soot and tire soot, and then these larger-sized carbon materials can be broken into CQDs by the chemical oxidation method using a strong oxidizing reagent such as HNO<sub>3</sub> or H<sub>2</sub>SO<sub>4</sub>, KMnO<sub>4</sub>. Zhu and co-workers have prepared CQDs with greenish-yellow emissive (g-CQDs) through the breaking of graphene oxide by microwave treatment under an acidic condition without further addition of any reducing agent.<sup>34</sup> Moreover, CQDs can be turned into blue emissive (b-CQDs) by reducing them with NaBH<sub>4</sub> as shown in **Figure 3.1.2 A**. Qu et al. have described the formation process of CQDs enriched with the oxygenated group (o-CQDs) using MWCNTs and concentrated nitric acid as oxidant. As shown in **Figure 3.1.2 B**, with the progress of reaction, MWCNTs breakdown into oxygenated functional group enriched CQDs.<sup>35</sup> It was also shown that in the presence of nitric acid, new defect sites, as well as carboxyl and carbonyl groups generate, along with the oxidation of hydroxyl groups to carboxyl groups.

Peng et al. developed a simple method to prepare CQDs from carbohydrates using concentrated H<sub>2</sub>SO<sub>4</sub> as a dehydrating agent, followed by breaking of bigger carbon particles into CQDs by treatment with HNO<sub>3</sub> and later functionalizing the CQD surface with amine-terminated compounds (4,7,10-trioxa-1,13-tridecanediamine).<sup>30</sup> By changing the precursor material and the duration of HNO<sub>3</sub> treatment, the emission wavelength of these CQDs can be tuned. The non-toxic nature and the multicolor emission capabilities of these CQDs allow them to be used in life-science research. Electrochemical soaking is one of the most powerful routes to prepare CQDs from various bulk carbon-based materials.<sup>36</sup> However, there are limited reports on the electrochemical formation of CQDs. Zhang and co-workers prepared CQDs from alcohols via electrochemical carbonization method in the basic medium where two Pt sheets were used as counter and working

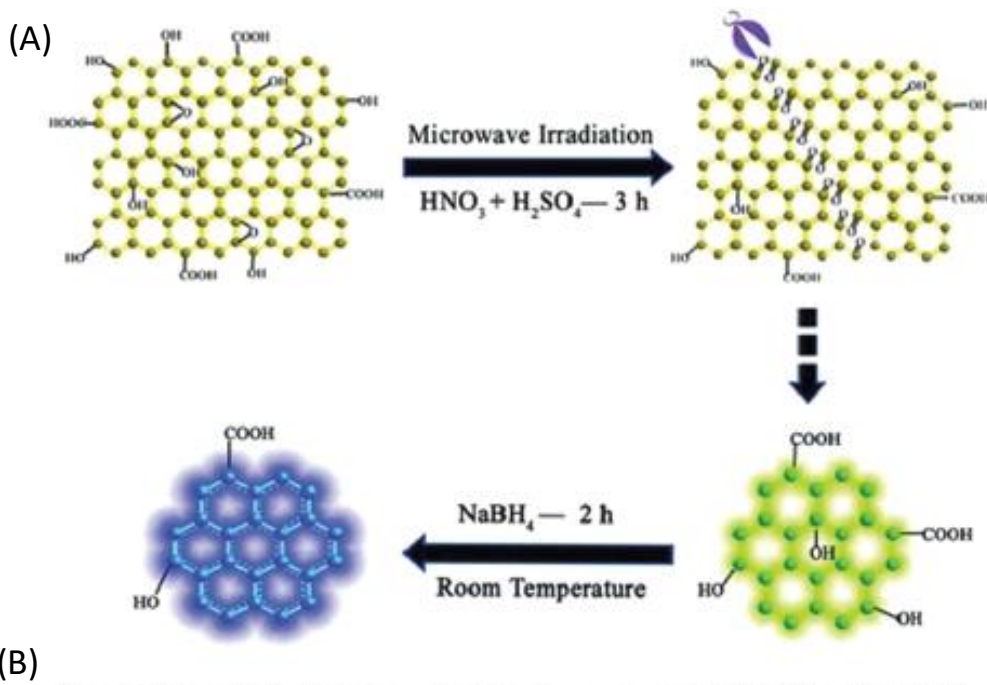


**Figure 3.1.2** (A) A schematic representation of the preparation method for greenish-yellow emissive CQDs (g-GQDs) and blue emissive CQDs (b-GQDs). (B) Gradual transformation of MWCNTs into oxygenated groups enriched CQDs (o-GQDs) with abundant carboxyl and carbonyl groups under the treatment of concentrated  $\text{HNO}_3$ . (a) TEM images of the products prepared by refluxing with  $\text{HNO}_3$  at different times. Inset is the schematic illustration of the corresponding solution colors. (Scale bars are 50 nm for 0 h, 6 h and 24 h, and 20 nm for 48 h. (b) O 1s XPS spectra of the products synthesized by refluxing with  $\text{HNO}_3$  at different time. Adapted with permission from [34 and 35].

electrode, and a saturated calomel electrode was used as the reference electrode.<sup>37</sup> It was observed that the sizes and degree of graphitization increases with an increase in the applied potential and the resultant amorphous-core CQDs exhibited excitation and size-dependent emission properties without any further passivation or purification having a quantum yield (QY) of 15.9 %.

### **3.1.3.2 Bottom-up synthetic route**

Bottom-up routes predominantly involve the thermally induced transformation of the small molecular precursors such as carbohydrates, citrates, and polymer-silica nanocomposites through combustion/thermal treatments and microwave synthetic routes.<sup>15,38-41</sup> For instance, Bourlinos et al. developed an easy, one-step thermal decomposition route to get fluorescent CQDs from ammonium citrate.<sup>42</sup> Zhu and co-workers reported the preparation of CQDs from a solution of saccharide and poly(ethylene glycol) (PEG) by the heating method using a 500 W microwave oven for 2 to 10 min.<sup>43</sup> The synthesized CQDs with abundant surface traps and various functional groups endowed them with stable, bright luminescence and excellent soluble in water. Hydroxyl or a carboxylic acid group-containing molecules like glucose or citric acid can be hydrothermally treated or pyrolysed, resulting in a carbon core and loss of small molecules ( $H_2O$ ,  $CO_2$ ).<sup>16</sup> A variety of waste products such as candle soot, watermelon peels, pomelo peel, orange juice, strawberry juice, sugar cane juice, chicken eggs, and chitosan have been used for the synthesis of CQDs.<sup>15</sup> In typical CQDs prepared by bottom-up syntheses have diameters in the range of 2-10 nm with different functional groups and different carbon cores, ranging from graphitic to amorphous ones. Generally, temperatures below 300 °C result in the amorphous carbon core while above 300 °C leads to graphitization.<sup>38,44</sup> Synthesis of CQDs from molecular precursors via bottom-up route can be divided into two different categories: (a) single-source precursor (SSP) approach, and (b) multi-component precursor (MCP) approach.

#### **3.1.3.2.1 Single-source precursor (SSP) approach**

In this approach, only one precursor material, typically a carbon backbone containing a compound with carboxylic acid or alcohol functionalities has been used to prepare CQDs. A very common precursor used for both SSP and MCP approach is citric acid as it is readily capable of CQD formation through decarboxylation and dehydration reactions.<sup>16</sup> Temperature plays an important role during the synthesis of CQDs. The temperature should be chosen above the decomposition

temperature of the carbon precursor material, higher the temperature faster would be the decomposition. However, the temperature should not be exceeding the boiling or sublimation temperature of the precursor materials. In general, bottom-up methods give significantly defect-rich particles than the top-down method. Further, it is possible to dope heteroatom in the CQDs by selecting appropriate precursor material such as N-doped graphitic CQDs that have been prepared from aspartic acid by the SPP approach (**Figure 3.1.3**).<sup>16</sup> The carboxylic acid-rich precursor compounds such as aspartic acid or citric acid result in the CQDs with carboxylic acid functionalization on the surface as displayed in **Figure 3.1.3**.

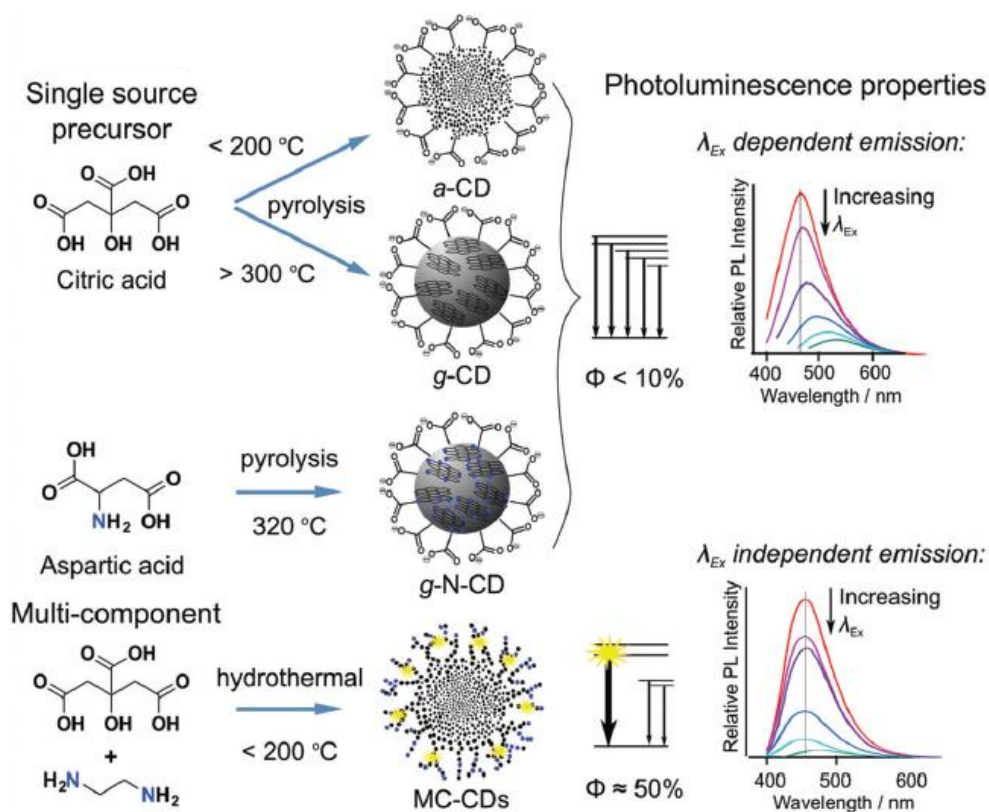


**Figure 3.1.3** Bottom-up approaches to CQD-synthesis are divided into two categories: single-source precursor (SSP) and multi-component precursor (MCP) synthetic route. SSP synthetic routes lead to CQDs of amorphous or graphitic composition depending on the synthesis temperature (with low photoluminescence quantum yield in both cases and excitation-dependent fluorescence properties). MCP synthetic routes result in amorphous CQDs with N-capping groups (blue colour), which result in molecular-like fluorophores (yellow stars) with higher quantum yield and excitation-independent emission properties. Adapted with permission from [16].

### 3.1.3.2.2 Multi-component precursor (MCP) approach

In this approach, a carbonaceous precursor material such as aspartic acid or citric acid are decomposed along with an additional heteroatom-containing species, such as urea or ethylenediamine for nitrogen,  $\text{H}_3\text{BO}_3$ , and  $\text{H}_3\text{PO}_4$  for boron and phosphorus respectively.<sup>45-47</sup> The incorporation of heteroatom is thought to be largely localized at the surface of CQDs with functionalities consisting of amide, amine, and carboxylic acid groups as shown in **Figure 3.1.3**. MCP synthetic approaches are often used for the synthesis of amine-terminated CQDs and also they are often termed as “surface passivated” or with the “hetero atom doped” CQDs. (ref) Typically, MCP syntheses take place in an autoclave by hydrothermal method and mostly result in amorphous CQDs. The low reaction temperature and closed system of the autoclave lead to the incomplete reaction of the precursor material. In contrast, greater degrees of graphitization can be achieved in the case of the SSP approach by increasing the synthesis temperatures. Furthermore, CQDs synthesized by the MCP synthetic approach generally require further purification via dialysis. Note that the MCP synthetic approach leading to the change in the optical properties of the CQD as compared to the SSP approach is advantageous as discussed in the optical property section.

### 3.1.3.2.3 Large-scale synthesis of CQDs

Synthesis of CQDs with high yield has always been challenging in the above-mentioned synthesis processes which produces various sizes of CQDs along with carbon particles and partially reacted precursors as residue. Hydrothermal method is the commonly used synthesis process to produce of CQDs from biomass. However, this method generates low CQD yield, as the traditional hydrothermal method would also produce large amounts of hydro-char as by-product.<sup>48</sup> Therefore, several groups have attempted to develop CQD synthesis strategies with high yield. Jing et al. have used an effective method for high yield synthesis of CQDs from the biomass-derived carbon (hydro-char and carbonized biomass) by using  $\text{NaOH}/\text{H}_2\text{O}_2$  solution as oxidizing reagent.<sup>49</sup> Nearly 76 wt% yield of CQDs with size of 2.4 nm was obtained in this synthesis route, which is much higher than the yield obtained from hydrothermal and strong acid-mediated oxidation processes. Liu et al. prepared CQDs from acrylamide/chitosan boost as precursor via microwave-hydrothermal carbonization for 3 minutes with a yield of nearly 46% and they used for the detection of ferrous ions.<sup>50</sup> Zhang and co-workers prepared N-doped CQDs from ethylenediamine

tetraacetic acid (EDTA) precursor by using one-step hydrothermal method with a yield of 78%.<sup>51</sup> Li et al. developed a versatile molten-salt method to prepare hydro-soluble CQDs from various precursors, in high yields.<sup>52</sup> Therein, citric acid derived CQDs were obtained in a maximum yield of ~37% and also exhibited a high fluorescence QY of 20.8%. Other precursor materials, such as sucrose, sodium lignosulphonate, p-phenylenediamine, and glucose result in the maximum yield of 66.7% and used for the bio-imaging.

However, the above synthesis process uses very energy and time consuming (4-5 days) purification and separation technique (dialysis, vacuum freeze-drying). Moreover, even if the yields are high, the amount of CQDs are not more than 1-2 g only. Therefore, more efforts are required to get high-yield CQDs involving simplified separation and purification processes.

#### **3.1.4 Surface passivation and functionalization**

Generally, CQDs surfaces are highly sensitive to environmental contaminants and hence their properties get easily affected by the surroundings. To overcome such a problem, passivation of CQDs surface is performed to minimize the effect of contamination. The attachment of some polymeric materials such as oligomeric PEG or PEG1500N on the surface of CQDs results in surface passivation by usually forming a thin insulating layer. In contrast, CQDs without any surface passivation might result in fluorescence emission but they generally exhibit low QY. A very high QY (60%) was achieved by Wang et al. after the surface passivation of CQDs with PEG<sub>1500N</sub>.<sup>53</sup> It is now emerged that the optical properties and fluorescence intensity of the CQDs depend on the surface passivation. The concept of crosslinking surface passivation for the better optical properties of CQDs was introduced by Anilkumar's group.<sup>54</sup> The CQDs surface with crosslinking of the passivating PEG<sub>1500N</sub> results in fluorescent particles which are multiple CQDs associated in covalently bound clusters as shown in **Figure 3.1.4**. Crosslinking stabilizes the surface functionalization by reinforcing the soft shell of PEG1500N molecules that surround the hard CQD cores, thereby achieving enhanced fluorescence emissions.

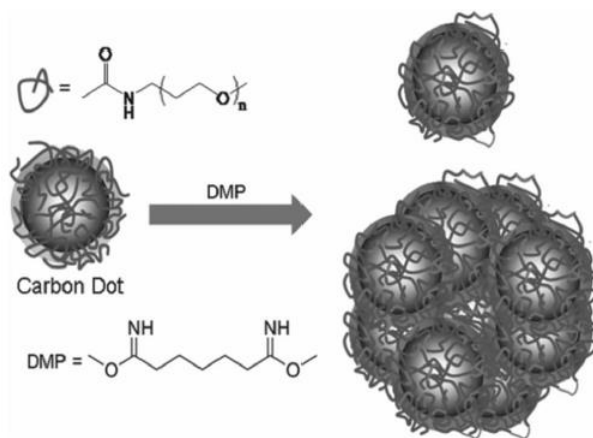


**Figure 3.1.4** Crosslinking of PEG<sub>1500</sub>N-functionalised carbon dots by reaction with dimethyl pimelimidate in phosphate buffer (pH 8). Adapted with permission from [54].

Surface passivating agents often act as functionalizing agents also, where along with physical properties, fluorescence properties of the CQDs also change. The introduction of surface functional groups such as carboxylic, amines can impose defects on their surface, leading to the variation in fluorescence emission properties.<sup>55,56</sup> One simple and effective method to introduce carboxyl and carbonyl groups on CQD surface is the oxidative treatment with strong acids. Li et al. showed that with oxidation, the fluorescence emission intensity increases.<sup>57</sup> **Table 3.1.1** provides an overview of the methods of CQDs synthesis using various precursor materials.

### 3.1.5 Optoelectronic properties of CQDs

CQDs typically show an optical absorbance in the UV region, with an extended tail to the visible range (**Figure 3.1.5**).<sup>71</sup> Most of the CQDs, such as those prepared by electrochemical oxidation, laser- ablation, microwave/ultrasonic, and hydrothermal methods have an absorption band in the range of 260-330 nm. The origin of absorption in CQDs has been attributed to the  $\pi-\pi^*$  (C=C) and  $n-\pi^*$  (C=O) transitions in the graphitic core. Besides, it was observed that the absorbance of the CQDs increases to lower energy after surface passivation with organosilane or 4,7,10-trioxa-1,13-tridecanediamine (TTDDA)<sub>2</sub> (340-410 nm and 350-550 nm respectively). CQDs with carboxylic acid-terminated synthesized by a single-source precursor (SSP), typically



**Table 3.1.1:** Summary of synthetic routes for CQDs from various precursors.

Precursor	Synthetic method	QY (%)	Application	Ref.
Ascorbic acid	Heat treatment at 90 °C	3.2	pH sensing	58
Carbohydrate	H <sub>2</sub> SO <sub>4</sub> and HNO <sub>3</sub> treatment, amine passivation	13	-	30
Citrate	Hydrothermal treatment 180 °C	68	Hg <sup>2+</sup> sensing	59
poly(ethylene glycol), saccharide	Microwave treatment (500 W)	3.1-6.3	-	43
Glucose	Hydrothermal treatment 200 °C	1.1-2.5	Bio-imaging	60
Candle soot	HNO <sub>3</sub> oxidation	3	Bio-imaging	61
Ionic liquids	Microwave oven (700 W)	1.6-5.1	Quercetin sensing	62
Grass	Hydrothermal treatment 150-200 °C	2.5-6.2	Cu <sup>2+</sup> sensing	63
Orange juice	Hydrothermal treatment 120 °C	26	Bio-imaging	64
Ethanol in NaOH solution	Electrochemical treatment (25–40 V)	4	-	65
Chitosan	Hydrothermal treatment at 180 °C	43	Bio-imaging	56
Chicken egg	Plasma irradiation (50 V, 2.4 A)	6.8	Printing	55
Citric acid & ethylenediamine	Hydrothermal treatment at 150-300 °C		Cu <sup>2+</sup> sensing printing	44
Gelatine	Hydrothermal treatment 200 °C	31	Bio-imaging	66
3-(3,4-Dihydroxyphenyl)-L-alanine, L-histidine, L-arginine	Carbonisation at 300 °C	-	Bio-imaging	67
Ascorbic acid	Hydrothermal treatment 200 °C	5.7	Bio-imaging, pH sensing	68
Hair fibre	H <sub>2</sub> SO <sub>4</sub> treatment	11	Bio-imaging	69
Acetic acid	Carbonisation with P <sub>2</sub> O <sub>5</sub>	-	Bio-imaging	27
Sucrose	Microwave oven at 100 W	-	Bio-imaging	70

have a broad UV-visible absorption band, whereas CQDs synthesized by multi-component (MP) procedures exhibit an additional characteristic band at around 355 nm for the  $n-\pi^*$  (amide) transition. CQDs with more graphitization within the structure display an absorption in higher wavelength than amorphous CQDs, because of the presence of extended  $\pi-\pi^*$  (C=C) systems.

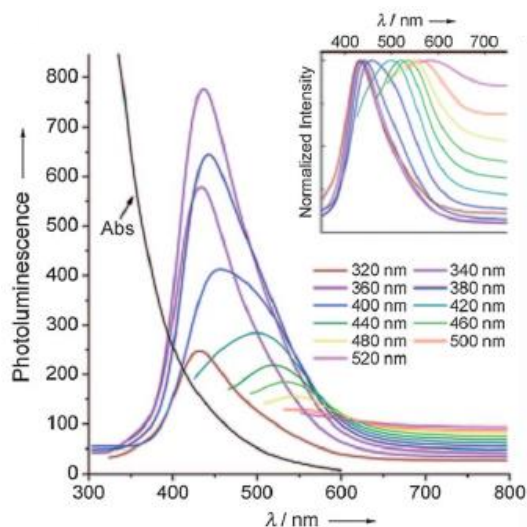


**Figure 3.1.5** UV-Vis absorption and PL emission spectra (recorded for different excitation wavelengths with 20 nm increments) of carbon dots surface-passivated with PEG<sub>1500N</sub> in water. The inset is normalized emission spectra. Adapted with permission from [71].

### 3.1.5.1 Photoluminescence

The intricate photoluminescence emission properties of CQDs have gained significant research attention, particularly in white light emission, bio-imaging, and sensing applications. CQDs prepared by the SSP method typically exhibit excitation wavelength-dependent emission properties, which distinguishes them from the traditional semiconductor quantum dots, showing a nanoparticle size-dependent emission because of their well-defined size-bandgap relationship. However, the origin of such fluorescence emission is still debatable. Though the origin of emission is unclear, the prevailing view is that there are two classes of fluorescence emission centers depending on their structure. The first one is that of bandgap transitions by conjugated  $\pi$  domains and the origin of the 2<sup>nd</sup> fluorescence emission is associated with the surface functional groups in CQDs, as discussed below.

### 3.1.5.2 Bandgap transitions originated from conjugated $\pi$ -domain

The band-gap transitions originate from the conjugated  $\pi$ -domains which are isolated, creating  $\pi$ -electrons rich  $sp^2$  hybridized islands. They occur in such a way that between the  $sp^2$  islands there are no  $\pi$ -connections, leading to the desired fluorescence emission without any quenching. Single-layer graphene sheets have been used to suppress the interlayer quenching in this band-gap transition. Such a structure also electronically divides isolated  $\pi$ -conjugated domains, resembling large aromatic molecules with an extended  $\pi$ -conjugation of the specific electronic energy bandgap. Such electronic transitions display strong absorption in the ultraviolet (UV) region, but very weak or negligible fluorescence emissions (**Figure 3.1.6 A**).<sup>72</sup> The strong absorption in the UV-region is due to the absorption of light by a large amount of high-density  $\pi$ - electrons in the islands. On the other hand, the weak emissions are possibly due to the quenching via non-radiative relaxation from the excited energy state to the ground state during the migration of exciton.

### 3.1.5.3 Fluorescence emissions originated via surface defects

Surface-related defective sites are generally the sites that do not have perfect  $sp^2$  domains, thereby results in surface trapping energy states. Functionalization on the CQDs surface creates surface defects, both  $sp^2$  and  $sp^3$  hybridized carbons which are responsible for multicolor emissions in the visible-light spectrum. The origin of multicolor emission is deemed to be the presence of multiple surface defects with different emission and excitation properties.<sup>73</sup> The recombination of the photo-excited electron-hole pairs in localized  $\pi$  and  $\pi^*$  energy levels of the  $sp^2$  hybridized site is responsible for the surface defect-derived fluorescence of CQDs.<sup>74</sup> This electronic transition generally exhibits strong emissions in the visible region but weak absorption in the near ultraviolet-visible (UV-Vis) region as shown in **Figure 3.1.6 B**. Additionally, upon surface functionalization, radiative recombination of surface-confined holes and electrons occurs due to isolated and more stable surface defects, which results in stronger fluorescence emissions.

CQDs have another unique property i.e., their tunable fluorescence emission. In general, without any surface functionalization, CQDs exhibit tuneable emission with very low QY because

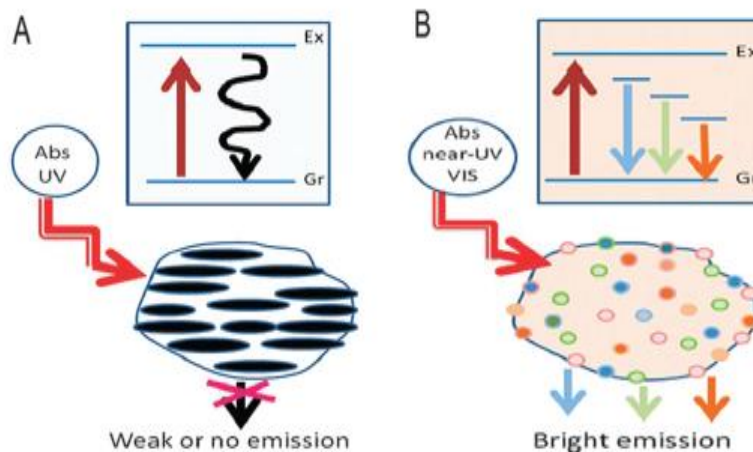


**Figure 3.1.6** (A) CQDs with strong absorption in the UV region (weak emissions) and (B) CQDs with strong and multicolour emissions in the visible region. Adapted with permission from [72].

of their reduced radiative recombination. There are many strategies developed to incorporate different functional groups on CQDs and thereby creating surface defects. Functional groups are generally created based on the choice of the synthesis method and the precursor materials which gives O, N, and S containing groups as discussed above. Another approach is the surface functionalization with polymeric or organic materials, such as poly(propionylethyleneimine-co-ethyleneimine) (PPEI-EI) attached to the surface of CQD.<sup>21</sup> Such functionalization stabilizes the defects and hence exhibits strong fluorescence emissions. The fluorescence emission of such surface-functionalized CQDs covers a broad visible range and also extended into the near-infrared region (NIR) as displayed in **Figure 3.1.7**. It should be noted that the fluorescence emission in the surface-functionalized CQDs do not originate from the functionalizing agents as those are emissive neither in the visible nor in the NIR region. The emission spectra of PPEI-EI-functionalized CQDs exhibit excitation wavelength-dependent emission and it is also noticeable that emissions are broad. Thus, the variation of particle size and different emissive sites distribution could be the reason for the tuneable emission of CQDs.<sup>21,75</sup>

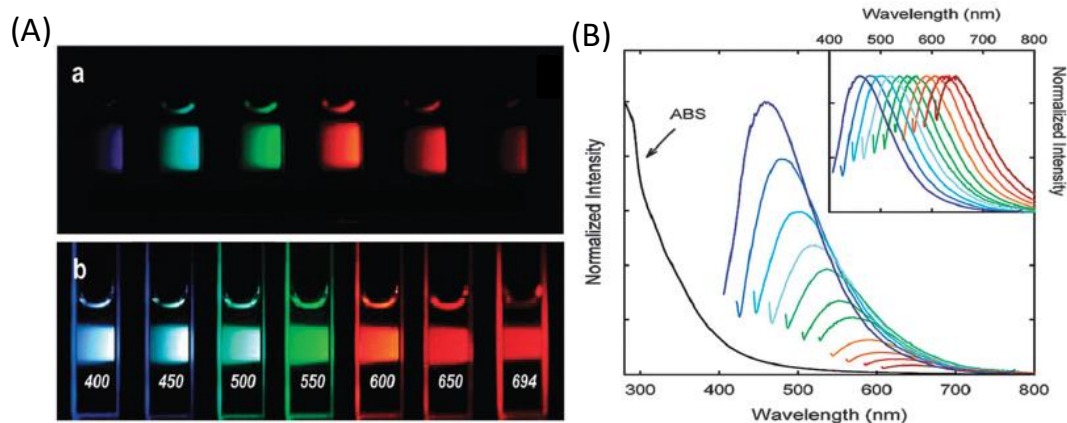


**Figure 3.1.7** (A) PEG<sub>1500N</sub>-passivated CQDs in aqueous solution (a) excited at 400 nm and (b) excited at the several (indicated) wavelengths. (B) The absorption and emission spectra of PPEI-EI passivated CQDs in an aqueous medium with increasing  $\lambda_{ex}$  from 400 nm on the left (20 nm increments). Inset is a plot of emission intensities normalized to corresponding quantum yields. Adapted with permission from [21].

However, the exact mechanism for the excitation wavelength-dependent fluorescence emission is still not established. Several reports suggest that the emission property depends on the synthesis route and the precursor materials which generate particles of different sizes having different emission maxima. Besides, it was observed that the fluorescence intensity also depends upon the pH of the CQDs solution. Jia et al. synthesized CQDs from ascorbic acid and explored the linear dependence of emission intensity with the pH of the solution ranging from 4.0 to 8.0. The emission intensity decreased ~90% from pH 4.0 to 8.0. As the pH increases, the carboxyl groups on the CQDs surface get deprotonated which might cause the electrostatic charging to the CQDs and thereby shift the Fermi level.<sup>76</sup> Liu et al. have noticed that the emission intensity of the CQDs prepared by combustion method is maximum at pH 7 and the intensity decreases whether pH decreases or increases.<sup>77</sup> As seen above, significant variation of the emission intensity with the solution pH and also the synthetic routes bring complexity to exploring the mechanism of fluorescence emission. Nonetheless, the excitation wavelength dependency on the emission property of CQDs gives an advantage in that the selection of different emission wavelengths is possible, which can be exploited for fluorescence imaging and optical labelling.

### 3.1.6 Applications of CQDs

The unique optical properties and highly emissive nature of the CQDs make them suitable for many applications such as chemical sensing, bio-sensing, bio-imaging, nanomedicine, light emission and photocatalysis.

#### 3.1.6.1 Chemical sensing

CQDs have been used in the field of chemical sensing such as heavy metal (e. g.  $\text{Hg}^{2+}$ ) detection in aqueous medium and living cells etc., due to their low toxicity, high photo-stability, water solubility, and superior chemical stability. Yan and co-workers adapted two different CQD systems CQDs-1 and CQDs-2 with a high QY of 65.5 and 55.5 % respectively prepared by hydrothermal method and showed their selectivity for the detection of  $\text{Hg}^{2+}$  in aqueous solution by fluorescence technique.<sup>78</sup> The fluorescence emission intensity of CQDs-1 and CQDs-2 solution was rapidly quenched after the addition of  $\text{Hg}^{2+}$ , by 80% and 55% respectively, and both the solution remained stable after 1 h of observation period as shown in **Figure 3.1.8**. Other metal ions such as  $\text{Cu}^{2+}$ ,  $\text{Fe}^{3+}$ ,  $\text{Pb}^{2+}$ ,  $\text{Cr(VI)}$ , and  $\text{Ag}^+$  have also been detected using CQDs by measuring fluorescence quenching after the addition of metal ions.<sup>15,79-82</sup> CQDs were used as fluorescent IFE-based chemosensors for the determination of metal ions. Apart from the sensing of metal ions, CQDs have also been used for the detections of pH,  $\text{PO}_4^{3-}$ ,  $\text{C}_2\text{O}_4^{2-}$ ,  $\text{F}^-$ ,  $\text{CN}^-$ ,  $\text{S}^{2-}$ ,  $\text{I}^-$ ,  $\text{ClO}^-$  and  $\text{NO}_2$  gas.<sup>83,84</sup> Contrary to the metal ion detection which is based on the fluorescence quenching mechanism, many of the anions detections are based on the enhancement of fluorescence (fluorescence recovery) of the quenched CQDs-metal complexes. For instance, in case of  $\text{I}^-$  assay, CQDs fluorescence was recovered due to the more stable complex formation between metal ions and  $\text{I}^-$ , and the detection limit was found to be 436 nM.

#### 3.1.6.2 Bio-sensing and bio-imaging

Non-toxicity, good biocompatibility, excellent non-photobleaching, and high fluorescence emission also make them suitable for bio-imaging and bio-sensing for a variety of biological species, such as bacteria and cells. Wang et al. showed the fluorescence sensing of *Escherichia coli* O157: H7 with a detection limit of  $9.5 \times 10^4$  CFU  $\text{mL}^{-1}$ , using water-soluble CQDs with a QY

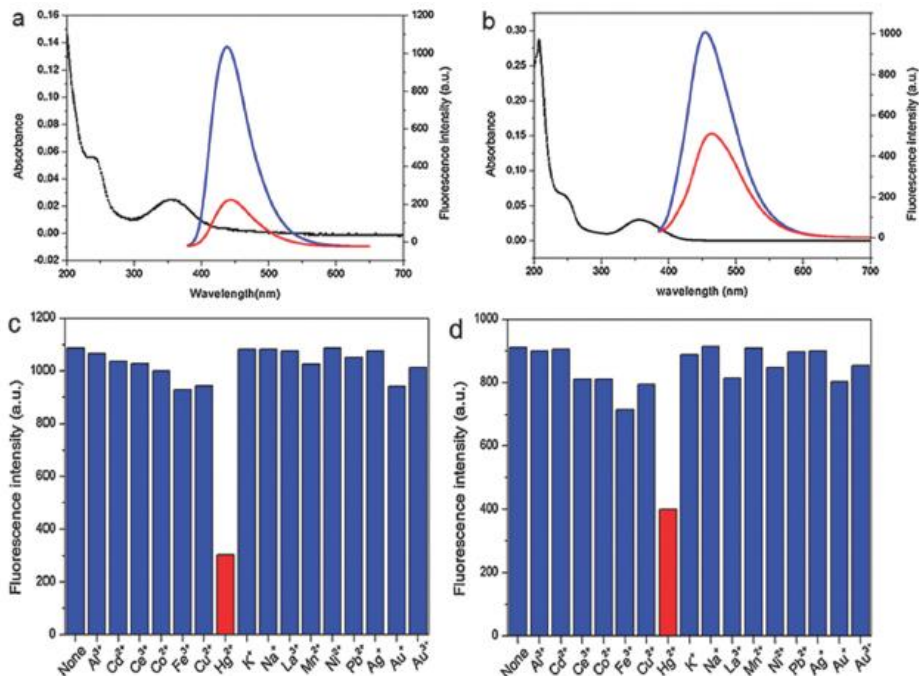


**Figure 3.1.8** UV-Vis absorption (black lines) and fluorescence spectra of (a) CQD-1 and (b) CQD-2 aqueous solutions in the presence (red lines) and absence (blue lines) of Hg<sup>2+</sup>. Fluorescence responses of CQD-1 (c) and CQD-2 (d) aqueous solutions in the presence of 20 mM of various metal ions. ( $\lambda_{ex} = 360$  nm). Adapted with permission from [78].

of 18.98% prepared by a solvothermal method.<sup>85</sup> Chen et al. prepared CQDs with a QY of 43% by a single-step heating reaction, which was used as multicolour labeling agents for bacteria such as *Escherichia coli* and *Staphylococcus aureus*.<sup>86</sup> Singh and co-workers used pH-sensitive CQDs in microgel and developed a platform to detect bacterial growth through encapsulating the bacteria as shown in **Figure 3.1.9**.<sup>87</sup> It has been shown that few bacteria inside the microgels can effectively change the pH of a small volume in lesser time as compared to the bulk culture, causing enhanced emission of CQDs with the increase of acidity of microgels. Bu and co-workers have proposed an immune-sensor for specific and fast detection of 4,40-dibrominated biphenyl (PBB15), an organic pollutant by employing the principle of homogenous immunoassay and Förster resonance energy transfer (FRET).<sup>88</sup> The fluorescence quenching concept has been also applied for the detection of nucleic acids where the selectivity level was high enough to identify even a single-base mismatch.

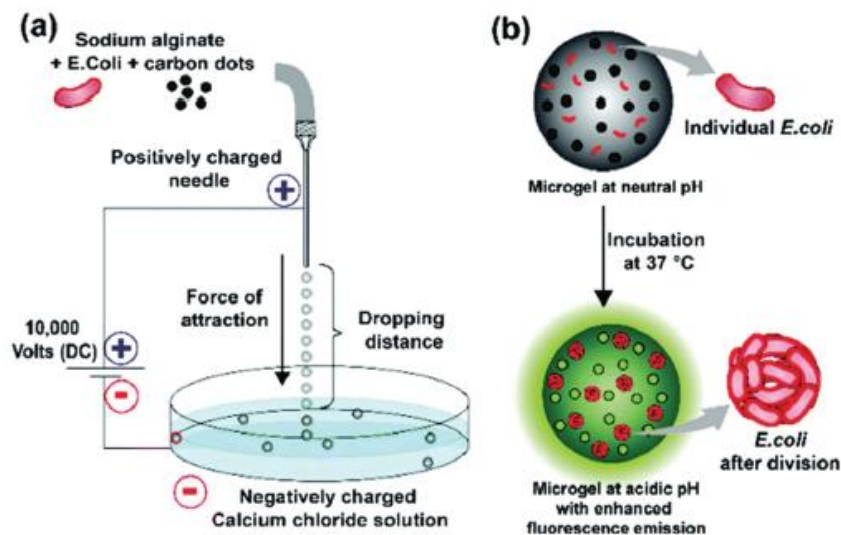


**Figure 3.1.9** Schematic representation of the apparatus used for the production of alginate microgels encapsulating *E. coli* and carbon dots. (b) A Scheme showing the growth of encapsulated *E. coli* causing an improvement of fluorescence emission due to a decrease in local pH. Adapted with permission from [87].

In addition to bio-sensing, CQDs have been widely used for bio-imaging both in-vivo and in-vitro, as alternatives to the metal-based semiconductor quantum dots due to their non-toxic nature.<sup>15</sup> Generally, the carbon cores of CQDs are non-toxic, however the occurrence of any cytotoxicity can be attributed to the surface functional groups on its surface which can be further reduced by the use of surface passivating agents of low cytotoxicity as those can be used even in high concentrations for in-vivo imaging.

### 3.1.6.3 Photocatalytic application

To achieve a sustainable photocatalytic system, a key requirement is the development of low-cost, efficient light harvesters. Photosensitizers that are commonly used for photocatalysis include organic dyes and semiconductor nanoparticles. Generally, dyes have high light absorption coefficients but they suffer from poor photo-stability in an aqueous medium. Recently CQDs have been applied as a photosensitizer to carry out many photocatalytic reactions due to their high visible-light absorption capability and photo-stability. CQDs alone have not been explored much for the photocatalytic applications but have mostly been used in conjunction with other



semiconductor photocatalysts such as  $\text{TiO}_2$ ,  $\text{Ag}_3\text{PO}_4$ ,  $\text{BiVO}_4$ ,  $\text{ZnO}$ ,  $\text{Cu}_2\text{O}$ , and  $\text{Fe}_2\text{O}_3$  for the degradation of organic dye molecules and toxic gases.<sup>17</sup> Besides, the electron reservoir behavior of CQDs has been applied to enhance the photocatalytic  $\text{H}_2$  evolution, by playing as a photogenerated electron relay between Pt nanoparticles and an organic photosensitizer. Several CQD-based photocatalysts have been reported for water splitting reaction. In contrast, photocatalytic fuel production using CQDs as the photocatalyst is limited and typically involves a composite material with other semiconductor photocatalysts such as CQD-sensitized  $\text{TiO}_2$ . CQD-modified P-25 ( $\text{TiO}_2$ ) composite photocatalyst was prepared by Zhang and co-workers via a hydrothermal approach as displayed in **Figure 3.1.10 a**, and the composite showed nearly 4-times-higher activity under visible light for  $\text{H}_2$  evolution rates as compared to bare P-25.<sup>89</sup> Based on transient photocurrent response measurements, hydroxyl radical tests, and surface photovoltage spectra, CQDs in the photocatalytic system were found to play a dual role. Upon UV irradiation, CQDs behaved as electron reservoirs to suppress the photogenerated charge carrier recombination in P-25, and under visible light, they acted as photo-sensitizers, transferring photogenerated excited electrons to the CB of P-25 to carry the  $\text{H}_2$  evolution reaction. It was proposed that the chemical bond between the P-25 and CQDs enhances the charge transfer process, resulting in a higher reaction rate.<sup>17</sup> Another research group synthesized CQDs/ $\text{TiO}_2$  nanocomposite in-situ hydrothermally using vitamin C as a carbon resource (**Figure 3.1.10 b**) and explained the enhanced activity as due to the chemical bond formation between CQDs and  $\text{TiO}_2$  during the synthesis.<sup>90</sup> Sun and co-workers incorporated S and N atoms into CQDs using thiourea and urea as source material respectively (**Figure 3.1.10 c**).<sup>91</sup> They proposed that electrons could be excited to the  $\pi^*$  orbitals of S, N, and O respectively, according to the incident light energy. Three absorption bands were observed at 338, 467, and 557 nm for S, N co-doped CQDs, and depending upon the excitation wavelength (340 to 540 nm), they emitted blue, green, or red light during de-excitation. The composite of S, N co-doped CQDs with  $\text{TiO}_2$  exhibited photocatalytic  $\text{H}_2$  evolution under visible-light illumination and excellent stability. Reisner and co-workers synthesized CQDs by the thermolysis of citric acid and used them as photosensitizers on a molecular Ni-catalyst for the  $\text{H}_2$  evolution reaction with long-term stability as shown in **Figure 3.1.10 d-f**.<sup>92</sup> In this system, CQDs can be excited by both visible and UV light and the photogenerated electrons transfer to molecular Ni catalysts. The turnover frequency (TOF) was found to be  $41 \text{ h}^{-1}$  for the first hour of the photocatalytic reaction which is almost similar to that of the Ru-based dye-sensitized system.

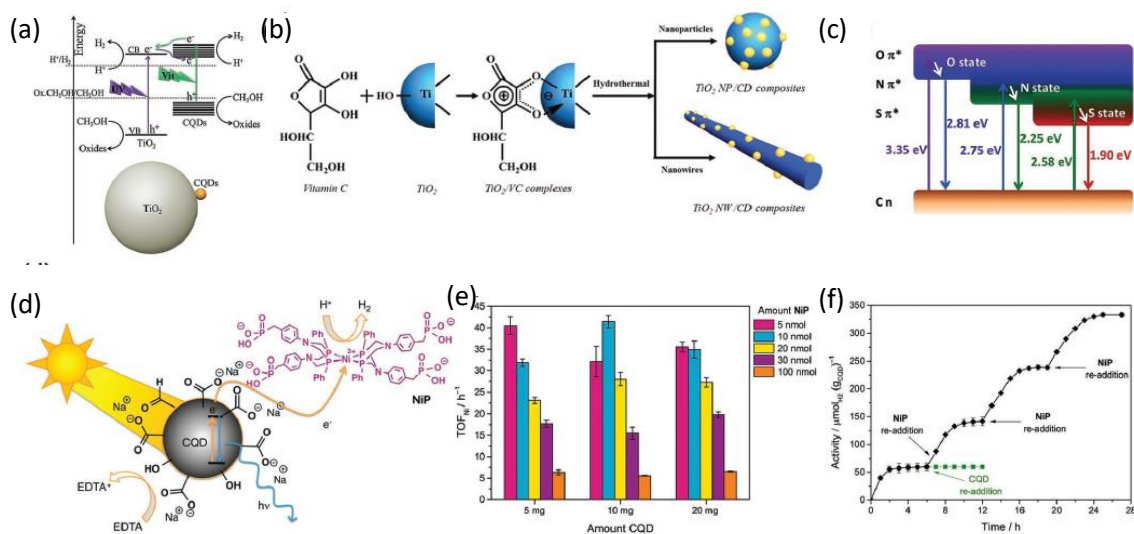


**Figure 3.1.10** (a) Band alignment and light-induced charge-transfer process of carbon dots-modified TiO<sub>2</sub> (P25). (b) In situ grown carbon dots on TiO<sub>2</sub> nanoparticles and nanowires to form bidentate Ti-O-C bonds for improved charge-transfer performance. (c) Proposed doping state diagram of S, N co-doped carbon dots. (d,e) Schematic of photocatalytic H<sub>2</sub> production by CQD-decorated nickel bis(diphosphine) molecular catalyst (NiP). (f) Re-addition experiment during long-term photocatalytic H<sub>2</sub> evolution. The decrease in catalytic activity is caused by the poor stability of the molecular catalyst. Adapted with permission from [89,90,91 and 92].

Recently, it was further found that by specific modifications of CQDs, they become highly capable of serving as a photocatalyst for the H<sub>2</sub> production for water-splitting. This was first discovered in 2011 by Sun and co-workers during the investigation of the CO<sub>2</sub> photo-conversion using platinum or gold-coated CQDs.<sup>93</sup> In absence of CO<sub>2</sub>, they irradiated an aqueous solution of CuSO<sub>4</sub> containing bare CQDs, and a visible change in the color and precipitate formation were observed, attributing to the reduction of Cu<sup>2+</sup> by H<sub>2</sub> generated via water-splitting. It has been proven that in the absence of other semiconductor substrates, CQDs alone can drive the water-splitting reaction.<sup>94</sup> However, the mechanism of H<sub>2</sub> photo-generation in presence of CQDs is still unknown. Teng and co-workers in 2014, showed that N-doped graphene oxide quantum dots (N-GOQDs) under visible light irradiation generate H<sub>2</sub> and O<sub>2</sub> in a molar ratio of 2:1, indicating their capability for overall water-splitting.<sup>95</sup> They proposed a possible reaction mechanism for the

photocatalytic water splitting as shown in **Figure 3.1.11**. The N-GOQDs have a band-gap of 2.2 eV, suggesting it is suitable for the generation of exciton under visible-light illumination. In addition, N-GOQDs consisted of stacked N- doped graphene sheets into crystals and oxygen-containing functional groups on the surface, introducing n- and p-type conductivity, respectively and hence through  $sp^2$  cluster, an ohmic contact gets build up between the p-and n-type photochemical diodes, producing efficient p-n junctions for separation of excited electron-holes. Consequently, at the p-and n-domains,  $H_2$  and  $O_2$  gas are generated separately (**Figure 3.1.11**).

It is worth mentioning that not all CQDs can perform photocatalytic  $H_2$  evolution reaction, as the HOMO and LOMO energy levels of CQDs widely vary depending upon their size and structure unlike general semiconductor materials, which has been confirmed by DFT calculations. Internal p-n junctions generated by N-doping and oxidation were demonstrated to be an excellent strategy to realize photocatalytic water-splitting using CQDs, but noble metal co-catalysts are highly necessary to achieve higher quantum efficiency for water-splitting reaction.

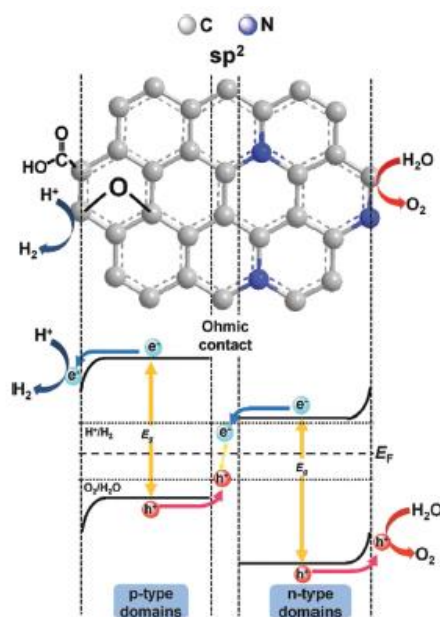


**Figure 3.1.11** The possible mechanism for photocatalytic water-splitting through a Z-scheme charge transfer pathway for nitrogen-doped graphene quantum dots (N-GOQDs). The Ohmic contact created by  $sp^2$  clusters could remove the energy barriers between p-type and n-type domains, leading to efficient charge separation for high photocatalytic performance. Adapted with permission from [95].

### 3.1.7 Concluding remarks

CQDs are emerging as the next generation of fluorescent nanomaterials with high luminescence due to their low cost, low cytotoxicity, water solubility, superior photo-stability and optical properties. Thus, the CQDs with unique optical properties are distinguishable from conventional semiconductor QDs or other carbon-based nanomaterials such as 1D CNT and 2D graphene. Generally, CQDs are consisted of carbon-core ( $sp^2$  graphene structure) and surface-domains (abundant functional groups). The origin of fluorescence of the CQDs is closely related to their surface components and intrinsic structure. Various methods and carbon precursors are used for CQDs synthesis. However, the high-yield synthesis of CQDs and their separation, purification has remained challenging. The structures, morphologies, compositions, and optical properties are highly dependent on the method and precursor used for the synthesis. Both chemical and photochemical stability of CQDs along with their non-toxic composition offer significant advantage in the context of in-vivo diagnostic and biomedical applications. CQDs have been realized as a promising photocatalysts for organic pollutant degradation and energy harvesting reactions, which may eventually reduce the burden of energy consumption. However, a green strategy needs to be developed for the synthesis (including separation and purification) of CQDs with high-yields. Besides the photocatalytic activities of the pristine CQDs for organic transformation has been barely investigated. Their high solubility creates difficulties in their separation from the reaction medium and their disposal strategies are needed to be developed.

## Bibliography

1. R. H. Baughman, A. A. Zakhidov and W. A. De Heer, *Science (80-. )*, 2002, **297**, 787–792.
2. R. Bakry, R. M. Vallant, M. Najam-ul-Haq, M. Rainer, Z. Szabo, C. W. Huck and G. K. Bonn, *Int. J. Nanomedicine*, 2007, **2**, 639–649.
3. P. M. Ajayan and O. Z. Zhou, *Carbon Nanotub.*, 2001, 391–425.
4. A. Bianco, K. Kostarelos, C. D. Partidos and M. Prato, *Chem. Commun.*, 2005, 571–577.
5. Y. Wang, Y. Shao, D. W. Matson, J. Li and Y. Lin, *ACS Nano*, 2010, **4**, 1790–1798.
6. Y. Song, K. Qu, C. Zhao, J. Ren and X. Qu, *Adv. Mater.*, 2010, **22**, 2206–2210.
7. A. L. M. Reddy, A. Srivastava, S. R. Gowda, H. Gullapalli, M. Dubey and P. M. Ajayan, *ACS Nano*, 2010, **4**, 6337–6342.
8. H. Nie, M. Li, Q. Li, S. Liang, Y. Tan, L. Sheng, W. Shi and S. X.-A. Zhang, *Chem. Mater.*, 2014, **26**, 3104–3112.
9. X. T. Zheng, A. Ananthanarayanan, K. Q. Luo and P. Chen, *small*, 2015, **11**, 1620–1636.
10. B. Zhi, X. Yao, Y. Cui, G. Orr and C. L. Haynes, *Nanoscale*, 2019, **11**, 20411–20428.
11. C.-H. Chang and Y.-L. Lee, *Appl. Phys. Lett.*, 2007, **91**, 53503.
12. F.-X. Xiao, J. Miao and B. Liu, *J. Am. Chem. Soc.*, 2014, **136**, 1559–1569.
13. Y. Choi, M. Seol, W. Kim and K. Yong, *J. Phys. Chem. C*, 2014, **118**, 5664–5670.
14. Q. Dai, J. Chen, L. Lu, J. Tang and W. Wang, *Nano Lett.*, 2012, **12**, 4187–4193.
15. S. Y. Lim, W. Shen and Z. Gao, *Chem. Soc. Rev.*, 2015, **44**, 362–381.
16. G. A. M. Hutton, B. C. M. Martindale and E. Reisner, *Chem. Soc. Rev.*, 2017, **46**, 6111–6123.
17. H. Yu, R. Shi, Y. Zhao, G. I. N. Waterhouse, L.-Z. Wu, C.-H. Tung and T. Zhang, *Adv. Mater.*, 2016, **28**, 9454–9477.
18. Y. Wang and A. Hu, *J. Mater. Chem. C*, 2014, **2**, 6921–6939.
19. S. N. Baker and G. A. Baker, *Angew. Chemie Int. Ed.*, 2010, **49**, 6726–6744.
20. X. Xu, R. Ray, Y. Gu, H. J. Ploehn, L. Gearheart, K. Raker and W. A. Scrivens, *J. Am. Chem. Soc.*, 2004, **126**, 12736–12737.
21. Y.-P. Sun, B. Zhou, Y. Lin, W. Wang, K. A. S. Fernando, P. Pathak, M. J. Mezziani, B. A. Harruff, X. Wang and H. Wang, *J. Am. Chem. Soc.*, 2006, **128**, 7756–7757.
22. H. Li, X. He, Z. Kang, H. Huang, Y. Liu, J. Liu, S. Lian, C. H. A. Tsang, X. Yang and S. Lee, *Angew. Chemie*, 2010, **122**, 4532–4536.
23. H. Li, Z. Kang, Y. Liu and S.-T. Lee, *J. Mater. Chem.*, 2012, **22**, 24230–24253.
24. S.-L. Hu, K.-Y. Niu, J. Sun, J. Yang, N.-Q. Zhao and X.-W. Du, *J. Mater. Chem.*, 2009, **19**, 484–488.
25. H. Ming, Z. Ma, Y. Liu, K. Pan, H. Yu, F. Wang and Z. Kang, *Dalt. Trans.*, 2012, **41**, 9526–9531.
26. B. Bin Chen, R. S. Li, M. L. Liu, H. Z. Zhang and C. Z. Huang, *Chem. Commun.*, 2017, **53**, 4958–4961.
27. Y. Fang, S. Guo, D. Li, C. Zhu, W. Ren, S. Dong and E. Wang, *ACS Nano*, 2012, **6**, 400–409.
28. Q. Lu, C. Wu, D. Liu, H. Wang, W. Su, H. Li, Y. Zhang and S. Yao, *Green Chem.*, 2017, **19**, 900–904.
29. K. Linehan and H. Doyle, *RSC Adv.*, 2014, **4**, 12094–12097.
30. H. Peng and J. Travas-Sejdic, *Chem. Mater.*, 2009, **21**, 5563–5565.
31. L. Tian, D. Ghosh, W. Chen, S. Pradhan, X. Chang and S. Chen, *Chem. Mater.*, 2009, **21**,

- 2803–2809.
32. J. Peng, W. Gao, B. K. Gupta, Z. Liu, R. Romero-Aburto, L. Ge, L. Song, L. B. Alemany, X. Zhan and G. Gao, *Nano Lett.*, 2012, **12**, 844–849.
  33. Z.-A. Qiao, Y. Wang, Y. Gao, H. Li, T. Dai, Y. Liu and Q. Huo, *Chem. Commun.*, 2010, **46**, 8812–8814.
  34. L. Li, J. Ji, R. Fei, C. Wang, Q. Lu, J. Zhang, L. Jiang and J. Zhu, *Adv. Funct. Mater.*, 2012, **22**, 2971–2979.
  35. H. Wang, C. Liu, Z. Liu, J. Ren and X. Qu, *Small*, 2018, **14**, 1703710.
  36. J. Zhou, C. Booker, R. Li, X. Zhou, T.-K. Sham, X. Sun and Z. Ding, *J. Am. Chem. Soc.*, 2007, **129**, 744–745.
  37. J. Deng, Q. Lu, N. Mi, H. Li, M. Liu, M. Xu, L. Tan, Q. Xie, Y. Zhang and S. Yao, *Chem. Eur. J.*, 2014, **20**, 4993–4999.
  38. A. Cayuela, M. L. Soriano, C. Carrillo-Carrión and M. Valcárcel, *Chem. Commun.*, 2016, **52**, 1311–1326.
  39. C. X. Guo, D. Zhao, Q. Zhao, P. Wang and X. Lu, *Chem. Commun.*, 2014, **50**, 7318–7321.
  40. B. J. Moon, Y. Oh, D. H. Shin, S. J. Kim, S. H. Lee, T.-W. Kim, M. Park and S. Bae, *Chem. Mater.*, 2016, **28**, 1481–1488.
  41. M. J. Krysmann, A. Kellarakis, P. Dallas and E. P. Giannelis, *J. Am. Chem. Soc.*, 2012, **134**, 747–750.
  42. A. B. Bourlinos, A. Stassinopoulos, D. Anglos, R. Zboril, M. Karakassides and E. P. Giannelis, *small*, 2008, **4**, 455–458.
  43. H. Zhu, X. Wang, Y. Li, Z. Wang, F. Yang and X. Yang, *Chem. Commun.*, 2009, 5118–5120.
  44. S. Zhu, Q. Meng, L. Wang, J. Zhang, Y. Song, H. Jin, K. Zhang, H. Sun, H. Wang and B. Yang, *Angew. Chemie*, 2013, **125**, 4045–4049.
  45. V. Strauss, J. T. Margraf, C. Dolle, B. Butz, T. J. Nacken, J. Walter, W. Bauer, W. Peukert, E. Spiecker and T. Clark, *J. Am. Chem. Soc.*, 2014, **136**, 17308–17316.
  46. J. Schneider, C. J. Reckmeier, Y. Xiong, M. von Seckendorff, A. S. Sussha, P. Kasák and A. L. Rogach, *J. Phys. Chem. C*, 2017, **121**, 2014–2022.
  47. F. Arcudi, L. Đorđević and M. Prato, *Angew. Chemie*, 2016, **128**, 2147–2152.
  48. X. Zhang, M. Jiang, N. Niu, Z. Chen, S. Li, S. Liu and J. Li, *ChemSusChem*, 2018, **11**, 11–24.
  49. S. Jing, Y. Zhao, R.-C. Sun, L. Zhong and X. Peng, *ACS Sustain. Chem. Eng.*, 2019, **7**, 7833–7843.
  50. G. Liu, B. Li, Y. Liu, Y. Feng, D. Jia and Y. Zhou, *Appl. Surf. Sci.*, 2019, **487**, 1167–1175.
  51. Q.-Q. Shi, Y.-H. Li, Y. Xu, Y. Wang, X.-B. Yin, X.-W. He and Y.-K. Zhang, *Rsc Adv.*, 2014, **4**, 1563–1566.
  52. L. Li, C. Lu, S. Li, S. Liu, L. Wang, W. Cai, W. Xu, X. Yang, Y. Liu and R. Zhang, *J. Mater. Chem. B*, 2017, **5**, 1935–1942.
  53. X. Wang, L. Cao, S. Yang, F. Lu, M. J. Meziani, L. Tian, K. W. Sun, M. A. Bloodgood and Y. Sun, *Angew. Chemie Int. Ed.*, 2010, **49**, 5310–5314.
  54. P. Anilkumar, L. Cao, J. Yu, K. N. Tackett, P. Wang, M. J. Meziani and Y. Sun, *Small*, 2013, **9**, 545–551.
  55. J. Wang, C. Wang and S. Chen, *Angew. Chemie Int. Ed.*, 2012, **51**, 9297–9301.
  56. Y. Yang, J. Cui, M. Zheng, C. Hu, S. Tan, Y. Xiao, Q. Yang and Y. Liu, *Chem. Commun.*,

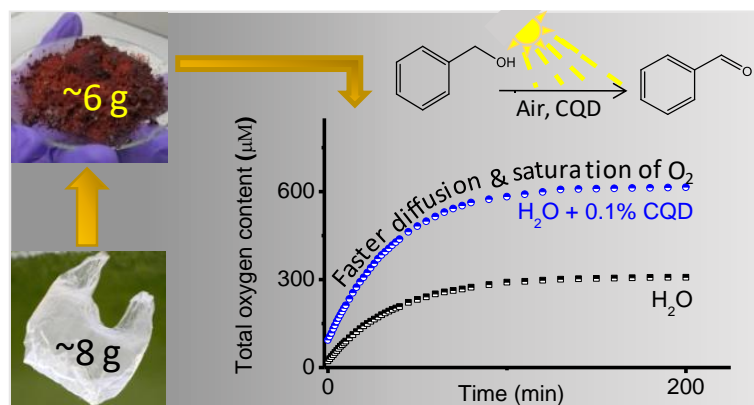
- 2012, **48**, 380–382.
57. X. Li, H. Wang, Y. Shimizu, A. Pyatenko, K. Kawaguchi and N. Koshizaki, *Chem. Commun.*, 2010, **47**, 932–934.
  58. X. Jia, J. Li and E. Wang, *Nanoscale*, 2012, **4**, 5572–5575.
  59. Y. Guo, Z. Wang, H. Shao and X. Jiang, *Carbon N. Y.*, 2013, **52**, 583–589.
  60. Z.-C. Yang, M. Wang, A. M. Yong, S. Y. Wong, X.-H. Zhang, H. Tan, A. Y. Chang, X. Li and J. Wang, *Chem. Commun.*, 2011, **47**, 11615–11617.
  61. S. C. Ray, A. Saha, N. R. Jana and R. Sarkar, *J. Phys. Chem. C*, 2009, **113**, 18546–18551.
  62. D. Xiao, D. Yuan, H. He and M. Gao, *J. Lumin.*, 2013, **140**, 120–125.
  63. S. Liu, J. Tian, L. Wang, Y. Zhang, X. Qin, Y. Luo, A. M. Asiri, A. O. Al-Youbi and X. Sun, *Adv. Mater.*, 2012, **24**, 2037–2041.
  64. S. Sahu, B. Behera, T. K. Maiti and S. Mohapatra, *Chem. Commun.*, 2012, **48**, 8835–8837.
  65. H. Li, H. Ming, Y. Liu, H. Yu, X. He, H. Huang, K. Pan, Z. Kang and S.-T. Lee, *New J. Chem.*, 2011, **35**, 2666–2670.
  66. Q. Liang, W. Ma, Y. Shi, Z. Li and X. Yang, *Carbon N. Y.*, 2013, **60**, 421–428.
  67. Y. Xu, M. Wu, Y. Liu, X. Feng, X. Yin, X. He and Y. Zhang, *Chem. Eur. J.*, 2013, **19**, 2276–2283.
  68. H. Wu, C. Mi, H. Huang, B. Han, J. Li and S. Xu, *J. Lumin.*, 2012, **132**, 1603–1607.
  69. D. Sun, R. Ban, P.-H. Zhang, G.-H. Wu, J.-R. Zhang and J.-J. Zhu, *Carbon N. Y.*, 2013, **64**, 424–434.
  70. S. Chandra, P. Das, S. Bag, D. Laha and P. Pramanik, *Nanoscale*, 2011, **3**, 1533–1540.
  71. R. Liu, D. Wu, S. Liu, K. Koynov, W. Knoll and Q. Li, *Angew. Chemie Int. Ed.*, 2009, **48**, 4598–4601.
  72. A. P. Demchenko and M. O. Dekaliuk, *Methods Appl. Fluoresc.*, 2013, **1**, 42001.
  73. L. I. Cao, M. J. Mezziani, S. Sahu and Y.-P. Sun, *Acc. Chem. Res.*, 2013, **46**, 171–180.
  74. J. Robertson and E. P. O'reilly, *Phys. Rev. B*, 1987, **35**, 2946.
  75. J. Shen, Y. Zhu, C. Chen, X. Yang and C. Li, *Chem. Commun.*, 2011, **47**, 2580–2582.
  76. W. Zhao, C. Song and P. E. Pehrsson, *J. Am. Chem. Soc.*, 2002, **124**, 12418–12419.
  77. H. Liu, T. Ye and C. Mao, *Angew. chemie*, 2007, **119**, 6593–6595.
  78. F. Yan, Y. Zou, M. Wang, X. Mu, N. Yang and L. Chen, *Sensors Actuators B Chem.*, 2014, **192**, 488–495.
  79. K. Qu, J. Wang, J. Ren and X. Qu, *Chem. Eur. J.*, 2013, **19**, 7243–7249.
  80. M. Zheng, Z. Xie, D. Qu, D. Li, P. Du, X. Jing and Z. Sun, *ACS Appl. Mater. Interfaces*, 2013, **5**, 13242–13247.
  81. X. Liu, N. Zhang, T. Bing and D. Shanguan, *Anal. Chem.*, 2014, **86**, 2289–2296.
  82. M. L. Liu, B. Bin Chen, C. M. Li and C. Z. Huang, *Green Chem.*, 2019, **21**, 449–471.
  83. S. Barman and M. Sadhukhan, *J. Mater. Chem.*, 2012, **22**, 21832–21837.
  84. J.-M. Liu, L. Lin, X.-X. Wang, L. Jiao, M.-L. Cui, S.-L. Jiang, W.-L. Cai, L.-H. Zhang and Z.-Y. Zheng, *Analyst*, 2013, **138**, 278–283.
  85. N. Wang, Y. Wang, T. Guo, T. Yang, M. Chen and J. Wang, *Biosens. Bioelectron.*, 2016, **85**, 68–75.
  86. M. M. F. Baig and Y.-C. Chen, *J. Colloid Interface Sci.*, 2017, **501**, 341–349.
  87. A. Chandra and N. Singh, *Chem. Commun.*, 2018, **54**, 1643–1646.
  88. R. S. Li, B. Yuan, J. H. Liu, M. L. Liu, P. F. Gao, Y. F. Li, M. Li and C. Z. Huang, *J. Mater. Chem. B*, 2017, **5**, 8719–8724.
  89. H. Yu, Y. Zhao, C. Zhou, L. Shang, Y. Peng, Y. Cao, L.-Z. Wu, C.-H. Tung and T.

- Zhang, *J. Mater. Chem. A*, 2014, **2**, 3344–3351.
90. J. Wang, M. Gao and G. W. Ho, *J. Mater. Chem. A*, 2014, **2**, 5703–5709.
  91. D. Qu, Z. Sun, M. Zheng, J. Li, Y. Zhang, G. Zhang, H. Zhao, X. Liu and Z. Xie, *Adv. Opt. Mater.*, 2015, **3**, 360–367.
  92. B. C. M. Martindale, G. A. M. Hutton, C. A. Caputo and E. Reisner, *J. Am. Chem. Soc.*, 2015, **137**, 6018–6025.
  93. L. Cao, S. Sahu, P. Anilkumar, C. E. Bunker, J. Xu, K. A. S. Fernando, P. Wang, E. A. Gulians, K. N. Tackett and Y.-P. Sun, *J. Am. Chem. Soc.*, 2011, **133**, 4754–4757.
  94. P. Yang, J. Zhao, J. Wang, H. Cui, L. Li and Z. Zhu, *RSC Adv.*, 2015, **5**, 21332–21335.
  95. T.-F. Yeh, C.-Y. Teng, S.-J. Chen and H. Teng, *Adv. Mater.*, 2014, **26**, 3297–3303.



## CHAPTER 3.2

### High and reversible oxygen uptake in carbon dot solutions generated from polyethylene



#### Summary

Oxidation reactions are at the heart of chemical industries. To make this a greener, fuel efficient process, numerous solar harvesting photocatalysts have been developed recently. O<sub>2</sub> enrichment plays a pivotal role in such transformations where dioxygen is a reactant, because high O<sub>2</sub> concentration in the reaction medium ensures its presence near the catalyst active-site. Therefore, large quantities of O<sub>2</sub>, obtained by separating it from air by an energy consuming process are purged through the reactor. We report here that CQDs have the ability to increase the oxygen content in a solution just like Haemoglobin in blood, in a reversible manner, so that an external supply is not necessary. We came across this breakthrough observation while developing a rational strategy for converting non-biodegradable polyethylene into a useful material based on carbonization strategies from 1980's and Hummers' method of graphene-oxide synthesis as reported here. These CQDs can perform photocatalytic-oxidation reactions in air with equal efficiency as in presence of excess oxygen, and even keeps own O<sub>2</sub> reserve in order to act in an inert atmosphere too. This is the first example of a nanomaterial exhibiting the dual role of a photocatalyst and reactant enricher, so that besides renewable energy harvesting, energy consumption during reactant supply can be reduced.

‡ Manuscript based on this work has appeared in *Nanoscale*, 2020, 12, 10480

### 3.2.1 Introduction

Photocatalytic reactions are gaining importance because of their potential to carry out chemical transformations that can assist renewable fuel generation and production of fine chemicals by using inexhaustible and green solar energy.<sup>1-4</sup> Interaction of light with a photocatalyst generates excited electrons and holes capable of carrying out reduction and oxidation reactions, respectively. However, suitable engineering of the catalysts is necessary in order to arrest recombination of excited electrons and holes, and to ensure a favourable interaction so that sufficient reactant molecules are attached to the catalyst surface ready to accept the excited electrons and holes.<sup>5,6</sup> The latter criteria is particularly difficult to meet in the case of aerial photocatalytic oxidation reactions where molecular oxygen is one of the reactants, which otherwise offers the possibility of avoiding the traditional toxic oxidizing reactants.<sup>7-9</sup> This drawback necessitates oxygen enrichment of the reaction medium by purging with oxygen in quantities much larger than the other reactants or special reaction set-up to create high oxygen pressure.<sup>10-14</sup> Therefore, photocatalytic oxidation reactions are indirectly associated with an additional energy consuming step of oxygen separation from air.<sup>15</sup> Besides photocatalysis, many other important industrial processes also require oxygen enrichment.<sup>16</sup> Thus developing a material which is capable of extracting oxygen from ambient air in large quantities while dispersed in a reaction medium, stable and efficient in harvesting solar energy is highly desirable.

### 3.2.2 Scope of the present investigation

Most of the aforementioned criteria are satisfied by the partially oxidized few-layer graphene nanostructures measuring few nanometers in size, often referred to as carbon quantum dots, (CQDs).<sup>17-20</sup> CQDs contain large number of surface functional groups leading to their high solubility in polar solvents. These absorb visible-light and exhibit tunable luminescence properties that have been used to construct white-light emitting and sensing devices.<sup>21-23</sup> In addition, these exhibit high photo-stability and biocompatibility which led to their utilization in bio-imaging and drug delivery.<sup>17,18,24,25</sup> In general, CQDs are synthesized from simple, environmentally benign precursors, and their properties have been shown to be dependent on the synthesis process.<sup>19,20,23,26</sup>

The properties of CQDs, including optical sensing which demonstrate their ability to respond to visible-light and transfer charge carriers to an analyte efficiently, also fulfil the necessary requirements in a desirable photocatalyst. However, their photocatalytic efficiencies so far have been shown to be moderate. One could argue that this may be because the CQDs have been used primarily for reduction reactions which prefer an oxygen-free atmosphere,<sup>27,28</sup> while there are many indirect evidences to suggest that the CQDs should exhibit high O<sub>2</sub> adsorption properties because of their similarity with graphene. Preferential physisorption has been observed on pure graphene basal plane, while the defects in them have been shown to induce a stronger adsorption.<sup>28-30</sup> Proximity of common functional groups in graphene-oxide to the oxygen adsorption site too is expected to augment carbon-oxygen interaction.<sup>31</sup> Therefore, rich in surface functional groups and defects, CQDs should be associated with large quantities of oxygen and hence useful in photocatalytic oxidation reactions involving molecular oxygen or ambient air.<sup>32</sup>

Here we present a new strategy wherein we used polyethylene (PE), a stubborn non-biodegradable waste and environmental hazard to synthesize CQDs (hereafter called as PE-CQD) with an aim to transform PE into a useful material in a quantitative manner.<sup>33,34</sup> We have discovered that when dissolved in water, CQDs have the ability to increase the total oxygen content (TO) to an unintuitively large quantity. In addition, we showed that it can also significantly accelerate the diffusion of O<sub>2</sub> in the solution. These CQDs can perform photocatalytic benzyl alcohol oxidation reactions in air with equal efficiency as in presence of excess oxygen, and even keeps own O<sub>2</sub> reserve in order to act in an inert atmosphere too.

### 3.2.3 METHODS

#### 3.2.3.1 Synthesis of PE-CQDs

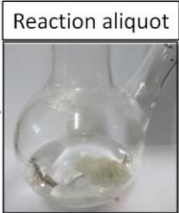




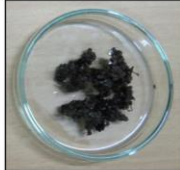


The PE-CQDs were synthesised from pure polyethylene (PE) beads as well as PE available in local market. In a typical experiment, 1 g of commercial PE sheet was cut into a smaller piece and added to 60 ml 18 M sulphuric acid in a round bottom flask. This mixture was refluxed at  $\sim 150$  °C with constant stirring at 600 rpm for 1 h. The transparent PE sheets initially swelled and gradually turned black. A solution of  $\text{KMnO}_4$  (1 g in 20 ml water) was then added slowly to the reaction mixture (drop-wise, within a period of 5 min) followed by addition of 1-2 ml of  $\text{H}_2\text{O}_2$  in a similar manner that resulted in an orange-yellow colour solution. After few minutes, the reaction mixture was allowed to cool to room temperature and further diluted with 60 ml water. The PE-CQDs were then repeatedly extracted to an organic phase in a separating funnel by adding ethyl acetate to the solution. The CQDs in the ethyl acetate was purified by two processes: (i) by column chromatography using neutral  $\text{Al}_2\text{O}_3$  as the stationary phase and methanol as eluting solvent (a process similar to other literature reports).<sup>35</sup> (ii) We also hypothesized that the extracted phase will not contain any metal based impurity. Any moisture in the organic phase was removed by filtering through  $\text{Na}_2\text{SO}_4$ . The dry organic phase was evaporated in a rotary evaporator under reduced pressure and red colour solid powder of PE-CQDs was collected. The CQDs obtained by both the methods exhibited identical elemental analysis. The later approach is much simpler and therefore all experiments were repeated using these samples.

#### 3.2.3.2 Control Experiments

In order to investigate the effect of the acid concentration, reactions were carried out with different  $\text{H}_2\text{SO}_4$  concentration (1M to 18M). It was observed that CQDs formation starts at 7M  $\text{H}_2\text{SO}_4$  though the yield was very less. The yield increases with the  $\text{H}_2\text{SO}_4$  concentration as given in the **table 3.2.1** (images given on the right of the table show the gradual increase of carbon dots yield). The complete conversion (100%) of PE into CQDs formation was observed at 18 M  $\text{H}_2\text{SO}_4$ , and therefore we have synthesized our PE-CQDs at this acid concentration. Apart from using  $\text{H}_2\text{SO}_4$ , we have also tried the same reaction with concentrated HCl, but the PE-sheets did not turn into black coloured char, suggesting HCl is not the proper reagent for this reaction. We studied the effect of reaction temperature on PE-CQDs formation. A temperature above the melting point of

the polymer favours sufficient swelling, uniform reactivity and maximum charring of PE. The conversion was progressively slower at lower temperatures, with negligible conversion at ~100 °C.

**Table 3.2.1:** To optimise the formation of PE-CQDs, we have carried out the reactions at different sulphuric acid concentrations. It was observed that C-dot formation starts at 7M H<sub>2</sub>SO<sub>4</sub> though the yield was very less. The yield increases with the H<sub>2</sub>SO<sub>4</sub> concentration (images given on the right of the table show the gradual increase of carbon dots yield).

H <sub>2</sub> SO <sub>4</sub> Conc. (M)	Observation	Reaction aliquot	Unreacted PE
1M	CQDs do not form		
3M	CQDs do not form		
5M	CQDs do not form		
7M	Formation of CQDs begins		
9M	Partial PE conversion with CQD formation		
11M	Partial PE conversion with CQD formation		
13M	Partial PE conversion with CQD formation		
15M	Near complete PE conversion with CQD formation		
18M	Complete PE conversion with CQD formation		

### 3.2.3.3 Measurement of oxygen content in the PE-CQD solutions

Concentration of oxygen in pure water and aqueous dispersion of PE-CQDs were quantified using non-invasive Ocean Optics Neofox-Kit-Probe.<sup>36</sup> To study adsorption of oxygen in aqueous dispersion of a photocatalyst, 30 ml of water containing 25mg of the photocatalyst was taken in a 50ml round bottom flask and continuously stirred at 300 rpm. The sensing patch was attached to the inner wall of the flask so that it is completely submerge in the solution. The exposure area to the atmosphere was kept as 7 cm<sup>2</sup> for all measurements. On the other hand, measurements were carried out at different depths from the solution surface. The higher the depth, the more time it takes to reach O<sub>2</sub> saturation. The solution was kept still during O<sub>2</sub> desorption while

purging with N<sub>2</sub> continuously. The N<sub>2</sub> flow rate was kept constant during all measurements. The kit was calibrated prior to each measurement using a two-point reading (20.9% O<sub>2</sub> in air and 0% O<sub>2</sub> in N<sub>2</sub>). Solutions containing 25 mg of phenol, p-toluene sulfonic acid, benzoic acid (compound containing similar functional groups as those in PE-CQDs) did not show any appreciable change in O<sub>2</sub> level from that of pure water. Besides, I expect no interference from the CQDs optical properties with the oxygen probe. This is because, the absorbance of CQDs in  $\lambda \geq 500$  nm is negligible, and therefore it can not influence the emission properties of the O<sub>2</sub> sensor (containing a Ru complex ( $\lambda_{em,max} = 600$  nm) embedded in a matrix which is permeable to O<sub>2</sub> only). On the other hand, CQD emission also has no effect on the phase shift measurements by the detector as its emission in N<sub>2</sub> and O<sub>2</sub> does not change at all. I also believe that the O<sub>2</sub> molecules are associated with CQDs in some form (weakly chemisorbed or frozen in the stern layer etc.) rather than strongly attached on the CQD surface so that when a CQD colloids the sensing patch, these O<sub>2</sub> molecules gets released, interacts with the Ru dye and thus contribute to the measurement. Also note that while CQDs have excess oxygen, the TO level of surrounding water is expected to remain same i. e.  $\sim 320$   $\mu$ M as it is in equilibrium with ambient air. Therefore, the TO value of the CQD solution is naturally higher than pure water.

#### **3.2.3.4 Photocatalytic performance of PE-CQDs**

Photodegradation of Rhodamine B (RhB) dye was chosen as a model reaction to test the photocatalytic activity of the PE-CQDs. Photocatalytic degradation reactions were performed in a 100 mL glass beaker using a 400 W Xe lamp (Newport, USA) attached with an IR filter. 10 mg of PE-CQD was added to a 25 ml solution of 12  $\mu$ M RhB and kept in dark for 30 min to ensure an adsorption/desorption equilibrium of the dye on catalyst surface and then the resulting aliquot was exposed to light. The degradation efficiencies of RhB were evaluated using the UV-Visible absorption spectroscopy and monitoring the absorption peak at 553 nm. The kinetics of the reaction was monitored by taking out 1 ml of solution from the reaction cell at regular intervals of time and analysing it based on Beer-Lambert law. We have calculated degradation efficiency ( $\eta$ ) by using the following equation:

$$\eta = [1 - (A_t/A_o)] \times 100\%$$

where  $A_0$  = initial absorbance and  $A_t$  = absorbance of dye solution at reaction time  $t$ . We have also carried out stability and recyclability test for the PE-CQDs for 100 cycles in the following manner: Once the first cycle of degradation was over, 10  $\mu$ L of 10 M stock solution of RhB was added to the same reaction mixture (which ensures that the absorption intensity at 553 nm becomes almost same as that at the beginning of the first cycle). This process was continued for 100 cycles without any intermittent cleaning of the PE-CQDs.

### 3.2.3.5 Benzyl alcohol oxidation using PE-CQDs

For oxidation of benzyl alcohol, typically, 25 mg of the photocatalyst was dissolved in 10 mL of acetonitrile containing 0.5 mmol of BA in a 10 mL round bottomed flask. The solution was stirred magnetically in dark for 1 h to establish equilibrium between adsorption and desorption. The reaction was carried out in ambience air (room temperature  $\sim$  25-27  $^{\circ}$ C) by irradiating with a 400 W Xenon lamp (Newport) for a specific time period. An IR filter was attached with the Xe-lamp to remove any temperature effect. The temperature of the reaction mixture was constantly monitored and found to be the same. 0.2 mL of the suspension was collected from the reaction aliquot and analysed using gas chromatography (GC, Shimadzu GC-2010 Plus). 25mg of commercial  $\text{TiO}_2$  (P-25, Aldrich) was used for the same reaction to compare the activities and the data was collected in a similar fashion. Similar reactions were carried out under direct sunlight for comparison. To correlate the oxygen adsorption capacity of the CQDs with their catalytic efficiency, the BA oxidation reactions were carried out in  $\text{D}_2\text{O}$  also (a poor solvent as the reactant solubility is less) and the product was analysed directly using NMR (400 MHz BrukerBiospinAvance III FT-NMR spectrometer).

### 3.2.3.6 Characterization

All other characterization techniques except the ones noted above are discussed in chapter 2.

## 3.2.4 Results and discussion

### 3.2.4.1 Mechanism of CQDs formation

We began by treating PE with conc.  $\text{H}_2\text{SO}_4$  under reflux conditions ( $\sim$ 150 $^{\circ}$ C) that led to its melting and swelling initially, followed by its charring (**Figure 3.2.1a**). The charred mass was thus oxidised by adding potassium permanganate solution first, that yielded a stable black dispersion.

Subsequently strongly oxidizing hydrogen peroxide was added to the reaction that led to the generation of the PE-CQDs and transformed the aliquot colour to transparent orange-yellow. The partial oxidation of the charred mass by  $\text{KMnO}_4$  is important, because  $\text{H}_2\text{O}_2$  treatment alone resulted in nearly complete oxidation and discoloration of the aliquot under the same the reaction conditions. 8 g of PE resulted in 6 g of CQDs that are highly soluble in water as well as in a number of polar organic solvents without any precipitation for over two years (insets in **Figure 3.2.1a vi**). The dispersion is so stable that the CQDs do not precipitate even upon centrifugation at 40,000 rpm.

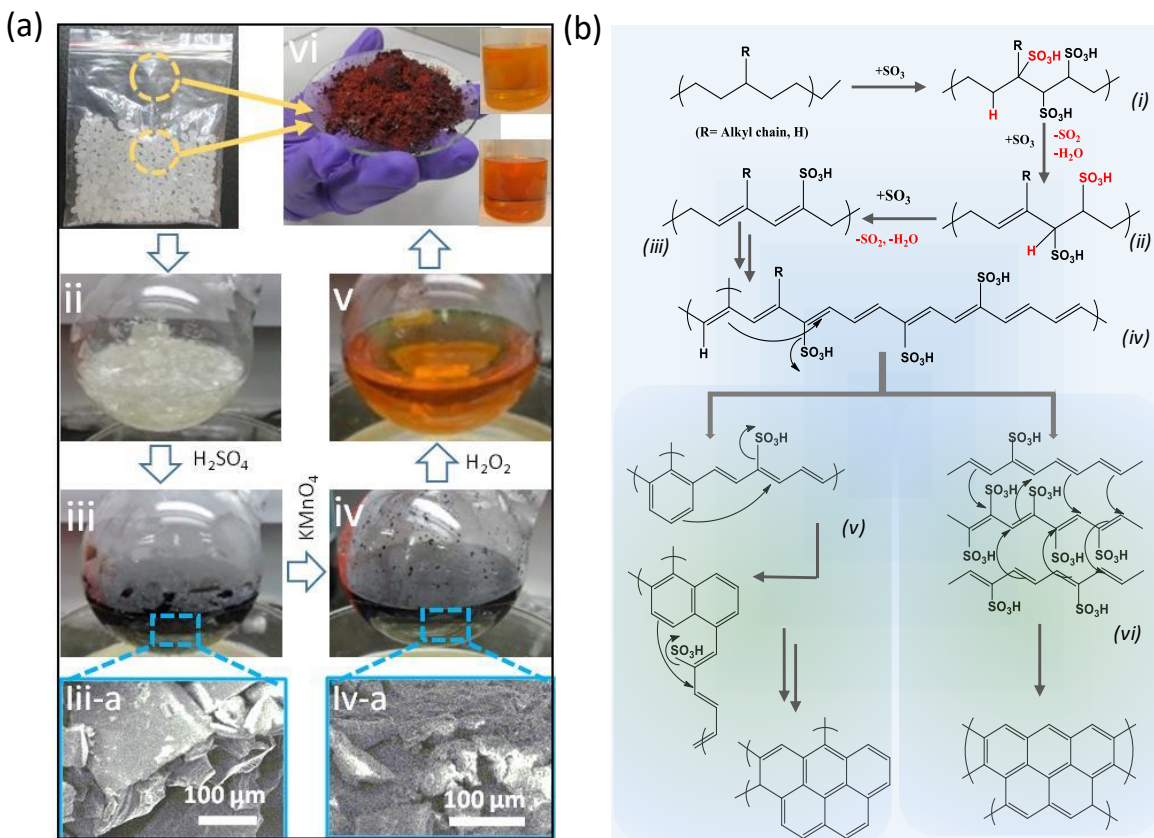


**Figure 3.2.1** (a) Illustration of the three-step synthesis route of PE-CQDs. First step is acid treatment of PE (i) at  $\sim 150^\circ\text{C}$  leading to swelling (ii) and charring (iii). iii-a shows SEM image of the charred product containing graphitic sheets.  $\text{KMnO}_4$  is added in the second-step resulting in a stable black dispersion (iv). The oxidation process leads to functionalization of the graphitic sheets creating a rough surface (iv-a). In the final step, hydrogen peroxide is added to the reaction aliquot yielding orange-yellow coloured stable dispersion of PE-CQDs (v). (vi) Photograph of solid PE-CQDs (5.4 g) obtained from 8 g of polyethylene. Inset images show undisturbed, two-year old PE-CQD solutions in water (bottom) and ethyl acetate (top). (b) Schematic showing



*transformation of polyethylene to graphitic CQDs. Concentrated sulfuric acid treatment of the alkane back-bone leads to dehydrogenation and to the formation of sulfonated alkene chains (iv), following a sequence of substitution and elimination reactions. iv undergoes aromatic annulation reaction either by an intra-molecular step-wise process or by intermolecular dominos process.*

PE backbone is very difficult to be broken down in mild conditions. However, concentrated sulphuric acid is known to induce dehydrogenation by first sulfonating PE at high temperature (**Figure 3.2.1b**).<sup>37</sup> Under the heating conditions, those sulfonate groups then leave in the form of H<sub>2</sub>SO<sub>3</sub> by extracting hydrogen from its neighbouring carbon atom and creating C=C bonds (**Figure 3.2.1b (ii, iii)**).<sup>38</sup> Prolonged treatment leads to cross-linking of the polymer chains and even to carbonization.<sup>39,40</sup> Such observations led us to hypothesize an alternate scenario where dehydrogenation involves two C atoms (a) in a single alkene chain, separated by four others (**Figure 3.2.1b (iv)**) or (b) from two different chains. A benzene derivative may form in each case, as shown in **Figure 3.2.1b (v), (vi)** and further continuation of the process should eventually yield tiny graphene-like structures. Furthermore, cyclization involving a wrong C-atom will lead to defective graphene derivative with enhanced oxygen affinity. The C-atoms outside the graphitic network can be removed by controlled oxidation, leading to the formation of CQDs.

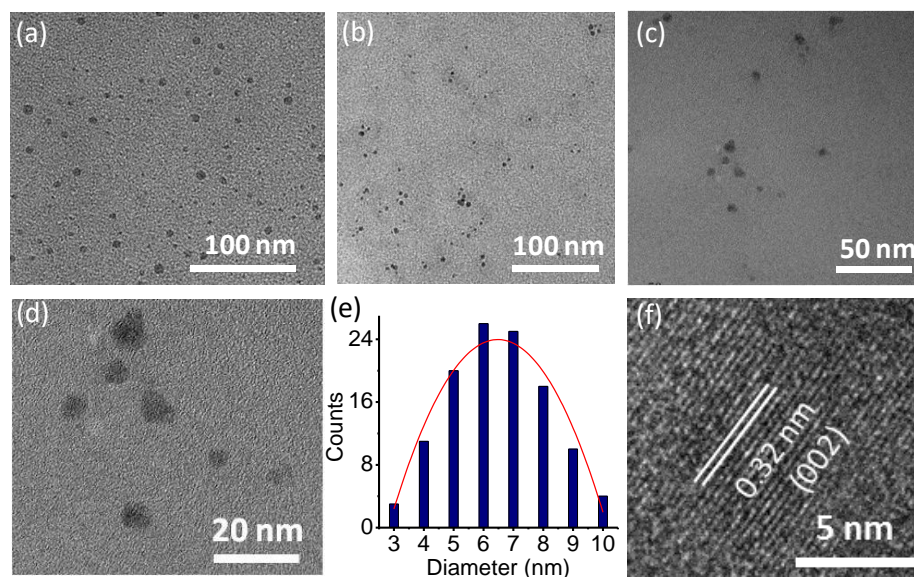


**Figure 3.2.2** (a, b, c, d) TEM images of PE-CQDs. (e) The particle size distribution plot of PE-CQDs. (f) HRTEM image of a PE-CQD showing the (002) plane of a graphite lattice.

The transmission electron microscopy (TEM) images showed that the PE-CQDs predominantly contain 3-10 nm particles with an average size of 6.5 nm (**Figure 3.2.2a,b,c,d,e**). High resolution TEM (HRTEM, **Figure 3.2.2f**) images revealed that the PE-CQDs were indeed consisted of the graphitic regions containing fringes corresponding to the (002) crystal planes separated by 0.32 nm as was initially hypothesized. Powder X-ray diffraction (XRD) analysis of the sample confirmed the graphitic nature of the entire sample (**Figure 3.2.3a**). Elemental analysis by energy dispersive X-ray spectroscopy (EDS) revealed the presence of S originating from the residual sulfonyl groups (**Figure 3.2.3b**).

Fourier transformed infrared (FT-IR) and Raman spectroscopy were used to examine the chemical-transformations during the synthesis. It revealed that the C-H stretching ( $\sim 2900\text{ cm}^{-1}$ ) and bending ( $\sim 740\text{ cm}^{-1}$ ) peaks in the FT-IR spectrum of untreated PE greatly reduced in intensity after the acid treatment due to charring (**Figure 3.2.3c**). Concurrently, a broad peak centered around  $3500\text{ cm}^{-1}$  indicative of OH functionalization appeared. In addition, two relatively prominent peaks associated with carbonyl groups and C=C appeared at  $1718\text{ cm}^{-1}$  and  $1635\text{ cm}^{-1}$  respectively. Elemental analysis in SEM confirmed the presence of S in the sample originating from sulfonyl groups at this stage, even though S=O vibrational modes at  $1150\text{ cm}^{-1}$  could not be ascertained. Any residual C-H moieties in this sample were eliminated during  $\text{KMnO}_4$  treatment.

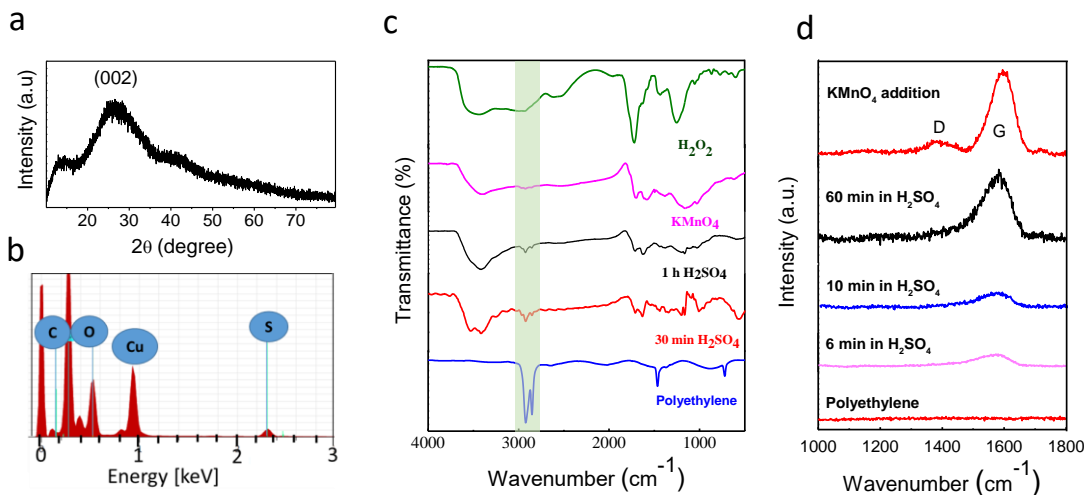


**Figure 3.2.3** (a) XRD pattern and (b) TEM-EDS spectrum recorded on PE-CQDs. (c) FT-IR spectra and (d) Raman spectra recorded on the precursor, partially or fully converted polyethylene during the different stages of preparation.

Sharp peaks at 1450, 1260 and 1725  $\text{cm}^{-1}$  corresponding to the C-O-C, C-O and C=O stretching vibrations respectively appeared after addition of  $\text{H}_2\text{O}_2$ , suggesting the formation of ether and carbonyl functional groups. Peak at 1100 and 1000  $\text{cm}^{-1}$  corresponds to the S-O stretching vibration. Raman spectra recorded during the course of the reaction showed that dehydrogenation and charring resulted in graphitization within 6 minutes of the reaction (**Figure 3.2.3d**) as revealed by appearance of the graphitic (G) band at 1575  $\text{cm}^{-1}$ . A new peak at 1384  $\text{cm}^{-1}$  corresponding to the defective (D) band was observed when  $\text{KMnO}_4$  was added to the reaction mixture. Addition of  $\text{H}_2\text{O}_2$  at this stage led to accelerated oxidation of the black carbon mass leading to a transparent PE-CQDs solution.

X-ray photoelectron spectroscopic (XPS) analysis of the PE-CQD powder suggested extensive functionalization with various groups such as hydroxyl, epoxy, carboxyl groups etc. with a C to O atomic ratio of 52:48, estimated from the 1s peak intensities weighted against their photoionization cross-section. **Figure 3.2.4a** shows the C 1s core-level XPS spectrum which could be fitted with 5 peaks. We assigned the peaks at  $\sim 284.5$  eV to  $\text{sp}^2$  C-C, 285.45 eV to  $\text{sp}^3$  C-C, 286.3 eV to C-O- (hydroxyl) and C-O-C (epoxy) groups, 287.9 eV to C=O (carbonyl) species and 288.9 eV to COOH (carboxyl) groups with relative abundance of 49%, 20%, 11%, 12% and 8%

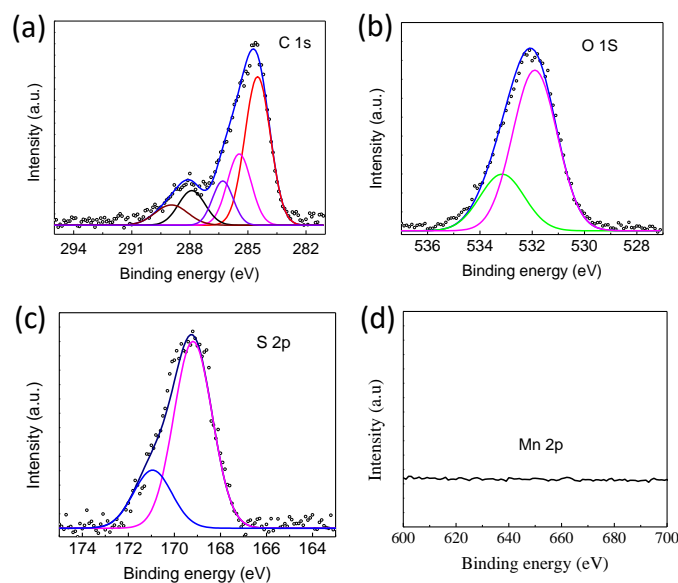


**Figure 3.2.4** (a) XPS spectrum recorded on the PE-CQDs corresponding to C 1s (a), O 1s (b), and S 2p (c). (d) In order to ensure the absence of any Mn impurity which might get incorporated into the CQDs during oxidation by  $\text{KMnO}_4$ , we recorded the XPS spectrum in the Mn region. No Mn signal was detected.

respectively.<sup>41-43</sup> The amount of oxygen forming double and single bond was estimated by deconvoluting the O 1s peak showed in **Figure 3.2.4b**. Assuming that peaks at 531.9 eV and 533.2 eV to be arising from a double bonded and single-bonded oxygen species respectively yielded an atomic ratio of ~74:26. We also confirmed the presence of strongly polar sulphur groups in the PE-CQDs from the S-2p core-level signal, as observed in EDS analysis showed in **Figure 3.2.4c**. Therein, the binding energy of 169.2 eV (S2p<sub>3/2</sub> component) is close to the binding energy of for sulfonic acids or sulfonates.<sup>44,45</sup> The overall atomic ratio of C, O and S in the PE-CQDs are ~48%, ~42% and ~10% respectively. In addition, XPS analysis also confirmed the absence of any Mn-based species (**Figure 3.2.4d**) in the PE-CQDs.

Decorated with acidic groups, an aqueous PE-CQD solution exhibits a pH that lowers with increase in its concentration. Accordingly, and notably, we observed partial deprotonation of the acidic groups leading to pH values of ~3.6, ~2.8 and ~2.7 for PE-CQD concentrations of 0.2 mg/ml, 2.5 mg/ml, 5 mg/ml in aq. Medium respectively (**Figure 3.2.5a**).

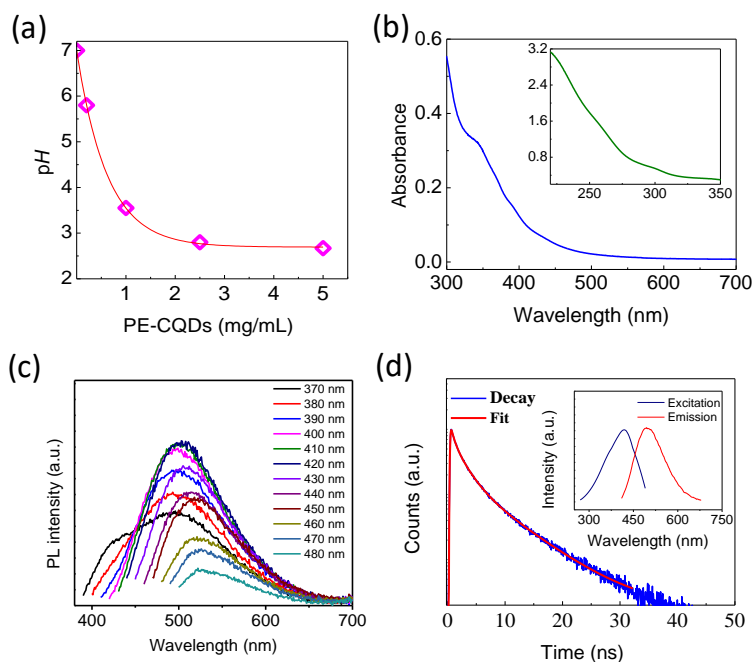


**Figure 3.2.5** (a) pH of an aqueous solution containing different amounts of PE-CQDs. (b) UV–visible absorption spectrum of an aqueous PE-CQD solution. The spectrum corresponding to the UV region is seen in the Inset. (c) Emission spectra of PE-CQDs under different excitation wavelengths (from 360 to 480 nm). (d) The time-resolved fluorescence decay plot of PE-CQDs at 530 nm emission, obtained using TCSPC technique (excitation at 375 nm). The inset shows photoluminescence spectrum of PE-CQDs.

We studied the photophysical exciton properties of the PE-CQDs by using UV-Visible (UV-Vis) absorption and fluorescence (FL) spectroscopy. A solution of PE-CQDs exhibits an onset of absorption at  $\sim 550$  nm (equivalent to a band-gap,  $E_g$ , of 2.59 eV) and other noticeable absorption features centered around 340, 370, 395, 430 nm (**Figure 3.2.5b**). PE-CQD solution appears bluish green under UV illumination and exhibits FL emission that varies with the excitation wavelength. We examined the emission behaviour in  $\lambda_{ex} \sim 370$ -480 nm range and found that a shift in  $\lambda_{ex}$  was accompanied by a similar shift of the emission peak **Figure 3.2.5c**. The maximum fluorescence intensity was observed at 500 nm using  $\lambda_{ex} = 420$  nm (inset in **Figure 3.2.5d**). The corresponding luminescence quantum efficiency was found to be 9.5% at 500 nm emission suggesting that only a minority of the photogenerated excitons recombine radiatively. The luminescence decay behaviour measured at room temperature by time-correlated single photon counting (TCSPC) method (**Figure 3.2.5d**) using excitation and emission wavelengths of 375 nm and 500 nm respectively can be fitted to a triple-exponential function accounting for lifetime components of 10.68 ns, 4.15 ns and 0.81 ns, and a mean lifetime of 3.71 ns.

We point out that the PE-CQD fabrication method has some similarities and at the same time, certain key differences with the Hummer's method as seen from the following discussion. In fact, we show below that Hummer's method using graphite as precursor cannot be extended for CQD synthesis. The main differences are: 1) PE-CQD method can be loosely considered as three step method: Step 1 is acid charring, step 2 is oxidation of the char, step 3 is the creation of OD CQDs from the oxidized char (as shown in **Figure 3.2.6**). Thus CQD method has an extra step of dehydrogenation and charring.

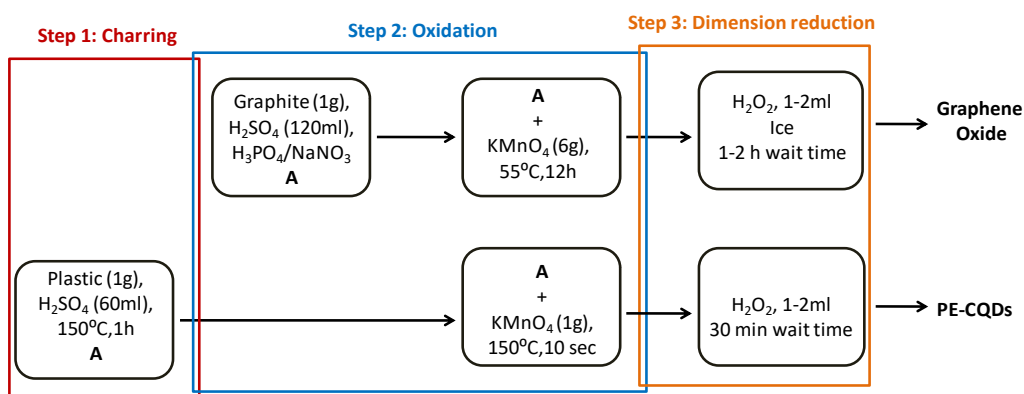


**Figure 3.2.6** Steps involve in our synthesis and comparison with Hummer's method.

However, there are key differences including rupturing of C-C covalent bonds in CQD method which does not take place in GO synthesis. Besides, PE-CQD method with graphite as starting materials does not yield CQDs highlighting the difference between them as shown in Figure 6. Hummer's method is 3D→2D conversion involving only Vander Waals bonds rupture while PE-CQD method is 3D→0D conversion involving both covalent & Vander Waals bond rupture. 3) Graphite as a precursor does not work in PE-CQD method and this is a vital difference between with Hummer's methods. To demonstrate the same we carried out the PE-CQD synthesis with graphite powder as a starting material. We kept the other reaction condition same. This did not result in any visible colour change, which confirms that CQDs formation did not occur appreciably. We have centrifuged the whole solution and washed with water followed by ethanol, dried at 90 °C and collected the unconverted graphite powder. Out of 1 g of graphite powder used, 0.91 g graphite powder was left-over as shown in **Figure 3.2.7**.

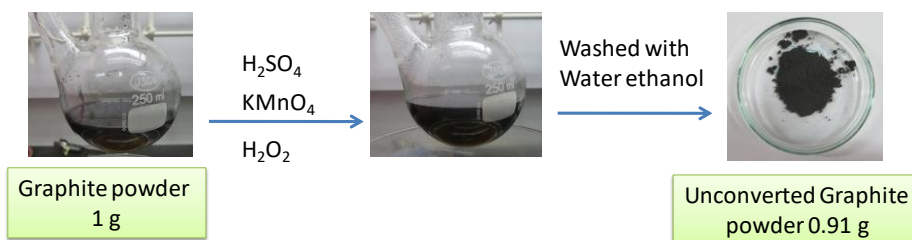


**Figure 3.2.7** Synthesis of CQDs using graphite powder as precursor. Barely any CQD was found after the reaction. Black powder was collected at the end of the reaction

### 3.2.4.2 Oxygen adsorption of PE-CQDs

Next, we examined our hypothesis of high oxygen affinity by PE-CQDs. We measured the  $O_2$  uptake in a deaerated (obtained by purging with  $N_2$ ) 30 ml aqueous solution containing 25 mg of PE-CQDs by exposing it to air and compared the same with that in pure water (**Figure 3.2.8a-b**). Oxygen uptake in both the solutions is initially fast before slowing down until reaching saturation. The PE-CQD solution attained a much higher  $O_2$  saturation level of  $\sim 640 \mu M$  as compared to  $\sim 320 \mu M$  in water. On the other hand, when  $N_2$  was purged through the  $O_2$  saturated solutions, oxygen concentration depleted and attained a minimum level of  $\sim 95 \mu M$  in the PE-CQD solution and  $\sim 5 \mu M$  in water. The amount of TO was found to increase monotonously with increase in the concentration of PE-CQD, measuring  $475 \mu M$  and  $705 \mu M$  when 5 and 30 mg of CQD was dissolved (**Figure 3.2.8c**). Subtraction of the oxygen amount value in pure water from the total

oxygen content in the PE-CQDs solution, as seen from the modified y-axis in **Figure 3.2.8c** also shows a linear increase. In order to examine the reversible nature of oxygen enrichment in the PE-

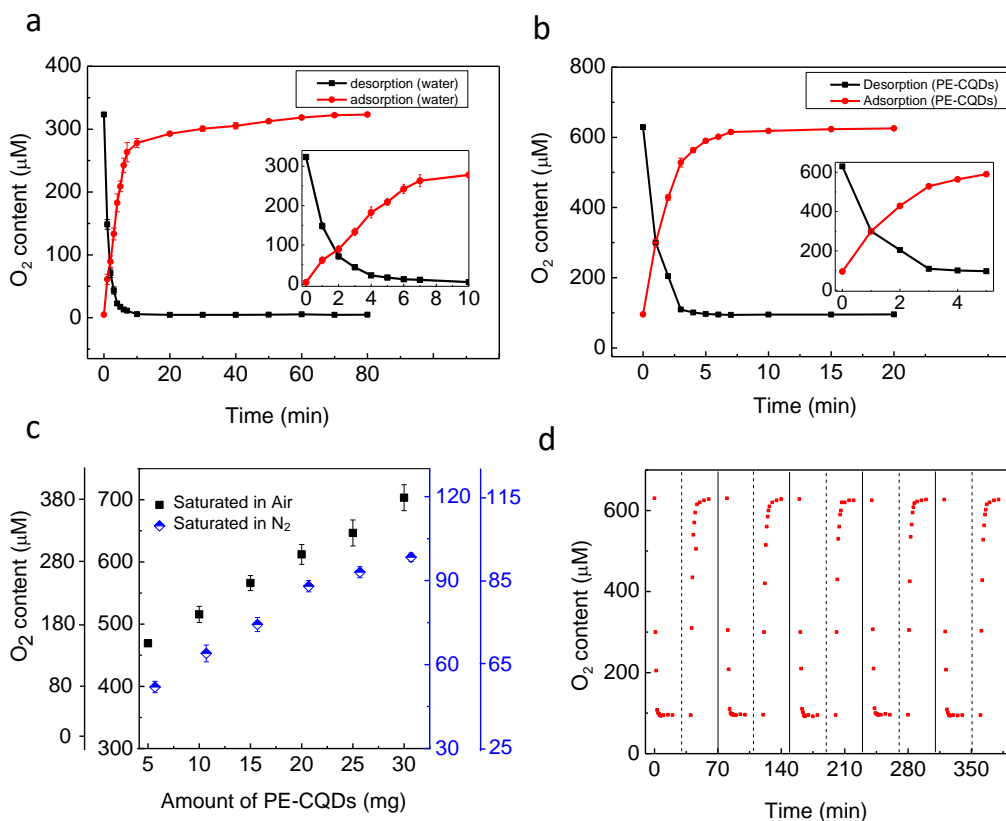


**Figure 3.2.8** Temporal variation of total oxygen content in (a) pure water and (b), aqueous PE-CQD solution during purging with nitrogen and subsequently during spontaneous oxygen uptake from air by the nitrogen saturated solutions. Insets in a and b highlight the rates of O<sub>2</sub> uptake and release. (c) Maximum and minimum amounts of O<sub>2</sub> levels estimated in a normal and N<sub>2</sub> purged solution containing different amount of PE-CQDs (the outer scales on both sides of the plot describe the increase in the TO level as compared to pure water). (d) Repeatability test for oxygen uptake and release using 25 mg of PE-CQDs in 30 ml water (measurements of oxygen content were carried out 0.5 mm below the aqueous surface having 20 cm<sup>2</sup> surface area).

CQDs solution, we have repeated the O<sub>2</sub> uptake and N<sub>2</sub> purging cycle for 5 times that showed nearly identical trends (**Figure 3.2.8d**). Since the PE-CQD solution is acidic in nature, the adsorption-desorption cycles were further carried out in water by maintaining a similar pH using HCl and H<sub>2</sub>SO<sub>4</sub>, which showed no appreciable differences in the O<sub>2</sub> level.

In addition, we also compared the oxygen contents in water in presence of CQDs obtained by a known method using glucose as precursor,<sup>46</sup> graphene oxide prepared by modified Hummer's method<sup>47</sup> and two other popular photocatalysts, TiO<sub>2</sub> and BiOCl to verify that oxygen uptake is specific to the PE-CQDs. In all instances, the differences in the total O<sub>2</sub> contents were not remarkable from that of pure water showed in **Figure 3.2.9**.

Apart from the high saturation level, the uptake of O<sub>2</sub> in the PE-CQD solution occurs at a faster rate than in water. To reach a level of 250 μM requires about 5 minutes in water, while less than a minute in PE-CQD solution. Reaching 80% of the O<sub>2</sub> saturation level takes about 7 min and 3 min in those two solutions respectively. On the other hand, 80% expulsion of O<sub>2</sub> in a constant flow of N<sub>2</sub> requires about 2.5 minutes in both the solutions. Since only 0.025 g of PE-CQD is present in the 30 g of water containing ~20 μmol of O<sub>2</sub>, the major fraction of water is expected to be free from the influence of PE-CQD and in there, O<sub>2</sub> levels

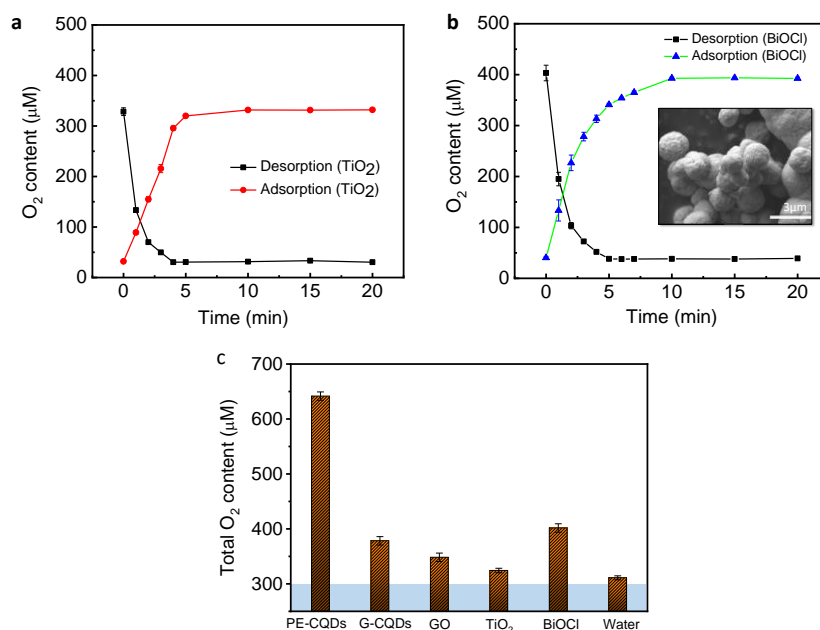


**Figure 3.2.9** Temporal variation of total oxygen content in (a) TiO<sub>2</sub> and (b), BiOCl aqueous solution during purging with nitrogen and subsequently during spontaneous oxygen uptake from air by the nitrogen saturated solutions. c, Total O<sub>2</sub> content measurement of G-CQDs, GO, TiO<sub>2</sub> and BiOCl materials.



is expected to be similar to that of pure water, as per Henry's law, containing  $\sim 11 \mu\text{mol O}_2$ . The remaining  $9 \mu\text{mol O}_2$  therefore should be associated with the PE-CQDs, suggesting  $\sim 0.01 \text{ g O}_2$  per  $1 \text{ g}$  of C-dot.

We found that the rate of oxygen uptake depends, as expected, on the depth of the measurement region from the liquid surface exposed to air as well as on the exposure area. **Figure 3.2.10** depicts the  $\text{O}_2$  uptake measurements carried out  $1 \text{ cm}$  and  $8 \text{ cm}$  below the exposed aqueous surface of area  $7 \text{ cm}^2$ . When we compared the ratio of the time taken by PE-CQD solution and water to attain  $80\%$  of overall oxygen saturation, the values were consistent within  $\pm 5\%$  confirming a higher diffusion rate for oxygen in PE-CQD solution. An enhanced apparent  $\text{O}_2$  diffusion in water by PE-CQDs is a new observation, to the best of our knowledge and can be attributed to a persistent high concentration gradient, since dissolved oxygen quickly associates with the CQDs depleting  $\text{O}_2$  level in the surrounding.

The origin of oxygen uptake by dissolved PE-CQDs from air may be related to absorption in other carbon forms,<sup>48</sup> nonetheless distinct due to exceptionally the high quantity that is comparable to metal organic frameworks and zeolites at ambient conditions.<sup>49</sup> This is conjunction

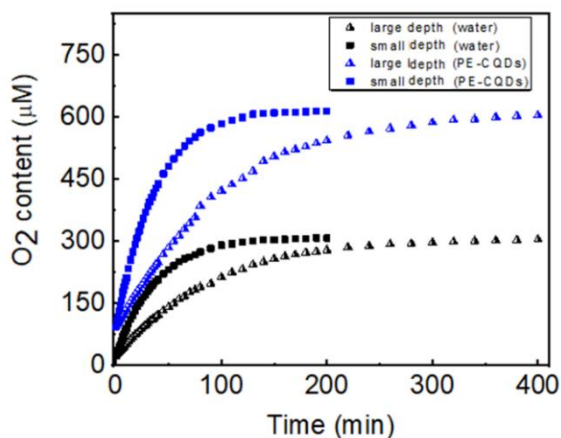


**Figure 3.2.10** Temporal variation of total oxygen content in pure water and PE-CQD solution during oxygen uptake from air by  $\text{N}_2$  saturated samples at depths of  $1 \text{ cm}$  and  $8 \text{ cm}$  below the exposed surface. (Exposure area =  $7 \text{ cm}^2$ )

with photo-activity, solvent compatibility and high stability suggests that PE-CQDs should be highly active photocatalyst for oxidation reactions (while they have been primarily used for photo-reduction reactions) where molecular oxygen is one of the reactants.

### 3.2.4.3 Photocatalytic performance

In order to compare the photocatalytic properties of these sulfonyl group containing acidic PE-CQDs with a wide range of photocatalysts, we first studied a well-known model reaction of Rhodamine B (RhB) photodegradation. **Figure 3.2.11a** shows the temporal evolution of UV-Visible absorption spectra of the RhB solution exposed to light in presence of PE-CQDs. The recyclability of the PE-CQDs were found to be remarkable in comparison to many other efficient photocatalysts reported till date, when investigated for the degradation of Rhodamine-B (RhB) dye, a notable color pollutant. The high activity even after 100<sup>th</sup> cycle is comparable with most *state-of-the-art* catalysts (**Figure 3.2.11b**). **Figure 3.2.12** shows the temporal evolution of UV-

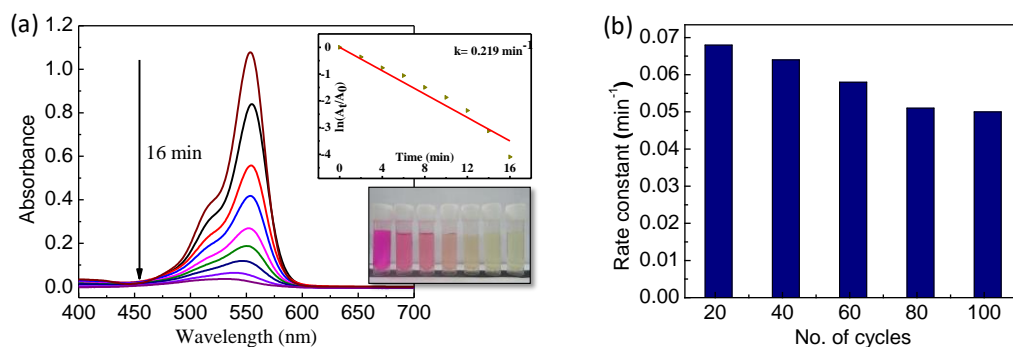


**Figure 3.2.11** (a) UV-visible absorption spectra of Rh-B at different time interval during catalytic degradation using PE-CQDs. Inset is plot of  $\ln(A/A_0)$  vs. time of Rh-B photo-degradation (top) and photographic images of Rh-B dye solution after different light illumination time. (b) Photocatalytic efficiency of the PE-CQDs were tested for 100 catalytic cycles. The plot shows the efficiency of the 20<sup>th</sup>, 40<sup>th</sup>, 60<sup>th</sup>, 80<sup>th</sup> and 100<sup>th</sup> cycle.

Visible absorption spectra of the RhB solution exposed to light in presence of PE-CQDs 1<sup>st</sup> cycle, after 40<sup>th</sup> and 100<sup>th</sup> cycle. The temporal UV-visible spectral changes of RhB aqueous solution during its photo-degradation using PE-CQD is shown in **Figure 3.2.12a**. The absorption corresponding to the  $\lambda_{\max}$  for RhB at 553 nm gradually decreased exhibiting a reaction rate-constant of 0.22 min<sup>-1</sup> and turnover frequency of 22.01 min<sup>-1</sup>g<sup>-1</sup> (**Figure 3.2.12b**). As seen in these plots, the variation in these cycles are not extensive. The rate constant and TOF for the reaction after 100<sup>th</sup> cycle is 0.05 min<sup>-1</sup>. 5.0 min<sup>-1</sup>g<sup>-1</sup> respectively, which is comparable to efficiencies of

fresh and efficient photocatalysts such as nanocrystalline TiO<sub>2</sub>, g-C<sub>3</sub>N<sub>4</sub> and Ag/AgFeO<sub>2</sub> exhibiting rate constants 0.0654 min<sup>-1</sup>, 0.0243min<sup>-1</sup>, 0.040 min<sup>-1</sup> respectively and TOF of 2.6 min<sup>-1</sup>g<sup>-1</sup>, 0.81 min<sup>-1</sup>g<sup>-1</sup> and 1.6 min<sup>-1</sup>g<sup>-1</sup> respectively. We have further carried out RhB degradation with commercial P-25 under identical conditions (i.e. weight of the catalyst, dye concentration, light intensity since there is considerable variation is reaction conditions in most literature reports). The rate constant and TOF values for P-25 were found to be 0.0956 min<sup>-1</sup>g<sup>-1</sup> and 9.5 min<sup>-1</sup>g<sup>-1</sup>. The reaction mechanism in both cases appeared to be similar.

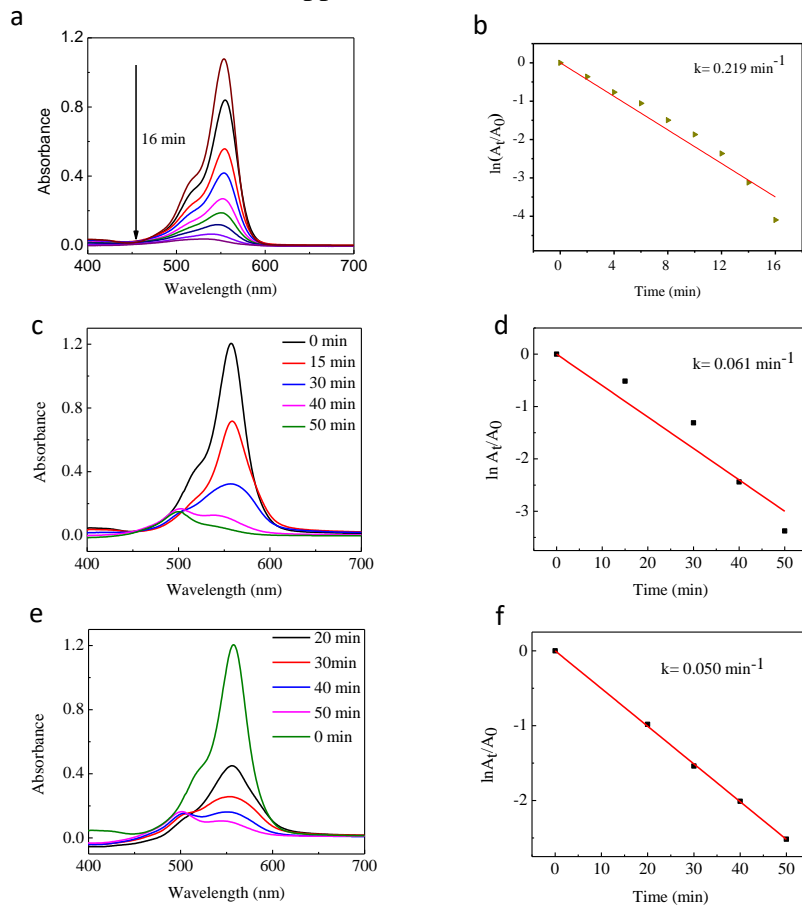


**Figure 3.2.12** UV-visible absorption spectra of Rh-B at different time interval during catalytic degradation using PE-CQDs for the 1<sup>st</sup> cycle (a), Plot of  $\ln(A_t/A_0)$  vs. time of Rh-B photo-degradation for the 1<sup>st</sup> cycle (b). UV-visible absorption spectra of Rh-B at different time interval during catalytic degradation using PE-CQDs after 40<sup>th</sup> cycle (c), Plot of  $\ln(A_t/A_0)$  vs. time of Rh-B photo-degradation after 40<sup>th</sup> cycle (d). UV-visible absorption spectra of Rh-B at different time interval during catalytic degradation using PE-CQDs after 100<sup>th</sup> cycle (e), Plot of  $\ln(A_t/A_0)$  vs. time of Rh-B photodegradation after 100<sup>th</sup> cycle (f).

The PE-CQDs were very stable over 100 catalytic cycles after an initial reduction in activity (**Figure 3.2.12a**). The rate constants after the 20<sup>th</sup> and 100<sup>th</sup> catalytic cycles were  $\sim 0.068 \text{ min}^{-1}$  and  $0.05 \text{ min}^{-1}$  respectively. With high photocatalytic activity and adsorbed  $\text{O}_2$ , the PE-CQDs appeared as an ideal candidate to catalyze photo-oxidation reactions.

***Selective photocatalytic oxidation of benzyl alcohol:***

Selective oxidation of aromatic alcohols to carbonyl compounds using molecular oxygen as oxidant is an important functional group transformation which has been realized using a number of photocatalysts recently.<sup>7,10,50,51</sup> In this oxidation process,  $\text{O}_2$  acts as an oxidizing agent and reduced to  $\text{H}_2\text{O}_2$  itself.<sup>11</sup> Therefore  $\text{O}_2$  is purged into the reaction mixture to ascertain its high concentration on the catalyst surface. Moreover, such reactions are often carried out at elevated temperatures.

We carried out photocatalytic oxidation of aromatic alcohols in presence of PE-CQDs in ambient conditions using direct sunlight as well as 400 W Xe-lamp and found that conversion efficiencies are nearly identical. Using 25 mg of PE-CQDs in acetonitrile solvent, conversion of benzyl alcohol (BA) to benzaldehyde (BD) was estimated to be 68% with selectivity of  $>90\%$  after 4 h. No oxidation product was obtained in dark even after 4 h, unlike the surface plasmon-based catalysts that drive the oxidation reaction in dark also.<sup>10</sup> The conversion efficiencies were 29% and 2% in the wavelength range of 500-600 nm and 600-700 nm respectively as compared to that in 400-500 nm, resembling optical density in the PE-CQD absorption spectrum.

***Apparent Quantum Efficiency (AQE):*** In order to calculate the AQE for the photocatalytic BA oxidation, we considered the reaction in direct sunlight with a reaction yield of 67% in 4 h and the solar spectrum at the sea-level (**Figure 3.2.13a**). Our sun-light intensity may slightly vary and therefore the calculated efficiencies can be considered representative, with a minimal deviation from expected values. An additional complicacy arises because the estimated AQE can be further increased by using larger amount of PE-CQDs or benzyl alcohol or by considering conversion in the first few minutes only (the reaction becomes slow progressively as BA gets consumed). For calculation of overall efficiency, we counted the number of incident photons from higher energies till 500 nm where, based on the UV-Vis absorption spectrum of PE-CQDs, the absorption is  $>95\%$ . For calculations of efficiencies in the 300-400 nm, 400-500 nm, 500-600 nm and 600-700 nm, the

photon numbers in the respective regions were calculated separately and yields were estimated using diode assemblies (Newport, USA) mimicking solar spectrum. The apparent quantum efficiency we report below, in all probability, is smaller than the actual quantum efficiency because the number of absorbed photons is expected to be lesser than that of incident ones.<sup>52</sup> The incident power on the sample can be represented as:

$$P_{\text{incident}} = \rho_{\text{incident}}(\lambda) \times A_{\text{sample}}$$

$A_{\text{sample}}$  is the area exposed to incident light (12 cm<sup>2</sup>),  $\rho_{\text{incident}}(\lambda)$  is the incident power on the sample corresponding to photon of wavelength  $\lambda$ .

The incident powers on the sample was estimated to be 168, 35 and 133 mW in the wavelength range of 300-500 nm, 300-400 nm, 400-500 nm (considering >95% photon absorption by PE-CQDs), and 155 and 144 mW in 500-600 nm and 600-700 nm (considering remaining <5% absorption) respectively. The number of incident photons per second, as a function of wavelength can be expressed as:

$$N_{ph}(\lambda) = \frac{\rho_{\text{incident}}(\lambda)}{E_{ph}(\lambda)}$$

Where  $E_{ph}(\lambda) = hc/\lambda$  is the photon energy for the corresponding wavelength. For example, the total number of photons incident on the sample per second within wavelength range of 400-500 nm can be calculated as:

$$N_{ph,incident}(400 - 500) = \int_{400}^{500} \frac{\rho_{\text{incident}}(\lambda) \times \lambda}{hc} d\lambda$$

The AQE can be derived from the following equation:

$$AQE = n (\text{No. of electron or hole}) \times \frac{\text{Number of benzaldehyde molecule produced}}{\text{Number of incident photons}} \times 100 (\%)$$

For benzyl alcohol oxidation n is 2.

(For 400-500 nm):

$$AQE = 2 \times \frac{0.0000425}{0.00182} \times 100(\%) = 2.3 \%$$

Similarly for 300-400, 500-600, 600-700 nm ranges, the calculated AQE are 4.8, 0.48 and 0.026 % respectively (**Figure 3.2.13b**). Overall AQE <500 nm where light absorption of PE-CQDs is >95 % = 7.7 %.

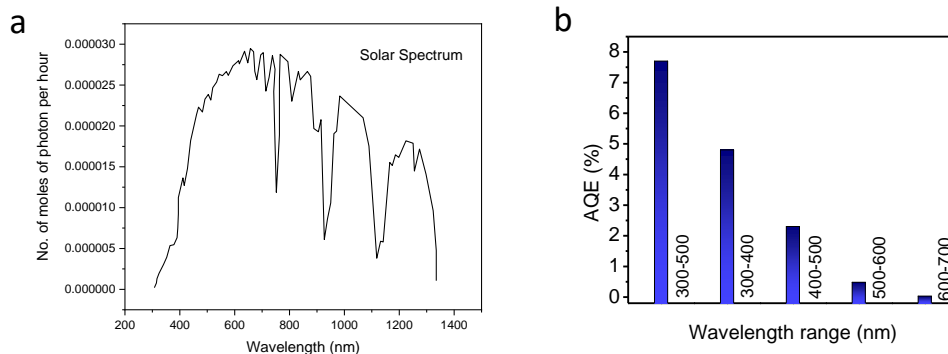


**Figure 3.2.13** a, Solar spectrum. b, The AQE (%) in different wavelength regions for the photocatalytic benzyl alcohol oxidation.

It is to be noted that there was no change in temperature of the reaction aliquot during the reaction. Since Xe lamp and sun light contain IR radiation, we performed the following experiments which suggest that the reaction involves a photocatalytic process and not a photo-induced thermocatalytic process. First as a preliminary check, we have carried out all catalysis reactions using water-based IR-filter. The reaction temperature was constantly monitored and found to be constant throughout the reaction period (~33-35°C) (Table 3.2.2). Second, we have also carried out the reaction in absence of light, but no conversion was noticed, confirming that the process is not purely thermocatalytic and irradiation by visible light is mandatory.

**Table 3.2.2:** Temperature of the reaction medium throughout the reaction period.

Reaction time	0 h	1 h	2 h	3 h	4 h
Temperature (°C)	33	34	33	33	35

To prove that this reaction is actually not a photo-induced thermocatalytic process we have carried out the reaction using light having 400-500 nm wavelength range by using a 3-LED setup (Newport, USA). The reactants indeed showed conversion to products, given in Table 3.2.3 inferring that the reaction is photocatalytic in nature.

**Table 3.2.3:** Conversion efficiency with different light sources.

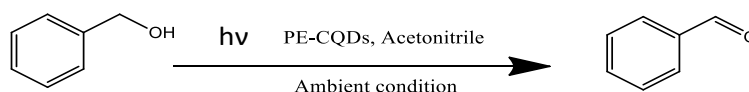
Reaction condition	Time (hour)	Conversion (%)
Xe-lamp with water circulation	4	68%
Reaction in dark	4	>1%
400-500 nm	4	17%

Further to check the relationship between oxygen content and photocatalytic activity, we (i) purged the reaction mixture with N<sub>2</sub> and added PE-CQDs (which must be containing high level of oxygen) and (ii) in reverse order, first added PE-CQDs to the reaction mixture and then purged with N<sub>2</sub>, before exposing the aliquots to lights. The reaction yields were 51% and 26% respectively affirming high O<sub>2</sub> level on PE-CQDs and its contribution to the oxidation reaction (**Table 3.2.4**, entry no.6<sup>a</sup> and 6<sup>b</sup>). The reaction was only marginally faster with O<sub>2</sub> purging (~70% yield in 4 h) suggesting that unlike other catalysts, PE-CQD surface is saturated with oxygen even in ambient conditions (**Table 3.2.4**, entry no.5). We examined the oxidation reaction using various *p*-substituted BA and found that the presence of substituent groups reduces the rate of the reaction moderately. A detailed comparison of the catalytic activity and substrate scope is given in **Table 3.2.5**. In **Table 3.2.6**, we compare the conversion efficiency exhibited by the PE-CQDs with that by other heterogeneous catalysts, which shows that the current efficiencies are higher in spite of the use of air atmosphere and room temperatures. It is to be noted that the influence of oxygen atmosphere on BA oxidation has been studied earlier which showed that the conversion efficiency decreases by 70-90% in ambient air (**Table 3.2.6**).<sup>11,53,54</sup>

**Origin of activity:** We have carried out 2 sets of experiments to demonstrate that high O<sub>2</sub> content can indeed improve the reaction rate. Set 1 is based on CH<sub>3</sub>CN solvent and Set 2 is based on water as solvent (since O<sub>2</sub> measurements were carried out in water only).

**Set 1:** Herein we have used 4 reactions with different amounts of O<sub>2</sub> content in CH<sub>3</sub>CN and water separately. The first one is by purging oxygen gas during reaction, as is usually done in other investigations from literature. The second was in air where O<sub>2</sub> enrichment occurred only because

**Table 3.2.4:** Aerobic oxidation of alcohols with the PE-CQDs photocatalyst under sunlight.



Entry	catalyst	Environment	Light	Time (h)	Conversion (%)	Selectivity (%)
1	PE-CQDs	Air	Xe-lamp	4	68	>90
2	PE-CQDs	Air	Xe-lamp	2	50	>90
3	PE-CQDs	Air	Sunlight	4	67	>90
4	PE-CQDs	Air	Sunlight	2	48	>90
5	PE-CQDs	O <sub>2</sub>	Xe-lamp	4	70	>90
6 <sup>a</sup>	PE-CQDs	N <sub>2</sub>	Xe-lamp	4	51	>90
6 <sup>b</sup>	PE-CQDs	N <sub>2</sub>	Xe-lamp	4	26	>90
7	PE-CQDs	Air	Dark	4	<1	-
8	TiO <sub>2</sub> -P25	Air	Xe-lamp	4	7	>90

a = reaction mixture was purged with N<sub>2</sub> & then PE-CQDs was added to it

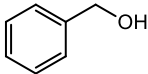
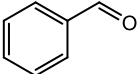
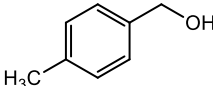
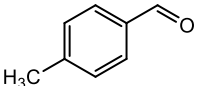
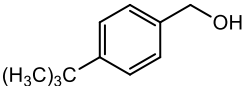
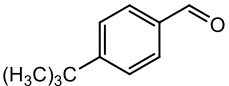
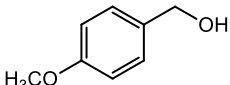
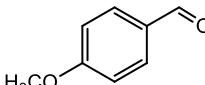
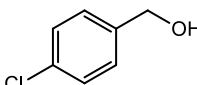
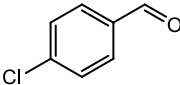
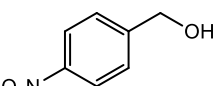
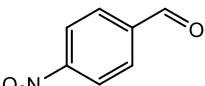
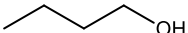
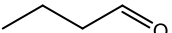
b = PE-CQDs was added first to the reaction mixture & then N<sub>2</sub> was purged

of PE-CQDs. In third attempt, we thoroughly purged N<sub>2</sub> in CH<sub>3</sub>CN and then added PE-CQD to it (here CQDs are already saturated with O<sub>2</sub>). In the fourth approach, we passed N<sub>2</sub> in the PE-CQD solution to expel maximum possible dissolved O<sub>2</sub>. We expected, based on observations in water, that there should not be much difference in reaction yield between the first and the second reaction. Between the third and the fourth approach, 3<sup>rd</sup> should provide better yield since we added PE-CQDs saturated with O<sub>2</sub> which would lead to more O<sub>2</sub> content. On the contrary, the 4<sup>th</sup> approach will drive away oxygen from the PE-CQDs as well as from solvent. We observed that the reaction yields varied accordingly, as given in the following **Figure 3.2.14a**.

**Set 2:** To ascertain the role of oxygen present on the CQDs we have performed the reaction in water medium (a poor medium due to poor solubility of reactants) and results are shown below.



**Table 3.2.5:** Aerobic oxidation of alcohols with the PE-CQD photocatalyst under sunlight

Entry	Substrate	Product	t [h]	Conv. [%]	Sel. [%]
1			4	68	>99
2			4	66	>99
3			4	62	>99
4			4	64	>99
5			4	56	>99
6			4	53	>99
7			4	-	-

**Reaction conditions:** The reactions were carried out in acetonitrile solutions (10 ml), containing substrates (0.5 mmol), photocatalyst (25 mg) under the sunlight, the products were analysed by GC.

For the sake of easy comparison, the maximum yields were considered as 100% yields. The actual yields in CH<sub>3</sub>CN solvents were 70%, 68%, 51% and 26%. The yields in water were 23%, 21%, 15% and 6% for oxygen contents of >1000 μM, 640 μM, 320 μM and 95 μM respectively (NOTE: >1000 μM and 640 μM is not expected to make much difference as in both cases, the CQD surface

**Table 3.2.6:** Comparison of BA oxidation activity reported in this study with that of other efficient heterogeneous catalysts.

Sr. No.	Catalyst	Catalyst Amount	Amount of BA (mmol)	Time (h)	Temp. (° C)	O <sub>2</sub> /Air	Solvent	Conv. (%)	Select. (%)	Ref.
1.	Carbon dots	25 mg	0.5	4	r.t	Air	CH <sub>3</sub> CN	68	>90	Our work
2.	mpg-C <sub>3</sub> N <sub>4</sub>	50 mg	0.65	3	100	O <sub>2</sub>	Trifluorotoluene	57	>99	55
						Air		11	>99	
3.	Ni-TiO <sub>2</sub>	80 mg	0.5	1	r.t	O <sub>2</sub>	BTF	86	99	56
						Air		6	99	
4.	Au <sub>9</sub> -Pd <sub>1</sub> /LDH	24 mg	0.1	5	r.t	O <sub>2</sub>	BTF	91	>99	57
						Air		27	>99	
5.	TiO <sub>2</sub> @CdS	8 mg	-	2	r.t	O <sub>2</sub>	BTF	55	95	58
6.	Ir/TiO <sub>2</sub>	300 mg	300	6	60	-	Solvent free	8.9	92	59
7.	Porous BiOCl	50 mg	0.05	8	r.t	-	Toluene	70	-	60
8.	BiOCl-Au	50 mg	0.5	8	r.t	O <sub>2</sub>	CH <sub>3</sub> CN	75	>99	61
9.	Dye -TiO <sub>2</sub>	8 mg & TEMPO	0.1	18	r.t	O <sub>2</sub>	BTF	80	98	62
10.	CdS-SnO <sub>2</sub>	50 mg	2	8	r.t	O <sub>2</sub>	CH <sub>3</sub> CN	82	96	63
11.	Bi <sub>4</sub> O <sub>3</sub> Br <sub>2</sub>	200 mg	0.025	8	r.t	O <sub>2</sub>	CH <sub>3</sub> CN	90	>99	64
12.	CsPbBr <sub>3</sub> /P-25	25 mg	0.0005	20	80	O <sub>2</sub>	Toluene	50	>99	65
13.	TiO <sub>2</sub> @NH <sub>2</sub> -(Ti) MOF	50 mg	0.3	10.5	r.t	O <sub>2</sub>	BTF	37	-	66
14.	CNx-Ni	5 mg	0.03	24	r.t	-	Phosphate buffer	72	99	67
15.	AuPd-TiO <sub>2</sub>	20 mg	0.04	5	r.t	O <sub>2</sub>	Toluene	87	>99	68

would be saturated, and the difference is only due to the oxygen dissolved in water, which is inconsequential). The data shows that the yield of the reaction is certainly dependent on the oxygen

content in the solution. The results of SET 1 and SET 2 are compared in **Figure 3.2.14b** (for easy comparison, the maximum yields were considered as 100% yields).

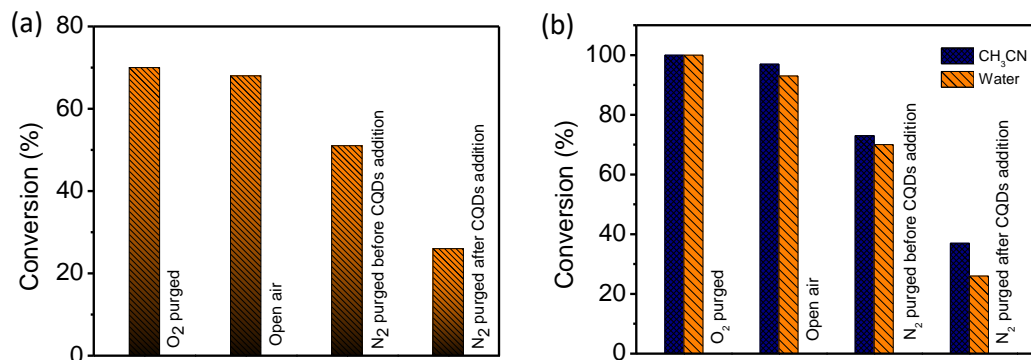


**Figure 3.2.14** (a) Relative conversion efficiency of PE-CQDs in CH<sub>3</sub>CN under different oxygenated conditions confirming that the higher oxygen solubility can improve the photocatalytic oxidation efficiency. (b) Relative conversion efficiency of PE-CQDs in CH<sub>3</sub>CN and in water under different oxygenated conditions demonstrating that the O<sub>2</sub> contents correspond to conversion efficiency.

### Investigations on the Reaction Mechanism

We analysed the reaction mechanism for BA oxidation based on several controlled experiments. Besides confirmed participation of molecular O<sub>2</sub>, we found that both photo-generated electrons and holes contribute to the reaction. Since O<sub>2</sub> alone could not oxidize BA in reasonable amounts,

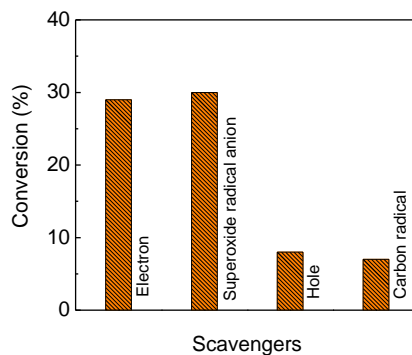


**Figure 3.2.15** Efficiency of BA oxidation in presence of different photogenerated reactive species scavengers.

O<sub>2</sub> activation by electrons is therefore vital. The activated O<sub>2</sub> responsible for BA oxidation was found to be superoxide radicals (O<sub>2</sub><sup>•-</sup>), as the addition of benzoquinone as superoxide radicals scavenger suppressed the conversion (30% yield after 4 h, **Figure 3.2.15**). We further assumed that if we carry out the oxidation reaction in presence of increasing amount benzoquinone, more of O<sub>2</sub><sup>•-</sup> will be lost and the reaction will be progressively slower. We indeed found the same when we increased the amount of benzoquinone (1, 2 and 10 mmol) in the reaction mixture, conversion efficiency decreased systematically (~50%, ~40% and ~32% respectively). We have then carried out electron trapping experiment using silver nitrate and the percentage of conversion was found to be 29% after 4 h. These two similar reaction rates suggest that both the electron transfer to molecular O<sub>2</sub> and O<sub>2</sub><sup>•-</sup> attack on BA are contributed comparably to the reaction rate.

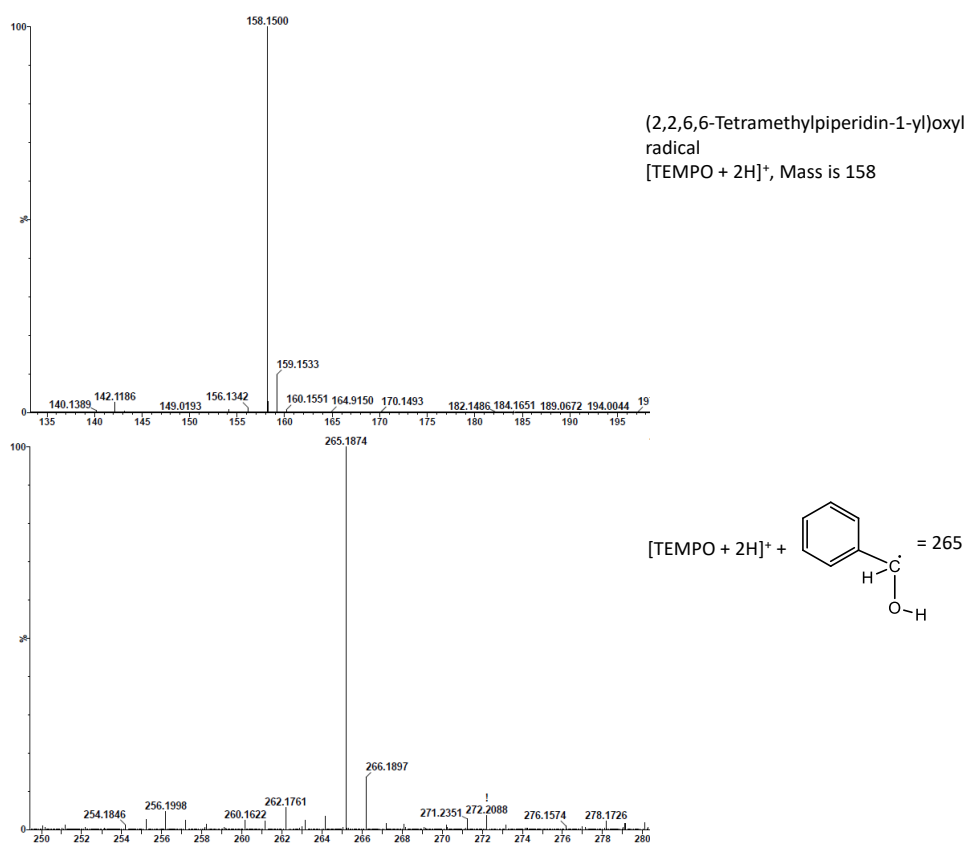
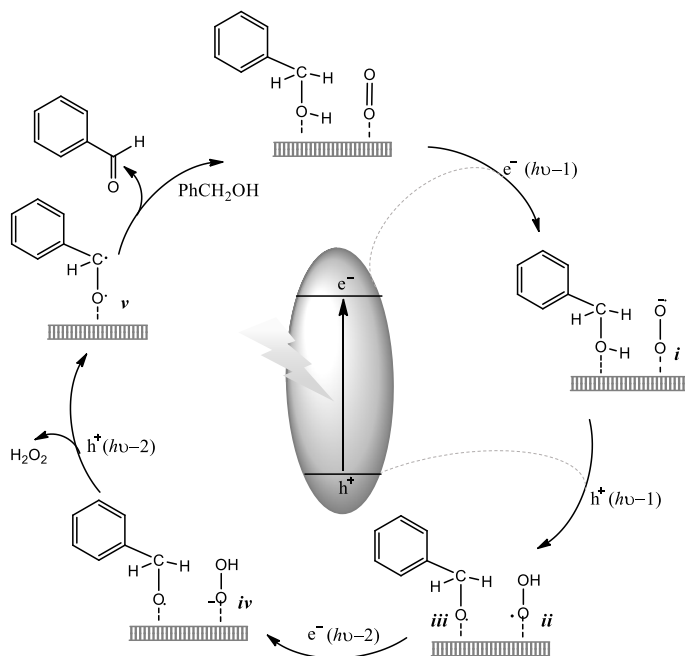


**Figure 3.2.16** TEMPO was introduced into the reaction mixture for BA oxidation by PE-CQDs. HRMS spectra were recorded before the start of the experiment and after irradiation with light for 2 h. Only [TEMPO+2H]<sup>+</sup> was observed at the beginning in due to the acidic PE-CQD solution (top), while TEMPO formed an adduct with the carbon radical species after irradiation with light (bottom).

It has been previously established that the transfer of photogenerated holes to the BA molecules results in formation of a carbon centered radical. Using sodium sulfate as hole scavenger, the conversion was suppressed to a similar extent (8% yield after 4 h). Further, we have performed a



**Scheme 3.2.1** Schematic representation of the probable mechanism for oxidation of benzyl alcohol in presence of PE-CQDs.

reaction in presence of butylatedhydroxytoluene as its scavenger. The BA conversion was suppressed to ~7% after 4 h suggesting that oxidation reaction indeed goes via formation of carbon radical species. We confirmed the generation of this radical by a trapping experiment using TEMPO ((2,2,6,6-Tetramethylpiperidin-1-yl)oxyl radical) and detecting the trapped radical by high-resolution mass-spectroscopy (HRMS, **Figure 3.2.16**).<sup>69</sup> The formation of a carbon centered radical as a rate determining step was also envisioned from these experiments. With these observations, literature reports and direct detection of reaction intermediates, we propose a reaction mechanism as shown in **Scheme 3.2.1**. A superoxide radical anion,  $O_2^{\bullet-}$  (i) first forms using a photo-generated electron. This extracts a proton from a neighbouring BA molecule with assistance from a photo-generated hole, forming an oxygen radical species (iii). The same oxygen radical, with the help of another excited electron-hole pair, expels the adsorbed superoxide radical

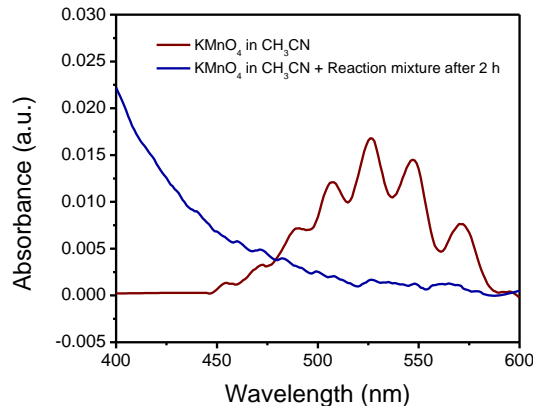


**Figure 3.2.17** The UV-Visible spectra recorded before and after addition of reaction aliquot in the  $\text{KMnO}_4$  solution.

as  $\text{H}_2\text{O}_2$  and converts itself to a carbon radical (*iv*). Generation of  $\text{H}_2\text{O}_2$  in the reaction mixture was also detected colorimetrically by  $\text{KMnO}_4$  titration (**Figure 3.2.17**).<sup>70</sup> Overall, two photons are used to oxidize one BA molecule to benzaldehyde and simultaneously reduce one oxygen molecule to  $\text{H}_2\text{O}_2$ . The PE-CQDs were recovered after the catalytic reaction by ethyl-acetate extraction and analysed which confirmed that the nature of the PE-CQDs do not change during the reaction (**Figure 3.2.18**).

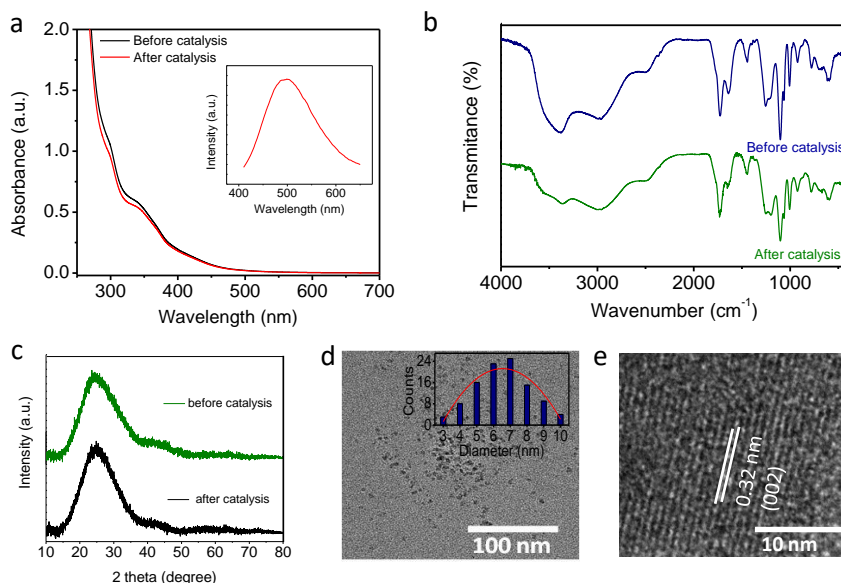


**Figure 3.2.18** *a*, UV-Visible absorption spectra of PE-CQDs before and after the catalysis. Inset in *b* is photoluminescence emission spectrum (excitation wavelength 390 nm) of PE-CQDs after catalysis and *b*, FT-IR spectra of PE-CQDs before and after the catalysis. *c*, PXRD pattern of fresh and used PE-CQDs. *d*, A low magnification TEM image of the used PE-CQDs (inset is the particle size distribution) *e*, HR-TEM image of an used PE-CQD.

### 3.2.5 Conclusions

In conclusion, we have presented a rational design for the synthesis of graphitic carbon quantum dots in gram-scale quantities using pollution causing polyethylene as a starting material. This is an interesting example of chemical transformation from an alkane to graphene where acid-mediated dehydrogenation of a PE backbone results in the formation of alkenes, which then undergoes cyclization reaction forming benzene derivatives and finally tiny functionalized graphene chunks. Furthermore, we demonstrated that in presence of these PE-CQDs, the ability of water to dissolve and diffuse molecular oxygen increases remarkably. Such O<sub>2</sub> enrichment is very useful in photocatalytic oxidation reactions because it offers the possibility of doing such reactions in air, without the need of creating an oxygen-rich environment. With these findings, we believe that PE-CQDs will be considered as one of the most efficient catalysts for photo-oxidation reaction and an efficient oxygen enricher for chemical transformations.

## Bibliography

1. M. R. Hoffmann, S. T. Martin, W. Choi and D. W. Bahnemann, *Chem. Rev.*, 1995, **95**, 69–96.
2. X. Wang, K. Maeda, A. Thomas, K. Takanabe, G. Xin, J. M. Carlsson, K. Domen and M. Antonietti, *Nat. Mater.*, 2008, **8**, 76.
3. X. Chen, L. Liu, P. Y. Yu and S. S. Mao, *Science.*, 2011, **331**, 746–750.
4. G. Zhang, G. Kim and W. Choi, *Energy Environ. Sci.*, 2014, **7**, 954–966.
5. H. Wang, L. Zhang, Z. Chen, J. Hu, S. Li, Z. Wang, J. Liu and X. Wang, *Chem. Soc. Rev.*, 2014, **43**, 5234–5244.
6. L. Wang and F.-S. Xiao, *ChemCatChem.*, 2014, **6**, 3048–3052.
7. H. Kasap, C. A. Caputo, B. C. M. Martindale, R. Godin, V. W. Lau, B. V Lotsch, J. R. Durrant and E. Reisner, *J. Am. Chem. Soc.*, 2016, **138**, 9183–9192.
8. D. Wang, A. B. Weinstein, P. B. White and S. S. Stahl, *Chem. Rev.*, 2018, **118**, 2636–2679.
9. W. Xu, D. Raftery and J. S. Francisco, *J. Phys. Chem. B*, 2003, **107**, 4537–4544.
10. H. Li, F. Qin, Z. Yang, X. Cui, J. Wang and L. Zhang, *J. Am. Chem. Soc.*, 2017, **139**, 3513–3521.
11. F. Su, S. C. Mathew, G. Lipner, X. Fu, M. Antonietti, S. Blechert and X. Wang, *J. Am. Chem. Soc.*, 2010, **132**, 16299–16301.
12. S. Sarina, H. Zhu, E. Jaatinen, Q. Xiao, H. Liu, J. Jia, C. Chen and J. Zhao, *J. Am. Chem. Soc.*, 2013, **135**, 5793–5801.
13. X. Chen, Y. Li, X. Pan, D. Cortie, X. Huang and Z. Yi, *Nat. Commun.*, 2016, **7**, 12273.
14. M. El-Maazawi, A. N. Finken, A. B. Nair and V. H. Grassian, *J. Catal.*, 2000, **191**, 138–146.
15. B. Belaissaoui, Y. Le Moullec, H. Hagi and E. Favre, *Sep. Purif. Technol.*, 2014, **125**, 142–150.
16. Y. Li, X. M. Hong, D. M. Collard and M. A. El-Sayed, *Org. Lett.*, 2000, **2**, 2385–2388.
17. S. Y. Lim, W. Shen and Z. Gao, *Chem. Soc. Rev.*, 2015, **44**, 362–381.
18. A. Anand, B. Unnikrishnan, S.-C. Wei, C. P. Chou, L.-Z. Zhang and C.-C. Huang, *Nanoscale Horizons*, 2019, **4**, 117–137.
19. R. Das, R. Bandyopadhyay and P. Pramanik, *Mater. Today Chem.*, 2018, **8**, 96–109.
20. G. A. M. Hutton, B. C. M. Martindale and E. Reisner, *Chem. Soc. Rev.*, 2017, **46**, 6111–6123.
21. Z. Xie, Z. Yin, Y. Wu, C. Liu, X. Hao, Q. Du and X. Xu, *Sci. Rep.*, 2017, **7**, 12146.
22. M. Shamsipur, A. Barati and S. Karami, *Carbon N. Y.*, 2017, **124**, 429–472.
23. Q. Xu, T. Kuang, Y. Liu, L. Cai, X. Peng, T. Sreenivasan Sreeprasad, P. Zhao, Z. Yu and N. Li, *J. Mater. Chem. B*, 2016, **4**, 7204–7219.
24. G. A. M. Hutton, B. Reuillard, B. C. M. Martindale, C. A. Caputo, C. W. J. Lockwood, J. N. Butt and E. Reisner, *J. Am. Chem. Soc.*, 2016, **138**, 16722–16730.
25. J. Ge, M. Lan, B. Zhou, W. Liu, L. Guo, H. Wang, Q. Jia, G. Niu, X. Huang, H. Zhou, X. Meng, P. Wang, C.-S. Lee, W. Zhang and X. Han, *Nat. Commun.*, 2014, **5**, 4596.
26. H. Yu, R. Shi, Y. Zhao, G. I. N. Waterhouse, L.-Z. Wu, C.-H. Tung and T. Zhang, *Adv. Mater.*, 2016, **28**, 9454–9477.
27. K. A. S. Fernando, S. Sahu, Y. Liu, W. K. Lewis, E. A. Guliyants, A. Jafariyan, P. Wang, C. E. Bunker and Y.-P. Sun, *ACS Appl. Mater. Interfaces*, 2015, **7**, 8363–8376.

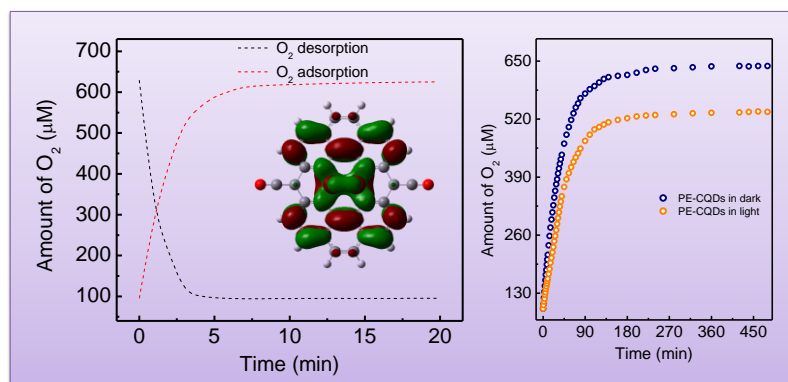


28. F. R. Bagsican, A. Winchester, S. Ghosh, X. Zhang, L. Ma, M. Wang, H. Murakami, S. Talapatra, R. Vajtai, P. M. Ajayan, J. Kono, M. Tonouchi and I. Kawayama, *Sci. Rep.*, 2017, **7**, 1774.
29. T. Li and J. A. Yarmoff, *Surf. Sci.*, 2018, **675**, 70–77.
30. M. T. Lusk, D. T. Wu and L. D. Carr, *Phys. Rev. B*, 2010, **81**, 155444.
31. X. Qi, W. Song and J. Shi, *PLoS One*, 2017, **12**, e0173864.
32. P. Roy, P.-C. Chen, A. P. Periasamy, Y.-N. Chen and H.-T. Chang, *Mater. Today*, 2015, **18**, 447–458.
33. C. M. Rochman, M. A. Browne, B. S. Halpern, B. T. Hentschel, E. Hoh, H. K. Karapanagioti, L. M. Rios-Mendoza, H. Takada, S. Teh and R. C. Thompson, *Nature*, 2013, **494**, 169.
34. K. Hamad, M. Kaseem and F. Deri, *Polym. Degrad. Stab.*, 2013, **98**, 2801–2812.
35. A. Koutsioukis, A. Akouros, R. Zboril and V. Georgakilas, *Nanoscale*, 2018, **10**, 11293–11296.
36. M. W. Kanan and D. G. Nocera, *Science.*, 2008, **321**, 1072-1075.
37. J. Ihata, *J. Polym. Sci. Part A Polym. Chem.*, 1988, **26**, 167–176.
38. M. Kaneko, S. Kumagai, T. Nakamura and H. Sato, *J. Appl. Polym. Sci.*, 2004, **91**, 2435–2442.
39. G. S. Bhat, *Mater. Manuf. Process.*, 1994, **9**, 221–235.
40. K.-W. Kim, H. Lee, B. Suhk Kim, S.-H. Hwang, L. Kwac, K.-H. An and B.-J. Kim, *Carbon letters.*, 2015,**1**, 62-66.
41. S. Kim, S. Zhou, Y. Hu, M. Acik, Y. J. Chabal, C. Berger, W. de Heer, A. Bongiorno and E. Riedo, *Nat. Mater.*, 2012, **11**, 544.
42. L. Pan, S. Sun, A. Zhang, K. Jiang, L. Zhang, C. Dong, Q. Huang, A. Wu and H. Lin, *Adv. Mater.*, 2015, **27**, 7782–7787.
43. J. Díaz, G. Paolicelli, S. Ferrer and F. Comin, *Phys. Rev. B*, 1996, **54**, 8064–8069.
44. J. M. Englert, C. Dotzer, G. Yang, M. Schmid, C. Papp, J. M. Gottfried, H.-P. Steinrück, E. Spiecker, F. Hauke and A. Hirsch, *Nat. Chem.*, 2011, **3**, 279.
45. B. J. Lindberg, K. Hamrin, G. Johansson, U. Gelius, A. Fahlman, C. Nordling and K. Siegbahn, *Phys. Scr.*, 1970, **1**, 286–298.
46. Yang, Z. C.; Wang, M.; Yong, A. M.; Wong, S. Y.; Zhang, X. H.; Tan, H.; Chang, A. Y.; Li, X.; Wang, J, *Chem. Commun.*, 2011, **47**, 11615–11617.
47. Daniela, C.; Marcano, V.; Dmitry.; Kosynkin, M.; Jacob.; Berlin, S.; Alexander, Z.; Sun, S.; Alexander, B.; Lawrence.; Alemany, L.; Wei.; James. T. M., *ACS Nano* 2010,**48**, 4806-4814.
48. L. A. Mitchell, T. M. Tovar and M. D. LeVan, *Carbon.*, 2014, **74**, 120–126.
49. J. B. DeCoste, M. H. Weston, P. E. Fuller, T. M. Tovar, G. W. Peterson, M. D. LeVan and O. K. Farha, *Angew. Chemie Int. Ed.*, 2014, **53**, 14092–14095.
50. L. Ding, H. Chen, Q. Wang, T. Zhou, Q. Jiang, Y. Yuan, J. Li and J. Hu, *Chem. Commun.*, 2016, **52**, 994–997.
51. M. Zhang, C. Chen, W. Ma and J. Zhao, *Angew. Chemie*, 2008, **120**, 9876–9879.
52. Kibria, M.G.; Chowdhury, F.A.; Zhao, S.; AlOtaibi, B.; Trudeau, M. L.; Guo, H.; Mi, Z., *Nat. Commun.* 2015, **6**, 1-8.
53. Z. Wang, Y. Song, J. Zou, L. Li, Y. Yu and L. Wu, *Catal. Sci. Technol.*, 2018, **8**, 268–275.
54. H. She, H. Zhou, L. Li, L. Wang, J. Huang and Q. Wang, *ACS Sustain. Chem. Eng.*, 2018,

- 6, 11939–11948.
55. F. Su, S. C. Mathew, G. Lipner, X. Fu, M. Antonietti, S. Blechert and X. Wang, *J. Am. Chem. Soc.*, 2010, **132**, 16299–16301.
  56. H. She, H. Zhou, L. Li, L. Wang, J. Huang and Q. Wang, *ACS Sustain. Chem. Eng.*, 2018, **6**, 11939–11948.
  57. Z. Wang, Y. Song, J. Zou, L. Li, Y. Yu and L. Wu, *Catal. Sci. Technol.*, 2018, **8**, 268–275.
  58. Z. Chen and Y. J. Xu, *ACS Appl. Mater. Interfaces*, 2013, **5**, 13353–13363.
  59. W. Feng, G. Wu, L. Li and N. Guan, *Green Chem.*, 2011, **13**, 3265–3272.
  60. H. Li, F. Qin, Z. Yang, X. Cui, J. Wang, L. Zhang, *J. Am. Chem. Soc.*, 2017, **139**, 3513–3521
  61. L. Ding, H. Chen, Q. Wang, T. Zhou, Q. Jiang, Y. Yuan, J. Li and J. Hu, *Chem. Commun.*, 2016, **52**, 994–997.
  62. M. Zhang, C. Chen, W. Ma and J. Zhao, *Angew. Chemie*, 2008, **120**, 9876–9879.
  63. Y. Liu, P. Zhang, B. Tian and J. Zhang, *ACS Appl. Mater. Interfaces*, 2015, **7**, 13849–13858
  64. C. Zheng, G. He, X. Xiao, M. Lu, H. Zhong, X. Zuo and J. Nan, *Appl. Catal. B Environ.*, 2017, **205**, 201–210.
  65. S. Schünemann, M. van Gastel and H. Tüysüz, *ChemSusChem*, 2018, **11**, 1, 2057–2061.
  66. X. Li, Y. Pi, Q. Hou, H. Yu, Z. Li, Y. Li and J. Xiao, *Chem. Commun.*, 2018, **54**, 1917–1920.
  67. H. Kasap, C. A. Caputo, B. C. M. Martindale, R. Godin, V. W. Lau, B. V Lotsch, J. R. Durrant and E. Reisner, *J. Am. Chem. Soc.*, 2016, **138**, 9183–9192.
  68. T. Jiang, C. Jia, L. Zhang, S. He, Y. Sang, H. Li, Y. Li, X. Xu and H. Liu, *Nanoscale*, 2015, **7**, 209–217.
  69. Marjasvaara, A.; Torvinen, M.; Vainiotalo, P., *J. Mass Spectrom.* 2004, **39**, 1139–1146.
  70. Chen, H.; Liu, C.; Wang, M.; Zhang, C.; Luo, N.; Wang, Y.; Abroshan, H.; Li, G., *ACS Catal.*, 2017, **7**, 3632–3638.

## CHAPTER 3.3

### Light-induced hypoxia in carbon quantum dots and ultrahigh photocatalytic efficiency



#### Summary

Carbon quantum dots (CQDs) represent a class of carbon materials exhibiting photo-response and many potential applications. Here, we present a unique property that the CQDs adsorb large quantities of molecular oxygen from the air when dispersed in solution, the quantity of which can be controlled by light irradiation. Thus, the O<sub>2</sub> content can be varied between 1 wt.% of the CQDs in dark to nearly half of it under illumination, in a reversible manner. Moreover, O<sub>2</sub> depletion is enhanced away from the air-solution interface as the nearby CQDs quickly regain them from air, creating a pronounced concentration gradient in the solution. We have elucidated the role of CQD functional groups in adsorbing O<sub>2</sub> and show that excitons generated under light are responsible for their tunable oxygen content. Due to their high O<sub>2</sub> content, we show that the photocatalytic efficiency of the CQDs towards controlled oxidation of benzylamine in ambient conditions is far higher than the existing photocatalysts.

‡ Manuscript based on this work is under revision.

### 3.3.1 Introduction

Increasing the adsorption of reactant molecules on the surface of a heterogeneous catalyst is necessary to attain high catalytic efficiencies for chemical transformations and energy harvesting applications. This is nonetheless rather difficult to achieve for gases such as O<sub>2</sub> having low solubility and diffusion-rates in solutions.<sup>1</sup> Even though pre-saturation or continuous gas purging can improve the reaction rates, the process becomes expensive and unfriendly for the industry. Moreover, under photocatalytic conditions, the adsorption-desorption equilibrium of the gases on the catalyst surface may significantly vary because of the modified electronic structure of the catalyst in the presence of the photo-excited electrons and holes.<sup>2,3</sup> However, the effect of light on the concentration of O<sub>2</sub> or other reactants on a catalyst-surface has remained poorly explored, hindering the development of highly active photocatalysts and the use of the ambient air as an inexpensive oxidizing reagent.

Semiconducting carbon quantum dots (CQDs), constituting of small functionalized graphene-layers, are a class of light-responsive materials with potential applications in photocatalysis, electrocatalysis, solar hydrogen generation, and also in biomedical diagnosis and therapeutic approaches where the interactions of O<sub>2</sub> and graphene play a central role.<sup>4-9</sup> Recently, while developing a rational strategy for a residue-free, large-scale production of carbon quantum dots using waste plastic (PE-CQDs), we serendipitously observed that the ability of water to dissolve and diffuse molecular oxygen increases significantly in their presence.<sup>10</sup> Using a tiny PE-CQD concentration of ~0.1 wt.%, the total oxygen content (TO) measures double that of pure water (320 μM) when the solution is exposed to air. The oxygen enrichment is reversible, shuttling between 640 μM and 95 μM in the air and N<sub>2</sub> atmosphere. It was further proposed that the O<sub>2</sub> enrichment ought to result in extraordinarily high efficiency for oxidation reactions while using PE-CQDs as photocatalysts, though these have primarily been utilized for photo-reduction reactions.<sup>11-15</sup>

### 3.3.2 Scope of the present investigation

The findings inspire several scientific inquiries that can lead to molecular O<sub>2</sub> or ambient air being used as a sustainable oxidizing agent, such as the enrichment mechanism and the nature of involvement of the functional groups on PE-CQDs in oxygen enrichment. Moreover, since the

PE-CQDs absorb visible light to generate excitons that can interact with the surface adsorbed  $O_2$  (to form superoxide radical anions, making the CQD transiently a positively charged entity), or may accept electrons from reactants or solvent, it is also essential to examine as to how and to what extent does exposure to light influences the oxygen enrichment properties.<sup>16-19</sup> Past theoretical studies on the interactions of oxygen with graphitic-carbon have revealed their bonding possibilities from the hybridization of the O 2p orbitals and the bonding  $\pi$  orbital of graphene, further tunable by the presence of defects and surface functionalities.<sup>20-23</sup> These studies, though form the basis of understanding oxygen enrichment in PE-CQDs, have considered the carbon structures to be in a vacuum while understanding the behavior of PE-CQDs in water requires the consideration of a dielectric surrounding mimicking the experimental design.

We present the origin of high oxygen adsorption on the PE-CQDs and the extraordinary effect of light illumination mimicking photocatalytic conditions on their  $O_2$  adsorption properties. The TO value of its aqueous solution exhibits a terse decrease in the presence of light from 640  $\mu\text{M}$  to 540  $\mu\text{M}$  due to the desorption of  $O_2$ . The variation in TO is reversible and regains the original value once the illumination ceases. The rate of TO depletion and the depleted saturation values are depth-dependent due to the variations in the diffusion path length of molecular  $O_2$  and CQDs from solution to air, yielding a remarkable TO gradient of  $\sim 4.5 \mu\text{M}/\text{cm}$ . Using Density Functional Theory, we show that the  $-\text{CO}$  and the  $-\text{OH}$  groups are responsible for stabilizing the  $O_2$  molecules on PE-CQDs in the dark. However, if a PE-CQD acquires some charge under photocatalytic conditions due to the interactions of excitons with reactants, the  $O_2$  to PE-CQD binding further attunes so that a fraction of the  $O_2$  molecules desorbs from the surface. In contrast, the binding of another fraction synergistically improves in the vicinity of the  $-\text{SO}_3\text{H}$  groups. By taking photo-oxidation of benzylamine derivatives as an example, we show that due to high oxygen content, the photocatalytic oxidation ability of the PE-CQDs is remarkably higher in ambient conditions and natural sunlight (apparent quantum efficiency  $\sim 35\%$ ) than the existing photocatalysts, including those containing noble metals that use harsh reaction conditions. The findings establish CQDs as a molecular  $O_2$  enricher in solution, paving the way for air as a sustainable oxidant in reactions.

### 3.3.3 Methods

#### 3.3.3.1 Measurement of oxygen content in the PE-CQD solutions

Total oxygen content (TO) in pure water and aqueous dispersion of PE-CQDs were measured at room temperature (25-27<sup>0</sup>C) using non-invasive Ocean Optics Neoflex-Kit-Probe.<sup>24,9</sup> Prior to all measurement, the oxygen sensing kit was calibrated using a two-point reading (20.9% O<sub>2</sub> in air & 0% O<sub>2</sub> in N<sub>2</sub>). 60 mL of water containing 50mg of the PE-CQDs (1mg/1.2 mL) was taken in a 50mL glass round bottom flask (RBF, total capacity ~65 mL). The sensing patch was attached to the inner wall of the flask in such a way that it completely submerge in the solution. The RBF was left open (neck radius 1.5 cm, opening area 7 cm<sup>2</sup>) so that the PE-CQD solution was in contact with air in order to uptake O<sub>2</sub> or release dissolved O<sub>2</sub>. During the O<sub>2</sub> desorption measurements, the solution was kept still and N<sub>2</sub> gas was bubbled through the solution a constant flow rate of 60-70 sccm. When the TO value did not decrease any further under the N<sub>2</sub> flow, the flow was stopped and the solution was then used to measure oxygen uptake properties from air. Under a constant stirring at 300 rpm for faster homogenization, the TO values of this solution were recorded at regular intervals of time. The effect of light illumination on TO was measured by exposing the same PE-CQD solution to light of appropriate wavelength using a Xe arc lamp (400 W, Newport and appropriate cut-off filters). The distance between the RBF and Xe Lamp was ~60 cm. TO data were recorded in 1,3 or 5 minutes intervals depending on the rate of change. The oxygen sensing patch was covered from light for ~15 seconds before each measurement. When the TO values reached a minimum in presence of light, the lamp was switched off and the measurements were continued until the initial TO value was reached. The variation in data points is about 14-16 μM in presence of light and 8-10 μM in dark.

#### 3.3.3.2 Benzyl amine oxidation using PE-CQDs

Selective photo-oxidation reactions of benzyl amine and its derivatives were carried out at room temperature (maintained at 32-33<sup>0</sup>C using a water bath) under the necessary atmospheres (air, O<sub>2</sub> or N<sub>2</sub> purging) using 0.5 mmol of BA in a RBF containing 15 mg PE-CQDs in 30 mL acetonitrile under either a Xe-lamp (400 W, Newport attached with an aqueous IR filter) or direct sunlight. Repeatability test was carried out by performing the photocatalytic reaction again in the previously used solution by adding equal amount of reactant molecules. Nuclear magnetic resonance

spectroscopy (400 MHz BrukerBiospinAvance III FT-NMR spectrometer) was used to analyze the products of the photocatalytic oxidation reactions.

### 3.3.3.3 Simulation studies

Density Functional Theory (DFT) calculations were performed for the structural optimization of the different edge functionalized PE-CQDs with the Becke three-parameter Lee-Yang-Parr hybrid functional (B3LYP)<sup>25</sup> and 6-31G basis set<sup>26</sup>. Using the relaxed structures, we did calculations based on time-dependent density functional theory (TD-DFT)<sup>27,28</sup> to obtain the theoretical UV-Vis spectra and study the optical properties of the excited states of PE-CQDs. We have considered a minimum of the first 50 lowest excited states in all the calculations. To simulate the experiments carried out in a water solvent, we have used the Polarizable Continuum Model (PCM)<sup>29,30</sup>. We have employed Gaussian09 software<sup>31</sup> for all our first-principles investigations and Gaussview software<sup>32</sup>, version 5, to visualize the PE-CQD systems and their corresponding excited state wave-functions.

For our study, we have defined the adsorption energy ( $E_A$ ) according to the expression,

$$E_A = E(\text{PE-CQD} + \text{Functional Group} + \text{O}_2) - E(\text{O}_2) - E(\text{PE-CQD} + \text{Functional Group})$$

Where  $E(\text{O}_2)$  is the total energy of an isolated oxygen molecule,  $E(\text{PE-CQD} + \text{Functional Group})$  is the total energy of the optimized edge functionalized PE-CQDs in the absence of any adsorbing  $\text{O}_2$ , and  $E(\text{PE-CQD} + \text{Functional Group} + \text{O}_2)$  corresponds to the total energy of the same system upon adsorption of  $\text{O}_2$  molecule on its surface. Each term is obtained with background dielectric as defined by PCM. The adsorption energy is endothermic (exothermic), depending on whether  $E_A$  is positive (negative).

We have further investigated the role of visible-light illumination to tailor oxygen adsorption on edge functionalized PE-CQDs. Light interaction generates excited electrons and holes in the system, capable of carrying out reduction and oxidation reactions. Consequently, the PE-CQDs under light illumination can become either a negatively or positively charged entity. Hence, to incorporate this effect, we have carried out theoretical TD-DFT calculations for a charged PE-CQD system by adding a positive and negative charge to the neutral quantum dots and study their optical properties.

### 3.3.3.4 Characterization

All other characterization techniques except the ones noted above are discussed in chapter 2.

### 3.3.4 Results and discussion

The PE-CQDs form a stable dispersion in water which is stable for over three years so far without any remarkable changes in the properties. Transmission electron microscopic (TEM) imaging of the sample shows that the average size of the PE-CQDs remains 8.5 nm (**Figure 3.3.1a,b**). Furthermore, the PE-CQDs are soluble in a wide range of solvents such as water, methanol, ethanol, ethyl acetate, acetonitrile, acetone and isopropanol without forming precipitation for months to make them potentially useful in many catalytic applications (**Figure 3.3.1c**). The quantum dots contain C atoms attached to hydroxyl (-OH), carbonyl (-C=O), carboxyl (-COOH) and sulphonyl (-SO<sub>3</sub>H) groups with a relative abundance in the range of 8-15%, and with an overall atomic ratio of ~48%, ~42% and ~10% for C, O and S.<sup>9</sup> We found that the Fourier transformed infrared (FT-IR) spectrum, X-ray diffraction pattern, UV-Visible absorption and photoluminescence spectra of the old PE-CQDs powder remain similar to a fresh sample (**Figure 3.3.1d,e,f,g**) suggesting their chemically-stable nature.

The measurements on the total oxygen content of an aqueous PE-CQDs solution were carried out using a typical concentration of 1 mg PE-CQD/1.2 mL water and keeping all conditions identical, unless mentioned otherwise. The TO value of this solution decreases from 640  $\mu$ M in air to ~95  $\mu$ M under continuous bubbling of N<sub>2</sub> gas. Subsequently when the N<sub>2</sub> flow is stopped, as seen in **Figure 3.3.2a**, oxygen diffuses again from air into the solution to attain the initial saturation value. The initial rise in TO is rapid, reaching half of the saturation value within 25 min. It took much longer, ~125 minutes thereafter for uptake of the remaining half of the oxygen molecules. Interestingly however, we found that the saturation value is significantly different when the uptake of O<sub>2</sub> from air occurred in presence of light. As shown from **Figure 3.3.2a**, when the solution was irradiated with a 400 W Xe lamp, the saturation TO value became 540 $\pm$ 10  $\mu$ M, nearly 90  $\mu$ M less than the same in absence of light. The contrast becomes apparent when compared with the same measurements carried out in pure water wherein the saturation TO values remains ~310 $\pm$ 8  $\mu$ M either in presence or absence of light (**Figure 3.3.2b**). The observations gave rise to a belief that



light, or probably the excitons generated by it in the PE-CQDs offer a possibility to control the total oxygen content in water.

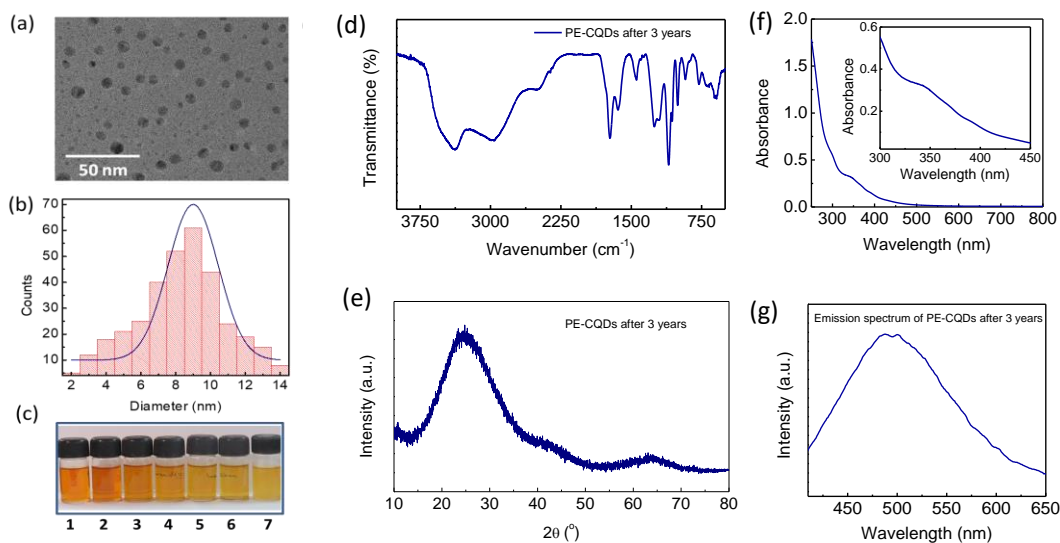


**Figure 3.3.1** Three years old PE-CQDs: (a) TEM image and (b) particle-size distribution. (c) Photograph of solutions of the PE-CQDs using different solvents (1mg/2 mL), stable for several months: 1. water, 2. methanol, 3. ethanol, 4. ethyl acetate, 5. acetonitrile, 6. acetone, and 7. isopropyl alcohol. (d) FT-IR spectrum, (e) PXRD pattern, (f) UV-Vis spectrum and (g) PL emission spectrum.

To examine the effect of light on total oxygen content in greater detail, we have exposed the aqueous PE-CQD solution continuously to irradiation from a 400 W Xe lamp and measured the TO values in regular intervals as shown in **Figure 3.3.2c**. The TO values exhibited a sharp drop initially within the first few minutes and continued to decline, though the variation became progressively slower until attaining a saturation value of  $540 \pm 8 \mu\text{M}$  in 80 minutes. No further changes in the TO value was observed at this point, even upon prolonged light irradiation.

The changes in the oxygen content is reversible in nature and the PE-CQD solution picks up oxygen again once the Xe-lamp is switched off (**Figure 3.3.2c**). The TO values begin to increase, initially rapidly regaining 25% and 50% of the lost oxygen in about 10 and 45 minutes respectively, and reaches  $\sim 620 \pm 8 \mu\text{M}$  in about 220 minutes. It takes about 10-12 h to reach the original TO value of  $\sim 640 \pm 8 \mu\text{M}$ . **Figure 3.3.2d** shows three such successive cycles with similar variations in presence and absence of light.

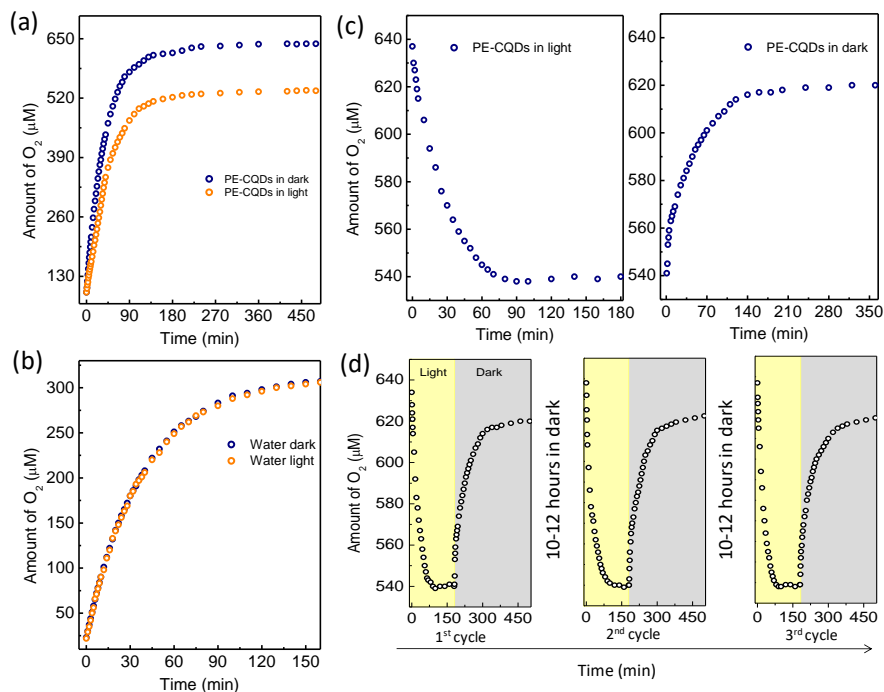


**Figure 3.3.2** (a) Temporal variation in TO in a previously deoxygenated (by  $N_2$  purging) aqueous PE-CQD solution (1 mg/1.2 mL) by spontaneous oxygen uptake from the air, in dark and under light, reaching saturated TO values of 640  $\mu\text{M}$  and 540  $\mu\text{M}$  respectively. (b) Oxygen uptake in deoxygenated water in dark and under light, reaching identical saturated TO values of 310  $\mu\text{M}$ . (c) Temporal variation in TO values in the aqueous PE-CQDs solution under constant irradiation of light (i), and the re-adsorption of  $O_2$  in the dark (ii). (d) Three repeat cycles showing a decrease in TO values of the PE-CQD solution under light and  $O_2$  re-adsorption in the dark. Note that the time taken to regain the saturation TO value in air is quite long, 12-15 h (deviation in TO from mean value:  $\pm 5-8 \mu\text{M}$ ).

The origin of the variation in oxygen level in the PE-CQD solution was examined from the following controlled experiments. It was found that the extent of variation in the TO values is dependent on the wavelength of the irradiating light. As seen in **Figure 3.3.3a**, the saturated TO values increased from 540  $\mu\text{M}$  when exposed to the full-spectrum of light to become 580  $\mu\text{M}$ , 625  $\mu\text{M}$ , and 640  $\mu\text{M}$  upon using 400 nm, 455 nm, and 495 nm cut-off filters respectively. The values did not change any further, as expected, using a 550 nm cut-off filter. Noting that the dependence of the TO values closely matches the UV-Vis absorption spectra of the PE-CQD solution (**Figure 3.3.3b**) where the absorption onsets at  $\sim 500$  nm) and the fact that light irradiation

makes a difference in the TO values only when PE-CQDs are present in water, and not in pure water, we attribute the variation in the oxygen content to the excitons generated in the PE-CQDs by light irradiation.

Furthermore, since the oxygen level reaches a depleted saturation value of 540  $\mu\text{M}$  upon light irradiation, we have presumed existence of an adsorption-desorption equilibrium on the PE-CQD surfaces i. e. the light induces desorption of the oxygen molecules and subsequently, the deficient CQD reabsorbs oxygen from the air. To confirm this hypothesis, first, the light irradiation experiment was repeated in a closed and completely filled vessel so that the PE-CQDs cannot get exposed to air. As seen in **Figure 3.3.3c**, no changes in the TO values were observed under light

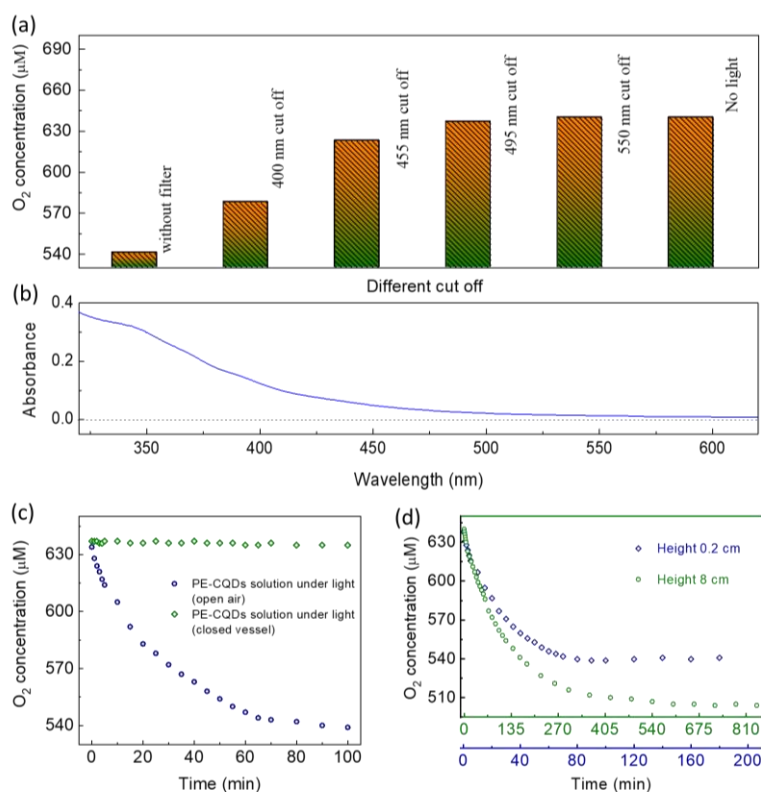


**Figure 3.3.3** (a) TO values observed in the PE-CQD solution under constant irradiation of the light using different cut-off filters. (b) UV-Vis absorption spectrum of the PE-CQD solution closely matching the variation in TO values in (a). Comparison of temporal variations in TO values in the aqueous PE-CQD solution under constant irradiation of light (c) in an open and a close vessel, (d) at two different depths from the solution-air interface: 0.2 cm and 8 cm in an open vessel (deviation in TO from mean value:  $\pm 5\text{-}8 \mu\text{M}$ ).

irradiation because even though the O<sub>2</sub> molecules were released from the PE-CQD surface, they could not escape and remained within the solution. Second, we have measured the TO level under light irradiation and open-air conditions at a different depth inside the vessel. In our previous study, we have demonstrated that oxygen enrichment becomes slower at larger depths. This is because the oxygen-deficient PE-CQDs must reach the solution surface to pick up oxygen from air or alternatively, if they adsorb O<sub>2</sub> from the surrounding water, oxygen from air must diffuse a longer distance to reach the CQD surrounding, both processes needing a longer time at larger depth. **Figure 3.3.3d** shows that TO depletion profiles at 0.2 cm and 8 cm below the solution surface under Xe-lamp irradiation. As expected, it took only 60 minutes to reach ~90% TO depletion at 0.2 cm, but 250 minutes at 8 cm. In addition, since the uptake is slower at 8 cm, but the light-induced O<sub>2</sub> desorption rate is expected to remain similar, the depleted saturation TO value at 8 cm is ~505 μM, 35 μM less than the same at 0.2 cm, thereby implying a negative downward gradient of 4.5 μM/cm in the TO values inside the solution.

The light irradiation experiments demonstrate that (i) the adsorbed oxygen content on the surface of a photoactive material can significantly vary in presence of light, (ii) in case of PE-CQDs, the surface bound oxygen contents are significantly high as compared to pure water and (iii) a depth dependent gradient in oxygen level may be created in a solution by containing a photoactive material using light.

#### **3.3.4.1 Origin of high oxygen adsorption and light-induced desorption (Experimental and theoretical studies)**

To theoretically study the light modulated oxygen adsorption property of PE-CQDs, we have taken a zigzag-edge planar carbon quantum dot structure arranged in 10 six-membered rings as our model system, as shown in **Figure 3.3.4a**. The edge carbons are saturated with hydrogen atoms. We have not considered the armchair edge PE-CQDs as it gets distorted upon functionalization.<sup>33</sup> We have estimated the oxygen adsorption energies ( $E_A$ , see **Table 3.3.1**) in the presence of the various oxygen-containing functional groups, that is, -SO<sub>3</sub>H, -OH, -COOH, and -C=O, placed symmetrically along the edges of the quantum dots. We have chosen this edge functionalization route, as they are more reactive than the basal plane surface of PE-CQDs.<sup>20</sup>

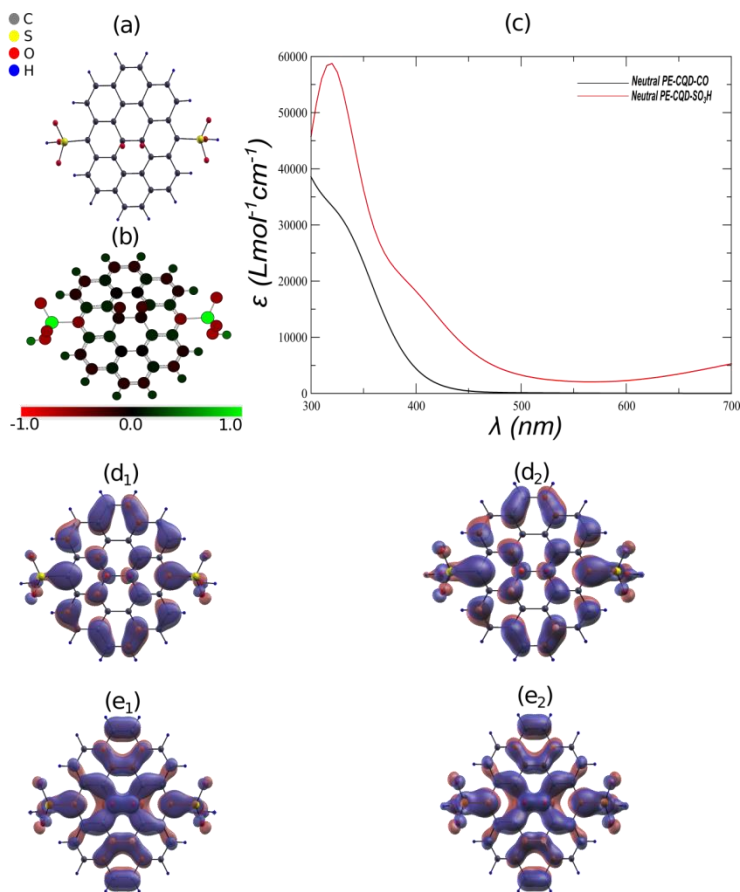


**Figure 3.3.4** (a) Top view of the molecular structure of a zigzag-edge PE-CQD functionalized with sulfonate group, containing one adsorbed oxygen molecule. (b) Side view of the system with a single oxygen molecule adsorbed on its surface. The contour plot depicts the Mulliken charge distribution. (c) The theoretical UV-Vis spectra of neutral PE-CQD system functionalized with -C=O and -SO<sub>3</sub>H group. (d) and (e) denote the isosurfaces of HOMO and LUMO of the system, respectively (isovalue: 0.02). The subscripts 1 and 2 denote the neutral and negatively charged system, respectively.

From our theoretical investigation, we have seen that O<sub>2</sub> molecule preferentially adsorbs over the center of PE-CQDs, away from their reactive edges. The functionalized quantum dots get buckled on oxygen adsorption upon geometrical optimization (see **Figure 3.3.4b**). The adsorption of the O<sub>2</sub> molecule is favorable at the center of the C-surface by forming a four-member ring (**Figure 3.3.4a,b**) as in other carbon systems.<sup>20,34</sup> In this configuration, a partial charge-transfer takes place

**Table 3.3.1** Adsorption energies of neutral, negatively and positively charged PE-CQDs, attached with different edge functional groups. One oxygen molecule is adsorbed on its surface. All the results are obtained in the presence of dielectric water solvent. “No Adsorption” refers to systems where we have not observed oxygen adsorption in PE-CQDs within the parameters of our theoretical optimization.

<i>PE-CQD System</i> (Functional Groups)	<i>Adsorption Energy (E<sub>A</sub>)</i> (in eV)		
	<i>Neutral</i>	<i>Negatively</i> <i>Charged</i>	<i>Positively</i> <i>Charged</i>
-SO <sub>3</sub> H	1.31	5.82	-7.07
-COOH	1.36	0.18	-0.27
-OH	1.09	No Adsorption	-0.27
-C=O	-0.5	No Adsorption	-0.29
-SO <sub>3</sub> H + -COOH	1.25	5.83	-7.17
-SO <sub>3</sub> H + -OH	0.97	6.01	-7.45
-SO <sub>3</sub> H + -CO	No Adsorption	No Adsorption	No Adsorption

from the PE-CQD to oxygen (see **Figure 3.3.4b**), leading to an increased O-O bond-length (~ 1.55 Å) and a loss in the planarity of the C atoms beneath the O<sub>2</sub> molecule. We further inferred that the solvent dielectric medium in which the PE-CQDs are dispersed also stabilizes the oxygen molecule to promote a high O<sub>2</sub> uptake since the present E<sub>A</sub> values are lower in comparison to graphitic quantum clusters in vacuum.<sup>2</sup>

In dark environment, we have observed that the adsorption is exothermic in the presence of the -C=O group due to an enhanced charge transfer, but endothermic for the other functional groups, suggesting a weaker O<sub>2</sub> binding (see **Table 3.3.1**). The theoretical UV-Vis absorption spectrum for the PE-CQDs with -C=O functional group (see **Figure 3.3.4c**) also matches closely with the experiment. Hence, the presence of the carbonyl group can be strongly linked to the unique oxygen enrichment in our synthesized PE-CQDs. **Figure 3.3.4c** also shows a close match of the theoretical UV-Vis absorption spectrum for the -SO<sub>3</sub>H functionalized PE-CQDs with the experiment, despite being less stable than the carbonyl group-containing system. Notably, the presence of the -SO<sub>3</sub>H

group is unique in our PE-CQDs as compared to most other carbon-dots as it originates from the sulfonation of the polyethylene backbone.<sup>10</sup>The Highest Occupied Molecular Orbital (HOMO) and the Lowest Unoccupied Molecular Orbital (LUMO) isosurfaceplots show that in the presence of the weakly O<sub>2</sub> adsorbing functional groups (sulfonate groups in **Figure 3.3.4d<sub>1</sub>,e<sub>1</sub>**), the excited state wavefunctions are de-localized along the PE-CQD surface and the O<sub>2</sub> molecule. On the contrary, the frontier orbital isosurfaces for the carbonyl group functionalized system show no contribution from the -C=O group. Such a difference becomes crucial for an adsorption event taking place in the proximity of mixed functional groups. Consequently, oxygen adsorption does not take place when another functional group such as -SO<sub>3</sub>H (**Table 3.3.1**) is attached to a PE-CQD containing a carbonyl group. However, the E<sub>A</sub> values do not vary significantly in the presence of different combinations of other endothermic functional groups. Hence, even though the carbonyl group functionalized PE-CQD systems show enhanced stability on oxygen adsorption, we have chosen the sulfonate group for our subsequent investigation.

We further investigated the role of visible-light illumination to tailor oxygen adsorption of the PE-CQDs since excited electrons and holes are generated in this process. Consequently, the PE-CQDs under solar illumination can become either a negatively or positively charged entity by transferring one of the charge carriers to another species (such as H<sup>+</sup>, OH<sup>-</sup> or molecular O<sub>2</sub>.) present in the solution. In such a charged system, the oxygen adsorption significantly varies from a neutral one depending on the functional group. Our calculations show that the endothermic adsorption energy increases four-fold in a negatively charged PE-CQD containing -SO<sub>3</sub>H functional groups (see **Table 3.3.1**). **Figure 3.3.4d<sub>2</sub>,e<sub>2</sub>** show the frontier orbitals isosurfaces for the negatively charged system, which is similar to the neutral PE-CQDs, with identical charge transfer from carbon to oxygen. The oxygen molecule still appears to form a four-member ring, but the high E<sub>A</sub> suggests that oxygen molecules are most likely to be present in the solution than near the system. Under light irradiation, oxygen desorbs from the PE-CQD surface to air when the experiment is conducted in an open vessel. Therefore, the TO value decreases in the presence of visible-light, to maintain the adsorption-desorption equilibrium.

Now, in the presence of visible-light, the electron that goes from HOMO to LUMO can be captured by the oxygen molecule to form the superoxide anion radical (as experimentally inferred in the previous PE-CQD study) and result in a positively charged PE-CQD. In this scenario, the

adsorption energy becomes highly exothermic for most functional groups (**Table 3.3.1**), favoring a strong bond between the oxygen molecule and the PE-CQD surface. Moreover, the positively charged PE-CQD is stabilized by the surrounding dielectric water solvent, as evident from the exothermic nature of such process.

Thus, the overall depletion of the TO content in the PE-CQD solution under light arises due to the interference from the excitons which may be attributed either to desorption of oxygen from the PE-CQD surface or to a very stronger adsorption so that O<sub>2</sub> becomes a part of the C-dot and do not contribute to the TO measurement. However, in the experiments, since we observed no changes in the TO content under the closed conditions and light irradiation (**Figure 3.3.3c**), we conclude that the desorption as the primary mechanism for the TO decrease.

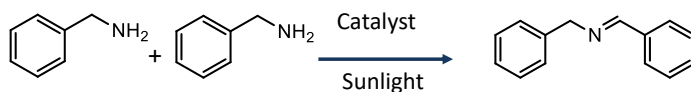
#### **3.3.4.2 Photocatalytic oxidation of benzylamine**

The as-synthesized PE-CQDs were used as photocatalyst for the selective oxidation of benzylamine (BA) and its derivatives to the corresponding imines using molecular oxygen present on the CQD surface as the oxidant. Recently, the development of amine to imine transformation methodologies that are mild and green has gained attention because of their use in functional organic and medicinal compounds.<sup>35,36</sup> Among these, the photocatalytic oxidation is particularly attractive due to its energy efficiency, leading to the development of many efficient photocatalysts.<sup>37-42</sup>

The transformations were performed in ambient air and at room temperature, using acetonitrile as the solvent. The conversion efficiency was excellent (97%) with >99% selectivity within a period of 55 minutes (~1h) of sunlight irradiation (**Table 3.3.2**, Entry No. 1). A similar performance was obtained by using a 400 W Xe-lamp (**Table 3.3.2**, Entry No. 2). In contrast, the conversion efficiency is negligible in dark in presence of the PE-CQDs, at room as well as elevated temperatures (**Table 3.3.2**, Entry No. 3, 4 and 5), signifying the photocatalytic nature of the reaction. The reaction yield in air and light was also negligible in absence of the PE-CQDs (<1%, **Table 3.3.2**, Entry No. 9), confirming its contribution as a photocatalyst.



**Table 3.3.2:** Optimization of benzylamine oxidation reaction at various conditions.



Entry	catalyst	Environment	Light	Time (min)	Conversion (%)	Selectivity (%)
1	PE-CQDs	Air	Sunlight	55	97	>99
2	PE-CQDs	Air	Xe-lamp	55	98	>99
3 <sup>a</sup>	PE-CQDs	Air	Dark	55	<1	-
4 <sup>b</sup>	PE-CQDs	Air	Dark	55	<1	-
5 <sup>c</sup>	PE-CQDs	Air	Dark	55	<1	-
6	PE-CQDs	O <sub>2</sub>	Xe-lamp	55	98	>99
7 <sup>d</sup>	PE-CQDs	N <sub>2</sub>	Xe-lamp	55	70	>99
8 <sup>e</sup>	PE-CQDs	N <sub>2</sub>	Xe-lamp	55	45	>99
9	-	Air	Sunlight	55	<1	-
10	TiO <sub>2</sub> -P25	Air	Xe-lamp	55	20	>99

**Reaction condition:** Acetonitrile solutions (30 mL), containing substrates (0.5 mmol), photocatalyst (15 mg), a; room temperature (23-26 °C, b; 40 °C, c; 50 °C, d; reaction mixture was purged with N<sub>2</sub> and then PE-CQDs added into it and e; PE-CQDs were first added to the reaction mixture then N<sub>2</sub> purged.

Usually, O<sub>2</sub> purging is carried out in this reaction to improve its kinetics significantly due to oxygen enrichment in the reaction medium.<sup>43-46</sup> This step is possible to be avoided with the PE-CQDs due to their intrinsic oxygen enrichment properties. When we purged O<sub>2</sub> during the reaction, the conversion efficiencies were nearly same as that in air i. e. ~63% and 98% (vs. 58% and 98% in air) after 30 min and 1 h respectively. On the contrary, the PE-CQDs were expected to perform this reaction even under an inert atmosphere since adsorbed oxygen cannot be completely displaced by N<sub>2</sub> even by prolonged purging.<sup>10</sup> To examine the influence of surface adsorbed O<sub>2</sub>, we carried out the reaction by (i) purging N<sub>2</sub> in the solvent and then adding the O<sub>2</sub> saturated PE-CQDs kept in air and (ii) the converse i. e. by adding the PE-CQDs to the reaction mixture first and then purging it with N<sub>2</sub>, assuming that the second reaction would be slower due to a reduced surface concentration of O<sub>2</sub>. As anticipated, the conversion efficiencies were rather decent after 1h, though dropped to ~70% and 45% in the first and the second case, asserting that the surface adsorbed O<sub>2</sub> is primarily responsible for the oxidation reaction.

The AQE under direct sunlight was estimated to be 34.5% for the BA oxidation reaction by considering all photons absorbed in the 300-500 nm range where the PE-CQDs absorb >95% of light.<sup>47</sup> For comparison, we have also carried out the reaction similarly using benchmark commercial TiO<sub>2</sub> (P-25), where the conversion was merely ~20 % after 1 h (**Table 3.3.2**, Entry No. 10). The catalytic reaction was performed for five consecutive runs using the same catalyst and the conversion efficiency was 92% (1 h light irradiation) at the end of the 5<sup>th</sup> cycle, suggesting high stability of the PE-CQDs (**Figure 3.3.5**).

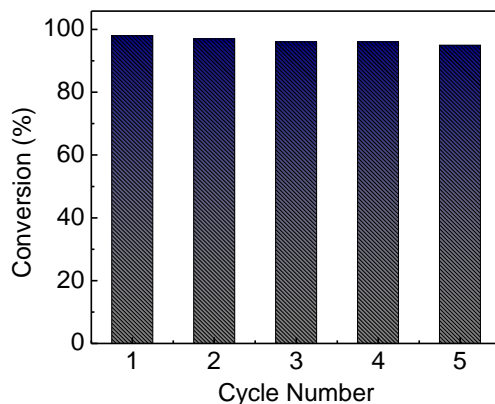


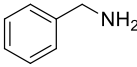
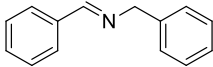
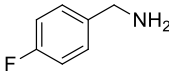
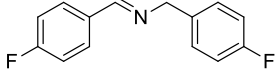
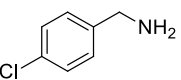
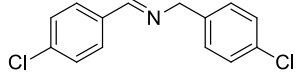
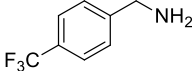
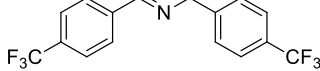
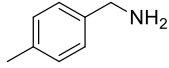
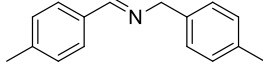
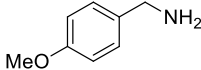
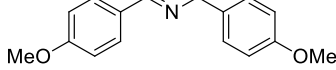
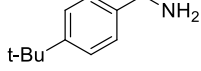
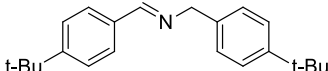
**Figure 3.3.5** Conversion efficiency during recycling of the PE-CQDs in five successive photocatalytic BA oxidation reactions.

It is to be pointed out that the performance of the PE-CQD photocatalyst under various gaseous environments exhibited a remarkable quality not observed in any other photocatalyst so far. Earlier investigations showed that the conversion is negligible when the reaction occurs in an inert atmosphere due to the absence of oxidant in the reaction medium. By contrast, at least ~50 % conversion was found under inert atmosphere in our system. More importantly, activity of the most *state-of-the-art* catalysts are significantly poorer in open air as compared to an oxygen saturated atmosphere, requiring an additional oxygen flow in the reaction set-up while the activity of the PE-CQDs in air is as high as under O<sub>2</sub> flow due to its intrinsic oxygen enrichment properties. Also, in many investigations, the reaction is needed to be carried out at elevated temperatures to improve

**Table 3.3.3:** Comparison of amine oxidation activity of PE-CQDs with that of other reported heterogeneous catalysts.

Sr. No.	Catalyst	Catalyst amount	BA (mmole)	O <sub>2</sub> /Air	Time (h)	Temp. (°C)	Solvent	Conv. (%)	Select. (%)	Ref.
1.	PE-CQDs	15 mg	0.5	Air	1	r.t	CH <sub>3</sub> CN	98	>99	This work
2.	Au/CeO <sub>2</sub>	-	0.2	O <sub>2</sub>	6	100	1,4 dioxane	96	97	48
3.	Au/Al <sub>2</sub> O <sub>3</sub>	100 mg	0.2	O <sub>2</sub>	24	100	Toluene	92	-	49
4.	Cd-organic framework	10 mg	0.48	Air	6	r.t	DMF	92	99	50
5.	BiVO <sub>4</sub> /g-C <sub>3</sub> N <sub>4</sub>	20 mg	0.35	-	16	r.t	CH <sub>3</sub> CN	87	100	51
6.	[Au <sub>25</sub> ]/TiO <sub>2</sub>	10 mg	0.2	O <sub>2</sub>	1.5	r.t	CH <sub>3</sub> CN	98	99	52
7.	Mo/Ta/W ternary polyoxometalate	1 mol%	0.2	Air	24	r.t	CH <sub>3</sub> CN	96	-	53
8.	NH <sub>2</sub> -MIL-125(Ti)	5 mg	0.1	O <sub>2</sub>	12	r.t	CH <sub>3</sub> CN	73	86	54
9.	TiO <sub>2</sub>	50 mg	0.2	O <sub>2</sub>	4	r.t	CH <sub>3</sub> CN	76	98	55
10.	Nb <sub>2</sub> O <sub>5</sub>	100 mg	5	O <sub>2</sub>	50	r.t	Benzene	99	98	56
11.	BiVO <sub>4</sub>	100 mg	0.1	O <sub>2</sub>	6	r.t	CH <sub>3</sub> CN	99	99	57
12.	N-doped TiO <sub>2</sub> @N-doped C	10 mg	0.2	O <sub>2</sub>	15	r.t	CH <sub>3</sub> CN	99	-	58
13.	BiOBr	100 mg	0.1	O <sub>2</sub>	14	r.t	CH <sub>3</sub> CN	100	100	59
14.	Fe based MOF	75 mg	4.8	O <sub>2</sub>	24	100	-	67	97	60
15.	WS <sub>2</sub> NS	-	0.1	O <sub>2</sub>	30	50	CH <sub>3</sub> CN	92	95	61
16.	mpg-C <sub>3</sub> N <sub>4</sub>	50 mg	1	O <sub>2</sub>	2	80	CH <sub>3</sub> CN	60	99	62
17.	Cu-graphene	100 mg	1	O <sub>2</sub>	6	40	CH <sub>3</sub> CN	99	93	63
18.	CQDs	25 mg	-	O <sub>2</sub>	12	90	-	-	-	64

**Table 3.3.4:** Aerobic-oxidation of different substituted amines with the PE-CQDs under sunlight.

Entry	Substrate	Product	Time	Conversion (%)	Selectivity (%)
1			55 min	98	>99
2			75 min	94	>99
3			75 min	93	>99
4			75 min	92	>99
5			55 min	94	>99
6			55 min	90	>99
7			55 min	84	>99

**Reaction conditions:** The reactions were carried out in acetonitrile solutions (30 mL), containing substrates (0.5 mmol), photocatalyst (15 mg) under the sunlight.

the kinetics.<sup>16,65-67</sup> By considering all such catalysts used in harsh conditions, including the ones with noble metals, the activity of the PE-CQDs under the mild conditions of room temperature and ambient air is still several times higher as shown in the comparison **Table 3.3.3**.

The versatility of the PE-CQDs was examined by using *p*-substituted benzylamine with electron-donating (-CH<sub>3</sub>, -OCH<sub>3</sub>, *t*-butyl) and electron-withdrawing (-F, -Cl, -CF<sub>3</sub>) groups (**Table 3.3.4**). The electron donating groups impart a somewhat better activity compared to the electron withdrawing groups. We have also examined the reactivity of aliphatic amines (**Table 3.3.4**, entry no. 8) to find that the PE-CQDs are highly specific to the amines containing aromatic side groups only.

### 3.3.4.3 Mechanistic investigation

Due to light irradiation, excited electrons and holes generated in the PE-CQDs activate the surface adsorbed  $O_2$  molecules to induce the oxidation reaction.<sup>39,68,69</sup> To develop further insight into the participating reactive species, several controlled experiments were carried out by using scavenger for excited electrons ( $K_2S_2O_8$ ), holes (ammonium oxalate) and superoxide radical anions,  $O_2^{\cdot-}$  (benzoquinone). The conversion drastically reduced by ~75% and ~82% respectively in presence of  $K_2S_2O_8$  and  $(NH_4)_2C_2O_4$  to suggest a strong participation of both the excitons in the reaction (**Figure 3.3.6**). The participation of  $O_2^{\cdot-}$  radical anion was also inferred from a slow (70%) reaction rate in presence of benzoquinone.

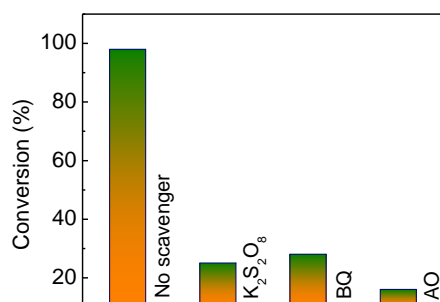
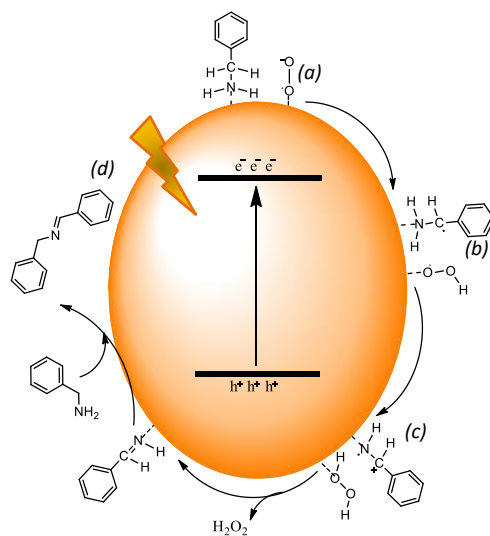


**Figure 3.3.6** Effect of different hole, electron and radical scavengers in the conversion efficiency of the oxidation reaction.



**Scheme 3.3.1** A plausible reaction mechanism for the photocatalytic BA oxidation using PE-CQDs.

Accordingly and with some additional experiments, we propose the following steps are involved in BA photo-oxidation: (i) the excited electrons of the PE-CQDs transfer to the surface-adsorbed  $O_2$  to produce  $O_2^{\cdot-}$ , **a**,<sup>70</sup> as shown in **Scheme 3.3.1**, (ii) an adsorbed BA molecule gets oxidized in the presence of a hole yielding a benzylamine cation radical intermediate, **b**, and  $HOO^{\cdot}$ .<sup>71,37</sup> The

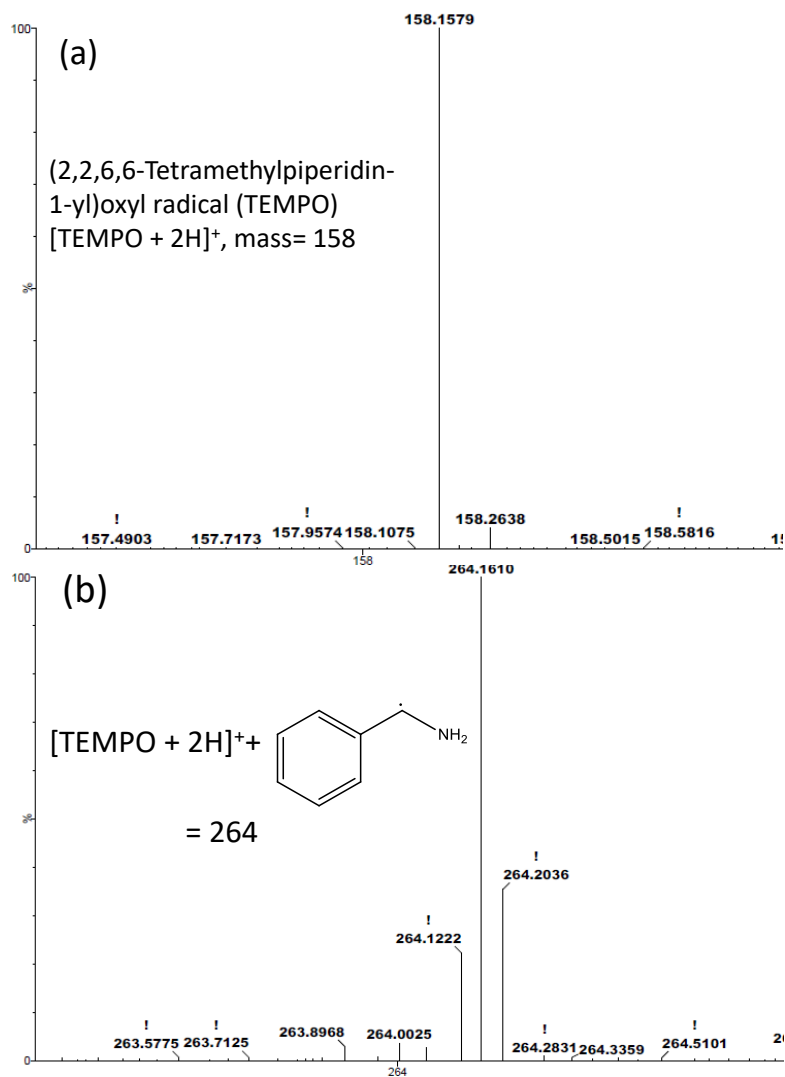


**Figure 3.3.7** HRMS spectra were recorded before and after irradiation with sunlight. [TEMPO+2H]<sup>+</sup> was observed at the beginning in acetonitrile solvent (a). TEMPO formed an adduct with the carbon radical species after sunlight irradiation for 1h (b).

formation of intermediate **b** was confirmed by trapping it with TEMPO ((2,2,6,6-Tetramethylpiperidin-1-yl)oxyl radical) and detecting the same by HRMS (**Figure 3.3.7**), (iii) extraction of an H· radical by HOO· to produce benzyliminium ion, **c** and H<sub>2</sub>O<sub>2</sub> as by-product.<sup>72</sup> H<sub>2</sub>O<sub>2</sub> formation was confirmed by KMnO<sub>4</sub> titration during the light irradiation. (iv) ‘**c**’ couples with another neighbouring BA molecule to give final product **d**, benzaldimine.<sup>16</sup>

### 3.3.5 Conclusions

In conclusion, we demonstrate that the concentration of the surface-adsorbed oxygen molecules on carbon quantum dots is extremely high, aided by specific combinations of its surface functional groups that lead to profound photocatalytic efficiency for oxidative chemical transformations. The apparent quantum efficiency for controlled oxidation of benzylamine is ~35% along with a reaction rate that is significantly faster than the existing photocatalysts, including those using expensive noble metals, an oxygenated atmosphere, and harsh reaction conditions. Rather unusually, we also establish that the concentration of adsorbed O<sub>2</sub> can be controlled by using an external light source so that a solution of carbon dot can have different oxygen contents at different portions of the solution. The effect arises due to the modulation of charge-transfer between the CQDs and the adsorbed O<sub>2</sub> molecules in the presence of light that generates excitons in the CQDs and can make them behave as charged particles. Barely little is known on the concentration of reactants on a catalyst surface under photocatalytic conditions as against conventional heterogeneous catalytic conditions, therefore our findings will inspire such studies and the consequences on catalytic efficiencies. Moreover, the use of light and distance from the air-interface offers an unusual possibility of creating a landscape of varied oxygen contents in a solution that may offer new opportunities in chemical reactions.

## Bibliography

1. L. Chen and X. Feng, *Chem. Sci.*, 2020, **11**, 3124–3131.
2. D. F. Ollis, *J. Phys. Chem. B*, 2005, **109**, 2439–2444.
3. Y. Nosaka and A. Y. Nosaka, *J. Phys. Chem. C*, 2018, **122**, 28748–28756.
4. S. Y. Lim, W. Shen and Z. Gao, *Chem. Soc. Rev.*, 2015, **44**, 362–381.
5. S. Mondal, A. Yucknovsky, K. Akulov, N. Ghorai, T. Schwartz, H. N. Ghosh and N. Amdursky, *J. Am. Chem. Soc.*, 2019, **141**, 15413–15422.
6. J. Ge, M. Lan, B. Zhou, W. Liu, L. Guo, H. Wang, Q. Jia, G. Niu, X. Huang, H. Zhou, X. Meng, P. Wang, C.-S. Lee, W. Zhang and X. Han, *Nat. Commun.*, 2014, **5**, 4596.
7. G. A. M. Hutton, B. Reuillard, B. C. M. Martindale, C. A. Caputo, C. W. J. Lockwood, J. N. Butt and E. Reisner, *J. Am. Chem. Soc.*, 2016, **138**, 16722–16730.
8. M. Shamsipur, A. Barati and S. Karami, *Carbon N. Y.*, 2017, **124**, 429–472.
9. A. Anand, B. Unnikrishnan, S.-C. Wei, C. P. Chou, L.-Z. Zhang and C.-C. Huang, *Nanoscale Horizons*, 2019, **4**, 117–137.
10. S. Mondal, E. K. Karthik, L. Sahoo, K. Chatterjee, S. Marappan and U. K. Gautam, *Nanoscale*, , DOI:10.1039/D0NR00266F.
11. Y. Wang, X. Liu, X. Han, R. Godin, J. Chen, W. Zhou, C. Jiang, J. F. Thompson, K. B. Mustafa, S. A. Shevlin, J. R. Durrant, Z. Guo and J. Tang, *Nat. Commun.*, 2020, **11**, 2531.
12. H. Yu, R. Shi, Y. Zhao, G. I. N. Waterhouse, L.-Z. Wu, C.-H. Tung and T. Zhang, *Adv. Mater.*, 2016, **28**, 9454–9477.
13. K. A. S. Fernando, S. Sahu, Y. Liu, W. K. Lewis, E. A. Gulians, A. Jafariyan, P. Wang, C. E. Bunker and Y.-P. Sun, *ACS Appl. Mater. Interfaces*, 2015, **7**, 8363–8376.
14. S. Guo, S. Zhao, X. Wu, H. Li, Y. Zhou, C. Zhu, N. Yang, X. Jiang, J. Gao, L. Bai, Y. Liu, Y. Lifshitz, S.-T. Lee and Z. Kang, *Nat. Commun.*, 2017, **8**, 1828.
15. J. Wu, S. Ma, J. Sun, J. I. Gold, C. Tiwary, B. Kim, L. Zhu, N. Chopra, I. N. Odeh, R. Vajtai, A. Z. Yu, R. Luo, J. Lou, G. Ding, P. J. A. Kenis and P. M. Ajayan, *Nat. Commun.*, 2016, **7**, 13869.
16. F. Su, S. C. Mathew, L. Möhlmann, M. Antonietti, X. Wang and S. Blechert, *Angew. Chemie Int. Ed.*, 2011, **50**, 657–660.
17. H. Li, F. Qin, Z. Yang, X. Cui, J. Wang and L. Zhang, *J. Am. Chem. Soc.*, 2017, **139**, 3513–3521.
18. F. Raza, J. H. Park, H.-R. Lee, H.-I. Kim, S.-J. Jeon and J.-H. Kim, *ACS Catal.*, 2016, **6**, 2754–2759.
19. B. Yuan, R. Chong, B. Zhang, J. Li, Y. Liu and C. Li, *Chem. Commun.*, 2014, **50**, 15593–15596.
20. X. Qi, W. Song and J. Shi, *PLoS One*, 2017, **12**, e0173864.
21. F. R. Bagsican, A. Winchester, S. Ghosh, X. Zhang, L. Ma, M. Wang, H. Murakami, S. Talapatra, R. Vajtai, P. M. Ajayan, J. Kono, M. Tonouchi and I. Kawayama, *Sci. Rep.*, 2017, **7**, 1774.
22. M. T. Lusk, D. T. Wu and L. D. Carr, *Phys. Rev. B*, 2010, **81**, 155444.
23. T. Li and J. A. Yarmoff, *Surf. Sci.*, 2018, **675**, 70–77.
24. M. W. Kanan and D. G. Nocera, *Science.*, 2008, **321**, 1072-1075.
25. A. D.Becke, *J. Chem. Phys.*, 1993,**98**, 5648–5652.
26. W. J. Hehre, R. Ditchfield, and J. A. Pople, *J. Chem. Phys.*, 1972,**56**, 2257–2261.
27. R. E.Stratmann, G. E.Scuseria, andM. J.Frisch, *J. Chem. Phys.*,1998, **109**, 8218–8224.

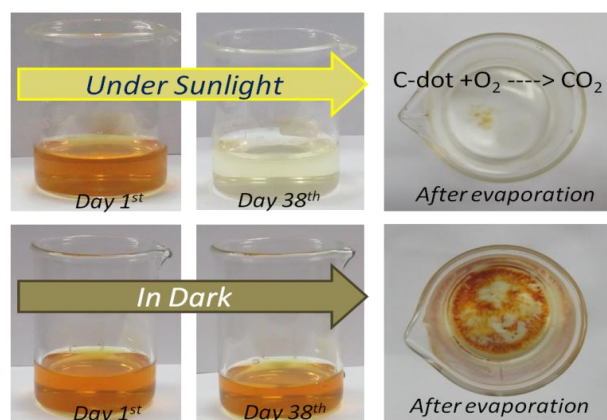


28. A. D. Laurent, and D. Jacquemin, *Int. J. Quantum Chem.*, 2013, **113**, 2019–2039.
29. J. Tomasi, B. Mennucci, and R. Cammi, *Chem. Rev.* 2005, **105**, 2999–3094.
30. M. Cossi and V. Barone, *J. Chem. Phys.*, 2001, **115**, 4708–4717.
31. M. J. Frisch, *Gaussian 09 Revision D.01*. 2009.
32. R. Dennington, T. A. Keith and J. M. Millam, *GaussView Version 5*. 2009.
33. C. Cocchi, D. Prezzi, A. Ruini, M. J. Caldas and E. Molinari, *J. Phys. Chem. C*, 2012, **116**, 17328–17335.
34. D. C. Sorescu, K. D. Jordan and P. Avouris, *J. Phys. Chem. B*, 2001, **105**, 11227–11232.
35. B. Gnanaprakasam, J. Zhang and D. Milstein, *Angew. Chemie Int. Ed.*, 2010, **49**, 1468–1471.
36. H. Sun, F.-Z. Su, J. Ni, Y. Cao, H.-Y. He and K.-N. Fan, *Angew. Chemie Int. Ed.*, 2009, **48**, 4390–4393.
37. S. Li, G. Li, P. Ji, J. Zhang, S. Liu, J. Zhang and X. Chen, *ACS Appl. Mater. Interfaces*, 2019, **11**, 43287–43293.
38. R. Garg, S. Mondal, L. Sahoo, C. P. Vinod and U. K. Gautam, *ACS Appl. Mater. Interfaces*, 2020, **12**, 29324–29334.
39. S. Li, L. Li, Y. Li, L. Dai, C. Liu, Y. Liu, J. Li, J. Lv, P. Li and B. Wang, *ACS Catal.*, 2020, **10**, 8717–8726.
40. F.-J. Zhao, G. Zhang, Z. Ju, Y.-X. Tan and D. Yuan, *Inorg. Chem.*, 2020, **59**, 3297–3303.
41. Y. Huang, C. Liu, M. Li, H. Li, Y. Li, R. Su and B. Zhang, *ACS Catal.*, 2020, **10**, 3904–3910.
42. X. Tu, Q. Wang, F. Zhang, F. Lan, H. Liu and R. Li, *Nanoscale*, 2020, **12**, 4410–4417.
43. H. Chen, C. Liu, M. Wang, C. Zhang, N. Luo, Y. Wang, H. Abroshan, G. Li and F. Wang, *ACS Catal.*, 2017, **7**, 3632–3638.
44. S. Furukawa, Y. Ohno, T. Shishido, K. Teramura and T. Tanaka, *ACS Catal.*, 2011, **1**, 1150–1153.
45. F. Wang, X. He, L. Sun, J. Chen, X. Wang, J. Xu and X. Han, *J. Mater. Chem. A*, 2018, **6**, 2091–2099.
46. A. Han, H. Zhang, G.-K. Chuah and S. Jaenicke, *Appl. Catal. B Environ.*, 2017, **219**, 269–275.
47. S. R. Lingampalli, U. K. Gautam and C. N. R. Rao, *Energy Environ. Sci.*, 2013, **6**, 3589–3594.
48. M. Wang, F. Wang, J. Ma, M. Li, Z. Zhang, Y. Wang, X. Zhang and J. Xu, *Chem. Commun.*, 2014, **50**, 292–294.
49. B. Zhu, M. Lazar, B. G. Trewyn and R. J. Angelici, *J. Catal.*, 2008, **260**, 1–6.
50. J. Shi, J. Zhang, T. Liang, D. Tan, X. Tan, Q. Wan, X. Cheng, B. Zhang, B. Han, L. Liu, F. Zhang and G. Chen, *ACS Appl. Mater. Interfaces*, 2019, **11**, 30953–30958.
51. S. Samanta, S. Khilari, D. Pradhan and R. Srivastava, *ACS Sustain. Chem. Eng.*, 2017, **5**, 2562–2577.
52. H. Chen, C. Liu, M. Wang, C. Zhang, N. Luo, Y. Wang, H. Abroshan, G. Li, F. Wang, *ACS Catal.*, 2017, **7**, 3632–3638.
53. S. Li, G. Li, P. Ji, J. Zhang, S. Liu, J. Zhang and X. Chen, *ACS Appl. Mater. Interfaces*, 2019, **11**, 43287–43293.
54. D. Sun, L. Ye and Z. Li, *Appl. Catal. B Environ.* 2015, **164**, 428–432.
55. X. Lang, W. Ma, Y. Zhao, C. Chen, H. Ji and J. Zhao, *Chem. – A Eur. J.*, 2012, **18**, 2624–2631.

56. S. Furukawa, Y. Ohno, T. Shishido, K. Teramura, T. Tanaka, *ACS Catal.*, 2011,**1**, 1150–1153.
57. B. Yuan, R. Chong, B. Zhang, J. Li, Y. Liu and C. Li, *Chem. Commun.*, 2014,**50**, 15593–15596.
58. F. Wang, X. He, L. Sun, J. Chen, X. Wang, J. Xu and X. Han, *J. Mater. Chem. A.*, 2018,**6**, 2091–2099.
59. A. Han, H. Zhang, G.-K. Chuah and S. Jaenicke, *Appl. Catal. B Environ.*, 2017,**219**, 269–275.
60. A. Dhakshinamoorthy, M. Alvaro and H. Garcia, *ChemCatChem.*, 2010,**2**,1438–1443.
61. F. Raza, J.H. Park, H.-R. Lee, H.-I. Kim, S.-J. Jeon and J.-H. Kim, *ACS Catal.*, 2016,**6**, 2754–2759.
62. F. Su, S.C. Mathew, L. Möhlmann, M. Antonietti, X. Wang and S. Blechert, *Angew. Chemie Int. Ed.*, 2011,**50**, 657–660.
63. Z.-Y. Zhai, X.-N. Guo, G.-Q. Jin and X.-Y. Guo, *Catal. Sci. Technol.*, 2015,**5**,4202–4207.
64. J. Ye, K. Ni, J. Liu, G. Chen, M. Ikram, Y. Zhu, *ChemCatChem.*, 2018,**10**, 259–265.
65. M. Wang, F. Wang, J. Ma, M. Li, Z. Zhang, Y. Wang, X. Zhang and J. Xu, *Chem. Commun.*, 2014, **50**, 292–294.
66. J. Ye, K. Ni, J. Liu, G. Chen, M. Ikram and Y. Zhu, *ChemCatChem.*, 2018, **10**, 259–265.
67. A. Dhakshinamoorthy, M. Alvaro and H. Garcia, *ChemCatChem.*, 2010, **2**, 1438–1443.
68. J.-Y. Li, Y.-H. Li, M.-Y. Qi, Q. Lin, Z.-R. Tang and Y.-J. Xu, *ACS Catal.*, 2020, **10**, 6262–6280.
69. J. Shi, J. Zhang, T. Liang, D. Tan, X. Tan, Q. Wan, X. Cheng, B. Zhang, B. Han, L. Liu, F. Zhang and G. Chen, *ACS Appl. Mater. Interfaces*, 2019, **11**, 30953–30958.
70. H. He, Z. Li, K. Li, G. Lei, X. Guan, G. Zhang, F. Zhang, X. Fan, W. Peng and Y. Li, *ACS Appl. Mater. Interfaces*, 2019, **11**, 31844–31850.
71. C. Mao, H. Cheng, H. Tian, H. Li, W.-J. Xiao, H. Xu, J. Zhao and L. Zhang, *Appl. Catal. B Environ.*, 2018, **228**, 87–96.
72. S. Naya, K. Kimura and H. Tada, *ACS Catal.*, 2013, **3**, 10–13.

## CHAPTER 3.4

### 'Autophagy' and unique aerial oxygen harvesting properties exhibited by highly photocatalytic carbon quantum dots



#### Summary

Plastic pollution is a serious threat to the environment as they are not bio-degradable. Herein using waste-polyethylene to create wealth, we report two important findings. First that they can be converted completely into highly photocatalytic carbon quantum-dots with  $H_2SO_4$  and  $H_2O_2$  treatment and they can enrich a reaction medium with molecular oxygen harvested from the air so that no separate oxygen source is needed while carrying out photocatalytic oxidation reactions. They enhance the diffusion rate of molecular oxygen in the water. Furthermore, they exhibit an ability to self-sensitized photo-oxidation to convert themselves completely to  $CO_2$  leaving behind no traces when exposed to sunlight for weeks, in the absence of reactants. Such extinction from the reaction media is unique as no other photocatalyst is known to do so and advantageous because the removal of carbon-dots from a solution is inefficient due to their high solubility. Moreover, waste-water treatment can be carried out with the notion that the photocatalyst will get eliminated by itself downstream. We demonstrate their high photocatalytic properties using photo-oxidation of benzyl alcohol derivatives and removal of pollutant dyes in ambient conditions with an efficiency better than the state-of-the-art photocatalysts, originating from their high oxygen enrichment ability.

‡ Manuscript based on this work has appeared in *Carbon*, 2021, 181, 16-27.

### 3.4.1 Introduction

The copious amounts of waste-plastic produced per year pose a serious threat to the environment due to their non-biodegradable nature and a tendency to absorb other pollutants,<sup>1-3</sup> menacing the marine life, soil, and freshwater quality, and the entire food cycle.<sup>4,5</sup> Therefore, the reduction of plastic-waste has emerged as a research priority, leading to many innovative approaches to convert them into useful materials such as liquid-fuels and related materials.<sup>6-8</sup> Recently, we have demonstrated a rational strategy to obtain carbon quantum-dots (CQDs) in large quantities using waste-polyethylene (PE) as a precursor.<sup>9</sup> The PE-backbone was subjected to controlled, H<sub>2</sub>SO<sub>4</sub> mediated and thermally induced dehydrogenation that thereafter undergoes cyclization to generate visible-light responsive CQDs (called hereafter as PE-CQDs) measuring 5-6 nm in size. The CQDs are a distinctive class of carbon-nanomaterials containing tiny graphene-sheets and soluble like fullerenes with potential applications in photocatalysis, optoelectronics, imaging, diagnostics etc.<sup>10-15</sup> Our findings further added a unique property that the PE-CQDs are capable of adsorbing exorbitantly large quantity of molecular O<sub>2</sub> (~1 wt.%) from air onto its surface under ambient conditions in a reversible manner, while suspended in a solution. Coupled this to their ability to absorb solar-light has resulted in high photocatalytic efficiency for oxidation reactions (while they have been primarily used for photo-reduction reactions) as well as waste-water treatment.<sup>16-18</sup>

### 3.4.2 Scope of the present investigation

This seemingly advantageous waste-to-wealth approach, however, it has two major concerns: (i) its synthesis requires toxic KMnO<sub>4</sub> that gets converted to MnO<sub>2</sub> and poses a serious health concern, while all other chemicals used in the process are potentially reusable, and (ii) the recovery of the PE-CQDs, as in the cases of other CQDs also, is difficult from a reaction medium due to high solubility and may eventually find its way to natural water bodies, when used in large quantities in industry. Therefore, it is necessary to improve the processing of the PE-CQDs by eliminating the use of KMnO<sub>4</sub> and, at the same time, to analyse the impact of the used PE-CQDs left unattended in an open environment.

We demonstrate an efficient route to produce the PE-CQDs from polyethylene using H<sub>2</sub>O<sub>2</sub> as a residue-free, non-toxic oxidant. These PE-CQDs exhibited an improved oxygen-harvesting

ability from the air and enhanced photocatalytic efficiency for the oxidative transformation of organic molecules and waste-water treatment. Furthermore importantly, we show that when these PE-CQDs are exposed to sunlight for several weeks, they completely disappear from the solution leaving no traces. They undergo a self-sensitized photo-oxidation process by using the reactive oxygen species generated from the molecular oxygen that they harvest from the air, to form carbon dioxide. As more CO<sub>2</sub> forms, the color of the sample fades away and disappears completely. This ‘self-devouring’ nature appears to be unique to the PE-CQDs as no other material and ever molecular species is known to undergo similar transformations. In this context, it may be pointed out that ‘bleaching’ or color-fading of carbon-dot solutions have been widely observed and researched leading to several hypotheses.<sup>19-22</sup> The findings here are an important benchmark that such hypotheses ought to be consistent with an eventual CO<sub>2</sub> formation.

We have demonstrated the high photocatalytic efficiency of the PE-CQDs from the controlled oxidation of benzyl alcohol (BA) and its derivatives to the corresponding aldehydes using ambient conditions. Semiconducting-material-driven photocatalytic reactions are emerging as a preferred process to utilize solar energy as a clean and renewable fuel.<sup>23-27</sup> The oxidation of BA and its derivatives is an important chemical transformation where the reaction products are widely used in fine-chemical synthesis.<sup>28-31</sup> Therein, the use of molecular O<sub>2</sub> as the oxidant from a flowing gas, or even better, ambient air, is preferred due to its green nature and abundance. Hence it occurs that the O<sub>2</sub> enriched PE-CQDs ought to be an outstanding photocatalyst for these selective oxidation reactions. The PE-CQDs induced ~75% conversion of benzylalcohol and its derivatives to the corresponding benzaldehydes with >90% selectivity under 4 h of natural sunlight exposure at ambient conditions. Apart from the high photocatalytic efficiency, the self-devouring nature of the PE-CQDs, a unique material property, is expected to be highly valuable to remove them from their site-of-use or in environmental remediation applications where their recovery is unfeasible.

### 3.4.3 Methods

#### 3.4.3.1 Synthesis of graphitic PE-CQDs

The PE-CQDs were prepared by using  $\text{H}_2\text{O}_2$  as oxidizing reagent after the carbonization of polyethylene. In a typical synthesis, 1g of small pieces of polyethylene sheets were added to 60 mL of 18 M sulphuric acid in a 250 mL round bottom flask. The solution was refluxed at ~140-150 °C with constant stirring at 600 rpm for 1 h. The PE sheets turned into black charred-mass. Thereafter, 1-2 ml of  $\text{H}_2\text{O}_2$  was slowly added to the reaction mixture drop-wise resulting in a red colour solution (**Figure 3.4.1**). The reaction mixture was allowed to cool to room temperature. The solution was then diluted by adding 60 mL of water and then filtered by using cotton on the top of glass funnel. The transparent red coloured solution was then extracted repeatedly by adding ethyl acetate using a separating funnel. The organic phase was then passed through the  $\text{Na}_2\text{SO}_4$  to remove moisture and dried using a rota-vapour under reduced pressure, yielding solid powder of the graphitic PE-CQDs.

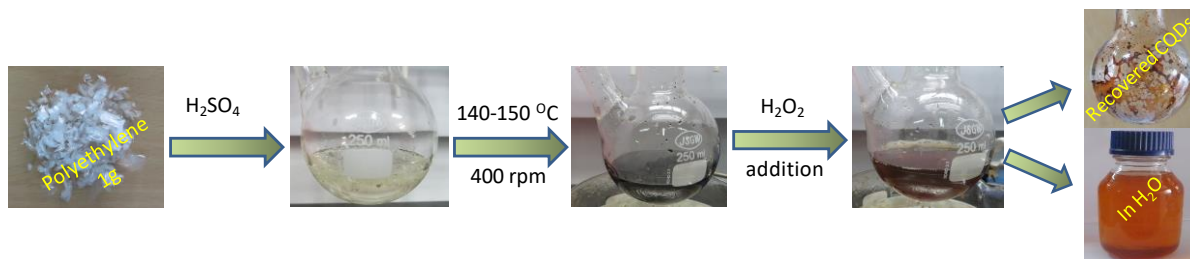


**Figure 3.4.1** Synthesis scheme for the formation of PE-CQDs taking polyethylene as starting material.

#### 3.4.3.2 Oxygen content measurements in the aqueous solution of PE-CQD

$\text{O}_2$  contents in pure water and aqueous solution of PE-CQDs were measured using non-invasive Ocean Optics Neofox-Kit-Probe.<sup>32</sup> 50 mg of PE-CQDs dispersed in 60 mL of water was placed in a round bottom flask (RBF, capacity ~70 mL) where the air-water interface area was 7 cm<sup>2</sup>. The sensing patch, attached to the inner wall of RBF, was completely submerged by the solution. During  $\text{O}_2$  uptake, the solution was stirred at 300 rpm and during  $\text{O}_2$  desorption the solution was kept still with a constant  $\text{N}_2$  flow (60-70 sccm). The kit was calibrated before all measurements using a two-point reading (0%  $\text{O}_2$  in  $\text{N}_2$  and 20.90%  $\text{O}_2$  in the air).

### **3.4.3.3 Photocatalytic benzyl alcohol oxidation using PE-CQDs**

The selective photo-oxidation of benzyl alcohol (BA) was carried out under direct sunlight as well as using a 400 W Xenon lamp (Newport) attached with an water-IR filter. Typically, 10 mg of PE-CQDs and 0.5 mmol of BA were dissolved in 10 mL of acetonitrile in a 10 mL RBF. Before the photocatalytic reaction, the reaction mixture was kept in dark for 1 h under constant magnetic stirring to establish an adsorption-desorption equilibrium. The temperature during the photocatalytic reaction was monitored and found to be ~28-30 °C throughout the reaction period. After 4 h light illumination, samples were analyzed by gas chromatography (GC). The same reaction was performed using 10 mg of commercial TiO<sub>2</sub> (P-25, Aldrich) to compare the catalytic activities.

### **3.4.3.4 Photocatalytic stability and self-oxidation tests for PE-CQDs**

Stability of the PE-CQDs was examined during the Rhodamine B (RhB) photo-degradation reaction under a 400 W Xe-lamp (attached with an water-IR filter) illumination. We have carried out the degradation reaction with PE-CQDs up to the 10<sup>th</sup> cycle by repeatedly adding the dye solution without intermittent cleaning of the photocatalyst. After completion of the 10<sup>th</sup> cycle, the same PE-CQD solution was kept under the Xe-lamp for 10 h without any further addition of RhB when it was observed that the colour of the solution (arising from PE-CQDs as there were no dye molecules left) becomes increasingly faint. On the other hand, two 50 mL glass beakers containing 10 mg PE-CQDs (10 ml water) in each were added separately and one of them was kept on continuous stirring under direct sunlight for 30 days while the other beaker was kept in dark for the same time. The solution was filtered and then the water content was allowed to evaporate naturally by keeping it open at room temperature.

The products of the self-sensitized photo-oxidation of PE-CQDs were investigated in a closed 50 mL RBF containing PE-CQDs aqueous solution with constant magnetic stirring at 300 rpm under different atmospheres. The PE-CQD concentration was kept same as O<sub>2</sub> adsorption-desorption. A 400 W Xe-lamp attached with a water-IR filter was used as light source. The gaseous product so formed with regular time interval was analyzed through gas-chromatography (Shimadzu GC-2014).

### 3.4.3.5 Characterization

All other characterization techniques except the ones noted above are discussed in chapter 2.

### 3.4.4 Results and Discussion

The PE-CQDs could be prepared using various high-density polyethylene (such as a kitchen-glove, **Figure 3.4.2a,b**). The small polyethylene pieces turned into a charred, black-colored carbon-mass after treatment with 18 M H<sub>2</sub>SO<sub>4</sub> under reflux conditions for one hour. H<sub>2</sub>O<sub>2</sub> was added drop-wise to this reaction aliquot for further oxidation, and the black-mass started disappearing almost immediately until a transparent, yellowish PE-CQD solution was obtained in about 2 minutes (See the schematic diagram in **Figure 3.4.1**). Transmission electron microscopy (TEM) images (**Figure 3.4.2c,d**) revealed that the particles are spherical, measuring 1.5 to 7 nm in size and an average size of 4 nm as shown in **Figure 3.4.2e**. Their size is somewhat smaller than the PE-CQDs synthesized using KMnO<sub>4</sub> (average size of 6.5 nm). The presence of the graphitic regions can be clearly observed in the high-resolution TEM (HRTEM) images (**Figure 3.4.2f**) having lattice-fringes separated by 0.32 nm corresponding to the (002) planes. Energy-dispersive X-ray spectroscopy (EDS) shows the presence of sulphur in the sample (**Figure 3.4.2g**) due to the functionalization of the PE-CQDs by sulphuric acid.<sup>9</sup> The nature of the various functional groups were examined by Fourier transform infrared (FT-IR) spectroscopy, as shown in **Figure 3.4.3a**, revealing the presence of several functional groups. The peak at 2900 cm<sup>-1</sup> can be assigned to the C-H stretching vibration while the peaks at 1175 and 978 cm<sup>-1</sup> arise due to the S-O stretching vibrations of -SO<sub>3</sub>H. The sharp peaks at 1254, 1445, and 1723 cm<sup>-1</sup> correspond to the C-O, C-O-C, and C=O stretching vibrations, respectively, suggesting the formation of carbonyl and ether functional groups in PE-CQDs. X-ray photoelectron spectroscopic (XPS) analysis further confirmed the functional groups present on the PE-CQDs. **Figure 3.4.3b** shows the core-level XPS spectrum of C 1s that could be fitted with 5 peaks. The peaks at 284.5 eV, 285.6 eV, 286.5 eV, 287.8 eV and 288.9 eV have been assigned to the *sp*<sup>2</sup> C-C, *sp*<sup>3</sup> C-C, C-O- (hydroxyl) and C-O-C (epoxy) groups, C=O (carbonyl) species COOH (carboxyl) groups respectively with a relative abundance of 31%, 19%, 25%, 13% and 11%. The amount of oxygen forming single and double bonds were also estimated by deconvoluting the O 1s peak as shown in **Figure 3.4.3c**. Since the peaks at 533.0 eV and 531.8 eV arise from the single-bonded and double-bonded oxygen species respectively,<sup>9</sup> they have an atomic ratio of ~40:60. A comparison with the KMnO<sub>4</sub> generated PE-



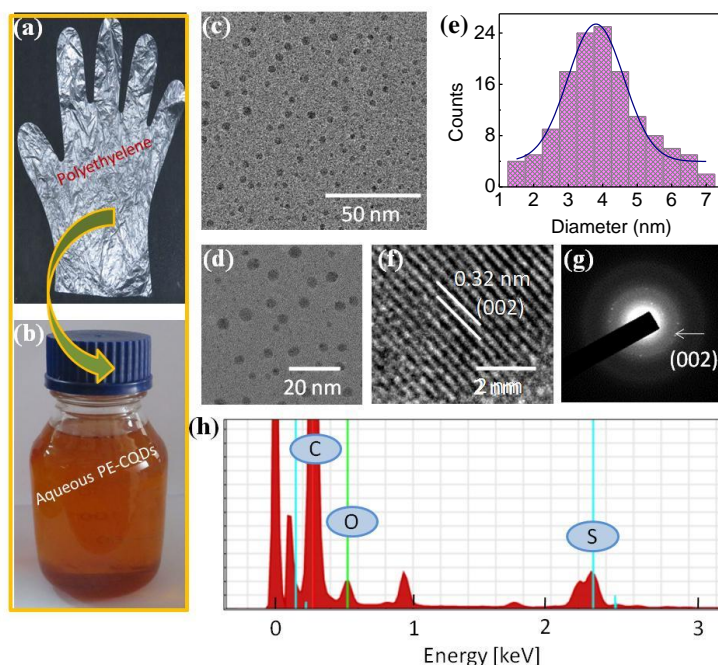


**Figure 3.4.2** Photograph of a typical polyethylene precursor (a kitchen-glove) (a) and the aqueous dispersion of the PE-CQDs prepared from it (b). (c, d) TEM image of the as-synthesized PE-CQDs. (e) Particle size distribution plot showing an average particle size of 4 nm. (f) High-resolution TEM image of a PE-CQD. (g) SAED pattern and (h) a typical EDS spectrum acquired on the PE-CQDs.

CQDs reveals that the present CQDs have less number of  $sp^2$  carbon (31% vs. 49%), but more number of C-atoms as parts of hydroxyl or epoxy groups (25% vs. 11%), suggesting a higher extent of oxidation by  $H_2O_2$  and a possibility to control the extent of functionalization by adjusting the oxidation step.

The aqueous solution of PE-CQDs exhibited novel optical properties as revealed by the UV-Visible (UV-Vis) absorption, photoluminescence (PL) spectroscopy, and time-correlated single-photon count (TCSPC) measurements. The UV-Vis absorption spectrum exhibited an absorption onset at  $\sim 550$  nm (Figure 3d) and other prominent absorption features at 340, 375, 395, and 425 nm. A typical PL spectrum of the solution is plotted in inset of **Figure 3.4.3d**. We also

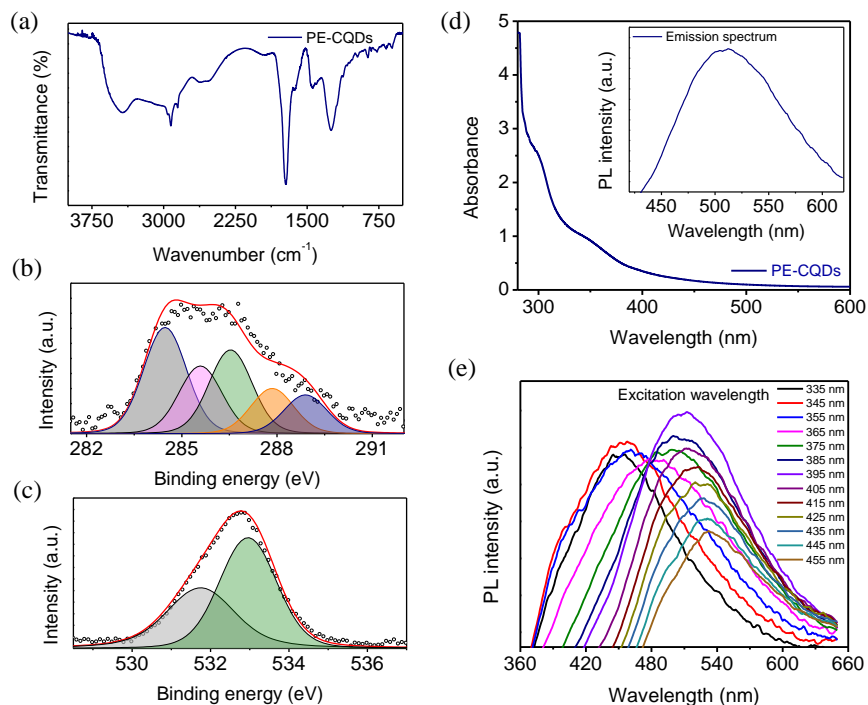


**Figure 3.4.3** (a) FT-IR spectrum of the PE-CQDs. XPS spectrum of (b) the C1s and (c) the O 1s core-levels in the PE-CQDs. (d) UV-Vis absorption spectrum of the as-synthesized PE-CQDs dispersed in water. Inset is the PL emission spectrum of PE-CQDs. (e) Photoluminescence emission spectra of the PE-CQDs at different excitation wavelengths.

recorded the PL spectra with different excitation-wavelengths ( $\lambda_{\text{ex}} \sim 335\text{--}455$  nm range) and observed that the emission peak wavelength ( $\lambda_{\text{em}}$ ) is red-shifted with longer  $\lambda_{\text{ex}}$  (**Figure 3.4.3e**). The most intense emission maximum was observed at 510 nm and  $\lambda_{\text{ex}} = 395$  nm, corresponding to an emission quantum yield (QY) of  $\sim 6.9\%$ . In comparison, the PE-CQDs prepared with  $\text{KMnO}_4$  exhibited an emission maximum at 523 nm with a QY of 9.5%.

The shifts observed in the  $\lambda_{\text{em}}$  with changing  $\lambda_{\text{ex}}$  are well-documented for many different CQDs.<sup>33</sup> However, the luminescence-decay measurements at various  $\lambda_{\text{em}}$  unveiled an interesting pattern. **Figure 3.4.4a** is the luminescence decay plot for the PE-CQDs at 510 nm ( $\lambda_{\text{ex}} = 375$ ) corresponding

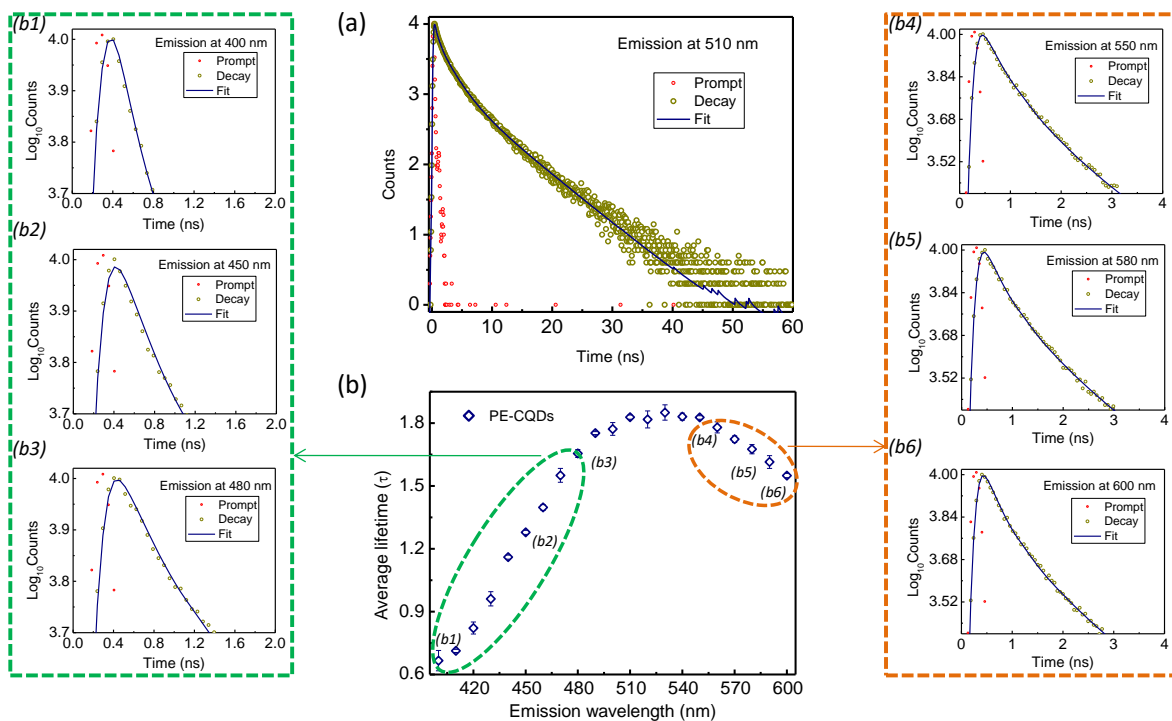


**Figure 3.4.4** (a) The PL decay plot of the aqueous PE-CQD solution at 510 nm emission ( $\lambda_{ex}=375$  nm). (b) The average emission lifetime of the PE-CQD solution at various emission wavelengths ( $\lambda_{ex}=375$  nm). (b1, b2, b3, b4, b5, and b6) are the time-resolved fluorescence decay plots at  $\lambda_{em}=400$  nm, 450 nm, 480 nm, 550 nm, 580 nm, and 600 nm respectively, keeping the same  $\lambda_{ex}$ , plotted for the first few nanoseconds to highlight the variations in the fast component of the decay profiles.

to an average lifetime ( $\tau$ ) of 1.82 ns. Further, the sample was excited at 375 nm and the emission decay kinetics data were recorded at regular  $\lambda_{em}$  intervals in the 400-600 nm range. The data were fitted to a tri-exponential function and the typical fitting parameters are given in **Table 3.4.1**. The average lifetime ( $\tau$ ), was calculated using the following formula:

$$\text{Average lifetime } (\tau) = (\tau_1 A_1 + \tau_2 A_2 + \tau_3 A_3) / (A_1 + A_2 + A_3)$$

where,  $\tau_1$ ,  $\tau_2$ , and  $\tau_3$  are emission lifetimes in three different time stages and  $A_1$ ,  $A_2$ , and  $A_3$  are the amplitude of the different emission lifetimes.  $\tau$  becomes maximum near the  $\lambda_{em, max}$ , but reduces at lower or higher  $\lambda_{em}$  (**Figure 3.4.4b**). The minimum value of  $\tau=0.62$  ns was recorded at  $\lambda_{em}=400$  nm, which gradually increases to 1.82 ns until  $\lambda_{em}=510$  nm or 520 nm and then goes on decreasing to 1.43 ns at  $\lambda_{em}=600$ . To underline the differences in  $\tau$ , the decay traces for the same decay counts

are plotted at different  $\lambda_{em}$  within the first few nanoseconds where the fast decay component is clearly observed (**Figure 3.4.4b1-b6**). Recently we serendipitously observed that in the case of a light-harvesting semiconductor (g-C<sub>3</sub>N<sub>4</sub>),  $\tau$  is  $\lambda_{em}$  dependent and gradually increases over ten times within the emission peak as  $\lambda_{em}$  becomes longer, thereby remarkably influencing the exciton-transfer dynamics in the event of photocatalytic reactions.<sup>34</sup> The effect was attributed to a vibrational relaxation process from the higher excited state to the band-edge. Surprisingly though, the behaviour of the PE-CQDs is quite different and probably complex in nature since the origin and the nature of the emission centers in CQDs are highly debatable.<sup>35-37</sup>

**Table 3.4.1:** PL decay lifetime analysis of the PE-CQD aqueous solution at an emission wavelength of 510 nm (excitation wavelength = 375 nm).

Tri-exponential Emission (nm)	$\langle\tau\rangle$ ns	$\chi^2$	$\tau_1$ (ns)	$\tau_2$ (ns)	$\tau_3$ (ns)	$A_1$	$A_2$	$A_3$
PE-CQDs	1.821	1.002	2.200	0.498	6.510	0.38	0.51	0.11

#### 3.4.4.1 Total oxygen content in PE-CQDs

Recently, it was shown that the PE-CQDs have the unique ability to capture oxygen molecules from the air and enrich the oxygen content of a solution. The molecular oxygen content per gram of the PE-CQDs is higher than those expected to be exhibited by the custom-made materials for gas adsorption such as zeolites and metal-organic frameworks.<sup>9,38</sup> We evaluated the oxygen enrichment properties of the H<sub>2</sub>O<sub>2</sub> generated PE-CQDs by measuring the total O<sub>2</sub> content (TO) of an aqueous solution containing 0.83 mg PE-CQDs per mL of water. The TO value of the solution was  $\sim 652 \pm 8$   $\mu$ M, more than double of that in pure water ( $\sim 340$   $\mu$ M, **Figure 3.4.5a,b**).

Notably, the TO value is higher than the same exhibited by PE-CQDs prepared by using KMnO<sub>4</sub> ( $640 \pm 8$   $\mu$ M).<sup>9</sup> Furthermore, it was argued in the previous study that the O<sub>2</sub> molecules are loosely bound to the CQD surface and therefore the O<sub>2</sub> level can be easily adjusted by replacing it

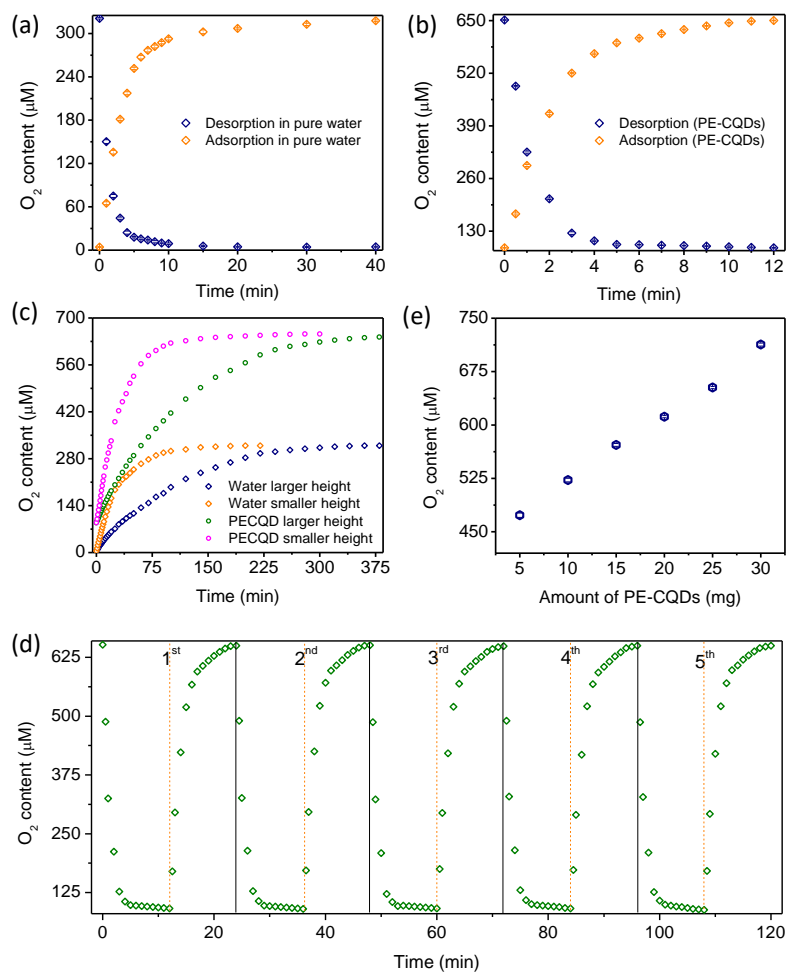


**Figure 3.4.5** (a) Temporal variation of the total oxygen content in (a) pure water, and (b) aqueous PE-CQD solution while purging with nitrogen and subsequently during the spontaneous oxygen uptake from the open air by the nitrogen saturated solutions. (c) Temporal variation of total oxygen content in pure water and PE-CQD solution (1mg/1.2 ml) during oxygen uptake from the air by  $N_2$  saturated samples at depths of 0.2 and 8 cm below the aqueous-air interface. (d) Repeatability test for oxygen uptake and release using the aqueous PE-CQDs solution. (e) The TO contents estimated for aqueous solutions containing different amounts of PE-CQDs.

with other gas molecules under high partial pressure. Thus, we studied the kinetics of  $O_2$  desorption under a continuous purging of  $N_2$  gas in the solution as shown in **Figure 3.4.5a,b**. The TO level decreases rapidly to  $125 \mu\text{M}$  within the first 3 minutes and attained a saturated depletion value of  $\sim 90 \mu\text{M}$  in  $\sim 5$ -6 minutes. In contrast, oxygen desorption from pure water is slower (**Figure 3.4.5a**), requiring  $\sim 20$  minutes to reach a saturated depletion value of  $5 \mu\text{M}$ .

The deoxygenated solution captures back the oxygen molecules from the air to attain the equilibrium value once the N<sub>2</sub> flow is stopped. The O<sub>2</sub> uptake features in the N<sub>2</sub> purged pure water and aqueous PE-CQD solution in open air are also shown in **Figure 3.4.5a,b**, suggesting a much faster rate of O<sub>2</sub> uptake (~3-4 times in the initial 2-3 minutes) in the case of the PE-CQD solution. Thus, by acting as carriers of O<sub>2</sub> molecules from the air-water interface to the bulk of the solution, in addition to the typical diffusion of the gaseous O<sub>2</sub> in the solution, the PE-CQDs are capable of inducing a markedly faster rate of O<sub>2</sub> diffusion. The O<sub>2</sub> uptake measurements were carried out at two different depths (0.2 cm and 8 cm) from the exposed air-aqueous interface to confirm the same. As expected (**Figure 3.4.5c**), the time taken by the solution to attain oxygen saturation is proportional to the depth, while the saturation levels remain the same. On the other hand, by considering the increase in the TO content per minute, the O<sub>2</sub> diffused rate is much smaller in pure water. We have attributed this high diffusion rate in the PE-CQD solution to a persistently high O<sub>2</sub> concentration gradient across the air-water interface since the dissolved oxygen quickly associates with the PE-CQDs depleting the O<sub>2</sub> levels in the surrounding.

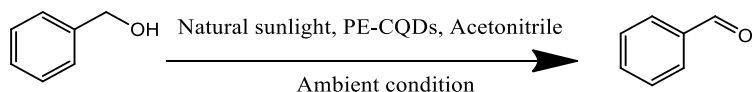
Finally, we show that (i) the oxygen enrichment properties of the PE-CQDs in the solution remain reversible, as shown in five successive N<sub>2</sub> purging cycles in **Figure 3.4.5d**, and (ii) the enrichment is PE-CQDs concentration-dependent. Thus, the TO content of the solutions containing 5 mg, 10 mg, 15 mg, 20 mg, 25 mg and 30 mg per 30 mL of water were 473, 522, 572, 611, 652, and 712  $\mu\text{M}$  respectively (**Figure 3.4.5e**). Overall, the PE-CQDs obtained using H<sub>2</sub>O<sub>2</sub> are similar to those prepared by using KMnO<sub>4</sub> while exhibits an improved oxygen adsorption behaviour. The higher oxygen content in PE-CQDs generated with H<sub>2</sub>O<sub>2</sub> is ascribed to the variation in functional groups from those prepared with KMnO<sub>4</sub>.

#### **3.4.4.2 Photocatalytic oxidation of Benzyl alcohol by PE-CQDs**

Selective photocatalytic oxidation of alcohols to the corresponding carbonyl compounds using molecular O<sub>2</sub> as an oxidant has gained significant recent interest due to the greener synthetic approach.<sup>39-41</sup> The high visible light response and the copious O<sub>2</sub> content on the PE-CQD surface make them an ideal catalyst for the selective and controlled photo-oxidation of benzyl alcohol (BA) and its derivatives using molecular O<sub>2</sub> from air and sunlight. BA oxidation was carried out in acetonitrile solvent in an open-air under direct sunlight and the conversion efficiency was found

to be 75% with >90% selectivity after 4 h of illumination. To confirm the role of molecular O<sub>2</sub> in the reaction, we have performed the reaction by varying the O<sub>2</sub> content in the reaction aliquot. **Table 3.4.2** summarizes the result of the various oxidation reactions. Interestingly, we noted that the reaction yield barely increases when we purged O<sub>2</sub> gas in the reaction vessel during oxidation, unlike other photocatalysts reported so far, suggesting that the PE-CQDs are sufficiently saturated with O<sub>2</sub> molecules (**Table 3.4.2**, entry 2).<sup>42-44</sup> To confirm this, two more sets of reactions were carried out by purging N<sub>2</sub> through the reaction mixture before starting the illumination. In the first set, we have purged N<sub>2</sub> through the reaction aliquot and then added PE-CQDs (which was kept in

**Table 3.4.2:** Selective photocatalytic oxidation of BA under various conditions.



Entry	Catalyst	Light	Environment	Time (h)	Conv.(%)	Selec.(%)
1	PE-CQDs	Sunlight	Air	4	75%	>90%
2	PE-CQDs	Sunlight	O <sub>2</sub>	4	77%	>90%
3 <sup>a</sup>	PE-CQDs	Sunlight	N <sub>2</sub>	4	54%	>90%
4 <sup>b</sup>	PE-CQDs	Sunlight	N <sub>2</sub>	4	34%	>90%
5	PE-CQDs	Dark	Air	4	-	-
6	PE-CQDs	Dark	Air, 40 °C	4	-	-
7	PE-CQDs	Dark	Air, 50 °C	4	-	-
8	No-catalyst	Sunlight	Air	4	-	-
9	PE-CQDs	Xe-lamp	Air	4	76%	>90%
10	TiO <sub>2</sub> -P25	Sunlight	Air	4	23%	>90%

*a= First N<sub>2</sub> was purged through the reaction mixture and then PE-CQDs were added to it. b= PE-CQDs were added to the reaction mixture and then N<sub>2</sub> was purged.*

the air) to it, resulting in 54% conversion after 4 h (**Table 3.4.2**, entry 3<sup>a</sup>). In the second set, N<sub>2</sub> was passed through the solution containing PE-CQDs to remove maximum possible dissolved O<sub>2</sub> from the reaction mixture as well as the PE-CQD surface; where the resultant conversion efficiency was still quite high, though dropped to ~34% after 4 h (**Table 3.4.2**, entry 4<sup>b</sup>). We anticipated that between the first and the second set of reactions, 1<sup>st</sup> should give a better yield as we did not remove the O<sub>2</sub> adsorbed on PE-CQDs surface, leading to a higher O<sub>2</sub> content in the medium. In contrast, when oxygen was removed from the solvent as well as from the PE-CQDs surface in the 2<sup>nd</sup> set, the reaction efficiency decreased further by 20%. The findings are in stark contrast to the earlier reports, where the conversion becomes negligible under an inert atmosphere due to the lack of O<sub>2</sub> in the reaction aliquot. A ~54 % conversion, even in an inert atmosphere, was observed for the first time because of the presence of O<sub>2</sub> molecule on PE-CQDs surface, earmarking the influence of their oxygen uptake ability in oxidation reactions.

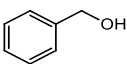
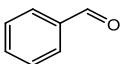
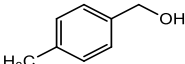
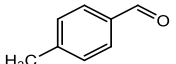
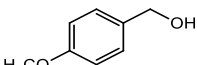
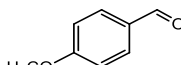
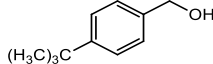
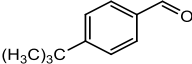
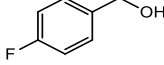
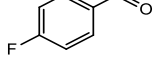
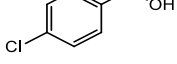
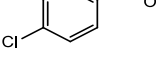
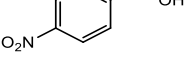
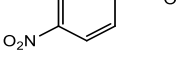


The conversion is negligible in the presence of PE-CQDs at room temperature under dark conditions inferring its photocatalytic nature. We then carried out the reaction by increasing the reaction temperatures to 40 °C and 50 °C under the dark conditions, but the yield did not improve (**Table 3.4.2**, entry 6&7). The conversion was negligible when the reaction was performed under sunlight in the open air in absence of PE-CQDs (**Table 3.4.2**, entry 8). Additionally, we have performed the same reaction using a 400 W Xe lamp (attached to an IR filter) and the conversion efficiency was found to be nearly identical to that of the reaction under direct sunlight (**Table 3.4.2**, entry 9).

The estimated AQE under direct sunlight was 8.36% for the BA oxidation reaction using the PE-CQDs at ambient conditions. The efficiency of the reaction was compared by using commercial TiO<sub>2</sub>-P25 as a photocatalyst and the conversion was ~23% under identical conditions (**Table 3.4.2**, entry 10). The BA oxidation efficiency of the PE-CQDs higher in comparison to the other recently developed photocatalysts and also the PE-CQDs previously prepared using toxic KMnO<sub>4</sub>. It is to be pointed out that such oxidation reactions are often carried out at elevated temperatures and high oxygen pressure using other photocatalysts to improve the reaction kinetics.<sup>40-48</sup> In comparison, PE-CQDs exhibited a superior performance despite using ambient conditions and air as the source of O<sub>2</sub>.



The versatility of the PE-CQDs was studied by performing the reaction with various electron-donating (-CH<sub>3</sub>, -OCH<sub>3</sub>, t-butyl) and electron-withdrawing (-F, -Cl, -NO<sub>2</sub>) group-substituted BA derivatives, as shown in **Table 3.4.3**. The reaction-rate is almost similar with the electron-donating substituent groups while slightly slower in the case of BA molecules with

**Table 3.4.3:** Aerobic photo-oxidation of BA derivatives with the PE-CQDs under natural sunlight.

Entry	Substrate	Product	t [h]	Conv. [%]	Sel. [%]
1			4	75	>90
2			4	72	>90
3			4	70	>90
4			4	68	>90
5			4	64	>90
6			4	62	>90
7			4	60	>90
8			4	-	-

**Reaction conditions:** The reactions were carried out in acetonitrile solutions (10 ml), containing substrates (0.5 mmol), photocatalyst (25 mg) under the sunlight, the products were analyzed by GC.

electron-withdrawing groups. However, the reaction did not proceed even after 8 h of light irradiation when aliphatic alcohol was used, suggesting a high efficiency and selectivity of the PE-CQDs for the oxidation of various substituted aromatic alcohols.

### 3.4.4.3 Mechanistic investigations

Several controlled reactions were performed to clarify the mechanism of BA photo-oxidation and to find out the active intermediates. Molecular  $O_2$  as the oxidizing agent was confirmed by changing the reaction environment to  $N_2$  as discussed earlier. Upon light-illumination on PE-CQDs, the photogenerated electrons and holes interact with  $O_2$  and BA. The scavengers used to find out the reaction mechanism are electron scavenger ( $K_2S_2O_8$ ), superoxide radical anion (benzoquinone), hole scavenger (ammonium oxalate), and carbon radical scavenger (butylated-hydroxyl toluene). The addition  $K_2S_2O_8$  to the reaction-mixture induces a sharp decrease in the conversion efficiency to ~23% (**Figure 3.4.6a**). We have also observed a decrease in efficiency by adding benzoquinone to the reaction (**Figure 3.4.6a,b**). When we performed the reaction in the presence of ammonium oxalate, the conversion decreased drastically to 8%, indicating the major influence of holes during oxidation (**Figure 3.4.6a**). Further, we have performed a reaction in the presence of butylatedhydroxytoluene as a carbon-radical scavenger and the conversion was suppressed to ~7% after 4 h suggesting that oxidation reaction indeed goes via formation of carbon radical species.

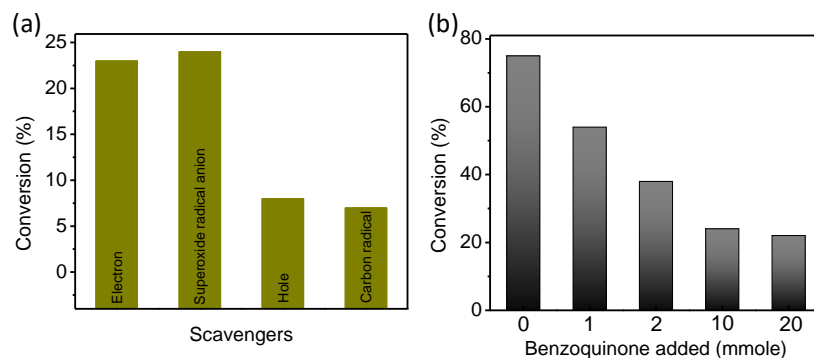
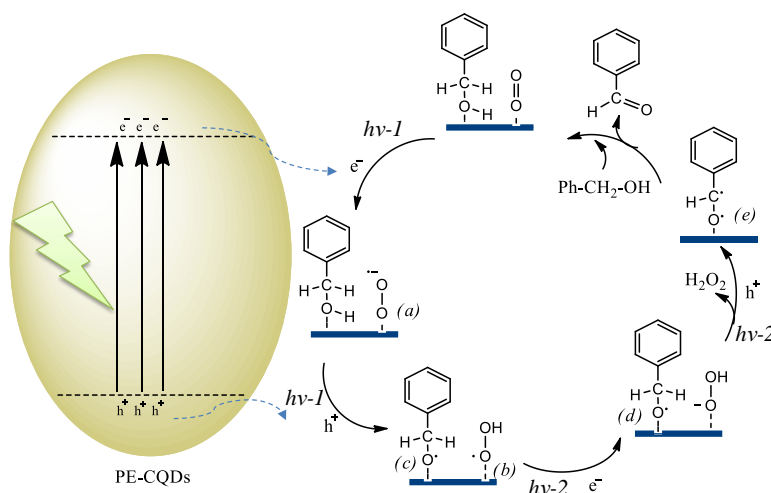


**Figure 3.4.6** (a) BA photo-oxidation efficiency in the presence of different photogenerated reactive species scavengers. (b) The BA oxidation efficiency while adding the different amounts of benzoquinone as superoxide radical anion scavenger.

Based on these observations, we propose a reaction mechanism as shown in **Scheme 3.4.1**. Briefly, an adsorbed  $O_2$  molecule takes one photogenerated electron and forms a superoxide radical anion,  $O_2^{\cdot-}$  (a). Next,  $O_2^{\cdot-}$  extracts a proton from a neighbouring BA molecule and a photogenerated hole, producing an oxygen radical species (c). Further, (c) converts to a carbon

radical species (*d*) with the help of another exciton and the adsorbed superoxide radical leaves in the form of H<sub>2</sub>O<sub>2</sub>. The *in-situ* generation of '*d*' was confirmed by using a trapping reagent, TEMPO ((2,2,6,6-tetramethylpiperidin-1-yl)oxyl radical) and detecting with high-resolution mass spectroscopy.<sup>49</sup> The formation of H<sub>2</sub>O<sub>2</sub> in the reaction aliquot was confirmed colorimetrically by KMnO<sub>4</sub> titration.<sup>50</sup>



**Scheme 3.4.1** The probable mechanism of photocatalytic BA oxidation in the presence of PE-CQDs.

#### 3.4.4.4 Of stability, light-induced oxidative elimination, or autophagy of the PE-CQDs

To examine the stability of the PE-CQDs, we have performed the photocatalytic degradation of Rhodamine-B (RhB) dye as model-reaction up to the 10<sup>th</sup> catalytic cycle and followed it by recording temporal UV-Vis spectra (**Figure 3.4.7** and **Figure 3.4.8**). 98% of degradation was observed in 14 minutes of light-illumination in the first cycle. It has become marginally slower with every cycle, though the degradation was >94% in 14 minutes at the end of the 10<sup>th</sup> cycle. The corresponding rate-constants observed in the consecutive cycles are given in **Figure 3.4.9a**, showing a minimal loss of efficiency. Notably, the RhB degradation follows the de-ethylation mechanism as confirmed by the formation of a new UV-Vis absorption peak at ~504 nm, which is

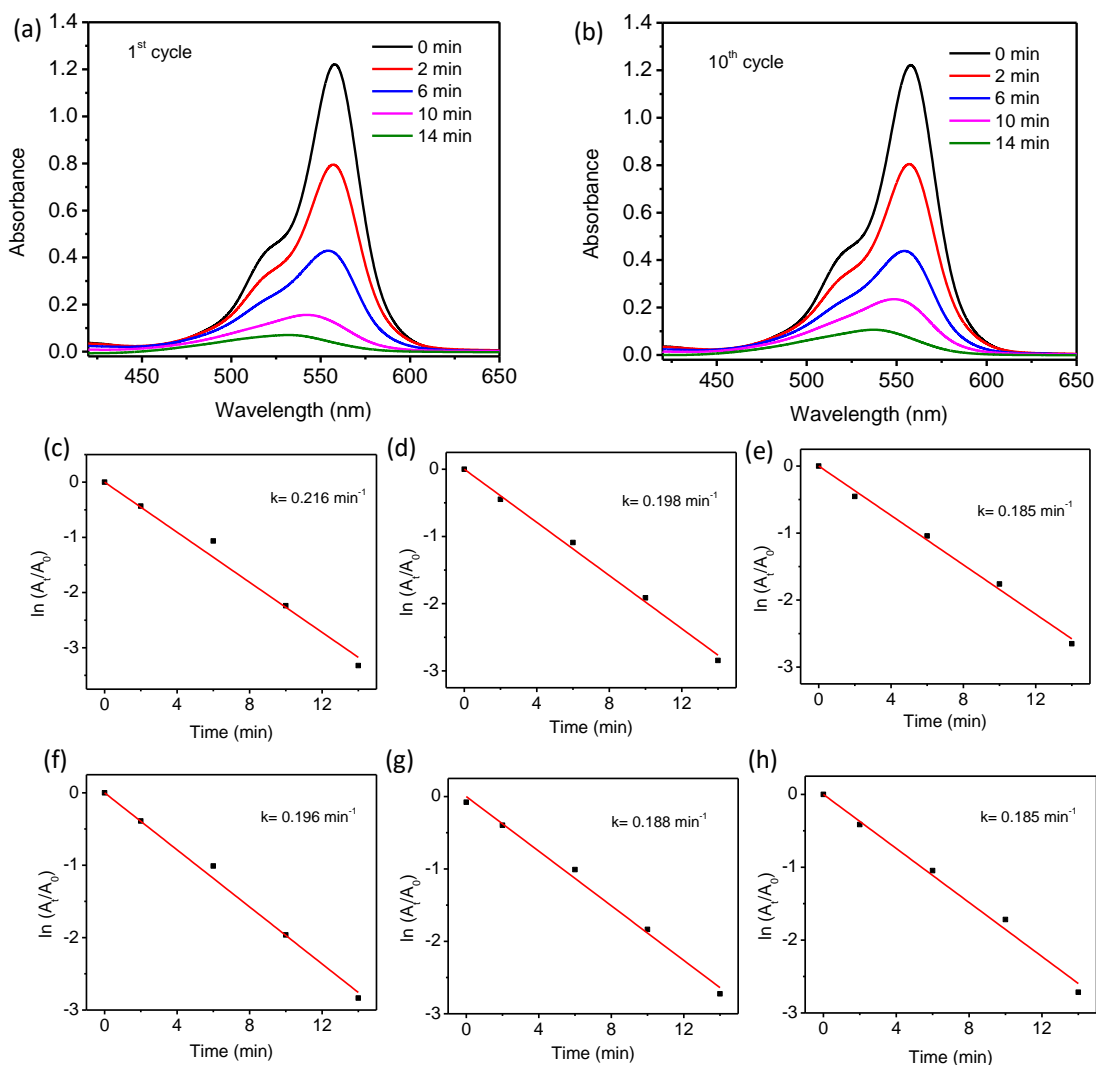


**Figure 3.4.7** Time-dependent UV-Vis spectra for the RhB photo-degradation under 400 W Xe-lamp using the PE-CQDs as photocatalyst: (a) 1<sup>st</sup> cycle and (b) 10<sup>th</sup> cycle. Plot of  $\ln(A/A_0)$  vs. time of RhB photo-degradation in 1<sup>st</sup> cycle (c), 2<sup>nd</sup> cycle (d), 4<sup>th</sup> cycle (e), 6<sup>th</sup> cycle (f), 8<sup>th</sup> cycle (g) and 10<sup>th</sup> cycle (h).

attributed to the formation of the Rhodamine 110 as an intermediate in the process and confirmed by using mass spectrometry.<sup>9</sup> We point out that the degradation efficiency exhibited by the PE-CQDs is extremely high, depicting at least 5-10 fold improvement over any state-of-the-art catalyst known to us, including the noble-metal based materials.

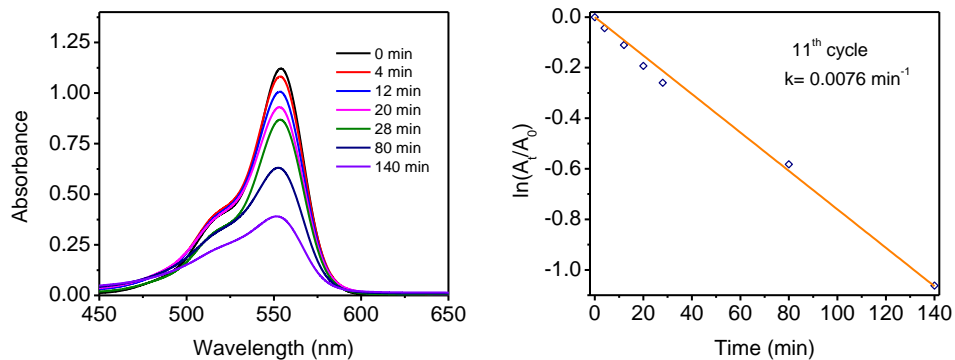


**Figure 3.4.8** (a) Time-dependent UV-Vis spectra for the RhB photo-degradation under 400 W Xe-lamp using PE-CQDs as photocatalyst in the 11<sup>th</sup> cycle. The 11<sup>th</sup> cycle was conducted after illuminating the PE-CQD solution with the same light for 10 h continuously, without adding RhB. (b) The plot of  $\ln(A_t/A_0)$  vs. time of RhB photo-degradation in the 11<sup>th</sup> cycle.

The PE-CQDs under illumination, however, exhibited a rather unexpected behaviour in the absence of the reactant molecules. Even though their stability is high during photocatalysis (earlier we demonstrated that the efficiency is quite remarkable even up to 100 cycles using the  $\text{KMnO}_4$  generated PE-CQDs), when we continued to irradiate the same PE-CQD solution at the end of the 10<sup>th</sup> cycle for a prolonged period (10 h) without further RhB addition, a visible and gradual change in the solution color was noticed, as perceived from the photographs shown in **Figure 3.4.9b (b1-b3)**. The UV-Vis absorption spectra of the solution (**Figure 3.4.9b and inset**) show that the absorption intensities decrease steadily with irradiation time indicating the loss of light absorption sites, or probably the PE-CQDs themselves. The intensity of PE-CQD absorption peak decreases during photocatalysis too, but slowly as indicated by the inflection point in the inset of **Figure 3.4.9b**. The PE-CQDs after catalysis (which took 2.5 h) were recovered and analyzed using TEM, UV-visible absorption, and PL measurements (**Figure 3.4.10**) to show that they remain unaffected by the catalysis process. The photobleaching on carbon-dots has been widely observed wherein the changes in their color (and luminescence intensity) are irreversible and occur at different rates in the presence or the absence of oxygen.<sup>19</sup> Partial removal or changes in the structure of the fluorophore functional groups have been proposed as the origin of photobleaching,

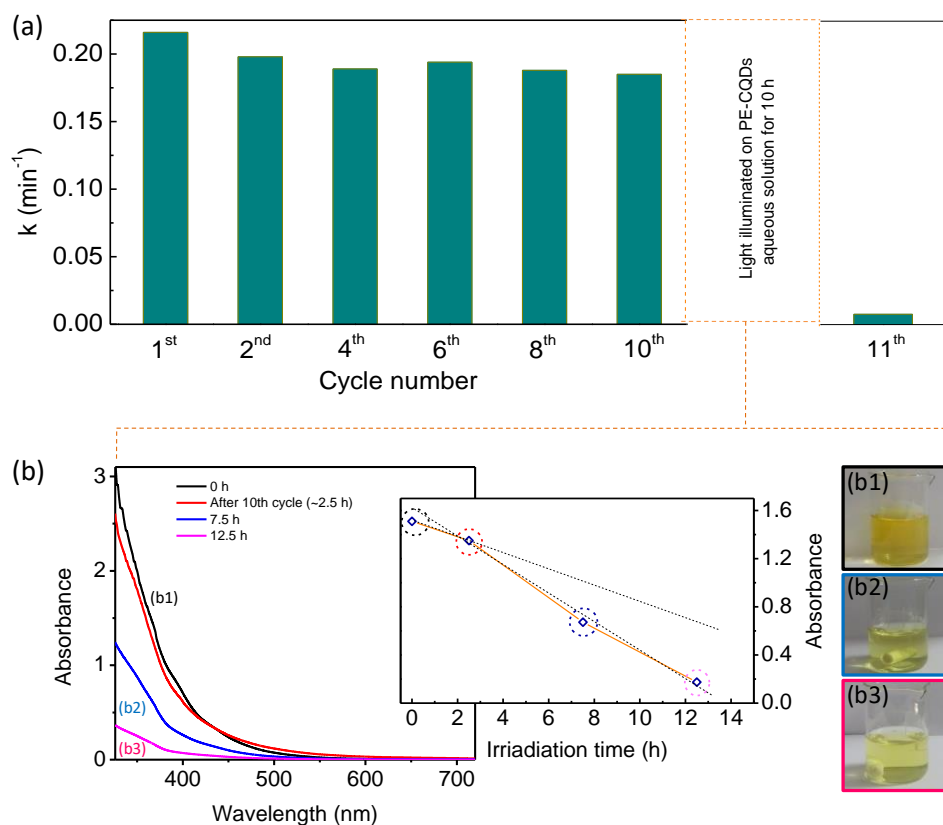


**Figure 3.4.9** (a) Plot of rate constants for the photocatalytic RhB degradation using PE-CQDs at different catalytic cycles. (b) UV-Vis absorption spectra of the PE-CQDs solution before the 1<sup>st</sup> cycle (0 h) and at different irradiation times after the 10<sup>th</sup> catalytic cycle (~2.5 h). (b1, b2, and b3) are the photographs of the PE-CQDs solution at different irradiation times.

accompanied by an increase in –C-O functionalities indicating that a photo-oxidation process takes part in it.<sup>20,22</sup> However, the extent of such an effect and if the same can be utilized usefully is not clear yet. To understand the origin of color change in our experiments, we illuminated an aqueous PE-CQD solution with the same Xe lamp in a closed-vessel and measured the variations in the TO content with illumination time. The TO content was nearly constant for the first 90 minutes and then started decreasing from 650  $\mu$ M to 230  $\mu$ M at a rate of ~40  $\mu$ M/h, as shown in **Figure 3.4.11a**, indicating that O<sub>2</sub> ought to be consumed in some process in the presence of light since it can not

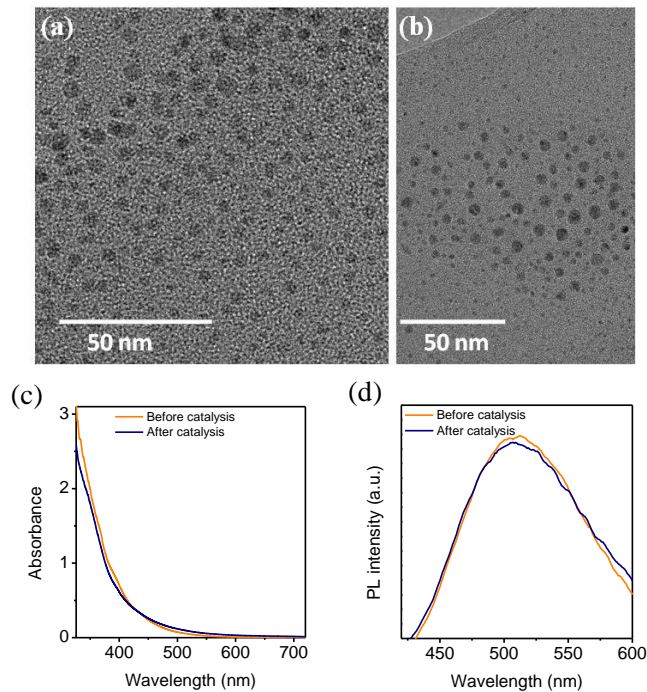


**Figure 3.4.10** (a, b) TEM images of the PE-CQDs collected after catalysis. UV-Vis absorption (c) and PL emission spectra (d) of the PE-CQDs before and after catalysis.

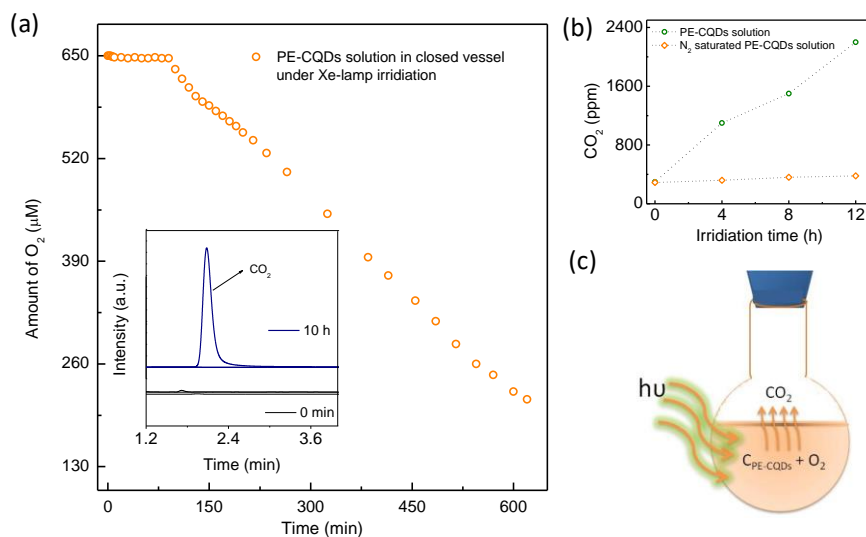


**Figure 3.4.11** (a) Plot of the total oxygen content in an aqueous PE-CQDs solution vs. irradiation time (Xe lamp, 450 W). Inset is the GC analysis of the gaseous product formed after light irradiation. (b) Amount of CO<sub>2</sub> produced with different illumination times in different atmospheres. (c) Schematic representation of the CO<sub>2</sub> formation during the measurements in the closed reaction vessel.

escape the vessel. Therefore, the air inside the vessel was analyzed before and after light-illumination. The gas chromatography analysis of the air inside the vessel confirmed the formation of carbon dioxide inside the vessel (**Figure 3.4.11a inset**). The CO<sub>2</sub> quantity steadily increases with irradiation time (**Figure 3.4.11b**) implying that the PE-CQDs self-oxidize to form CO<sub>2</sub> in the solution. To examine if the CO<sub>2</sub> formation is a consequence of aerial oxidation or at the expense of the oxygenated functional groups, we have further carried out the same experiment but first purging the PE-CQD solution thoroughly with N<sub>2</sub>. No appreciable amount for CO<sub>2</sub> was found to be forming in that case even after 12 h (**Figure 3.4.11b**) suggesting that the photo-oxidation of the PE-CQDs occurs using the dissolved or surface-adsorbed O<sub>2</sub> molecules (**Figure 3.4.11c**). It further implies that their photobleaching can be initiated or arrested by using an appropriate atmosphere. Thus, the PE-CQD photo-oxidation accelerates once the desired reaction is over, while on the other hand, it remains more-or-less intact while catalyzing it.

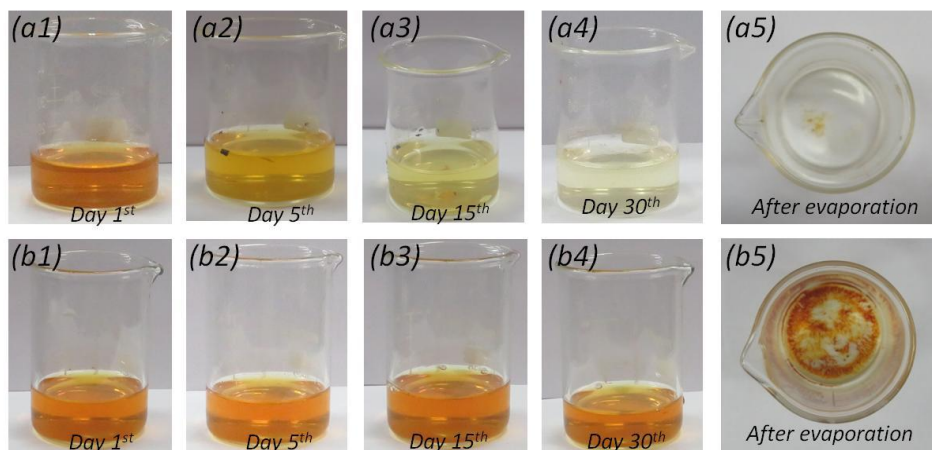


**Figure 3.4.12** Photographs of an aqueous PE-CQD solution (10 mg in 10 ml) irradiated under natural sunlight for several days (a1-a4) and a similar aqueous PE-CQDs solution kept in dark (b1-b4). (a5, b5) PE-CQDs recovered after the evaporation of the water-content.

A probable reason for not detecting the CO<sub>2</sub> formation by others so far is that the formation is a rather slow process and also, we could observe sufficient CO<sub>2</sub> only when using a larger quantity of CQDs. At the same time, the larger quantity makes it difficult to notice minute colour-changes. Therefore, we investigated as to what extent the photo-oxidation continues and does it stop at all.



As shown in **Figure 3.4.12**, we took 10 mg PE-CQD in 10 ml water in an open beaker and monitored it in natural sunlight for 38 days. The color slowly faded with each passing day and became nearly colorless on the 38<sup>th</sup> day. No color change was observed in a similar beaker kept in dark. The water-content was then allowed to be evaporated naturally, upon which it was observed that the PE-CQDs disappeared from the beaker exposed to sunlight, while those in the beaker kept in dark could be fully recovered. Therefore, we conclude that the PE-CQDs got oxidized to CO<sub>2</sub>. Uncommon photo-degradation pathways of self-sensitized photo-oxidation of organic pollutants in aqueous solution have been observed in certain compounds.<sup>51-53</sup> Therein, degradation is mediated by the *in-situ* generated reactive species such as singlet oxygen, superoxide anion radical, hydroxyl radical, etc. We too have demonstrated that the O<sub>2</sub> molecules adsorbed on PE-CQDs form superoxide radicals in presence of light, and this radical is responsible for the BA photo-oxidation reactions, as discussed above.

Therefore, given that the PE-CQDs are more stable in the presence of reactants, it seems that the superoxide radicals exert a choice between the reactant molecules or the carbon atoms on the PE-CQDs to react with and when left with no choice, it rapidly oxidizes the PE-CQDs to CO<sub>2</sub>. The self-sensitized photo-oxidation of CQDs is unique among nanomaterials as it does not leave behind any residue. No other nanomaterial is known to do so (or even organic molecules that completely convert to CO<sub>2</sub>), to the best of our knowledge. Considering that a PE-CQD eliminates itself rapidly from the system after completing its task, we propose that the process is termed as '*carbon-dot autophagy (CDA)*' (meaning 'self-devouring' or eating its own parts hungrily). CDA may be very useful because if the CQDs are exposed to or left unattended in the atmosphere, they will disappear with time and merge in air.

### 3.4.5 Conclusions

In summary, we have been able to convert waste polyethylene completely to carbon quantum dots in a greener way by a simple acid-mediated heat treatment method. The reagents used for this conversion may either be recovered back or leave behind no residue. The PE-CQDs enrich its solution with molecular oxygen harvested from the air with more than 1% of its weight under ambient conditions (and also induces a faster oxygen diffusion rate) which is higher than the same

expected from conventional materials such as zeolites, etc. The number of surface functional groups on PE-CQDs can be controlled by tuning the oxidation step of the carbon material derived from polyethylene to realize improved oxygen enrichment properties and photocatalytic oxidation efficiency. This was demonstrated using photo-oxidation of benzyl alcohols using ambient conditions, where the oxidation rate is higher than most state-of-the-art photocatalysts despite using the milder conditions. Similarly, the rate of pollutant dye degradation is at least five times better than other photocatalysts reported to date. Importantly, we observed that in the absence of the reactants, the PE-CQDs undergo self-sensitized photo-oxidation forming CO<sub>2</sub> and leading to its complete removal from the system. The extinction process that is unlike any other photocatalyst known to date, maybe termed as '*carbon-dot autophagy*' and is deemed advantageous as no separation process for the PE-CQDs is required. Particularly so because the separation of carbon-dots from a reaction mixture is tedious as they are highly soluble and also when they may be used for waste-water treatment from where recovery is not desired.

## Bibliography

1. C. M. Rochman, M. A. Browne, B. S. Halpern, B. T. Hentschel, E. Hoh, H. K. Karapanagioti, L. M. Rios-Mendoza, H. Takada, S. Teh and R. C. Thompson, *Nature*, 2013, **494**, 169.
2. W. W. Y. Lau, Y. Shiran, R. M. Bailey, E. Cook, M. R. Stuchtey, J. Koskella, C. A. Velis, L. Godfrey, J. Boucher, M. B. Murphy, R. C. Thompson, E. Jankowska, A. Castillo Castillo, T. D. Pilditch, B. Dixon, L. Koerselman, E. Kosior, E. Favoino, J. Gutberlet, S. Baulch, M. E. Atreya, D. Fischer, K. K. He, M. M. Petit, U. R. Sumaila, E. Neil, M. V Bernhofen, K. Lawrence and J. E. Palardy, *Science*, 2020, **369**, 1455–1461.
3. L. Jia, S. Evans and S. van der Linden, *Nat. Commun.*, 2019, **10**, 4582.
4. A. Löhr, H. Savelli, R. Beunen, M. Kalz, A. Ragas and F. Van Belleghem, *Curr. Opin. Environ. Sustain.*, 2017, **28**, 90–99.
5. K. Hamad, M. Kaseem and F. Deri, *Polym. Degrad. Stab.*, 2013, **98**, 2801–2812.
6. X. Jie, W. Li, D. Slocombe, Y. Gao, I. Banerjee, S. Gonzalez-Cortes, B. Yao, H. AlMegren, S. Alshihri, J. Dilworth, J. Thomas, T. Xiao and P. Edwards, *Nat. Catal.*, 2020, **3**, 902–912.
7. S. S. Lam, W. A. Wan Mahari, Y. S. Ok, W. Peng, C. T. Chong, N. L. Ma, H. A. Chase, Z. Liew, S. Yusup, E. E. Kwon and D. C. W. Tsang, *Renew. Sustain. Energy Rev.*, 2019, **115**, 109359.
8. R. D. Arjanggi and J. Kansedo, *J. Energy Inst.*, 2020, **93**, 934–952.
9. S. Mondal, E. K. Karthik, L. Sahoo, K. Chatterjee, S. Marappan and U. K. Gautam, *Nanoscale*, , DOI:10.1039/D0NR00266F.
10. S. Y. Lim, W. Shen and Z. Gao, *Chem. Soc. Rev.*, 2015, **44**, 362–381.
11. I. Shown, S. Samireddi, Y.-C. Chang, R. Putikam, P.-H. Chang, A. Sabbah, F.-Y. Fu, W.-F. Chen, C.-I. Wu, T.-Y. Yu, P.-W. Chung, M. C. Lin, L.-C. Chen and K.-H. Chen, *Nat. Commun.*, 2018, **9**, 169.
12. M. Semeniuk, Z. Yi, V. Poursorkhabi, J. Tjong, S. Jaffer, Z.-H. Lu and M. Sain, *ACS Nano*, 2019, **13**, 6224–6255.
13. A. Anand, B. Unnikrishnan, S.-C. Wei, C. P. Chou, L.-Z. Zhang and C.-C. Huang, *Nanoscale Horizons*, 2019, **4**, 117–137.
14. J. Ge, M. Lan, B. Zhou, W. Liu, L. Guo, H. Wang, Q. Jia, G. Niu, X. Huang, H. Zhou, X. Meng, P. Wang, C.-S. Lee, W. Zhang and X. Han, *Nat. Commun.*, 2014, **5**, 4596.
15. G. A. M. Hutton, B. Reuillard, B. C. M. Martindale, C. A. Caputo, C. W. J. Lockwood, J. N. Butt and E. Reisner, *J. Am. Chem. Soc.*, 2016, **138**, 16722–16730.
16. K. A. S. Fernando, S. Sahu, Y. Liu, W. K. Lewis, E. A. Gulians, A. Jafariyan, P. Wang, C. E. Bunker and Y.-P. Sun, *ACS Appl. Mater. Interfaces*, 2015, **7**, 8363–8376.
17. S. Guo, S. Zhao, X. Wu, H. Li, Y. Zhou, C. Zhu, N. Yang, X. Jiang, J. Gao, L. Bai, Y. Liu, Y. Lifshitz, S.-T. Lee and Z. Kang, *Nat. Commun.*, 2017, **8**, 1828.
18. G. S. Das, J. P. Shim, A. Bhatnagar, K. M. Tripathi and T. Kim, *Sci. Rep.*, 2019, **9**, 15084.
19. W. Wang, C. Damm, J. Walter, T. J. Nacken and W. Peukert, *Phys. Chem. Chem. Phys.*, 2016, **18**, 466–475.
20. M. L. Liu, L. Yang, R. S. Li, B. Bin Chen, H. Liu and C. Z. Huang, *Green Chem.*, 2017, **19**, 3611–3617.
21. A. V Longo, A. Sciortino, M. Cannas and F. Messina, *Phys. Chem. Chem. Phys.*, 2020, **22**, 13398–13407.
22. D. Tan, S. Zhou, Y. Shimotsuma, K. Miura and J. Qiu, *Opt. Mater. Express*, 2014, **4**, 213–219.

23. M. R. Hoffmann, S. T. Martin, W. Choi and D. W. Bahnemann, *Chem. Rev.*, 1995, **95**, 69–96.
24. X. Chen, L. Liu, P. Y. Yu and S. S. Mao, *Science (80-. )*, 2011, **331**, 746 LP – 750.
25. X. Wang, K. Maeda, A. Thomas, K. Takanabe, G. Xin, J. M. Carlsson, K. Domen and M. Antonietti, *Nat. Mater.*, 2009, **8**, 76–80.
26. S. R. Lingampalli, U. K. Gautam and C. N. R. Rao, *Energy Environ. Sci.*, 2013, **6**, 3589–3594.
27. S. Mondal, L. Sahoo, C. P. Vinod and U. K. Gautam, *Appl. Catal. B Environ.*, 2021, 119927.
28. G.-J. ten Brink, I. W. C. E. Arends and R. A. Sheldon, *Science*, 2000, **287**, 1636 – 1639.
29. G. Palmisano, V. Augugliaro, M. Pagliaro and L. Palmisano, *Chem. Commun.*, 2007, 3425–3437.
30. G. Palmisano, E. García-López, G. Marci, V. Loddo, S. Yurdakal, V. Augugliaro and L. Palmisano, *Chem. Commun.*, 2010, **46**, 7074–7089.
31. H. Kasap, C. A. Caputo, B. C. M. Martindale, R. Godin, V. W. Lau, B. V Lotsch, J. R. Durrant and E. Reisner, *J. Am. Chem. Soc.*, 2016, **138**, 9183–9192.
32. M. W. Kanan and D. G. Nocera, *Science*, 2008, **321**, 1072–1075.
33. F. Khan and J. H. Kim, *Sci. Rep.*, 2019, **9**, 10803.
34. S. Mondal, L. Sahoo, Y. Vaishnav, S. Mishra, R. S. Roy, C. P. Vinod, A. K. De and U. K. Gautam, *J. Mater. Chem. A*, 2020, **8**, 20581–20592.
35. M. L. Liu, B. Bin Chen, C. M. Li and C. Z. Huang, *Green Chem.*, 2019, **21**, 449–471.
36. H. Li, Z. Kang, Y. Liu and S.-T. Lee, *J. Mater. Chem.*, 2012, **22**, 24230–24253.
37. Y. Wang and A. Hu, *J. Mater. Chem. C*, 2014, **2**, 6921–6939.
38. J. B. DeCoste, M. H. Weston, P. E. Fuller, T. M. Tovar, G. W. Peterson, M. D. LeVan and O. K. Farha, *Angew. Chemie Int. Ed.*, 2014, **53**, 14092–14095.
39. H. Li, F. Qin, Z. Yang, X. Cui, J. Wang and L. Zhang, *J. Am. Chem. Soc.*, 2017, **139**, 3513–3521.
40. L. Ding, H. Chen, Q. Wang, T. Zhou, Q. Jiang, Y. Yuan, J. Li and J. Hu, *Chem. Commun.*, 2016, **52**, 994–997.
41. M. Zhang, C. Chen, W. Ma and J. Zhao, *Angew. Chemie*, 2008, **120**, 9876–9879.
42. F. Su, S. C. Mathew, G. Lipner, X. Fu, M. Antonietti, S. Blechert and X. Wang, *J. Am. Chem. Soc.*, 2010, **132**, 16299–16301.
43. H. She, H. Zhou, L. Li, L. Wang, J. Huang and Q. Wang, *ACS Sustain. Chem. Eng.*, 2018, **6**, 11939–11948.
44. Z. Wang, Y. Song, J. Zou, L. Li, Y. Yu and L. Wu, *Catal. Sci. Technol.*, 2018, **8**, 268–275.
45. S. Schünemann, M. van Gastel and H. Tüysüz, *ChemSusChem*, 2018, **11**, 1, 2057–2061.
46. W. Feng, G. Wu, L. Li and N. Guan, *Green Chem.*, 2011, **13**, 3265–3272.
47. X. Li, Y. Pi, Q. Hou, H. Yu, Z. Li, Y. Li and J. Xiao, *Chem. Commun.*, 2018, **54**, 1917–1920.
48. T. Jiang, C. Jia, L. Zhang, S. He, Y. Sang, H. Li, Y. Li, X. Xu and H. Liu, *Nanoscale*, 2015, **7**, 209–217.
49. A. Marjasvaara, M. Torvinen and P. Vainiotalo, *J. Mass Spectrom.*, 2004, **39**, 1139–1146.
50. H. Chen, C. Liu, M. Wang, C. Zhang, N. Luo, Y. Wang, H. Abroshan, G. Li and F. Wang, *ACS Catal.*, 2017, **7**, 3632–3638.
51. X. Xie, Z. Zhang, Y. Hu and H. Cheng, *Chem. Eng. J.*, 2018, **334**, 1242–1251.
52. M. Krieg and D. G. Whitten, *J. Photochem.*, 1984, **25**, 235–252.
53. M. P. Fasnacht and N. V Blough, *Environ. Sci. Technol.*, 2002, **36**, 4364–4369.

## CHAPTER 3.5

### Conclusions of part 1 & future directions

#### Conclusions

Plastic pollution is a serious threat to the environment as it is not bio-degradable. The reduction of plastic-waste has emerged as a research priority, leading to many innovative approaches to convert them into useful materials such as liquid fuels and related materials. Therefore, the development of carbon-based semiconductor photocatalyst (CQDs) from waste plastic with surface adsorbed O<sub>2</sub> is highly demanding. Chapter 3.2 and 3.3 are focused on the strategies to convert plastics into O<sub>2</sub> enriched CQDs and the effect of functional groups on O<sub>2</sub> adsorption in CQDs. In addition, the effect of light energy on O<sub>2</sub> enrichment has been also investigated. Chapter 3.4 discussed the improved synthesis of CQDs and the self-oxidation of CQDs into CO<sub>2</sub>. The key findings of Chapter 3 of the thesis are summarized below.

Chapter 3.2 describes the noble large-scale synthesis strategy of CQDs from waste-polyethylene. This is an interesting example of chemical transformation from an alkane to graphene where acid-mediated dehydrogenation of a PE backbone results in the formation of alkenes, which then undergoes cyclization reaction forming benzene derivatives and finally tiny functionalized graphene chunks. Furthermore, it was found that in the presence of these PE-CQDs, the ability of water to dissolve and diffuse molecular oxygen significantly increases. Therein, the PE-CQDs adsorbs molecular O<sub>2</sub> from the air with more than 1% of its weight under ambient conditions which is higher than the same expected from conventional materials such as zeolites, etc. We show that such O<sub>2</sub> enrichment is very useful in photocatalytic oxidation reactions because it offers the possibility of doing such reactions in the air, without the need of creating an oxygen-rich environment. Therefore, it was observed that when the CQDs were used to catalyze photo-oxidation of aromatic alcohols by sunlight, the efficiency was higher than in previous instances despite those employing high oxygen pressure, temperature, and expensive materials.

Chapter 3.3 describes that surface-adsorbed oxygen molecules on CQDs are extremely high, aided by specific combinations of its surface functional groups that lead to profound

photocatalytic efficiency for oxidative chemical transformations. The apparent quantum efficiency for selective oxidation of benzylamine was found to be ~35% along with a reaction rate that is significantly faster than the existing photocatalysts, including those using expensive noble metals, an oxygenated atmosphere, and harsh reaction conditions. It was also established that the concentration of adsorbed O<sub>2</sub> on CQDs surface decreases in the presence of light (called as ‘hypoxia’) and the same can be tuned by using an external light source of different wavelengths so that a CQDs solution can have different oxygen contents at different portions of the solution. The effect arises due to the modulation of charge-transfer between the CQDs and the adsorbed O<sub>2</sub> molecules in the presence of light that generates excitons in the CQDs and can make them behave as charged particles.

Chapter 3.4 narrates the complete conversion of waste polyethylene into CQDs in a greener way by a simple acid-mediated heat treatment method. In doing so, the nature of surface functional groups on PE-CQDs and their sizes can be controlled by tuning the oxidation step of the carbon material derived from polyethylene to realize improved oxygen enrichment properties and therefore enhanced photocatalytic benzyl alcohol oxidation efficiency at ambient conditions. Also, the rate of pollutant dye degradation is at least five times better than any other photocatalyst reported to date. Importantly, we observed that in the absence of the reactants, the PE-CQDs undergo self-sensitized photo-oxidation forming CO<sub>2</sub> and leading to its complete removal from the system. The extinction process is unlike any other photocatalyst known to date, and termed as ‘*carbon-dot autophagy*’, which is deemed advantageous as no separation process for the PE-CQDs is required.

Even though, I cannot give a cost-benefit analysis of our process at this stage, I feel it is fairly advantageous while comparing CQD synthesis by other approaches. This is for several reasons. First that the synthesis described in Chapter 3.4 uses H<sub>2</sub>SO<sub>4</sub> and a few drops of H<sub>2</sub>O<sub>2</sub> only. Since H<sub>2</sub>O<sub>2</sub> decomposes and CQDs are extracted, the H<sub>2</sub>SO<sub>4</sub> can be repeatedly used. Second, the purification process is significantly simpler and faster (as while PE-CQD synthesis is impurity free) because simple evaporation of the solvent gives back the PE-CQD powder. In comparison, the literature processes use either column chromatography or dialysis membranes, where very large amounts of solvents have to be used and process time is very long. Besides, a large quantity of solvent has to be removed by evaporation to retrieve the CQDs.

## Future directions

The development of strategies to convert waste-polyethylene into useful carbon-based materials or fuel is generating extensive research interest in the present days. However, the limited approach for the conversion of plastics into useful materials hinders its use in industrial applications. Therefore, our new strategy to convert waste-polyethylene into O<sub>2</sub> enriched CQDs (gram-scale), provides a platform in the field of heterogeneous photocatalysis. Besides, the O<sub>2</sub> enrichment properties of CQDs open a new direction in the controlled oxidation of many organic compounds, in which molecular O<sub>2</sub> harvested from air acts as the primary oxidizing source.

It will now be important to examine the possibility of converting much larger quantities of waste polyethylene (kilogram quantities) for use in industrial-scale applications. In addition, even though polyethylene has been used in this studies, the scope of the conversion for other waste plastics such as PET, polystyrene, PVC, etc. can be investigated.

Next, the extension of this new method by adding different hetero-atoms to the CQDs synthesis by adding suitable precursors along with the waste-polyethylene can become a promising approach to get hetero-atom doped CQDs. In addition, the use of different acids (such as HNO<sub>3</sub>) along with H<sub>2</sub>SO<sub>4</sub> might result in different surface modified CQDs with different capabilities for surface adsorbed molecular oxygen.

The photoluminescence quantum yield (QY) of the PE-CQDs is low compared to many other CQDs reported in the literature, limiting its prospects in metal atom sensing and imaging applications.<sup>1-3</sup> Therefore, it will be interesting to investigate the PL properties by controlling the synthesis steps or by post-processing to increase the QY.<sup>4-6</sup>

Apart from their use in benzyl alcohol and benzylamine oxidation reactions, these PE-CQDs with the uniqueness of oxygen enrichment in solution may offer a much more facile route for various other oxidative organic transformation reactions such as photo-oxidation of cyclohexane, benzene etc.

The absorption of the visible fraction of the solar light by the PE-CQDs is limited to ~500 nm (and higher energy). This can be further tuned towards the lower energy visible light by

changing the size of the CQDs. Besides, CQDs in conjugation with plasmonic Au/Ag NPs may further enhance the visible light absorption via LSPR induced ‘hot-electron injection’.

## Bibliography

1. D. Yoo, Y. Park, B. Cheon and M.-H. Park, *Nanoscale Res. Lett.*, 2019, **14**, 1–13.
2. P. Devi, A. Thakur, S. K. Bhardwaj, S. Saini, P. Rajput and P. Kumar, *J. Mater. Sci. Mater. Electron.*, 2018, **29**, 17254–17261.
3. W. Wei, C. Xu, J. Ren, B. Xu and X. Qu, *Chem. Commun.*, 2012, **48**, 1284–1286.
4. L. Hu, Y. Sun, S. Li, X. Wang, K. Hu, L. Wang, X. Liang and Y. Wu, *Carbon N. Y.*, 2014, **67**, 508–513.
5. Y. Zhuo, H. Miao, D. Zhong, S. Zhu and X. Yang, *Mater. Lett.*, 2015, **139**, 197–200.
6. W. U. Khan, D. Wang, W. Zhang, Z. Tang, X. Ma, X. Ding, S. Du and Y. Wang, *Sci. Rep.*, 2017, **7**, 1–9.



## Part 2

### *Novel syntheses of g-C<sub>3</sub>N<sub>4</sub> based highly active photocatalysts*



## CHAPTER 4.1

### Introduction

#### 4.1.1 Graphitic C<sub>3</sub>N<sub>4</sub>

Two-dimensional (2D) materials have shown tremendous application in various fields such as energy storage and conversion, (opto)electronics, catalysis, sensors, and biomedicine due to their unique properties such as exceptional thermal and electric conductivity, ultrahigh carrier mobility, large specific surface area, and excellent optical transparency.<sup>1-6</sup> 2D nanomaterials are composed of thin layers having thicknesses of at least one atomic layer.<sup>7</sup> Recently, 2D metal-free semiconductor photocatalysts have gained significant interest in the field of renewable energy harvesting, catalysis, and environmental remediation-related applications due to their high surface-to-volume ratio. Graphene, graphene-oxide, g-C<sub>3</sub>N<sub>4</sub>, layered double hydroxide, hexagonal boron nitride, transition metal dichalcogenides etc., are few examples of 2D nanomaterials.

The development of g-C<sub>3</sub>N<sub>4</sub> based semiconductor photocatalysts is anticipated to assist in overcoming the issues of increase in fossil fuel depletion and environmental threats arising from the combustion of fossil fuels. Graphitic carbon nitride (g-C<sub>3</sub>N<sub>4</sub>) has gained attention in 2009, after demonstrating their efficiency in photocatalytic H<sub>2</sub> evolution reaction by Wang et al.<sup>8</sup> Non-toxicity, earth-abundant nature, excellent chemical and thermal stability, relative ease of synthesis, visible-light absorption, appropriate band-structure and electronic properties make this material a suitable photocatalyst to drive diverse chemical reaction.

#### 4.1.2 History of Carbon Nitrides

In the early 19th century, Jöns Jakob Berzelius has synthesized carbon nitride material through the heating of Hg(SCN)<sub>2</sub>. Later, in 1834, Justus von Liebig has identified several compounds which are triazine and heptazine-based moieties such as melamine, melam, melem, and melon as shown in **Figure 4.1.1**.<sup>9</sup> His synthesis method was based on the pyrolysis of mixtures of ammonium chloride and potassium thiocyanate, yielding a yellow, insoluble, and amorphous product named

‘melon’ which is a linear polymer of tri-*s*-triazine moiety interconnected through secondary nitrogen.<sup>10</sup> However, the utilization of g-C<sub>3</sub>N<sub>4</sub> in the field of heterogeneous catalysis has started around 15 years ago in 2006.<sup>11</sup> In 2009, Wang et al. have discovered g-C<sub>3</sub>N<sub>4</sub> as a non-metal semiconductor photocatalyst for the generation of H<sub>2</sub> from H<sub>2</sub>O, which potentially switched the research exploration from inorganic to polymeric conjugated semiconductor photocatalysts.

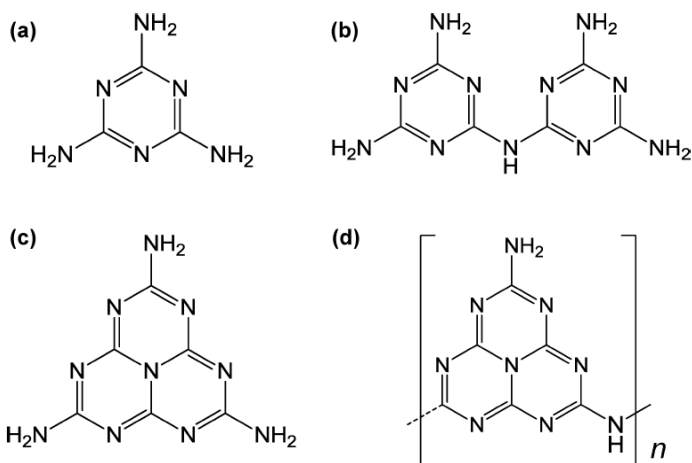


**Figure 4.1.1** C and N containing materials: (a) melamine, (b) melam, (c) melem, and (d) melon obtained after the thermolysis of mercury (II) thiocyanate as presented by Liebig. Adapted with permission from [10].

### 4.1.3 Structure of carbon nitride

Carbon nitride can be found in the form of several allotropes such as  $\alpha$ -C<sub>3</sub>N<sub>4</sub>,  $\beta$ -C<sub>3</sub>N<sub>4</sub>, pseudocubic-C<sub>3</sub>N<sub>4</sub>, cubic-C<sub>3</sub>N<sub>4</sub>, and graphitic-C<sub>3</sub>N<sub>4</sub> (g-C<sub>3</sub>N<sub>4</sub>), having different properties.<sup>12</sup> First-principle density functional theory (DFT) calculation showed that g-C<sub>3</sub>N<sub>4</sub> has the lowest total energy (more stable under ambient condition) among all carbon nitride and hence, various forms of g-C<sub>3</sub>N<sub>4</sub> were studied, including *s*-triazine-based hexagonal structure, tri-*s*-triazine (heptazine)-based structure, and *s*-triazine-based orthorhombic structure and it was found that among all, the tri-*s*-triazine-based structure was the most stable one. g-C<sub>3</sub>N<sub>4</sub> is a conjugated system with a polymeric network, which is comprising of tri-*s*-triazine or *s*-triazine units interconnected via tertiary amines (**Figure 4.1.2**) forming a two-dimensional (2D) structure consisting of covalently linked carbon and nitrogen atoms in sp<sup>2</sup> hybridized form.<sup>13,14</sup>

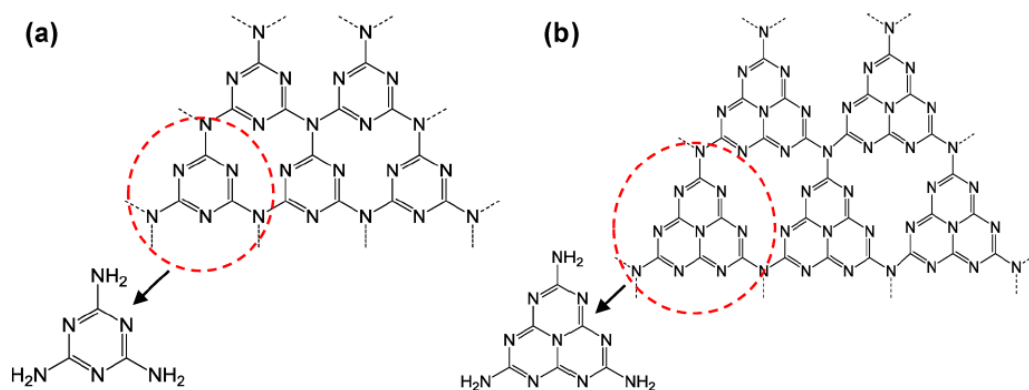


**Figure 4.1.2** (a) Triazine and (b) tri-*s*-triazine (heptazine) structures of  $g\text{-C}_3\text{N}_4$ . Adapted with permission from [10].

It is a layered structure and, in each layer, triazine or tri-*s*-triazine units are connected through the nitrogen atoms. In the structure, two non-equivalent C atoms and three non-equivalent N atoms are present, labelled as C1, C2, N1, N2, and N3 respectively as shown in **Figure 4.1.3a**.<sup>15</sup> C1, C2, N1, and N3 are three-coordinated and N2 is two coordinated. In a  $g\text{-C}_3\text{N}_4$  layer, atoms are arranged in a honeycomb configuration, connected through strong covalent bonds, and a weak Vander Waals force is present between the different layers. The bulk  $g\text{-C}_3\text{N}_4$  is formed by the “AB-stacking” of various layers. In addition, DFT calculations revealed that the valance- band (VB) edge of  $g\text{-C}_3\text{N}_4$  mainly consists of the N 2p states whereas the conduction band (CB) edge is composed of hybridization of the C 2p and N 2p states (**Figure 4.1.3b**).<sup>16</sup> Therefore, photogenerated holes appear at the N sites. Due to the hybridization of the N 2p and C 2p states in CB, the photogenerated electrons suffer from the high recombination of electron-hole pairs, which deteriorates their photocatalytic performance.

#### 4.1.4 Optical properties of $g\text{-C}_3\text{N}_4$

Considering their extensive use in photocatalysis and prolific catalytic activity, the optical properties of the  $g\text{-C}_3\text{N}_4$ , as compared to the other properties, have been investigated in great depths in the last decade. In general, the optical properties of disordered carbon-based materials are associated with the transitions in the  $\pi$  bonding and  $\pi^*$  antibonding states acting in the range of near-ultraviolet-visible energy.<sup>17</sup> The photoluminescence (PL) property of  $g\text{-C}_3\text{N}_4$  is mainly

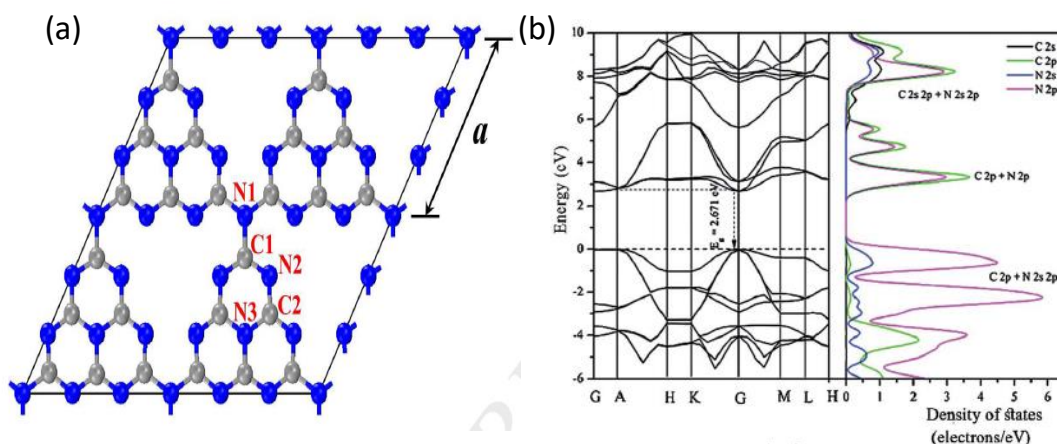


**Figure 4.1.3** (a) Geometric structures of a single layer of  $g\text{-C}_3\text{N}_4$ . The blue and gray balls are nitrogen and carbon atoms, respectively. (b) The energy-band structure diagram and DOS of  $g\text{-C}_3\text{N}_4$ . Adapted with permission from [15,16].

affected by the size of the  $sp^2$  C-N clusters and the lone-pair (LP) of electrons present on N. There occurs the formation of the LP energy state as the LP electrons are located near the  $sp^2$  C-N  $\pi$  VB and do not take part in hybridization with carbon.<sup>18,19</sup> The PL peak originates from multiple transitions involving the lone pair of nitrogen, the  $\pi$ ,  $\pi^*$ ,  $\sigma$ , and  $\sigma^*$  orbitals, and is usually centered around 440-470 nm with an average radiative recombination lifetime of 1-10 ns. The  $g\text{-C}_3\text{N}_4$  absorbs in the visible range with an optical band-gap of 2.7 eV. Therefore, the tunable PL properties of the  $g\text{-C}_3\text{N}_4$  materials are proposed as follows:

(a) The polymeric network of the  $g\text{-C}_3\text{N}_4$  extends by connecting more tri-s-triazine, as the reaction temperature increases and the polymeric domains become bigger in size, and therefore optical band-gap decreases at high synthesis temperature.

(b) During prolonged thermal condensation, the denser packing of the  $sp^2$  hybridized aromatic cluster is formed, and therefore a stronger orbital overlap appears which leads to a decrease in the band-gap of  $g\text{-C}_3\text{N}_4$ .

In addition to that, it was also found that some distortion of the  $g\text{-C}_3\text{N}_4$  structure may also enhance the optical properties by allowing more  $n$  to  $\pi^*$  electronic transitions, leading to a new visible light absorption band beyond 460 nm. It is noteworthy that the monolayer distorted  $g\text{-C}_3\text{N}_4$

exhibits an enhanced visible light absorption with a new absorption band centered at  $\sim 450$  nm.<sup>10</sup> Besides, the quantum confinement effect of nanosized  $g\text{-C}_3\text{N}_4$  results in various extents of blue-shifts of PL peaks for samples prepared at temperatures of 650, 675, and 700 °C. A new absorption

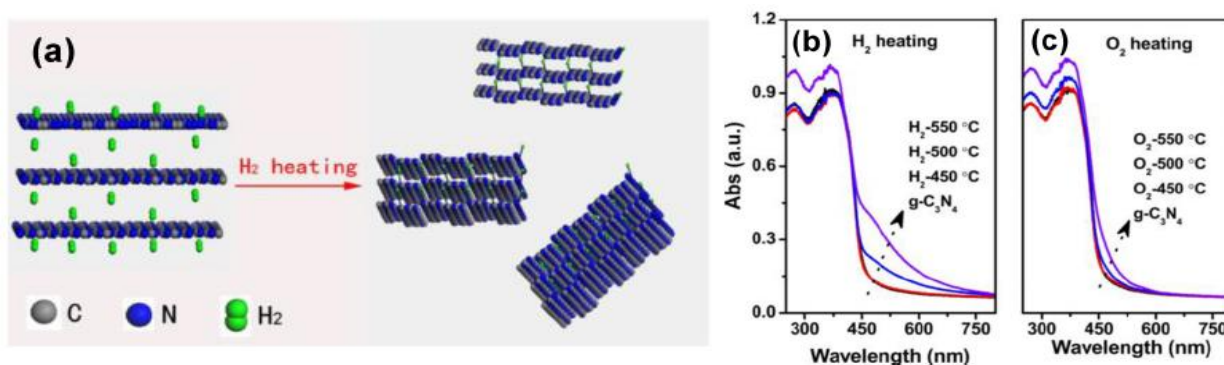


**Figure 4.1.4** (a) Synthesis process of layer distortion of  $g\text{-C}_3\text{N}_4$  via  $\text{H}_2$  heating. UV-Vis absorption spectra of modified  $g\text{-C}_3\text{N}_4$  samples synthesized by heating the pristine  $g\text{-C}_3\text{N}_4$  under (b)  $\text{H}_2$  and (c)  $\text{O}_2$  atmosphere. Adapted with permission from [20].

peak at  $\sim 500$  nm was also observed at temperatures above 650 °C, which was due to the  $n$  to  $\pi^*$  transitions. Ho et al. utilized an  $\text{H}_2$  and  $\text{O}_2$  purge post calcination process to synthesize structurally distorted  $g\text{-C}_3\text{N}_4$  layers (**Figure 4.1.4**) having tunable optical properties.<sup>20</sup> The  $\text{H}_2$  modified  $g\text{-C}_3\text{N}_4$  in comparison to the  $\text{O}_2$  modified  $g\text{-C}_3\text{N}_4$  shows an additional optical absorption  $\sim 460$  nm which suggest that a smaller size of the H atom can easily access the channels among layers as compared to the O-atom which enhances the interaction with atoms present in  $g\text{-C}_3\text{N}_4$ . In general, when H atoms form a bond with the N atoms present in the  $g\text{-C}_3\text{N}_4$  network, it results in the formation of amino functional groups. The presence of amino groups supported a stronger H-bonding interaction between the layers of  $g\text{-C}_3\text{N}_4$ . Since in  $g\text{-C}_3\text{N}_4$ , the interplanar layer distance is 0.32 nm, which is much larger than the N-H bond length in the amino group (0.1 nm), it enables the formation of the amino group in between the layers. As a result of better hydrogen bonding interaction, distortion in the planar arrangement of  $g\text{-C}_3\text{N}_4$  occurs consequently forming lone pairs on N atoms present at the edges in the tri-s-triazine rings inside the  $\pi$ -conjugated system, resulting in the  $n$  to  $\pi^*$  electronic transitions.

### 4.1.5 Synthesis of g-C<sub>3</sub>N<sub>4</sub>

Crystalline g-C<sub>3</sub>N<sub>4</sub> can be easily prepared using nitrogen-containing precursor materials such as urea, thiourea, cyanamide, dicyandiamide, and melamine via a simple one-step thermal process as shown in **Figure 4.1.5**.<sup>10</sup> However, the g-C<sub>3</sub>N<sub>4</sub> obtained from the above process is bulk material with a very low surface area (less than 10 m<sup>2</sup>/g). The photocatalytic activities of the g-C<sub>3</sub>N<sub>4</sub> materials synthesized from different precursors are quite different and not easily comprehensible. Besides, the correlation of their photocatalytic activity with the physicochemical properties such as morphology, specific surface area, and optical properties is also unclear. In this context, Zhang et al. have employed the synthesis of porous g-C<sub>3</sub>N<sub>4</sub> from urea, thiourea, and dicyandiamide, suggesting the surface area and porous nature are the deciding parameters for enhanced photocatalytic H<sub>2</sub> evolution from water-splitting under visible light.<sup>21</sup> In another study, Martha et al. have prepared g-C<sub>3</sub>N<sub>4</sub> from urea, melamine and using a mixture of both, and studied the photocatalytic activities.<sup>22</sup> However, the trends were different and they argued that the charge

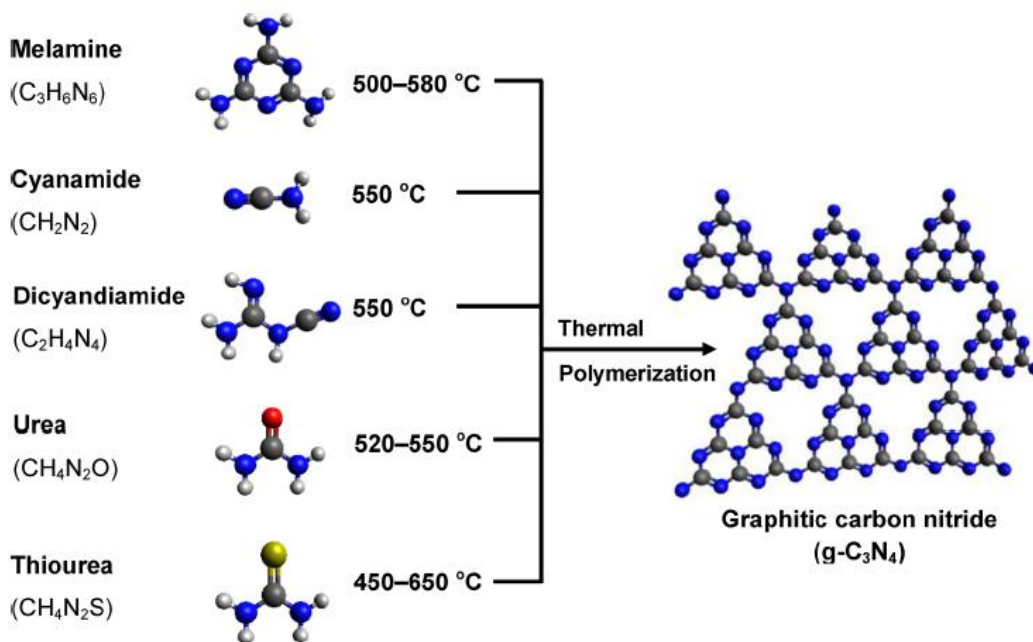


**Figure 4.1.5** Schematic representation of the synthesis process of g-C<sub>3</sub>N<sub>4</sub> by thermal polymerization of several precursors.<sup>23,24,25,26</sup> The black, white, blue, red, and yellow balls denote C, H, N, O, and S atoms, respectively. Adapted with permission from [10].



separation is the main factor for the high catalytic activity, not the surface area. Likewise, Yan et al. have prepared g-C<sub>3</sub>N<sub>4</sub> photocatalyst by heating melamine at various calcination temperatures and observed an increase in the C/N ratio and smaller bandgap in g-C<sub>3</sub>N<sub>4</sub> with an increase in the calcination temperature.<sup>23</sup> Mo et al. investigated the effect of calcination temperature in the crystal structure, morphology, and band-gap tuning in g-C<sub>3</sub>N<sub>4</sub> photocatalyst prepared from the thermal treatment of melamine.<sup>27</sup> It was noticed that at 450°C, the material shows the presence of melem-like derivatives in PXRD pattern, whereas at 500°C pure g-C<sub>3</sub>N<sub>4</sub> was formed and a further increase in temperature led to the structural loss of the parent g-C<sub>3</sub>N<sub>4</sub>.

2D g-C<sub>3</sub>N<sub>4</sub> has attracted attention in photocatalysis due to their exceptionally high surface area, high light absorption coefficient, high charge mobility, and improvable exciton separation. Niu et al. (**Figure 4.1.6A**) have developed a simple route to prepare g-C<sub>3</sub>N<sub>4</sub> nanosheets (NSs) from the bulk g-C<sub>3</sub>N<sub>4</sub> by thermal oxidation (etching) process in air.<sup>28</sup> The thickness of the nanosheets is about 2 nm with an increased bandgap compared to the bulk g-C<sub>3</sub>N<sub>4</sub>. The basic of this route is the

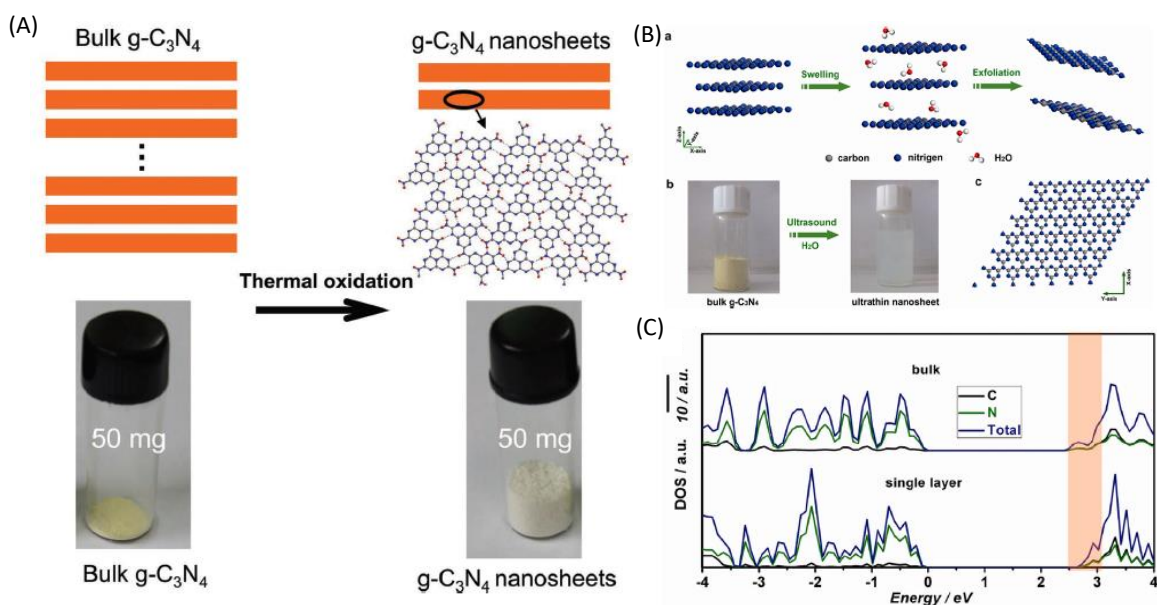


**Figure 4.1.6** (A) Schematic of the structures of the bulk g-C<sub>3</sub>N<sub>4</sub> and the g-C<sub>3</sub>N<sub>4</sub> nanosheets. A comparison of the volume of 50 mg powder of bulk g-C<sub>3</sub>N<sub>4</sub> and g-C<sub>3</sub>N<sub>4</sub> nanosheets is provided. (B) Schematic illustration of liquid-exfoliation route from bulk g-C<sub>3</sub>N<sub>4</sub> to ultrathin nanosheets (a). Photograph of bulk and suspension of ultrathin g-C<sub>3</sub>N<sub>4</sub> nanosheets (b). A theoretically crystal structure of the g-C<sub>3</sub>N<sub>4</sub> projected along the z-axis (c). (C) Calculated DOS of the single-layered g-C<sub>3</sub>N<sub>4</sub> NS and bulk g-C<sub>3</sub>N<sub>4</sub>. The shadow part indicates the increase of DOS at the CB edge of the g-C<sub>3</sub>N<sub>4</sub> NS. Adapted with permission from [28,29].

hydrogen bond association between two melon units present in layers that are unstable during the thermal aerial oxidation process, leading to a decrease in the thickness of the sheets. Moreover, the g-C<sub>3</sub>N<sub>4</sub> nanosheets exhibited higher photocatalytic H<sub>2</sub> evolution for water-splitting as compared to the bulk powder. The higher activity in nanosheets originated from their higher surface area (306 m<sup>2</sup>/g), longer lifetime of the photoexcited carriers, and enhanced electron transfer ability. In another study, Zhang et al. developed a greener method to prepare ultrathin g-C<sub>3</sub>N<sub>4</sub> from the bulk g-C<sub>3</sub>N<sub>4</sub> using a simple liquid exfoliation method.<sup>29</sup> The sonication of the bulk g-C<sub>3</sub>N<sub>4</sub> in water solvent (0.15 mg/mL) led to the formation of transparent ultrathin g-C<sub>3</sub>N<sub>4</sub> sheets which are very stable in both alkali and acidic medium and not aggregate even after several months (**Figure 4.1.6B**). From the DFT calculations, it was revealed that single-layered g-C<sub>3</sub>N<sub>4</sub> nanosheets showed an obvious increase of density of states (DOS) at the CB edge with respect to the bulk g-C<sub>3</sub>N<sub>4</sub>, which indicates the presence of more charge carriers in ultrathin g-C<sub>3</sub>N<sub>4</sub> nanosheets (**Figure 4.1.6C**). Moreover, the ultrathin g-C<sub>3</sub>N<sub>4</sub> NSs exhibited enhanced photo-absorption and extremely high photoluminescence QY up to 19.6%.

0D g-C<sub>3</sub>N<sub>4</sub> nanomaterials such as quantum dots have also received a great deal of interest in photocatalysis. Unlike 2D sheets which can be as big as a micrometer even though only of nanometer thickness, the 0D g-C<sub>3</sub>N<sub>4</sub> is just a few nanometer in size. Wang et al. demonstrated a controllable route for direct conversion of 3D bulk g-C<sub>3</sub>N<sub>4</sub> into 2D nanosheets, 1D nanoribbons, and 0D g-C<sub>3</sub>N<sub>4</sub> quantum dots by a thermal/chemical etching method.<sup>30</sup> The thermal treatment of bulk g-C<sub>3</sub>N<sub>4</sub> results in the formation of nanosheets. Next, acidic etching of the nanosheets produces nanoribbons, and finally, hydrothermal treatment of nanoribbon results in g-C<sub>3</sub>N<sub>4</sub> quantum dots formation with an average diameter of 6.7 nm. In another study, Wang et al. have designed a heterostructure of Sb<sub>2</sub>S<sub>3</sub>/ultrathin g-C<sub>3</sub>N<sub>4</sub> sheets embedded with g-C<sub>3</sub>N<sub>4</sub> quantum dots (CNS) and studied the photocatalytic activity.<sup>31</sup> It was inferred that the CNS composite has an enhanced light absorption and fast electron transfer compared to the Sb<sub>2</sub>S<sub>3</sub>/ultrathin g-C<sub>3</sub>N<sub>4</sub> sheets. Furthermore, the CNS composite shows a significant photocatalytic activity for photo-degradation of methyl orange (MO) in the near-infrared (NIR) range due to the efficient separation of electron-hole pairs, improved absorption in the NIR wavelength range, and the up-converted photoluminescence property of g-C<sub>3</sub>N<sub>4</sub> quantum dots.

One-dimensional (1D) g-C<sub>3</sub>N<sub>4</sub> nanostructures are also promising photocatalytic candidates as compared to the bulk due to their intrinsic light-harvesting properties. The increase in optical absorbance in the case of the 1D nanostructure is primarily due to the high aspect ratio (length:diameter), which allows more interaction with light. Moreover, it also exhibits fast charge-carrier transport through long distance. The above desirable properties make them suitable for photocatalysis applications. Pawar et al. demonstrated a template-free synthesis strategy to make nanoporous g-C<sub>3</sub>N<sub>4</sub> microrods at room temperature using concentrated sulphuric acid.<sup>32</sup> The acid ions intercalation and uneven bonding within bulk particles induced 1D morphology formation with interconnected nanopores. The porous 1D microrod structure exhibited remarkable photocatalytic performance (five times higher) under visible light for methylene blue (MB) degradation as compared to the bulk g-C<sub>3</sub>N<sub>4</sub>. The improved catalytic activity was attributed to the efficient separation of excitons and fast transport, more active sites for the catalytic reaction, and a broad spectral absorbance range in case of nanoporous g-C<sub>3</sub>N<sub>4</sub> microrods. In another study, Zhou et al. prepared 1D g-C<sub>3</sub>N<sub>4</sub> microtubes via a template-free simple hydrothermal-assisted thermal polymerization of cyanuric acid-melamine complex under an inert atmosphere.<sup>33</sup> The as-synthesized 1D g-C<sub>3</sub>N<sub>4</sub> microtubes showed improved photocatalytic H<sub>2</sub> evolution under visible light, which was nearly 3.1 times higher than the bulk g-C<sub>3</sub>N<sub>4</sub>. The improved catalytic activity of the 1D g-C<sub>3</sub>N<sub>4</sub> microtubes originates from the large surface-area of the 1D tubular structure, which provided more active sites for H<sup>+</sup> reduction and facilitated the charge transfer processes.

Furthermore, three-dimensional (3D) nanomaterials open an extensive and complex design for developing a new catalyst system. Tian et al. described a novel strategy to prepare mesoporous ultrathin 3D g-C<sub>3</sub>N<sub>4</sub> via precursor re-crystallization.<sup>34</sup> The 3D g-C<sub>3</sub>N<sub>4</sub> showed higher photocatalytic H<sub>2</sub> evolution under visible light irradiation as compared to conventional thermal-derived g-C<sub>3</sub>N<sub>4</sub>. In another study, Luo et al. synthesized 3D porous g-C<sub>3</sub>N<sub>4</sub> with high yield by both thermal oxidation and acid treatment.<sup>35</sup> The porous 3D g-C<sub>3</sub>N<sub>4</sub> exhibited an enhanced rate of H<sub>2</sub> evolution compared to the pristine g-C<sub>3</sub>N<sub>4</sub>. The significant increase in activity was attributed to the improved surface areas and facile separation of charge carriers and migration efficiency.

#### **4.1.6 Applications of g-C<sub>3</sub>N<sub>4</sub>**

The unique optical and electronic properties, exceptional chemical and thermal stability, ultrahigh carrier mobility, and large surface area of g-C<sub>3</sub>N<sub>4</sub> enable their application in various fields such as

energy storage and conversion, (opto)electronics, photocatalysis, sensors, bio-imaging and biomedicine. Among all, the photocatalysis field has gained tremendous research attention in recent years.

**Photocatalytic applications:** Their above-mentioned unique property makes  $g\text{-C}_3\text{N}_4$  a suitable material for efficient photocatalysis under visible light irradiation for various reactions (**Figure 4.1.7**).<sup>10</sup> The photocatalytic efficiency of  $g\text{-C}_3\text{N}_4$  is inhibited by the fast rate of photo-generated electron-hole recombination and low visible light absorption ability. However, to date, several strategies have been employed to enhance the photocatalytic activity and stability, such as noble metal incorporation as co-catalyst, plasmonic metal loading, and the combination with other semiconductor photocatalysts. For example, Cao et al. (**Figure 4.1.8a**) demonstrated that loading of Pt nanoparticles on the  $g\text{-C}_3\text{N}_4$  surfaces with different shapes has a significant influence on the rate of  $\text{H}_2$ -evolution.<sup>36</sup> The Pt nanoparticles with different shapes (spherical, cubic, and octahedral) were ex-situ deposited on the  $g\text{-C}_3\text{N}_4$  surface using a colloidal adsorption-desorption route. Among all different shaped Pt nanoparticles, spherical shape nanoparticle composite exhibited the highest catalytic activity due to the favourable exposed facets, energies developed by the spherical shape.

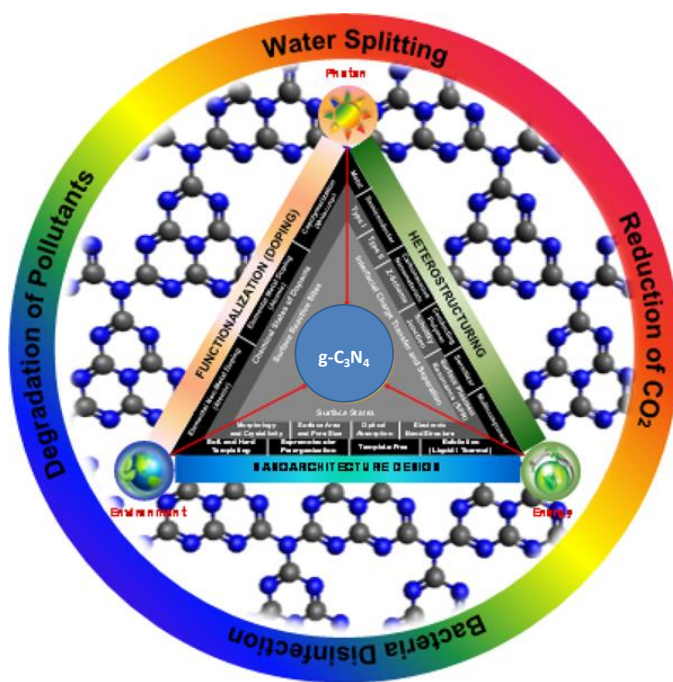


**Figure 4.1.7** Various photocatalytic applications of  $g\text{-C}_3\text{N}_4$  photocatalyst. Adapted with permission from [10].

Li et al. found that the photocatalytic H<sub>2</sub> evolution rate under visible light increased when g-C<sub>3</sub>N<sub>4</sub> surface was uniformly loaded by Pt-nanoparticles, which demonstrate that the enhancement in activity is possible due to the trapping of the photogenerated electrons by Pt nanoparticles.<sup>37</sup> The Pt-nanoparticles acted as co-catalysts.

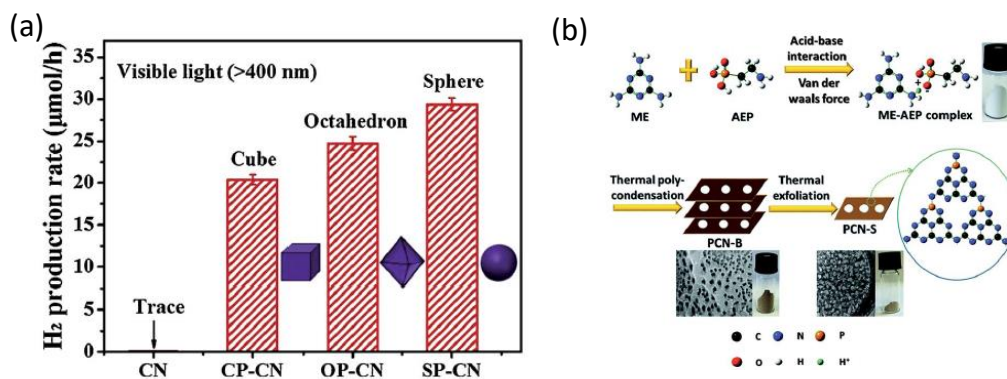


**Figure 4.1.8** (a) Photocatalytic H<sub>2</sub> evolution activities of bare g-C<sub>3</sub>N<sub>4</sub> and g-C<sub>3</sub>N<sub>4</sub> modified by Pt co-catalysts with different shapes under visible light. (b) Synthesis procedure of porous PCN-S. Adapted with permission from [36,38].

Ran et al. (**Figure 4.1.8b**) prepared porous P-doped g-C<sub>3</sub>N<sub>4</sub> nanosheets (PCN-S) by simple thermal exfoliation strategies and performed photocatalytic water-splitting under visible light.<sup>38</sup> The as-synthesized PCN-S shows an outstanding photocatalytic H<sub>2</sub>-production activity of 1596 μmol h<sup>-1</sup> g<sup>-1</sup> and an AQE of 3.56% at 420 nm. This excellent photocatalytic activity is suggested to have originated from the mid-gap states (-0.16 V vs. SHE) created by P-doped conjugated system, which significantly extends the light-responsive wavelength region up to 557 nm. The experimental studies were supported by and the density functional theory. Besides, the macroporous nanosheet morphology promotes the mass transfer process which further enhances the photocatalytic performance. Similarly, Zhou et al. described the synthesis of nitrogen-doped g-C<sub>3</sub>N<sub>4</sub> using urea and citric acid as the precursors for thermal polymerization.<sup>39</sup> The H<sub>2</sub> production rate on these N-doped g-C<sub>3</sub>N<sub>4</sub> was found 64 μmol h<sup>-1</sup>, which is nearly 4.3 times higher than the pure g-C<sub>3</sub>N<sub>4</sub>. The incorporation of N as dopant into the g-C<sub>3</sub>N<sub>4</sub> planar framework greatly enhances the photocatalytic H<sub>2</sub> evolution activity under visible light irradiation.

The photocatalytic performances of g-C<sub>3</sub>N<sub>4</sub> have also been enhanced through localized surface Plasmon resonance (LSPR) by incorporating plasmonic metal nanoparticle (Au, Ag etc.) with g-C<sub>3</sub>N<sub>4</sub>. Xue et al. have reported Au/Pt/g-C<sub>3</sub>N<sub>4</sub> hetero-structure by a facile calcination photo-deposition route.<sup>40</sup> The as-synthesized hetero-structure exhibited an enhanced photocatalytic performance for antibiotic degradation with a catalytic rate 3.4 times greater than that of bare g-C<sub>3</sub>N<sub>4</sub> under visible light. The enhanced activity has been attributed to the LSPR effect of Au NPs and the co-catalytic effect of Pt NPs that synergistically improve the optical absorption property and decrease the recombination of photogenerated charge carriers. In another study, Zhang et al. designed a plasmonic and up-converted photocatalyst (Au NPs and NaYF<sub>4</sub>:Yb<sup>3+</sup>, Er<sup>3+</sup>, Tm<sup>3+</sup> (NYF) microsphere loaded g-C<sub>3</sub>N<sub>4</sub> nanosheets by a simple one-step hydrothermal method. The Au-NYF/g-C<sub>3</sub>N<sub>4</sub> hetero-structure showed high stability, wide range photon absorption from the UV to visible and near-infrared regions, which greatly enhanced photocatalytic performance compared with the pure g-C<sub>3</sub>N<sub>4</sub> sample (5-fold enhancement).

Maeda and co-workers (**Figure 4.1.9a**) reported a photocatalyst consisting of Ru-complex decorated on g-C<sub>3</sub>N<sub>4</sub> by physical mixing of both the materials in methanol solution at room temperature.<sup>41</sup> The composite materials exhibited an excellent photocatalytic reduction of CO<sub>2</sub> into formic acid. The high activity originated due to the transfer of electrons from g-C<sub>3</sub>N<sub>4</sub> into Ru-complex, aided by a stronger interaction between them. It has been found that the catalytic performances can be further improved (AQY ~5.7% at 400 nm) by using a suitable solvent (N,N-dimethylacetamide). Li et al. constructed a multi-component hetero-structure (**Figure 4.1.9b-d**) of AgBr nanoparticles (NPs) supported on g-C<sub>3</sub>N<sub>4</sub> decorated nitrogen-doped graphene ternary nanocomposites (ACNNG-*x*) via a multistep process, exhibiting very high efficiency for photocatalytic removal of pollutant and reduction of CO<sub>2</sub> into methanol and ethanol under visible light.<sup>42</sup> ACNNG-*x* ternary photocatalytic system has overcome the drawbacks due to the effective charge separation, long-term stability, and strong redox potential as compared to the single components. In general, coupling of g-C<sub>3</sub>N<sub>4</sub> with other semiconductor materials leads to improved separation of photogenerated carriers and thereby, enhancing the photocatalytic performances of the composite materials. In this context, Ismael et al. synthesized a composite of ZrO<sub>2</sub>/g-C<sub>3</sub>N<sub>4</sub> by a calcination method and checked for photocatalytic activity for MO photo-degradation.<sup>43</sup> The improved catalytic activity was attributed to the facile charge separation by the interfacial connection between g-C<sub>3</sub>N<sub>4</sub> and ZrO<sub>2</sub>. Other metal oxides such as SnO<sub>2</sub>, TiO<sub>2</sub> and bimetallic

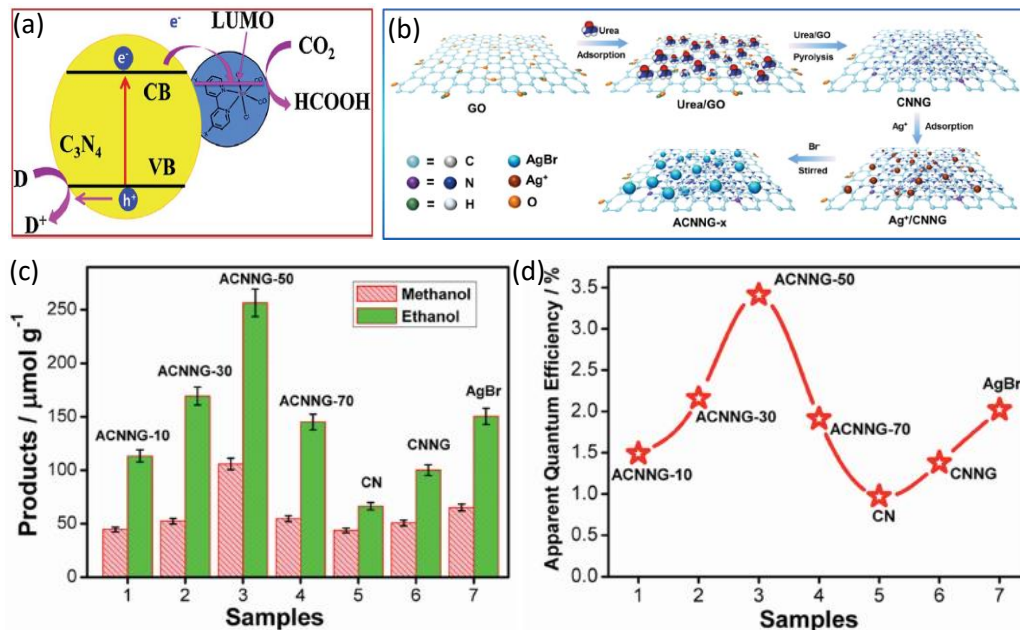


**Figure 4.1.9** (a) Schematic illustration of CO<sub>2</sub> reduction using a Ru complex/C<sub>3</sub>N<sub>4</sub> hybrid photocatalyst. (a) Synthetic strategy of AgBr NPs supported on g-C<sub>3</sub>N<sub>4</sub> decorated N-doped graphene ternary nanocomposites (ACNNG-x). Photocatalytic performance for the CO<sub>2</sub> reduction of ACNNG-x nanocomposite under visible light irradiation (c), and the corresponding apparent quantum efficiencies (d). Adapted with permission from [41,42].

oxides (SnNb<sub>2</sub>O<sub>6</sub> nanosheets, CuFe<sub>2</sub>O<sub>4</sub>, NaNbO<sub>3</sub>, and Ag<sub>3</sub>VO<sub>4</sub>) were also used to make heterostructures with g-C<sub>3</sub>N<sub>4</sub> and the improved catalytic activity was observed in each of these composite nanostructures. To get an overview of various heterojunctions engineered for g-C<sub>3</sub>N<sub>4</sub>, I refer to the **Table 4.1.1**.

Moreover, it was noticed that control in morphology has a vital role in enhancing the performance of g-C<sub>3</sub>N<sub>4</sub> photocatalysts. For example, Liu et al. prepared horn-like mesoporous ultrathin g-C<sub>3</sub>N<sub>4</sub> hollow tubes with a very high surface area which drastically improved the charge separation, surface charge transfer efficiency, and carrier density, which results in an enhanced photocatalytic activity for the H<sub>2</sub> evolution reaction and CO<sub>2</sub> reduction into CO and CH<sub>4</sub>.<sup>67</sup> More

**Table 4.1.1:** *g-C<sub>3</sub>N<sub>4</sub> based heterojunction photocatalysts for photocatalytic applications.*

Photocatalysts	Type of hetrojunction	Photocatalytic application	Ref.
<b>TiO<sub>2</sub>/g-C<sub>3</sub>N<sub>4</sub></b>	Type II	H <sub>2</sub> production and degradation of ciprofloxacin	44
<b>TiO<sub>2</sub>/g-C<sub>3</sub>N<sub>4</sub></b>	Semiconductor-semiconductor Z-scheme	Degradation of toluene	45
<b>N-doped TiO<sub>2</sub>/g-C<sub>3</sub>N<sub>4</sub></b>	Type II	H <sub>2</sub> evolution and degradation of rhodamine B	46
<b>C-N-dopedTiO<sub>2</sub>/g-C<sub>3</sub>N<sub>4</sub></b>	Type II	H <sub>2</sub> evolution	47
<b>N-doped TiO<sub>2</sub>/g-C<sub>3</sub>N<sub>4</sub></b>	Type II	CO <sub>2</sub> reduction to CO and CH <sub>4</sub>	48
<b>TiO<sub>2</sub>-B/g-C<sub>3</sub>N<sub>4</sub></b>	Type II	Type II	49
<b>Ag<sub>3</sub>PO<sub>4</sub>/g-C<sub>3</sub>N<sub>4</sub></b>	Type II	Degradation of rhodamine B	50
<b>Ag<sub>2</sub>CO<sub>3</sub>/g-C<sub>3</sub>N<sub>4</sub></b>	Type II	Degradation of methyl orange and rhodamine B	51
<b>AgBr/g-C<sub>3</sub>N<sub>4</sub></b>	Type II	Degradation of methyl orange and 4-chlorophenol	52
<b>Bi<sub>20</sub>TiO<sub>32</sub>/g-C<sub>3</sub>N<sub>4</sub></b>	Semiconductor-semiconductor Z-scheme	Degradation of rhodamine B and 4-chlorophenol	53
<b>Bi<sub>2</sub>WO<sub>6</sub>/g-C<sub>3</sub>N<sub>4</sub></b>	Semiconductor-semiconductor Z-scheme	CO <sub>2</sub> reduction to CO	54
<b>BiOBr/g-C<sub>3</sub>N<sub>4</sub></b>	Type II	Degradation of rhodamine B	55
<b>Bi<sub>2</sub>WO<sub>6</sub> quantum dots/g-C<sub>3</sub>N<sub>4</sub></b>	Semiconductor-semiconductor Z-scheme	Degradation of rhodamine B	56
<b>CaIn<sub>2</sub>S<sub>4</sub>/g-C<sub>3</sub>N<sub>4</sub></b>	Type I	H <sub>2</sub> evolution and degradation of methyl orange	57
<b>BiVO<sub>4</sub>/g-C<sub>3</sub>N<sub>4</sub></b>	Semiconductor-semiconductor Z-scheme	Degradation of rhodamine B	58
<b>CeO<sub>2</sub>/g-C<sub>3</sub>N<sub>4</sub></b>	Type II	CO <sub>2</sub> reduction to CO and CH <sub>4</sub>	59
<b>CdS QDs/g-C<sub>3</sub>N<sub>4</sub></b>	Type II	H <sub>2</sub> evolution	60
<b>Cu<sub>2</sub>O/g-C<sub>3</sub>N<sub>4</sub></b>	Type II	H <sub>2</sub> evolution	61
<b>CdS/Au/g-C<sub>3</sub>N<sub>4</sub></b>	Semiconductor-conductor-semiconductor Z-scheme	H <sub>2</sub> evolution and CO <sub>2</sub> reduction to CO	62
<b>g-C<sub>3</sub>N<sub>4</sub>/B-doped g-C<sub>3</sub>N<sub>4</sub></b>	Type II	H <sub>2</sub> evolution and degradation of methyl orange and phenol	63
<b>MoS<sub>2</sub>/g-C<sub>3</sub>N<sub>4</sub></b>	Type II	H <sub>2</sub> evolution	64
<b>Fe<sub>2</sub>O<sub>3</sub>/g-C<sub>3</sub>N<sub>4</sub></b>	Type II	Degradation of rhodamine B	65
<b>Red phosphor/g-C<sub>3</sub>N<sub>4</sub></b>	Type II	H <sub>2</sub> evolution and CO <sub>2</sub> reduction to CH <sub>4</sub>	66

details on the investigations of photocatalytic activity of g-C<sub>3</sub>N<sub>4</sub> can be found in a few recent reviews as given in **Table 4.1.2**.



**Table 4.1.2:** Review articles related to the g-C<sub>3</sub>N<sub>4</sub> photocatalyst.

Sr. No.	Reference
1	Ong et al., Graphitic Carbon Nitride (g-C <sub>3</sub> N <sub>4</sub> )-Based Photocatalysts for Artificial Photosynthesis and Environmental Remediation: Are We a Step Closer To Achieving Sustainability? <i>Chem. Rev.</i> , <b>2016</b> , 116, 7159–7329.
2	Khan et al., Recent developments in emerging two-dimensional materials and their applications. <i>J. Mater. Chem. C</i> , <b>2020</b> , 8, 387.
3	Miller et al., Carbon nitrides: synthesis and characterization of a new class of functional materials. <i>Phys. Chem. Chem. Phys.</i> , <b>2017</b> , 19, 15613.
4	Dong et al., A fantastic graphitic carbon nitride (g-C <sub>3</sub> N <sub>4</sub> ) material: Electronic structure, photocatalytic and photoelectronic properties. <i>Journal of Photochemistry and Photobiology C: Photochemistry Reviews</i> . <b>2014</b> , 20, 33–50
5	Tan et al., Novel two-dimensional crystalline carbon nitrides beyond g-C <sub>3</sub> N <sub>4</sub> : structure and applications. <i>J. Mater. Chem. A.</i> , <b>2020</b> , DOI: 10.1039/d0ta07437c.
6	Zhou et al., Recent advances in non-metal modification of graphitic carbon nitride for photocatalysis: a historic review. <i>Catal. Sci. Technol.</i> , <b>2016</b> , 6, 7002.
7	Fu et al., g-C <sub>3</sub> N <sub>4</sub> -Based Heterostructured Photocatalysts. <i>Adv. Energy Mater.</i> <b>2017</b> , 1701503
8	Maeda et al., Z-Scheme Water Splitting Using Two Different Semiconductor Photocatalysts. <i>ACS Catal.</i> 2013, 3, 1486–1503.

#### 4.1.7 Concluding remarks

g-C<sub>3</sub>N<sub>4</sub> is a conjugated system with a polymeric network, which is comprising of s-triazine or tri-s-triazine units interconnected via tertiary amines forming a 2D structure consisting of covalently linked carbon and nitrogen atoms in sp<sup>2</sup> hybridized form. They got attention in 2009, after the discovery of their photocatalytic H<sub>2</sub> evolution activity from splitting of water. Non-toxicity, earth-abundant nature, excellent chemical and thermal stability, relative ease of synthesis, visible-light absorption, high-surface area, high charge mobility, improvable exciton separation, appropriate band structure and electronic properties make this material a suitable photocatalyst to drive diverse chemical reactions. Although bulk g-C<sub>3</sub>N<sub>4</sub> can be easily synthesized by thermal polymerization of N-rich precursors, but these have disadvantages in regards to photochemical efficiency due to low surface area and partial utilization of a solar spectrum. To solve these aforementioned issues and enhance the photocatalytic activity of g-C<sub>3</sub>N<sub>4</sub>, several strategies have been developed, including noble metal loading, metal and non-metal doping, porous nanostructure generation, and coupling with other semiconductor photocatalysts, etc. g-C<sub>3</sub>N<sub>4</sub> based materials have been widely applied in solar energy conversion (H<sub>2</sub>-production and reduction of CO<sub>2</sub>) and environmental remediation

(degradation of organic pollutants). However, further improvements and investigation need to be done in their synthesis and application in other photocatalytic reactions.

## Bibliography

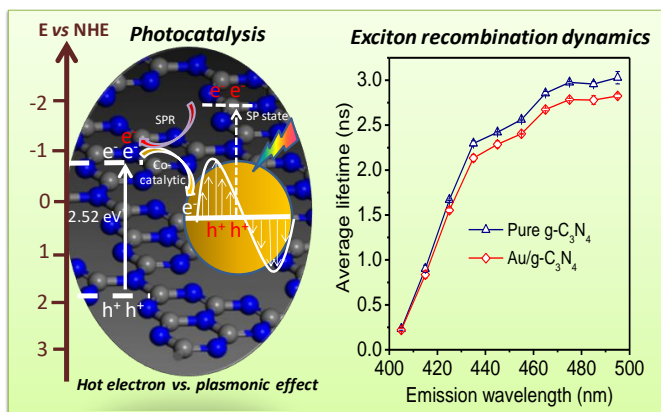
1. G. S. Duesberg, *Nat. Mater.*, 2014, **13**, 1075–1076.
2. N. R. Glavin, R. Rao, V. Varshney, E. Bianco, A. Apte, A. Roy, E. Ringe and P. M. Ajayan, *Adv. Mater.*, 2020, **32**, 1904302.
3. R. Mas-Balleste, C. Gomez-Navarro, J. Gomez-Herrero and F. Zamora, *Nanoscale*, 2011, **3**, 20–30.
4. K. S. Novoselov, V. I. Fal, L. Colombo, P. R. Gellert, M. G. Schwab and K. Kim, *Nature*, 2012, **490**, 192–200.
5. A. K. Geim and K. S. Novoselov, in *Nanoscience and technology: a collection of reviews from nature journals*, World Scientific, 2010, pp. 11–19.
6. S. Kang, D. Lee, J. Kim, A. Capasso, H. S. Kang, J.-W. Park, C.-H. Lee and G.-H. Lee, *2D Mater.*, 2020, **7**, 22003.
7. H. Zhang, M. Chhowalla and Z. Liu, *Chem. Soc. Rev.*, 2018, **47**, 3015–3017.
8. X. Wang, K. Maeda, A. Thomas, K. Takane, G. Xin, J. M. Carlsson, K. Domen and M. Antonietti, *Nat. Mater.*, 2009, **8**, 76–80.
9. J. Liebig, *Ann. der Pharm.*, 1834, **10**, 1–47.
10. W.-J. Ong, L.-L. Tan, Y. H. Ng, S.-T. Yong and S.-P. Chai, *Chem. Rev.*, 2016, **116**, 7159–7329.
11. F. Goettmann, A. Fischer, M. Antonietti and A. Thomas, *Chem. Commun.*, 2006, 4530–4532.
12. D. M. Teter and R. J. Hemley, *Science (80-. )*, 1996, **271**, 53–55.
13. A. Zambon, J.-M. Mouesca, C. Gheorghiu, P.-A. Bayle, J. Pecaut, M. Claeys-Bruno, S. Gambarelli and L. Dubois, *Chem. Sci.*, 2016, **7**, 945–950.
14. Y. Zheng, L. Lin, B. Wang and X. Wang, *Angew. Chemie Int. Ed.*, 2015, **54**, 12868–12884.
15. B. Zhu, L. Zhang, B. Cheng and J. Yu, *Appl. Catal. B Environ.*, 2018, **224**, 983–999.
16. A. Naseri, M. Samadi, A. Pourjavadi, A. Z. Moshfegh and S. Ramakrishna, *J. Mater. Chem. A*, 2017, **5**, 23406–23433.
17. Y. Zhang, Q. Pan, G. Chai, M. Liang, G. Dong, Q. Zhang and J. Qiu, *Sci. Rep.*, 2013, **3**, 1943.
18. Y. Chen, B. Wang, S. Lin, Y. Zhang and X. Wang, *J. Phys. Chem. C*, 2014, **118**, 29981–29989.
19. Y. Li, J. Zhang, Q. Wang, Y. Jin, D. Huang, Q. Cui and G. Zou, *J. Phys. Chem. B*, 2010, **114**, 9429–9434.
20. W. Ho, Z. Zhang, M. Xu, X. Zhang, X. Wang and Y. Huang, *Appl. Catal. B Environ.*, 2015, **179**, 106–112.
21. Y. Zhang, J. Liu, G. Wu and W. Chen, *Nanoscale*, 2012, **4**, 5300–5303.
22. S. Martha, A. Nashim and K. M. Parida, *J. Mater. Chem. A*, 2013, **1**, 7816–7824.
23. S. C. Yan, Z. S. Li and Z. G. Zou, *Langmuir*, 2009, **25**, 10397–10401.

24. X. Wang, K. Maeda, X. Chen, K. Takanaabe, K. Domen, Y. Hou, X. Fu and M. Antonietti, *J. Am. Chem. Soc.*, 2009, **131**, 1680–1681.
25. X. Bai, S. Yan, J. Wang, L. Wang, W. Jiang, S. Wu, C. Sun and Y. Zhu, *J. Mater. Chem. A*, 2014, **2**, 17521–17529.
26. W.-J. Ong, L.-L. Tan, S.-P. Chai and S.-T. Yong, *Chem. Commun.*, 2015, **51**, 858–861.
27. Z. Mo, X. She, Y. Li, L. Liu, L. Huang, Z. Chen, Q. Zhang, H. Xu and H. Li, *RSC Adv.*, 2015, **5**, 101552–101562.
28. P. Niu, L. Zhang, G. Liu and H.-M. Cheng, *Adv. Funct. Mater.*, 2012, **22**, 4763–4770.
29. X. Zhang, X. Xie, H. Wang, J. Zhang, B. Pan and Y. Xie, *J. Am. Chem. Soc.*, 2013, **135**, 18–21.
30. W. Wang, C. Y. Jimmy, Z. Shen, D. K. L. Chan and T. Gu, *Chem. Commun.*, 2014, **50**, 10148–10150.
31. H. Wang, X. Yuan, H. Wang, X. Chen, Z. Wu, L. Jiang, W. Xiong and G. Zeng, *Appl. Catal. B Environ.*, 2016, **193**, 36–46.
32. R. C. Pawar, S. Kang, J. H. Park, J. Kim, S. Ahn and C. S. Lee, *Sci. Rep.*, 2016, **6**, 1–14.
33. C. Zhou, R. Shi, L. Shang, L.-Z. Wu, C.-H. Tung and T. Zhang, *Nano Res.*, 2018, **11**, 3462–3468.
34. N. Tian, Y. Zhang, X. Li, K. Xiao, X. Du, F. Dong, G. I. N. Waterhouse, T. Zhang and H. Huang, *Nano Energy*, 2017, **38**, 72–81.
35. B. Luo, R. Song, J. Geng, D. Jing and Y. Zhang, *Appl. Catal. B Environ.*, 2018, **238**, 294–301.
36. S. Cao, J. Jiang, B. Zhu and J. Yu, *Phys. Chem. Chem. Phys.*, 2016, **18**, 19457–19463.
37. X. Li, W. Bi, L. Zhang, S. Tao, W. Chu, Q. Zhang, Y. Luo, C. Wu and Y. Xie, *Adv. Mater.*, 2016, **28**, 2427–2431.
38. J. Ran, T. Y. Ma, G. Gao, X.-W. Du and S. Z. Qiao, *Energy Environ. Sci.*, 2015, **8**, 3708–3717.
39. Y. Zhou, L. Zhang, W. Huang, Q. Kong, X. Fan, M. Wang and J. Shi, *Carbon N. Y.*, 2016, **99**, 111–117.
40. J. Xue, S. Ma, Y. Zhou, Z. Zhang and M. He, *ACS Appl. Mater. Interfaces*, 2015, **7**, 9630–9637.
41. R. Kuriki, K. Sekizawa, O. Ishitani and K. Maeda, *Angew. Chemie Int. Ed.*, 2015, **54**, 2406–2409.
42. H. Li, S. Gan, H. Wang, D. Han and L. Niu, *Adv. Mater.*, 2015, **27**, 6906–6913.
43. M. Ismael, Y. Wu and M. Wark, *New J. Chem.*, 2019, **43**, 4455–4462.
44. Z. Jiang, C. Zhu, W. Wan, K. Qian and J. Xie, *J. Mater. Chem. A*, 2016, **4**, 1806–1818.
45. M. J. Muñoz-Batista, A. Kubacka and M. Fernández-García, *Catal. Sci. Technol.*, 2014, **4**, 2006–2015.
46. C. Han, Y. Wang, Y. Lei, B. Wang, N. Wu, Q. Shi and Q. Li, *Nano Res.*, 2015, **8**, 1199–1209.
47. W. Chen, T.-Y. Liu, T. Huang, X.-H. Liu, G.-R. Duan, X.-J. Yang and S.-M. Chen, *Rsc Adv.*, 2015, **5**, 101214–101220.
48. S. Zhou, Y. Liu, J. Li, Y. Wang, G. Jiang, Z. Zhao, D. Wang, A. Duan, J. Liu and Y. Wei, *Appl. Catal. B Environ.*, 2014, **158**, 20–29.
49. H. Chen, Y. Xie, X. Sun, M. Lv, F. Wu, L. Zhang, L. Li and X. Xu, *Dalt. Trans.*, 2015, **44**, 13030–13039.
50. D. Jiang, J. Zhu, M. Chen and J. Xie, *J. Colloid Interface Sci.*, 2014, **417**, 115–120.

51. Y. Li, L. Fang, R. Jin, Y. Yang, X. Fang, Y. Xing and S. Song, *Nanoscale*, 2015, **7**, 758–764.
52. H. Xu, J. Yan, Y. Xu, Y. Song, H. Li, J. Xia, C. Huang and H. Wan, *Appl. Catal. B Environ.*, 2013, **129**, 182–193.
53. H. Cheng, J. Hou, O. Takeda, X.-M. Guo and H. Zhu, *J. Mater. Chem. A*, 2015, **3**, 11006–11013.
54. M. Li, L. Zhang, X. Fan, Y. Zhou, M. Wu and J. Shi, *J. Mater. Chem. A*, 2015, **3**, 5189–5196.
55. L. Ye, J. Liu, Z. Jiang, T. Peng and L. Zan, *Appl. Catal. B Environ.*, 2013, **142**, 1–7.
56. W. Chen, T.-Y. Liu, T. Huang, X.-H. Liu, J.-W. Zhu, G.-R. Duan and X.-J. Yang, *Appl. Surf. Sci.*, 2015, **355**, 379–387.
57. D. Jiang, J. Li, C. Xing, Z. Zhang, S. Meng and M. Chen, *ACS Appl. Mater. Interfaces*, 2015, **7**, 19234–19242.
58. N. Tian, H. Huang, Y. He, Y. Guo, T. Zhang and Y. Zhang, *Dalt. Trans.*, 2015, **44**, 4297–4307.
59. M. Li, L. Zhang, M. Wu, Y. Du, X. Fan, M. Wang, L. Zhang, Q. Kong and J. Shi, *Nano Energy*, 2016, **19**, 145–155.
60. D. Zheng and X. Wang, *Appl. Catal. B Environ.*, 2015, **179**, 479–488.
61. J. Chen, S. Shen, P. Guo, M. Wang, P. Wu, X. Wang and L. Guo, *Appl. Catal. B Environ.*, 2014, **152**, 335–341.
62. D. Zheng, C. Pang and X. Wang, *Chem. Commun.*, 2015, **51**, 17467–17470.
63. H. Li, Y. Liu, X. Gao, C. Fu and X. Wang, *ChemSusChem*, 2015, **8**, 1189–1196.
64. Y. Hou, A. B. Laursen, J. Zhang, G. Zhang, Y. Zhu, X. Wang, S. Dahl and I. Chorkendorff, *Angew. Chemie Int. Ed.*, 2013, **52**, 3621–3625.
65. X. Liu, A. Jin, Y. Jia, J. Jiang, N. Hu and X. Chen, *RSC Adv.*, 2015, **5**, 92033–92041.
66. Y.-P. Yuan, S.-W. Cao, Y.-S. Liao, L.-S. Yin and C. Xue, *Appl. Catal. B Environ.*, 2013, **140**, 164–168.
67. C. Liu, H. Huang, L. Ye, S. Yu, N. Tian, X. Du, T. Zhang and Y. Zhang, *Nano Energy*, 2017, **41**, 738–748.

## CHAPTER 4.2

### Wavelength-dependent luminescence decay kinetics in g-C<sub>3</sub>N<sub>4</sub> NSs; plasmonic enhancement



#### Summary

Serendipitous observations offer newer insights into materials properties. Here we describe the g-C<sub>3</sub>N<sub>4</sub> NSs exhibiting remarkably blue-shifted PL within the 390-580 nm range centring at 425 nm which matches more closely its ‘quantum-dots’, and yet excitation-wavelength independent. Moreover surprisingly, the luminescence decay becomes increasingly slower at higher emission wavelengths, by upto 10 times. The nanosheets absorb only a fraction of visible-light. To improve this, when we designed a nanocomposite of g-C<sub>3</sub>N<sub>4</sub> and Au NPs, it retained the PL characteristics and also exhibited excellent light-harvesting and photocatalytic efficiency for benzylamine (BA) oxidation. The SPR of the Au NPs is responsible for high visible-light response and assisting the reaction by ‘hot-electron’ injection mechanism, while an uncharacteristic, pronounced co-catalytic effect by them further improves the efficiency. The conversion is 98% with >99% selectivity under 1.5 h of natural sunlight and open-air. Even though such a dual role by plasmonic NPs has remained unscrutinized, we argue that the charge-transfer processes for the ‘hot-carrier’ injection and co-catalytic events are well-separated in time due to a much slower photon incident frequency on a catalyst particle, enabling both to occur simultaneously in the same particle.

‡ Manuscript based on this work has appeared in *Journal of Materials Chemistry A*, **2021**, 8, 20581.

### 4.2.1 Introduction

Graphitic carbon nitride (g-C<sub>3</sub>N<sub>4</sub>) has exhibited tremendous potential as a sunlight responsive photocatalyst by assisting large number reactions.<sup>1-6</sup> While a low cost, non-toxic nature and high chemical stability of g-C<sub>3</sub>N<sub>4</sub> is promising, its unfavourable optoelectronic properties such as the rapid exciton recombination and partial absorption of visible light have created a fertile ground for many fundamental studies. The size and excitation energy dependence of its luminescence properties is another such example. The photoluminescence (PL) peak originates from multiple transitions involving a lone pair of nitrogen, the  $\pi$ ,  $\pi^*$ ,  $\sigma$  and  $\sigma^*$  orbitals, and is usually centred around 440-470 nm with an average radiative recombination lifetime of 1-10 ns.<sup>7-10</sup> This emission exhibits a significant shift to a higher energy (emission maxima ~430-440 nm) when the size of g-C<sub>3</sub>N<sub>4</sub> becomes just a few nanometers, referred to as quantum dots (QDs), which may occur due to different reasons and is rather arbitrarily attributed to ‘quantum-confinement’ effects.<sup>11-13</sup> Moreover, the PL emission of the QDs has been suggested to be size-selective and dependent on the excitation wavelengths.<sup>12,14</sup> Similar kind of emission properties have not been observed in nanosheets of g-C<sub>3</sub>N<sub>4</sub> yet and in the absence of a thorough understanding, PL blue-shift and the effect of the interplay of the different radiative emissions pathways on exciton recombination kinetics has remained unpredictable in them.

An efficient way of extending optical response of g-C<sub>3</sub>N<sub>4</sub> to radiation with lower energies than the band-gap limit of 2.7 eV (~460 nm) is to decorate the nanosheets with metal nanoparticles (NP) having a Localized Surface Plasmon (LSP) band in that visible range of light.<sup>15-17</sup> LSP resonance (LSPR) refers to the coherent oscillation of conduction band electrons in the metal NP, in response to an external electromagnetic radiation and can be tuned to absorb all frequencies of visible light with high absorption cross-section by using NP, usually of Au, of appropriate sizes and shapes.<sup>18-20</sup> The decay of LSPR generates a short-lived electron-hole pair separated by the resonance energy. However, if the NP is in contact with a semiconductor such as TiO<sub>2</sub>, ZnO, CdS, g-C<sub>3</sub>N<sub>4</sub> etc., these electrons and holes with appropriate energies get injected in to the semiconductor, called as ‘hot-carrier’ injection. A large number of recent investigations have demonstrated that such excited electrons and holes on the semiconductor induce a variety of photocatalytic reactions such as water-splitting, abatement of pollutants and various organic transformations.<sup>21-25</sup>

#### 4.2.2 Scope of the present investigation

In recent past, many researchers have proposed to improve the efficiency of Au loaded semiconductors further by using another noble metal (e. g. Pt), which would act as a co-catalyst to the reaction, suggesting that in their understanding, Au doesnot or poorly contribute as a co-catalyst.<sup>21,22,26</sup> Contrary to this, PL quenching has been frequently observed in plasmonically coupled semiconductors, including g-C<sub>3</sub>N<sub>4</sub>, indicating that there exists a noticeable transfer of photo-excited electrons from the semiconductor to the Au nanoparticles.<sup>22,27</sup> Therefore the role of the plasmonically coupled Au nanocrystals as a co-catalyst, in addition to injecting hot-electrons, may not be negligible under white light irradiation, provided these two events are well separated in time. In that respect, average photon count under 1 Sun condition is estimated to be 1 in ~10 microseconds in an area of 100 nm<sup>2</sup> of the semiconductor. The decay lifetimes of the excited electrons and holes in the Au NP (tens of femtoseconds) and the semiconductor (a few nanoseconds) are much shorter than photon fall frequency and therefore, the dual role of Au NP during photocatalysis should be permissible in time. However, their co-catalytic activity vs. hot-electron injection prowess has not been clearly established yet, which could have helped a more systematic design and optimization of catalytic properties.

The absence of such optimization and the rather poor catalytic ability of g-C<sub>3</sub>N<sub>4</sub> for photo-oxidation of amines to imines,<sup>28</sup> despite its high efficiency for a large number of other organic transformations has been surprising. Controlled amine photo-oxidation has gained attention because of the versatile applications of the products in pharmaceuticals and in organic chemistry such as in neucleophilic addition, cycloaddition and condensation.<sup>29,30</sup> In addition, imines are also important intermediates in the synthesis of natural products, and biologically active heterocycles.<sup>31,32</sup> This inspired the development of many photocatalysts for amine oxidation such as organometallic compounds, metal-organic frameworks, semiconductor oxides (i.e. TiO<sub>2</sub>, WO<sub>3</sub>, Nb<sub>2</sub>O<sub>5</sub>, BiVO<sub>4</sub>, LDH, BiOCl), sulfides (WS<sub>2</sub>, CdS), and other carbon materials.<sup>33-38,23</sup> In spite of extensive studies, the conversion efficiencies of theses catalysts are still quite poor. Besides, many catalysts require high reaction temperatures and oxygenated atmosphere to increase the oxygen content on the surface of the photocatalyst, making the process economically less promising.<sup>39,40,28</sup> There is another reason specific to this transformation that requires rapid product formation. The imines produced in these reactions are susceptible to hydrolysis in ambient conditions and

therefore efficient photocatalysts should be able to complete the conversion in minimal time improving the product yield.

Herein, we describe the ‘quantum-confined’ g-C<sub>3</sub>N<sub>4</sub> nanosheets with highly blue-shifted, excitation-energy independent PL emission centred ~425 nm. Surprisingly the PL emission decay exhibits an increase in lifetime by up to 10-fold, from 0.3 ns to 3.1 ns, in the 400-500 nm range. Au loading (1 wt%) on the nanosheets retains these properties but induces a decrease in the decay time due to the transfer of excited electrons from the nanosheets to Au NPs. Such behaviour, we believe, has not been observed in other materials so far. The LSP in the Au led to good visible-light response of the Au-g-C<sub>3</sub>N<sub>4</sub> composite that resulted in high efficiency for photocatalytic oxidation of various benzylamine derivatives to the corresponding imines. The optimal design of this material features a significant contribution from the Au NP as a co-catalyst for the reaction (>30%), from using the excited electrons transferred from the nanosheets, apart from their usual role as ‘hot-carrier’ injector. A key reaction intermediate has been detected for the first time in support of a reaction mechanism for BA photo-oxidation.

### **4.2.3 Methods**

#### **4.2.3.1 Synthesis of ‘quantum-confined’ g-C<sub>3</sub>N<sub>4</sub> nanosheets**

The synthesis of g-C<sub>3</sub>N<sub>4</sub> powder was carried out using melamine as precursor materials. Typically, 6 g of melamine was taken in a crucible and covered with a lid. The crucible was placed in a muffle furnace and heated at 520 °C in air for 4 h and naturally cooled to obtain a yellow-coloured powder of g-C<sub>3</sub>N<sub>4</sub>. The powder (1 g) was dispersed in 250 ml distilled water (the dispersion was not stable and the particles accumulated at the bottom of the container within few minutes) and sonicated for 30 minutes. The solution was then kept undisturbed for 12 h when the bigger g-C<sub>3</sub>N<sub>4</sub> particles settled down. The upper part of the light-yellow dispersion (which was stable and did not settle down even after days) was centrifuged at 11000 rpm to recover the thin g-C<sub>3</sub>N<sub>4</sub> sheets (15-20% yield) and used for further studies.



#### 4.2.3.2 Deposition of Au NPs on ‘quantum-confined’ g-C<sub>3</sub>N<sub>4</sub> nanosheets (Au/g-C<sub>3</sub>N<sub>4</sub>)

The deposition of metal on g-C<sub>3</sub>N<sub>4</sub> was done photochemically in a 50 ml round bottom flask using a 400-W Xenon lamp. It was believed that unlike using pre-synthesized metal nanoparticles having a stabilizer layer on its surface, photo-deposition will provide the most intimate contact of the metal and semiconductor. In a typical synthesis, 100 mg g-C<sub>3</sub>N<sub>4</sub> was dispersed in 30 ml water containing 10 ml methanol and sonicated for 5 minutes. The solution was first bubbled with N<sub>2</sub> for 30 minutes and then the inert atmosphere was maintained during rest of the reaction. To deposit 1 wt% of Au, 0.2 ml of 25.4 mM gold(III) chloride trihydrate solution was slowly added by a syringe within 5 min and the vessel was illuminated under constant stirring at 600 rpm for 4 h. After addition of the gold solution, the colour of the g-C<sub>3</sub>N<sub>4</sub> dispersion gradually changed from yellow to brown (indicating the deposition of Au on the g-C<sub>3</sub>N<sub>4</sub>). Au/g-C<sub>3</sub>N<sub>4</sub>so obtained was collected by centrifugation at 11000 rpm. The leftover liquid was colourless and therefore it was assumed that all of Au salt has deposited on g-C<sub>3</sub>N<sub>4</sub>. The powder was then washed twice with water and once with ethanol and dried overnight at 55 °C.

#### 4.2.3.3 Photocatalytic Oxidation of Benzyl amine

25 mg of the photocatalyst was suspended in acetonitrile (30 ml) containing benzylamine (BA, 0.5 mmol) in a 50 ml beaker. Subsequently, the solution was kept in dark with constant stirring for half an hour before light irradiation to ensure an adsorption/desorption equilibrium. Then the reaction aliquot was kept under the direct sunlight (summer noon time) in open air for 1.5 h. Since sunlight intensity can vary, to benchmark the reaction efficiency, the same reaction was also carried out under LED solar-simulator (400-800 nm, NEWPORT) and a 400W Xe-lamp attached with a water-filter to remove the IR radiation and heating of the reaction medium. The reactions were performed at room temperature (around 25° C). The temperature was monitored throughout the reaction period and the obtained range was found to be 25-28 °C. To estimate irradiation wavelength dependent conversion efficiencies, the reactions were carried out using LED irradiation in the 400-500, 500-600, 600-700, 700-800 nm ranges by maintaining an irradiation power of 0.12 kW/m<sup>2</sup>. The catalyst particles were separated from the reaction mixture by centrifugation and the solvent in rest of the reaction aliquot was evaporated using rotavap to collect

the crude reaction product. The crude products were analysed using NMR spectroscopy. To find out the apparent quantum yield, an LED solar simulator (VERSAPOLE, NEWPORT) was used.

#### 4.2.3.4 Characterization

All other characterization techniques except the ones noted above are discussed in chapter 2.

#### 4.2.4 Results and discussion

The  $g\text{-C}_3\text{N}_4$  nanosheets prepared by sonication of its powder in water exhibited remarkable differences in optoelectronic properties and also retained them upon loading with Au NPs. The fraction of the sample that got dispersed in water upon sonication did not settle down for days (while the as-synthesized sample took just a few minutes to settle), as was observed previous studies also, and appeared relatively pale when collected by centrifugation as (**Figure 4.2.1a,b**). **Figure 4.2.1c** shows the XRD pattern of the  $g\text{-C}_3\text{N}_4$  sample obtained by sonication, revealing its hexagonal crystal structure (JCPDF#87-1526), free of impurities. The peak at  $2\theta = 27.5^\circ$  corresponds to (002) plane and stacking of the  $\text{C}_3\text{N}_4$  layers with an interlayer distance of  $d = 0.32$  nm. The XRD pattern remained similar upon loading the sample with Au NPs (**Figure 4.2.1c**). However, there were additional diffraction peaks at  $2\theta = 38.2^\circ$  and  $44.4^\circ$  corresponding to the (111) and (200) planes of Au respectively (JCPDF#89-3697), indicating that Au NPs were successfully deposited on  $g\text{-C}_3\text{N}_4$ .

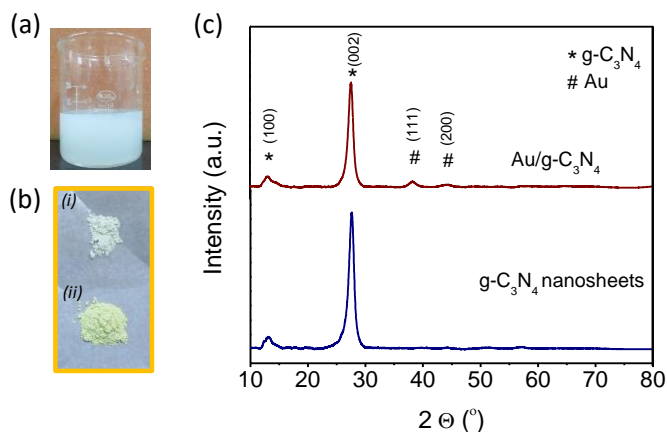


**Figure 4.2.1** (a) Photograph of the stable dispersion of  $g\text{-C}_3\text{N}_4$  powder in water after sonication and (b) the corresponding powder collected by centrifugation (i). (ii) The settled  $g\text{-C}_3\text{N}_4$  powder after sonication. (c) XRD patterns of the  $g\text{-C}_3\text{N}_4$  powder recovered from the stable dispersion and the same after Au photo-deposition.

Transmission electron microscopy (TEM) images showed that sonication leads to the formation of thin g-C<sub>3</sub>N<sub>4</sub> Sheets. **Figure 4.2.2a** displays a few such images of g-C<sub>3</sub>N<sub>4</sub> nanosheets measuring 100-300 nm and relatively transparent to the electron beam. Photo-deposition of Au (III) salt has led to a uniform decoration of Au NPs with an average size of 5-8 nm on the g-C<sub>3</sub>N<sub>4</sub> nanosheets as seen in the **Figure 4.2.2b,c**. The average distance between two adjacent Au NPs is about 10-12 nm (inset in **Figure 4.2.2c**) suggesting that about 100-150 nm<sup>2</sup> area of g-C<sub>3</sub>N<sub>4</sub> contains a single Au NP. From the high-resolution (HR) TEM investigations, we confirmed that the NPs are spherical and single-crystalline, exhibiting the lattice fringes for the (111) planes (**Figure 4.2.2d**). **Figure 4.2.2e** is typical selected area electron diffraction (SAED) pattern acquired on a nanosheet containing the Au NPs. **Figure 4.2.2f** is a line map of energy-dispersive X-ray spectroscopy (EDS) signal from the sample showing three Au particles separated by about 20 nm. A careful TEM and EDS analysis of the entire sample confirmed that there were no g-C<sub>3</sub>N<sub>4</sub> quantum-dots in both the samples.

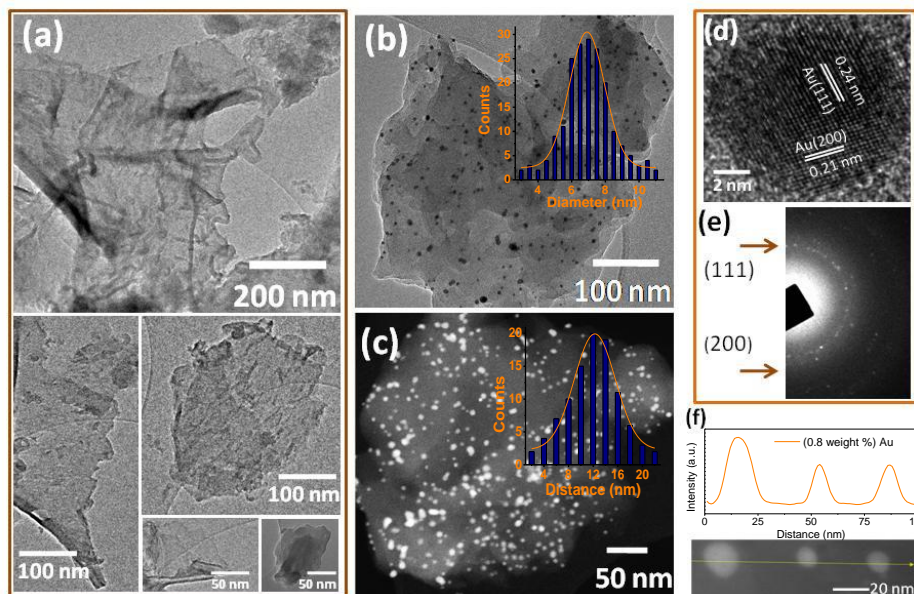


**Figure 4.2.2** (a) Typical TEM images of g-C<sub>3</sub>N<sub>4</sub> nanosheets obtained after sonication in water. (b) TEM images of Au/g-C<sub>3</sub>N<sub>4</sub> nanosheets. Inset in (b) shows the size distribution of the Au NPs. (c) STEM image of the Au/g-C<sub>3</sub>N<sub>4</sub> nanosheets. Inset in (c) shows the average distance between two neighbouring Au-NPs. (d) HRTEM image of an Au NP on Au/g-C<sub>3</sub>N<sub>4</sub> showing the (111) and (200) planes of Au NPs. (e) SAED pattern acquired on the Au/g-C<sub>3</sub>N<sub>4</sub> nanosheets. (f) EDS line scan on the Au/g-C<sub>3</sub>N<sub>4</sub> nanosheets. The scan position is displayed in bottom of the Fig. (f) with an arrow.

The surface areas (SAs) of the g-C<sub>3</sub>N<sub>4</sub> nanosheets and Au/g-C<sub>3</sub>N<sub>4</sub> composite were found to be 102 and 106 m<sup>2</sup>/g respectively from the Brunauer-Emmett-Teller (BET) method (**Figure 4.2.3**). The increase in SA after Au-deposition may be attributed to the extra undulation they create

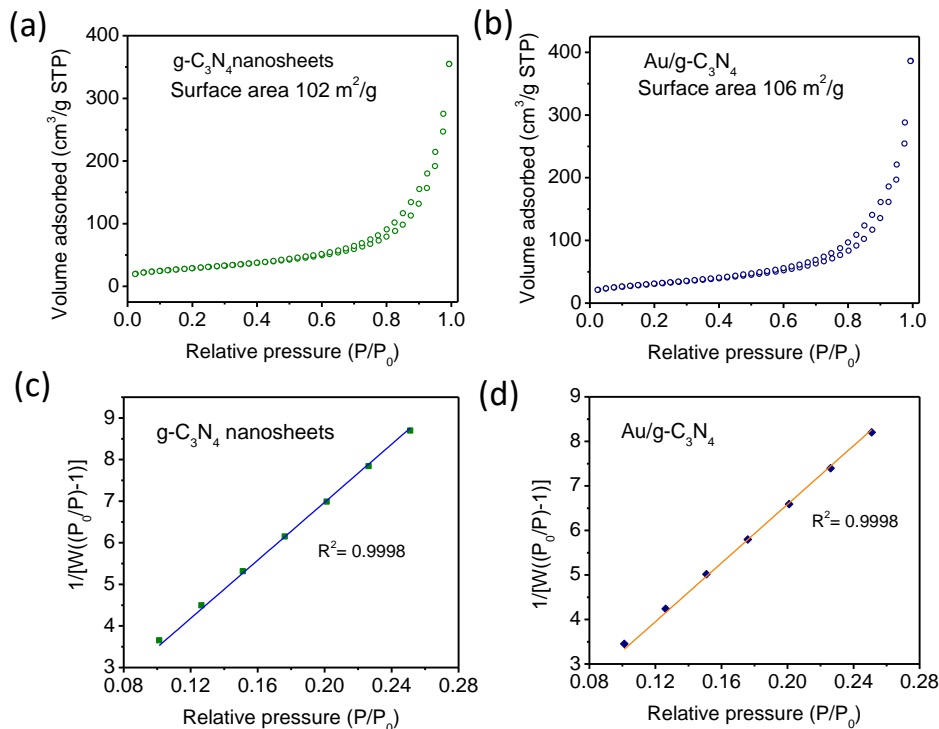


**Figure 4.2.3** N<sub>2</sub> gas adsorption-desorption plots for pure g-C<sub>3</sub>N<sub>4</sub> nanosheets (a), and Au/g-C<sub>3</sub>N<sub>4</sub> nanosheets (b). Multi-point BET surface area plots for pure g-C<sub>3</sub>N<sub>4</sub> nanosheets (c) and Au/g-C<sub>3</sub>N<sub>4</sub> nanosheets (d).

on the surface. In comparison, the surface area of the bulk g-C<sub>3</sub>N<sub>4</sub> was found to be rather small (10-20 m<sup>2</sup>/g) suggesting a high efficiency of exfoliation in the sonication process. The yield of the nanosheets was ~20 wt% and further sonication of the settled sample did not yield any NSs. It is noteworthy that a simple sonication approach has yielded the thin nanosheets with high surface area while most other methods use acid mediated exfoliation. We believe that in our case, the exfoliation occurred upon sonication of the as-synthesized powder because the top few layers of g-C<sub>3</sub>N<sub>4</sub> in the bulk crystallites were poorly held to the bottom layers. We further found that if the un-exfoliated sample is heated further and sonicated, g-C<sub>3</sub>N<sub>4</sub> nanosheets with slightly different optical properties can be generated again with yield >60%. This is an exciting approach for high yield synthesis of the g-C<sub>3</sub>N<sub>4</sub> nanosheets deserving extensive studies on the mechanism.

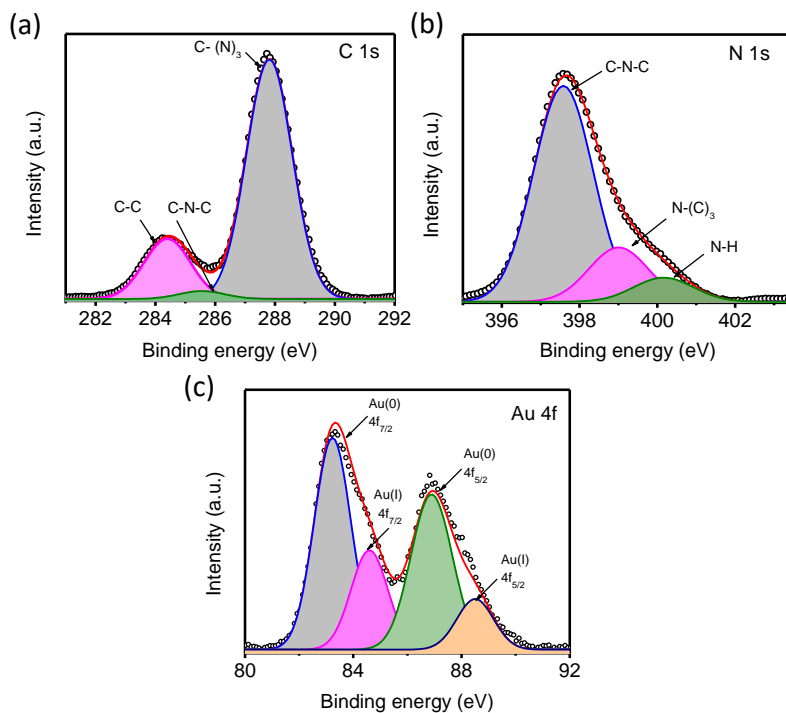


**Figure 4.2.4** The high-resolution XPS spectra for the Au/g-C<sub>3</sub>N<sub>4</sub> nanosheets, C 1s (a), N 1s (b) and Au 4f (c).

X-ray photoelectron spectroscopy (XPS) was used to analyze the chemical states and composition of Au/g-C<sub>3</sub>N<sub>4</sub> nanosheets. The high-resolution C 1s, N 1s and Au 4f peaks were deconvoluted in order to examine chemical bonding of C, N and Au. As in **Figure 4.2.4a**, the C 1s spectrum contains three peaks at binding energies of 284.4, 285.6 and 287.8 eV respectively. The 285.6 and 287.8 eV peaks can be attributed to the sp<sup>2</sup> C-atoms bonded to the nitrogen in an aromatic ring (C-N-C) and sp<sup>2</sup>-hybridized carbon in the aromatic ring attached to the NH<sub>2</sub> group (C-(N)<sub>3</sub>) respectively. The peak at 284.4 eV is graphitic carbon.<sup>22,41</sup> **Figure 4.2.4b** is N1s spectrum consists of three peaks at binding energies 397.5, 398.9 and 400.1 eV that are ascribed to (C-N-C), N-(C)<sub>3</sub> and N-H configuration respectively. The Au 4f spectrum in **Figure 4.2.4c** consists of four peaks. The peaks with binding energies 83.3 and 86.9 eV are for 4f<sub>7/2</sub> and Au 4f<sub>5/2</sub> respectively of metallic Au(0). The higher binding energy peaks at 84.6 and 88.5 eV correspond to the same transitions for Au (I) state indicating either some charge transfer to the nanosheets or the presence of surface oxidized Au atoms (about ~20%).

#### 4.2.4.1 The unusual optical properties of the nanosheets

The UV-visible diffuse reflectance spectra (DRS) of the bare and Au loaded  $g\text{-C}_3\text{N}_4$  nanosheets (**Figure 4.2.5**) show the onset to a strong absorption band at  $\sim 460$  nm. In addition, Au/ $g\text{-C}_3\text{N}_4$ NSs

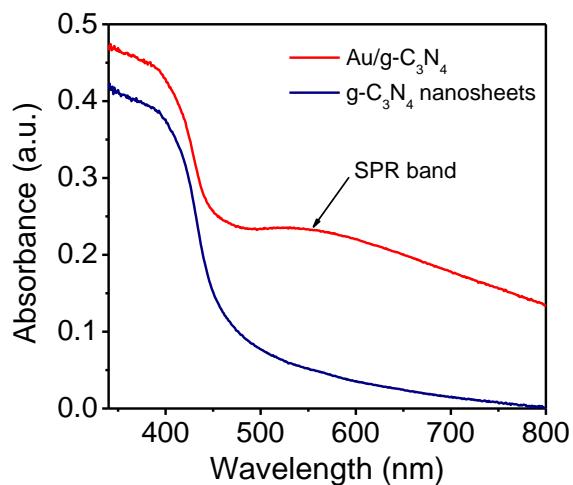


**Figure 4.2.5** UV-Visible diffuse reflectance spectra of bare and Au-loaded (1wt%)  $g\text{-C}_3\text{N}_4$  nanosheets.

exhibited another broad absorption band centered at  $\sim 550$  nm due to the LSPR of the Au NPs<sup>18,21,22</sup> indicating, as desired for the intended photocatalytic applications, a wholesome response to the entire spectrum of visible light.

Photoluminescence (PL) properties of the bare and Au loaded  $g\text{-C}_3\text{N}_4$  nanosheets are rather distinct and unexpected. The PL spectrum of nanosheets showed an emission band centred at 425 nm, which is blue-shifted in comparison to the as-prepared sample (**Figure 6a,b,c,d**). The PL excitation (PLE) spectra of these samples are also given in **Figure 4.2.6e,f**.

The emission peak could be fitted to three major bands centred at 425nm, 450 nm and 480nm representing the  $\sigma^*$  to lone-pair (LP),  $\pi^*$  to LP and  $\pi^*$  to  $\pi$  transitions respectively (**Figure 4.2.7a**).<sup>9,42</sup> The Au loaded  $g\text{-C}_3\text{N}_4$ nanosheets retained the same features in the PL and PLE spectra. However, Au loading resulted in a lower emission intensity due to the transfer of excited state electron from  $\sigma^*$  and  $\pi^*$  to the Fermi level of Au (**Figure 4.2.7a, pathway iv**), as discussed in

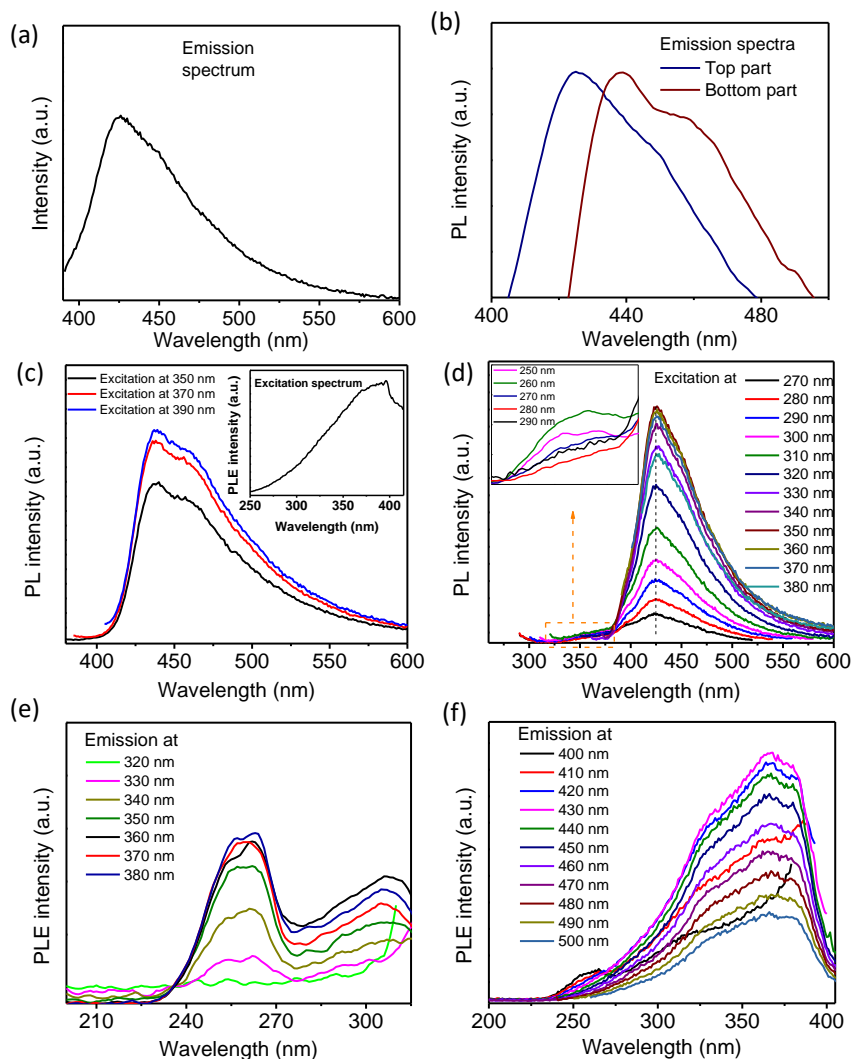


**Figure 4.2.6** (a) The blue-shifted PL spectrum of  $g\text{-C}_3\text{N}_4$  nanosheets. (b) The PL spectra of the top and the bottom parts of the sonicated  $g\text{-C}_3\text{N}_4$  sample highlighting the blue-shift. (c) PL spectra of as-prepared  $g\text{-C}_3\text{N}_4$  sample showing the emission maxima at  $\sim 440$  nm with 390 nm excitation wavelength. The inset of (c) is the corresponding PLE spectrum. (d) The PL spectra of  $g\text{-C}_3\text{N}_4$  nanosheets at different excitation wavelengths, showing the unshifted emission maxima at  $\sim 425$  nm. Inset shows a tiny PL peak emerging at  $\sim 370$  nm corresponding to a trace amount of melem present in the sample. (e,f) The PLE spectra of  $g\text{-C}_3\text{N}_4$  nanosheets at different emission wavelengths corresponding to the nanosheets and tiny fraction of melem, showing that the two peaks originate broadly of independent excitations. Notably there is a distinct shift in the PLE spectra of the as-prepared sample and the nanosheets.

detail in the ‘co-catalytic *vs.* plasmonic enhancement of activity’ section. The transfer of ‘hot-electrons’ from the Au NP to the nanosheet may also be pointed out here when the Au/g-C<sub>3</sub>N<sub>4</sub> sheets get exposed to light with  $\lambda \geq 460$  nm and matching the LSP frequency of the Au NPs (**Figure 4.2.7a, pathway  $\nu$** ). A careful analysis of the PL spectra also show a tiny shoulder at  $\sim 370$  nm, indicating that a small amount of melem may be present in the sample.<sup>43</sup>

Blue-shifted PL spectra of exfoliated g-C<sub>3</sub>N<sub>4</sub> nanosheets have been commonly observed with emission maxima centred at  $\sim 435$ - $465$  nm.<sup>44-47</sup> Acid induced exfoliation is highly effective in such transformation. Zhang et al could obtain g-C<sub>3</sub>N<sub>4</sub> nanosheets by exfoliation in water exhibiting one of the highest shifts to emission peak at  $\sim 440$  nm.<sup>45</sup> In contrast, the blue-shift in our samples to 425 nm is significantly larger and matches more closely the g-C<sub>3</sub>N<sub>4</sub> quantum dots (QDs). QDs usually emit in the range of 430-440 nm due to confinement effects,<sup>48,44,11</sup> (though QDs with more blue-shifted PL, even matching that of melem have also been observed at times<sup>49,50</sup>) and can be

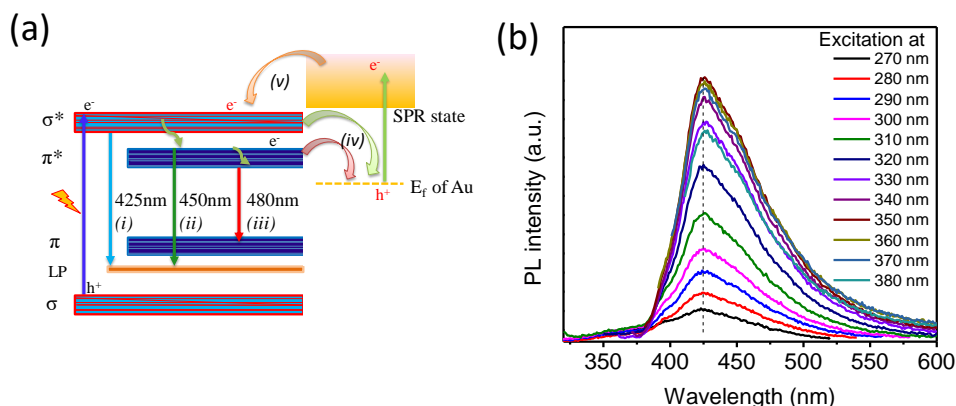


**Figure 4.2.7** (a) A Schematic representation of the various emissive electron transitions in g-C<sub>3</sub>N<sub>4</sub> nanosheets during light irradiations (i, ii, iii,) and potential electron transfer processes when loaded with Au. (b) PL spectra of g-C<sub>3</sub>N<sub>4</sub> nanosheets when excited with different energies in the 270-380 nm range.

distinguished from nanosheets as their emission maxima shift when excited with different wavelengths. Therefore, even though we did not find any QD in our sample during TEM analysis, we further recorded PL spectra of the nanosheets at different excitation wavelengths selected from the PLE spectrum. The PL peaks, however, did not shift at all (**Figure 4.2.7b**). The Au loaded



sample also exhibited a similar behaviour (**Figure 4.2.8**). These experiments suggest that the present g-C<sub>3</sub>N<sub>4</sub> nanosheets exhibit the largest blue-shifted PL emission or ‘quantum-confinement’ effect among the nanosheets and even closely match their QDs.

Since the nanosheets have multiple excitation decay pathways, each having a potentially different decay kinetics and interaction with the plasmonic field of the Au NPs,<sup>25,51</sup> we have further analyzed their behaviour by using time-correlated single photon count (TCSPC) measurements at different emission wavelengths. The sample was excited at 375 nm (the maximum of the PLE spectrum) and emission decay kinetics were analyzed at regular wavelength intervals in the 400–500 nm range. Typical PL decay profiles of pure and Au loaded g-C<sub>3</sub>N<sub>4</sub> nanosheets at the emission maxima (425 nm) are shown in **Figure 4.2.9a**.

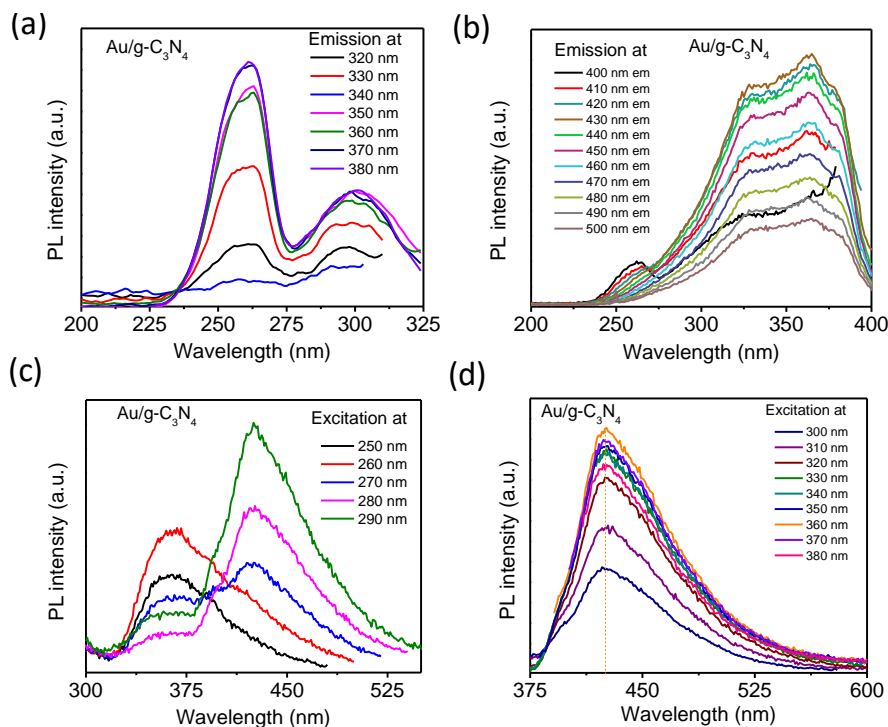


**Figure 4.2.8** PLE spectra of Au/g-C<sub>3</sub>N<sub>4</sub> nanosheets at different emission energies (a, b). The PL emission spectra of Au/g-C<sub>3</sub>N<sub>4</sub> nanosheets at different excitation wavelength (c,d). The peak position remained same (~425 nm) at all excitation wavelengths.

The data were fitted to a triple-exponential function (fitting parameters are given in the **Table 4.2.1**) and the average lifetime ( $\tau$ ), was calculated using the formula:

$$\text{Average lifetime } (\tau) = (\tau_1 A_1 + \tau_2 A_2 + \tau_3 A_3) / (A_1 + A_2 + A_3)$$

where,  $\tau_1$ ,  $\tau_2$ , and  $\tau_3$  represent emission lifetimes in three different time stages and  $A_1$ ,  $A_2$ , and  $A_3$  represent the amplitude of different emission lifetimes. The average emission lifetime of the g-C<sub>3</sub>N<sub>4</sub> (~1.68 ns) is marginally longer than the Au/g-C<sub>3</sub>N<sub>4</sub> (~1.58 ns).

**Table 4.2.1:** PL decay lifetime analysis of pure and Au loaded g-C<sub>3</sub>N<sub>4</sub> nanosheets at an emission wavelength of 425 nm.

Tri-exponential Emission (nm)	$\langle \tau \rangle$ ns	$\chi^2$	$\tau_1$ (ns)	$\tau_2$ (ns)	$\tau_3$ (ns)	$A_1$	$A_2$	$A_3$
425 (g-C <sub>3</sub> N <sub>4</sub> nanosheets)	1.679	1.244	3.278	13.700	0.728	0.29	0.02	0.70
425 (Au/g-C <sub>3</sub> N <sub>4</sub> )	1.581	1.234	3.056	12.653	0.699	0.28	0.02	0.70

There were however marked changes when we measured the luminescence decay lifetime at different emission wavelengths. For the pure nanosheets, the  $\tau$  is much shorter (~0.3 ns) at  $\lambda_{em}$ = 405 nm, but increases quickly to 2.2 ns at  $\lambda_{em}$ = 435 nm and then gradually reaches a value of 3.1 ns at  $\lambda_{em}$ = 495 nm (**Figure 4.2.9b,c**), a total 10 fold increase in the  $\tau$ .

A similar study was found on Cu(In,Ga)Se<sub>2</sub> showing much lesser changes in  $\tau$ , though the underlying reasons were not clearly outlined.<sup>52</sup> Longer  $\tau$  at higher  $\lambda_{em}$  is most likely due to involvement of multiple emissive states as the initially photo-excited population relaxes from higher excited state to the band-edge via vibrational relaxation as well as internal conversion. In comparison, though Au/g-C<sub>3</sub>N<sub>4</sub> nanosheets also showed a similar behaviour, the  $\tau$  values were consistently lower than the pure nanosheets. Moreover, the increase in  $\tau$  at the red side of emission is relatively slower for Au/g-C<sub>3</sub>N<sub>4</sub> nanosheets (**Figure 4.2.9d**).

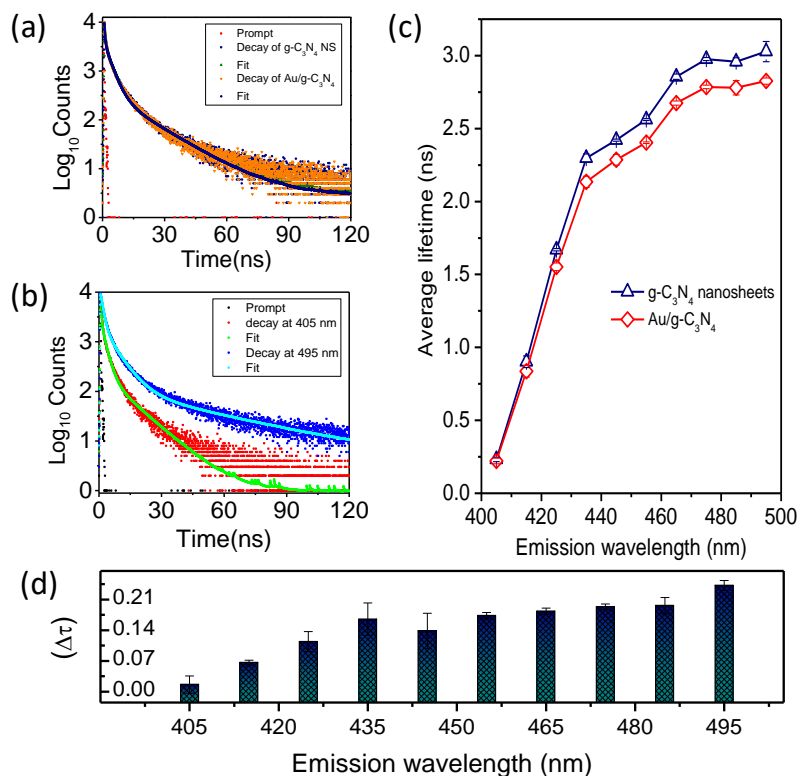


**Figure 4.2.9** (a) The PL decay plots for  $g-C_3N_4$  and  $Au/g-C_3N_4$  nanosheets at 425 nm emission ( $\lambda_{ex} = 375$  nm). (b) Similar decay plots for  $g-C_3N_4$  nanosheets at 405 nm and 495 nm emission. (c) The average emission lifetime, ( $\tau$ ) of  $g-C_3N_4$  and  $Au/g-C_3N_4$  nanosheets at various emission wavelengths. (d) Plot highlighting differences in  $\tau$  values of the two samples ( $\tau_{g-C_3N_4} - \tau_{Au/g-C_3N_4}$ ) at different emission wavelengths.

**Figure 4.2.10** displays the TCSPC plots for all different wavelengths. To further highlight the differences in  $\tau$ , we have plotted the decay traces (for the same decay counts) for pure and Au NPs

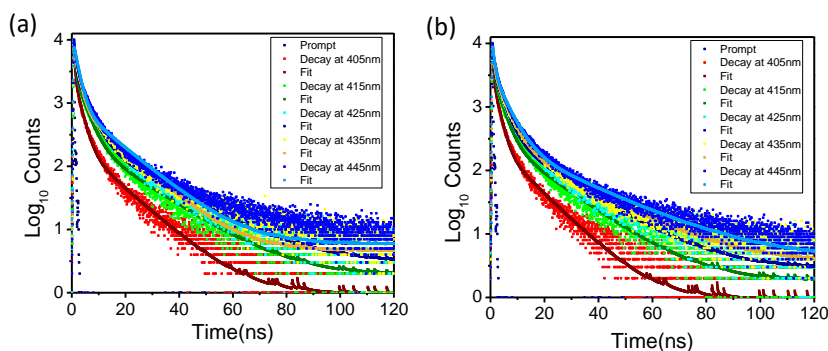


**Figure 4.2.10** Typical TCSPC decay plots of  $g-C_3N_4$  and  $Au/g-C_3N_4$  nanosheets at different emission wavelengths when excited with a 375 nm laser.

loaded nanosheets at 405, 445 and 495 nm within the first few nanoseconds where the fast decay component is prominent (**Figure 4.2.11**). A faster decay in the case of Au/g-C<sub>3</sub>N<sub>4</sub> nanosheets can be clearly observed in all plots. The decrease in  $\tau$  in presence of the Au NP is attributed to the transfer of the excited state electrons from g-C<sub>3</sub>N<sub>4</sub> to the Fermi level of Au. In such a scenario, preferential transfer of long-lived excited electrons would result in lower  $\tau$  in the Au loaded sample.

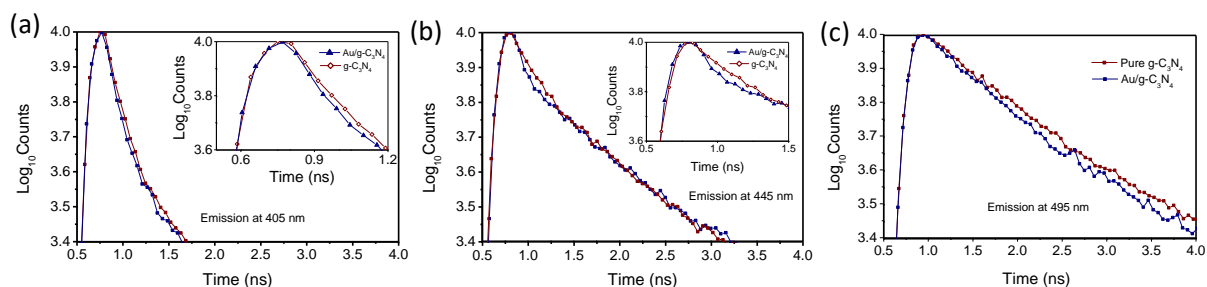


**Figure 4.2.11** The time-resolved fluorescence decay plots for pure and Au loaded nanosheets at 405 nm (a), 445 nm (b) and 495 nm (c) within the first few nanoseconds.

Mott-Schottky analysis was performed to calculate the flat band potential of the materials. The obtained flat-band potentials ( $V_{fb}$ ) were -0.79 V, -0.73V (vs. RHE) for g-C<sub>3</sub>N<sub>4</sub> and Au/g-C<sub>3</sub>N<sub>4</sub> nanosheets respectively (see **Figure 4.2.12**).

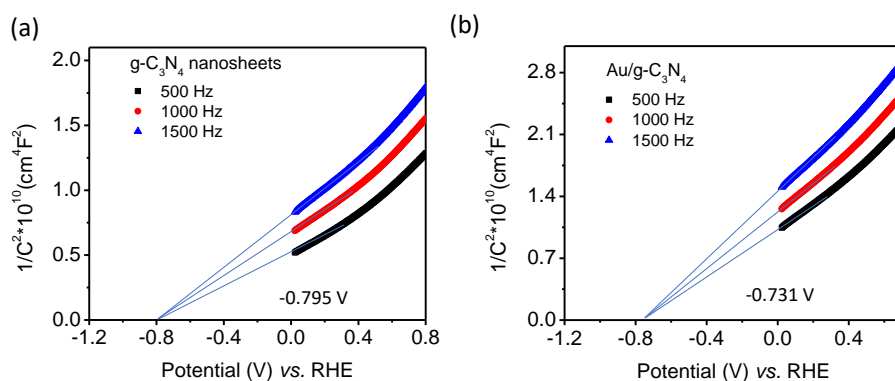
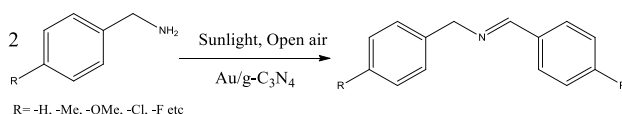


**Figure 4.2.12** Mott-Schottky plots for the nanosheets of g-C<sub>3</sub>N<sub>4</sub> (a) and Au/g-C<sub>3</sub>N<sub>4</sub> (b).

#### 4.2.4.2 Photocatalytic oxidation of Benzylamine and its derivatives

Since the previous attempts to carry out this reaction by  $g\text{-C}_3\text{N}_4$  resulted in rather poor efficiencies,<sup>28</sup> we attempted to improve it by using the  $\text{Au}/g\text{-C}_3\text{N}_4$  nanosheets. This reaction is usually carried out at elevated temperatures to improve the kinetics,<sup>40,39,53</sup> using molecular  $\text{O}_2$  which acts as an oxidizing agent. We attempted two major modifications: using (i) ambient air instead of a stream of  $\text{O}_2$  since oxygen harvesting is expensive and (ii) natural sunlight containing 44% of visible and 3% of UV light as the source of inexpensive energy.<sup>54</sup> The performance was benchmarked using a 400 W Xe lamp and solar simulator.

**Table 4.2.2:** Selective oxidation of BA under various conditions.



Entry	Catalyst	Environment	Light	Time	Conv. (%)	Select. (%)
1	$\text{Au}/g\text{-C}_3\text{N}_4$	Air	Sunlight	1.5 h	98	>99
2	$\text{Au}/g\text{-C}_3\text{N}_4$	Air	Xe-lamp	1.5 h	99	>99
3	$\text{Au}/g\text{-C}_3\text{N}_4$	Air	Dark	1.5 h	<1	-
4	No catalyst	Air	Sunlight	1.5 h	<1	-
5	$g\text{-C}_3\text{N}_4$	Air	Sunlight	1.5 h	21	>99
6	$g\text{-C}_3\text{N}_4$	Air	Xe-lamp	1.5 h	25	>99
7	$\text{Au}/g\text{-C}_3\text{N}_4$	$\text{O}_2$	Sunlight	1.5 h	98	>99
8	$\text{Au}/g\text{-C}_3\text{N}_4$	$\text{N}_2$	Sunlight	1.5 h	9	>99
9	$\text{Au}/g\text{-C}_3\text{N}_4$	Air	Sunlight	15 min	24	>99
10	$\text{Au}/g\text{-C}_3\text{N}_4$	$\text{O}_2$	Sunlight	15 min	27	>99
11	$\text{TiO}_2\text{-P25}$	Air	Sunlight	1.5 h	17	>99

The conversion efficiency using 1 wt% Au loaded  $g\text{-C}_3\text{N}_4$  nanosheets in ambient air was found to be extremely high with 96-98% yield and >99% selectivity after 1.5 h of reaction under natural sunlight (Table 4.2.2, entry 1 and 2). The conversion was, nonetheless, negligible in the absence of light or the catalyst asserting the photocatalytic nature of this reaction (Table 4.2.2, entry 3 and 4). As a control experiment, the reaction was further checked using a 400 W Xe-

lamp attached with an IR filter and maintaining a constant temperature of 35 °C. This and a few other experiments (**Table 4.2.3**) demonstrated that the reaction is photocatalytic and not photo-induced thermocatalytic in nature. We also examined the efficiency of the 0.5 wt% and 1.5 wt% Au loaded g-C<sub>3</sub>N<sub>4</sub> nanosheets for the photooxidation reactions, yielding 48% and 98% products. Since a 1 wt% sample exhibited the best efficiency with a lower Au loading, further investigations were carried out using this sample.

**Table 4.2.3:** Temperature profile of the reaction medium monitored throughout the reaction under sunlight.

Reaction time	20 min	30 min	40 min	50 min	60 min	70 min	80 min	90 min
Temperature (°C)	30	31	30	31	32	29	31	31

The performance of the catalyst in various gaseous environments showed a remarkable quality not observed in other photocatalysts so far. The conversion after 1.5 h in sunlight dropped to a mere 10%, as expected, when the reaction was carried out in a N<sub>2</sub> atmosphere (**Table 4.2.2**, entry 8). However, surprisingly, we didn't observe a notable change in the reaction rate when it was carried out under an O<sub>2</sub> atmosphere (99% conversion yield in 1.5 h). The corresponding conversions after 15 min of reaction were 23% (air) and 27% (O<sub>2</sub> purging), suggesting that unlike other catalysts, oxygen in open air is sufficient to saturate the catalyst surface (**Table 4.2.2**, entry 9 and 10). We propose that the graphitic C present in the sample, as observed from XPS studies, or probably defects in the g-C<sub>3</sub>N<sub>4</sub> framework are responsible for high O<sub>2</sub> adsorption by the photocatalyst.<sup>58-61</sup> The oxidation efficiencies of the bare g-C<sub>3</sub>N<sub>4</sub> NSs and the bulk g-C<sub>3</sub>N<sub>4</sub> sample were also examined to understand the effect of exfoliation and high surface area. As seen in **Table 4.2.4**, bulk sample exhibited noticeably poorer catalytic activity. The difference is even more prominent when we performed the catalytic reaction after loading 1 wt% Au on bulk g-C<sub>3</sub>N<sub>4</sub> and the nanosheets (51% and 98% conversion, respectively, after 1.5 h of light irradiation). The catalytic activity of the nanosheets was benchmarked using commercial TiO<sub>2</sub> (P-25). Under identical conditions, the conversion efficiency after 1.5 h of sunlight irradiation was found to be only 15% (**Table 4.2.2**, entry 11). We have also examined the effect of the loading of AuPNs.

**Table 4.2.4:** Comparison of photocatalytic activities for the amine oxidation reaction under ambient conditions by the bulk g-C<sub>3</sub>N<sub>4</sub> sample and the NSs.

Material	Reaction time	Conversion (%)
Bulk g-C <sub>3</sub> N <sub>4</sub>	1.5 h	17
	3 h	26
	6 h	41
g-C <sub>3</sub> N <sub>4</sub> NSs	1.5 h	21
	3 h	30
	6 h	52

The activity of bare g-C<sub>3</sub>N<sub>4</sub> nanosheets was nearly 4 times lower than that of Au/g-C<sub>3</sub>N<sub>4</sub> (Table 4.2.2). The apparent quantum efficiency (AQE), defined as the number of all incident photons (UV-800 nm range) vs. the number that was utilized by Au/g-C<sub>3</sub>N<sub>4</sub> for catalysis, was found to be 6.3%. Recyclability tests showed that the catalyst is very stable and exhibits minimal loss of catalytic activity in each successive cycle (Figure 4.2.13 and Figure 4.2.14).

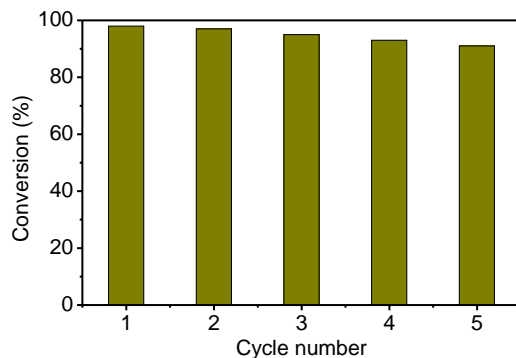


**Figure 4.2.13** Reusability data showing the efficiency of Au/g-C<sub>3</sub>N<sub>4</sub> nanosheets tested for five successive photocatalytic BA oxidation reactions under sunlight. (The catalysts were recovered by centrifugation, washed with acetonitrile and ethanol and dried at 60 °C before reuse).

We felt that Au NPs have not only improved the optical response of the material, but also offered a facile transfer of electrons between itself and g-C<sub>3</sub>N<sub>4</sub> nanosheets as they must retain an intimate electrical contact which was necessary for the deposition of the NPs. Electrochemical impedance spectroscopy (EIS) measurement was performed to investigate the charge transfer property of the photocatalysts. The Nyquist plots of Au/g-C<sub>3</sub>N<sub>4</sub> and the pure g-C<sub>3</sub>N<sub>4</sub> nanosheets are given in **Figure 4.2.15a**. The diameter of the semicircle in the highfrequency region can be correlated to the charge transfer resistance ( $R_{ct}$ ) at the electrode and electrolyte interface.<sup>59</sup> The Au/g-C<sub>3</sub>N<sub>4</sub> nanosheets has a low  $R_{ct}$  (73 ohm) as compared to pure g-C<sub>3</sub>N<sub>4</sub> (91 ohm), demonstrating that there was indeed improved charge-transfer property in the Au/g-C<sub>3</sub>N<sub>4</sub> nanocomposite. The photocatalytic reactions demonstrate a remarkable improvement in oxidation efficiency by C<sub>3</sub>N<sub>4</sub> when loaded with Au.

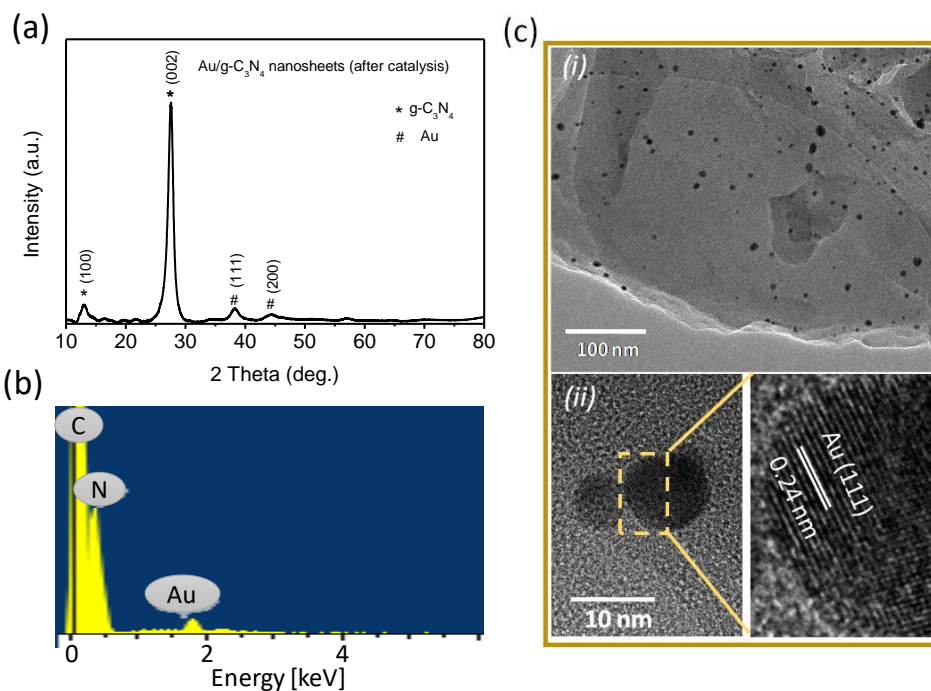


**Figure 4.2.14** XRD pattern of the used Au/g-C<sub>3</sub>N<sub>4</sub> nanosheets infive successive catalytic cycles. (b) SEM-EDS spectrum of the used Au/g-C<sub>3</sub>N<sub>4</sub> nanosheets for catalysis reaction. (c) TEM image (i), HR-TEM image (ii) of the Au/g-C<sub>3</sub>N<sub>4</sub> nanosheets obtained after catalysis.



#### 4.2.4.3 Co-catalytic vs. plasmonic enhancement of activity

To further investigate the origin of high catalytic activity we have studied wave-length specificity of the photocatalyst. The activity of the catalyst was tested by irradiating the reaction mixture with lights of different wavelengths (400-500, 500-600, 600-700 and 700-800 nm). The Au loaded and

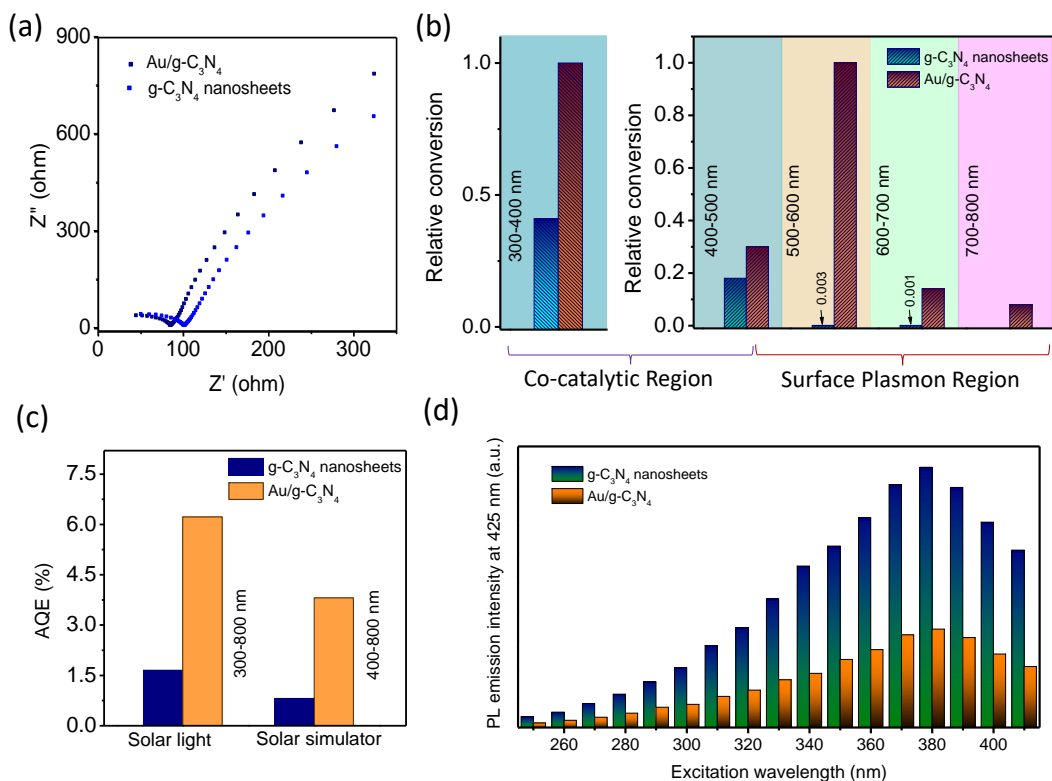


**Figure 4.2.15** (a) EIS Nyquist plots of g-C<sub>3</sub>N<sub>4</sub> and Au/g-C<sub>3</sub>N<sub>4</sub> nanosheets. (b) Plot of relative conversion of amines under illumination with different wavelengths using g-C<sub>3</sub>N<sub>4</sub> and Au/g-C<sub>3</sub>N<sub>4</sub> nanosheets. (c) AQE of g-C<sub>3</sub>N<sub>4</sub> and Au/g-C<sub>3</sub>N<sub>4</sub> nanosheets under direct sunlight and solar simulator. (d) PL emission intensities (425 nm emission band) at different excitation wavelengths showing the intensity quenching in case of Au/g-C<sub>3</sub>N<sub>4</sub> (after 4 h deposition) as compared to the pure g-C<sub>3</sub>N<sub>4</sub> nanosheets.

bare catalyst exhibited very different behaviour at higher wavelengths. The conversion is maximum in the 500-600 nm region while using Au/g-C<sub>3</sub>N<sub>4</sub> and ~300 times more than bare g-C<sub>3</sub>N<sub>4</sub>. In comparison to the maximum conversion, the relative conversions for the Au/g-C<sub>3</sub>N<sub>4</sub> (bare

g-C<sub>3</sub>N<sub>4</sub> nanosheets) in the wavelength ranges of 400-500, 600-700 and 700-800 nm were estimated to be 30% (18%), and 14% (0.1%) and 8% (0%) respectively as shown in **Figure 4.2.15b**. For Au/g-C<sub>3</sub>N<sub>4</sub>, the conversion in 500-600 nm range is higher compared to 400-500 nm range, showing that the efficiency is majorly boosted by the Au SPR. In addition, the conversion in the wavelength range 300-400 nm was also estimated to be substantially higher (~3 times) than that of the g-C<sub>3</sub>N<sub>4</sub> nanosheets, suggesting a major co-catalytic contribution by the Au NPs. The overall co-catalytic contribution appears to be about ~35% for BA oxidation reaction. This is of special important in view of the calls by previous researchers for newer designs to improve plasmonically active photocatalysts by adding a separate co-catalyst while we find that Au itself can have a significant co-catalytic contribution.<sup>19,20,24</sup> AQE in the range of 300-800 nm for both under solar simulator and solar light is shown in **Figure 4.2.15c**.

We performed PL quenching studies to further verify the co-catalytic phenomenon. PL is related to the extent of radiative recombination of the photogenerated electron-hole pairs which would be suppressed if the excited electrons in g-C<sub>3</sub>N<sub>4</sub> migrate to the co-catalyst particles.<sup>60-62</sup> Thus, first we recorded PL emission spectra from the sample during the course of Au photo-deposition. It was observed that as the deposition of Au increased with time, the PL intensity of the sample progressively reduced confirming transfer of excited electrons from g-C<sub>3</sub>N<sub>4</sub> to Au. We have also recorded the PL spectra of the g-C<sub>3</sub>N<sub>4</sub> and Au/g-C<sub>3</sub>N<sub>4</sub> nanosheets using the various excitation wavelengths (in the 250-400 nm range found to be active in the PLE spectrum). As given in the **Figure 4.2.15d**, the PL intensity for Au/g-C<sub>3</sub>N<sub>4</sub> is much lower than g-C<sub>3</sub>N<sub>4</sub> nanosheets at all excitation energies, confirming a suppressed recombination of photogenerated electron-hole pairs in Au/g-C<sub>3</sub>N<sub>4</sub> and the co-catalyst role of Au during photocatalysis.

#### 4.2.4.4 Mechanistic investigations

The suppressed reaction yield in inert N<sub>2</sub> atmosphere (**Table 4.2.2**) confirmed the role of molecular O<sub>2</sub> from air as the oxidant in the reaction. The same in dark showed that the photogenerated electrons and holes are responsible for the oxidation reaction in the g-C<sub>3</sub>N<sub>4</sub> nanosheets. Additionally, for Au/g-C<sub>3</sub>N<sub>4</sub>, hot-electrons generated on Au-NPs are also transferred to the conduction band of g-C<sub>3</sub>N<sub>4</sub>. To confirm the respective roles, we performed several controlled experiments using scavengers for these electrons, holes and the superoxide radical anion obtained by oxidation of O<sub>2</sub>.<sup>25,63</sup>

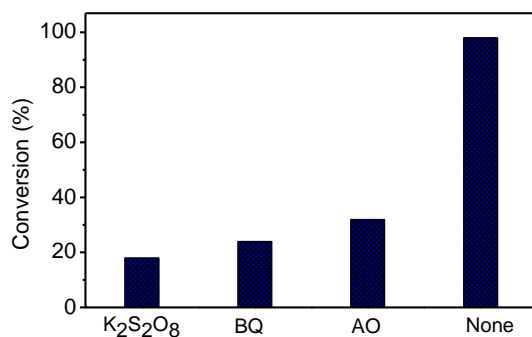
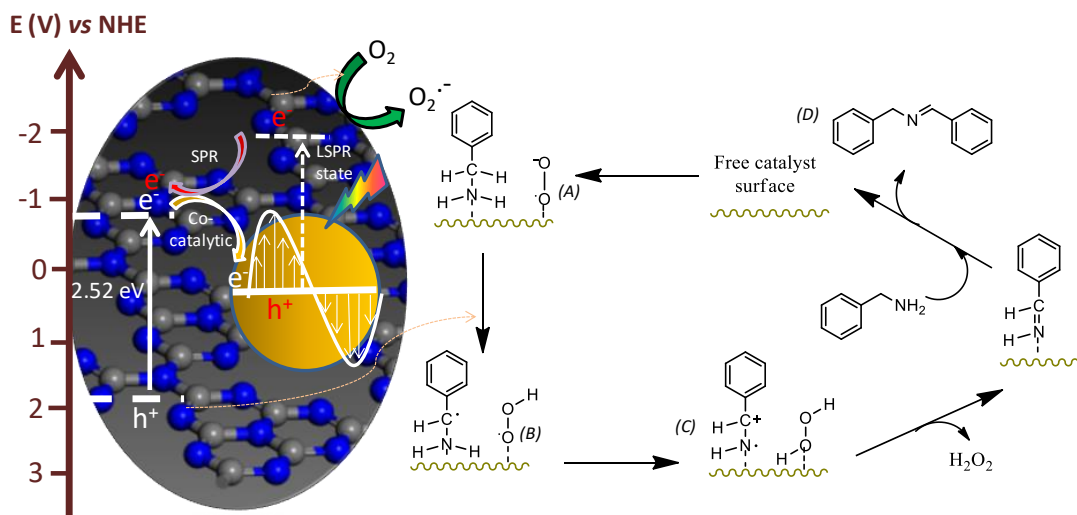


**Figure 4.2.16** Role of different scavengers in the photocatalytic BA oxidation. 3.0 mmol of scavengers were used in each set of reaction, keeping all other parameters same.

The conversion efficiency reduced to 19% after 1.5 h reaction by adding an electron scavenger (K<sub>2</sub>S<sub>2</sub>O<sub>8</sub>), indicating their strong influence in the reaction rate (**Figure 4.2.16**). We further carried out the reaction in the presence of benzoquinone and the conversion efficiency saw a sharp decrease to ~26%, suggesting in-situ O<sub>2</sub><sup>·-</sup> formation and its participation in the reaction (**Figure 4.2.16**). The contribution of the holes was checked by adding ammonium oxalate and the conversion drastically dropped to 29%, implying that the reaction is hole mediated as well.

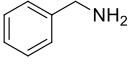
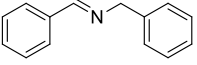
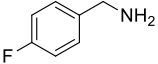
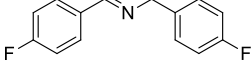
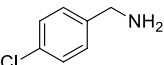
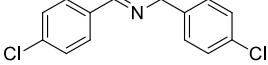
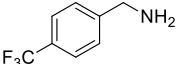
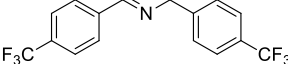
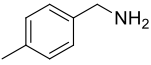
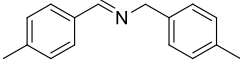
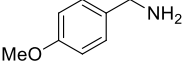
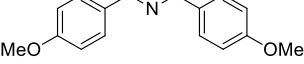
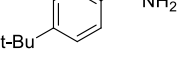
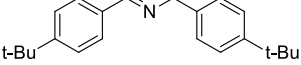
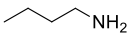
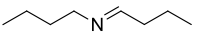
Accordingly, we have proposed a reaction mechanism and tried to prove it by directly detecting some of the reaction intermediates (**Scheme 4.2.1**). The steps involved in the reaction are: (i) the excited electron was first captured by O<sub>2</sub> attached to the catalyst surface to produce a superoxide radical anion (O<sub>2</sub><sup>·-</sup>), **A**, as shown in **Scheme 4.2.1**. (ii) Somewhere nearby, a photogenerated hole oxidizes an adsorbed benzylamine molecule to gives benzylamine radical intermediate, **B**, and HOO·. We confirmed the formation of intermediate **B** by using radical trapping reagent TEMPO ((2,2,6,6-Tetramethylpiperidin-1-yl)oxyl radical)) and detecting it by high-resolution mass-spectroscopy. We underline that eventhough this intermediate was proposed earlier, it was never been trapped so far. (iii) HOO· extracts one hydrogen radical (H·) and yielding benzylium ion, **C** and hydrogen peroxide as by-product. The formation of H<sub>2</sub>O<sub>2</sub> as a by-product was detected by spectroscopically after adding KMnO<sub>4</sub> solution. (iv) The benzylium ion couples with another neighbouring benzylamine molecule to give benzaldimine, **D** as the final product.



**Scheme 4.2.1** A proposed reaction mechanism for BA oxidation.

The versatility of the catalyst was examined by using various *p*-substituted benzylamine having various electron-donating (-CH<sub>3</sub>, -OCH<sub>3</sub>, *t*-butyl) and electron-withdrawing (-F, -Cl, -CF<sub>3</sub>) groups (**Table 4.2.5**). We found that the reaction is comparatively slow for both electron-donating as well as withdrawing groups (**Table 4.2.5**, entry 2, 3, 4, 5, 6 and 7) with conversion efficiencies of ~85-90% with 99% selectivity after 3-4 h reaction time (corresponding turn over frequencies (TOF) are in the range of 5.7-16, **Table 4.2.5**). However, electron-withdrawing group shows better activity compared to the electron-donating groups. We have also examined the reactivity of aliphatic amines (**Table 4.2.5**, entry 8) and found that our catalyst is specific to amines containing an aromatic group only. These results show that the Au/g-C<sub>3</sub>N<sub>4</sub> nanosheets is a very promising photocatalyst with very high efficiency and selectivity for controlled oxidation of amines using molecular oxygen.

**Table 4.2.5:** Oxidation of various amines with the Au/g-C<sub>3</sub>N<sub>4</sub> nanosheets.

Entry	Substrate	Product	Time	Conversion (%)	Selectivity (%)	TOF <sup>a</sup>
1			1.5 h	98	>99	16.3
2			2.5 h	90	>99	9
3			2.5 h	93	>99	9.3
4			2.5 h	94	>99	9.4
5			3.5 h	88	>99	6.3
6			3.5 h	85	>99	6.1
7			3.5 h	80	>99	5.7
8			4 h	0	-	-

**Reaction conditions:** Reactions were carried out in acetonitrile (30 ml) using 0.5 mmol of substrate, 25 mg photocatalyst under natural sunlight in air.

#### 4.2.5 Conclusions

In conclusion, we have realized new g-C<sub>3</sub>N<sub>4</sub> nanosheets exhibiting highly blue-shifted, excitation-energy independent photoluminescence centred at ~425 nm. Within the emission band, however, the PL decay kinetics becomes progressively slower by up to 10 times towards the red side of emission. When the g-C<sub>3</sub>N<sub>4</sub> nanosheets are loaded with Au nanoparticles, the composite retains the PL characteristics but the slowdown of its decay kinetics became less pronounced due to transfer of the long-lived photoexcited electrons in g-C<sub>3</sub>N<sub>4</sub> to the adjacent Au NPs. The Au/g-C<sub>3</sub>N<sub>4</sub> nanosheets exhibited excellent photocatalytic efficiency for benzylamine oxidation, emanating not only from a typical Surface Plasmon induced ‘hot-electron’ injection mechanism, but also from a less-cared-for, pronounced co-catalytic effect by the Au NPs. The new findings on the semiconductor exciton dynamics in the vicinity of a plasmonic NP and the subsequent dual role

offered by the NP towards realizing high photocatalytic activity will inspire the design of other superior photocatalysts for a wide range of organic transformations driven by sun-light.

## Bibliography

1. W.-J. Ong, L.-L. Tan, Y. H. Ng, S.-T. Yong and S.-P. Chai, *Chem. Rev.*, 2016, **116**, 7159–7329.
2. Y. Wang, X. Wang and M. Antonietti, *Angew. Chemie Int. Ed.*, 2012, **51**, 68–89.
3. X. Wang, K. Maeda, A. Thomas, K. Takane, G. Xin, J. M. Carlsson, K. Domen and M. Antonietti, *Nat. Mater.*, 2009, **8**, 76–80.
4. A. Naseri, M. Samadi, A. Pourjavadi, A. Z. Moshfegh and S. Ramakrishna, *J. Mater. Chem. A*, 2017, **5**, 23406–23433.
5. P. Geng, Y. Tang, G. Pan, W. Wang, J. Hu and Y. Cai, *Green Chem.*, 2019, **21**, 6116–6122.
6. D. Das, S. L. Shinde and K. K. Nanda, *ACS Appl. Mater. Interfaces*, 2016, **8**, 2181–2186.
7. Q. Xu, B. Cheng, J. Yu and G. Liu, *Carbon N. Y.*, 2017, **118**, 241–249.
8. L. Yang, J. Huang, L. Shi, L. Cao, Q. Yu, Y. Jie, J. Fei, H. Ouyang and J. Ye, *Appl. Catal. B Environ.*, 2017, **204**, 335–345.
9. Y. Zhang, Q. Pan, G. Chai, M. Liang, G. Dong, Q. Zhang and J. Qiu, *Sci. Rep.*, 2013, **3**, 1943.
10. B. B. Wang, Q. J. Cheng, L. H. Wang, K. Zheng and K. Ostrikov, *Carbon N. Y.*, 2012, **50**, 3561–3571.
11. Q. Cui, J. Xu, X. Wang, L. Li, M. Antonietti and M. Shalom, *Angew. Chemie Int. Ed.*, 2016, **55**, 3672–3676.
12. T. Wang, C. Nie, Z. Ao, S. Wang and T. An, *J. Mater. Chem. A*, 2020, **8**, 485–502.
13. S. Barman and M. Sadhukhan, *J. Mater. Chem.*, 2012, **22**, 21832–21837.
14. X. Chen, Q. Liu, Q. Wu, P. Du, J. Zhu, S. Dai and S. Yang, *Adv. Funct. Mater.*, 2016, **26**, 1719–1728.
15. G. Yu, J. Qian, P. Zhang, B. Zhang, W. Zhang, W. Yan and G. Liu, *Nat. Commun.*, 2019, **10**, 4912.
16. X. Zhang, X. Li, D. Zhang, N. Q. Su, W. Yang, H. O. Everitt and J. Liu, *Nat. Commun.*, 2017, **8**, 14542.
17. W. Hou and S. B. Cronin, *Adv. Funct. Mater.*, 2013, **23**, 1612–1619.
18. X. Zhou, G. Liu, J. Yu and W. Fan, *J. Mater. Chem.*, 2012, **22**, 21337–21354.
19. S. Eustis and M. A. El-Sayed, *Chem. Soc. Rev.*, 2006, **35**, 209–217.
20. C. Wang and D. Astruc, *Chem. Soc. Rev.*, 2014, **43**, 7188–7216.
21. B. Wu, D. Liu, S. Mubeen, T. T. Chuong, M. Moskovits and G. D. Stucky, *J. Am. Chem. Soc.*, 2016, **138**, 1114–1117.
22. J. Xue, S. Ma, Y. Zhou, Z. Zhang and M. He, *ACS Appl. Mater. Interfaces*, 2015, **7**, 9630–9637.
23. S. Naya, K. Kimura and H. Tada, *ACS Catal.*, 2013, **3**, 10–13.
24. C.-H. Hao, X.-N. Guo, Y.-T. Pan, S. Chen, Z.-F. Jiao, H. Yang and X.-Y. Guo, *J. Am. Chem. Soc.*, 2016, **138**, 9361–9364.
25. H. Li, F. Qin, Z. Yang, X. Cui, J. Wang and L. Zhang, *J. Am. Chem. Soc.*, 2017, **139**,

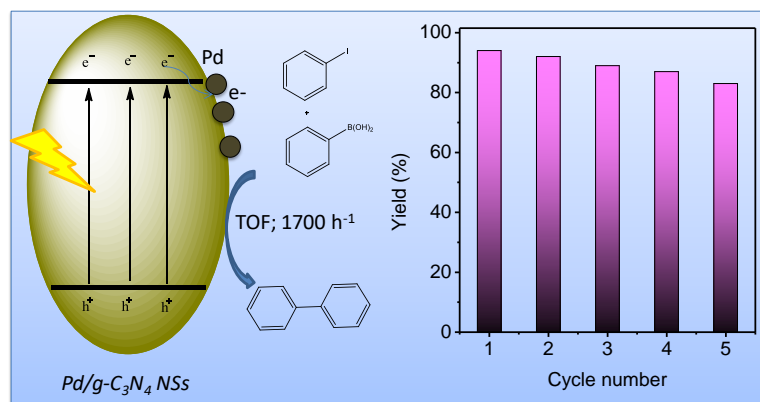
- 3513–3521.
26. S. Shuang, R. Lv, Z. Xie and Z. Zhang, *Sci. Rep.*, 2016, **6**, 26670.
  27. S. Mukhopadhyay, D. Maiti, S. Chatterjee, P. S. Devi and G. Suresh Kumar, *Phys. Chem. Chem. Phys.*, 2016, **18**, 31622–31633.
  28. F. Su, S. C. Mathew, L. Möhlmann, M. Antonietti, X. Wang and S. Blechert, *Angew. Chemie Int. Ed.*, 2011, **50**, 657–660.
  29. S.-I. Murahashi, *Angew. Chemie Int. Ed. English*, 1995, **34**, 2443–2465.
  30. H. Wang, R. E. Partch and Y. Li, *J. Org. Chem.*, 1997, **62**, 5222–5225.
  31. H. Sun, F.-Z. Su, J. Ni, Y. Cao, H.-Y. He and K.-N. Fan, *Angew. Chemie Int. Ed.*, 2009, **48**, 4390–4393.
  32. B. Gnanaprakasam, J. Zhang and D. Milstein, *Angew. Chemie Int. Ed.*, 2010, **49**, 1468–1471.
  33. S. Li, G. Li, P. Ji, J. Zhang, S. Liu, J. Zhang and X. Chen, *ACS Appl. Mater. Interfaces*, 2019, **11**, 43287–43293.
  34. J. Shi, J. Zhang, T. Liang, D. Tan, X. Tan, Q. Wan, X. Cheng, B. Zhang, B. Han, L. Liu, F. Zhang and G. Chen, *ACS Appl. Mater. Interfaces*, 2019, **11**, 30953–30958.
  35. D. Sun, L. Ye and Z. Li, *Appl. Catal. B Environ.*, 2015, **164**, 428–432.
  36. F. Wang, X. He, L. Sun, J. Chen, X. Wang, J. Xu and X. Han, *J. Mater. Chem. A*, 2018, **6**, 2091–2099.
  37. F. Raza, J. H. Park, H.-R. Lee, H.-I. Kim, S.-J. Jeon and J.-H. Kim, *ACS Catal.*, 2016, **6**, 2754–2759.
  38. H. He, Z. Li, K. Li, G. Lei, X. Guan, G. Zhang, F. Zhang, X. Fan, W. Peng and Y. Li, *ACS Appl. Mater. Interfaces*, 2019, **11**, 31844–31850.
  39. M. Wang, F. Wang, J. Ma, M. Li, Z. Zhang, Y. Wang, X. Zhang and J. Xu, *Chem. Commun.*, 2014, **50**, 292–294.
  40. A. Dhakshinamoorthy, M. Alvaro and H. Garcia, *ChemCatChem*, 2010, **2**, 1438–1443.
  41. F. Dong, L. Wu, Y. Sun, M. Fu, Z. Wu and S. C. Lee, *J. Mater. Chem.*, 2011, **21**, 15171–15174.
  42. Y. Yuan, L. Zhang, J. Xing, M. I. B. Utama, X. Lu, K. Du, Y. Li, X. Hu, S. Wang, A. Genç, R. Dunin-Borkowski, J. Arbiol and Q. Xiong, *Nanoscale*, 2015, **7**, 12343–12350.
  43. B. Jürgens, E. Irran, J. Senker, P. Kroll, H. Müller and W. Schnick, *J. Am. Chem. Soc.*, 2003, **125**, 10288–10300.
  44. J. Liu, H. Wang and M. Antonietti, *Chem. Soc. Rev.*, 2016, **45**, 2308–2326.
  45. X. Zhang, X. Xie, H. Wang, J. Zhang, B. Pan and Y. Xie, *J. Am. Chem. Soc.*, 2013, **135**, 18–21.
  46. L. Shi, K. Chang, H. Zhang, X. Hai, L. Yang, T. Wang and J. Ye, *Small*, 2016, **12**, 4431–4439.
  47. J. Fu, J. Yu, C. Jiang and B. Cheng, *Adv. Energy Mater.*, 2018, **8**, 1701503.
  48. X. Wang, G. Sun, N. Li and P. Chen, *Chem. Soc. Rev.*, 2016, **45**, 2239–2262.
  49. Z. Song, T. Lin, L. Lin, S. Lin, F. Fu, X. Wang and L. Guo, *Angew. Chemie Int. Ed.*, 2016, **55**, 2773–2777.
  50. X. Zhang, H. Wang, H. Wang, Q. Zhang, J. Xie, Y. Tian, J. Wang and Y. Xie, *Adv. Mater.*, 2014, **26**, 4438–4443.
  51. Z. Bian, T. Tachikawa, P. Zhang, M. Fujitsuka and T. Majima, *J. Am. Chem. Soc.*, 2014, **136**, 458–465.
  52. F. Khan and J. H. Kim, *Sci. Rep.*, 2019, **9**, 10803.

53. J. Ye, K. Ni, J. Liu, G. Chen, M. Ikram and Y. Zhu, *ChemCatChem*, 2018, **10**, 259–265.
54. V. R. Battula, H. Singh, S. Kumar, I. Bala, S. K. Pal and K. Kailasam, *ACS Catal.*, 2018, **8**, 6751–6759.
55. F. R. Bagsican, A. Winchester, S. Ghosh, X. Zhang, L. Ma, M. Wang, H. Murakami, S. Talapatra, R. Vajtai, P. M. Ajayan, J. Kono, M. Tonouchi and I. Kawayama, *Sci. Rep.*, 2017, **7**, 1774.
56. M. T. Lusk, D. T. Wu and L. D. Carr, *Phys. Rev. B*, 2010, **81**, 155444.
57. X. Qi, W. Song and J. Shi, *PLoS One*, 2017, **12**, 173864.
58. S. Mondal, E. K. Karthik, L. Sahoo, K. Chatterjee, S. Marappan and U. K. Gautam, *Nanoscale*, , DOI:10.1039/D0NR00266F.
59. Y. Zhang, Z. Chen and Z. Lu, *Nanomaterials*, 2018, **8**, 261.
60. S. R. Lingampalli, U. K. Gautam and C. N. R. Rao, *Energy Environ. Sci.*, 2013, **6**, 3589–3594.
61. H.-T. Ren, S.-Y. Jia, Y. Wu, S.-H. Wu, T.-H. Zhang and X. Han, *Ind. Eng. Chem. Res.*, 2014, **53**, 17645–17653.
62. K. Chatterjee, M. Banoo, S. Mondal, L. Sahoo and U. K. Gautam, *Dalt. Trans.*, 2019, **48**, 7110–7116.
63. F. Su, S. C. Mathew, G. Lipner, X. Fu, M. Antonietti, S. Blechert and X. Wang, *J. Am. Chem. Soc.*, 2010, **132**, 16299–16301.



## CHAPTER 4.3

### Enhanced catalytic activity of Pd NPs towards Suzuki Cross-Coupling by g-C<sub>3</sub>N<sub>4</sub> photosensitization



#### Summary

The Suzuki coupling reactions are one of the most important class of catalytic C-C bond formation reaction. The development of new means of activating molecules and bonds over traditional catalysts for C-C bond formation is highly desirable for industrial application. Here, we report an effective strategy to improve the efficiency of traditional Pd catalysts for the Suzuki-Miyaura cross-coupling reactions by visible light irradiation using g-C<sub>3</sub>N<sub>4</sub> nanosheets as sensitizer. Pd NPs loaded onto g-C<sub>3</sub>N<sub>4</sub> NSs become electron-rich under visible-light irradiation due to generation excited electrons in g-C<sub>3</sub>N<sub>4</sub> which get transferred to the Pd NPs and thereby accelerates the rate-determining step by facilitating the oxidative addition of aryl halides. The Suzuki-Miyaura cross-coupling reaction was carried out in environmentally friendly aqueous media at room temperature. As synthesized Pd/g-C<sub>3</sub>N<sub>4</sub> NSs exhibited a very high turnover frequency of 1700 h<sup>-1</sup> for photocatalytic cross-coupling reactions as compared to the previously reported photocatalysts. The catalyst also demonstrated high recyclability for Suzuki cross-coupling reactions. The findings provide a facile design strategy for various C-C coupling reactions driven by visible light and sensitized by g-C<sub>3</sub>N<sub>4</sub>.

‡ Manuscript based on this work is under preparation.

### 4.3.1 Introduction

Cross-coupling reactions are versatile and powerful tools in organic synthesis for the carbon-carbon bond formation.<sup>1-5</sup> The Suzuki cross coupling reaction invented by the 2010 Nobel laureate Akira Suzuki is one of the most important reactions among all other C-C coupling reactions which has great significance in synthetic chemistry for production of biaryl compounds.<sup>6</sup> Therein, less reactive functionalized aryl halides are reacted with innocuous boronic acids, which are thermally stable, and moisture-stable, as well as non-toxic which is one of the major practical advantages of the Suzuki reaction. The Suzuki coupling reactions are generally performed using homogeneous catalysts such as palladium containing phosphine ligand, which has demonstrated relatively high activity as well as selectivity.<sup>7-12</sup> However, the recovery and separation of the molecular catalysts represent a major issue for sustainable development of the chemical industry.<sup>13,14</sup> Therefore, enormous efforts have been put to develop heterogeneous Pd based catalysts for Suzuki coupling reactions, including the stabilization or immobilization of Pd NPs on various supports, such as carbon nanotubes, high surface-area silica, polymers, double hydroxides, dendrimers, magnetic nanomaterials and metal oxides.<sup>15-19</sup> For instance, Au-Pd bimetallic NPs were reported as efficient catalysts for Suzuki coupling reactions.<sup>20</sup> Recently from our group, Pd NPs have been reported as an efficient catalyst towards Suzuki coupling reaction with very high TOF value.<sup>21,22</sup> Moreover, many of the processes with heterogeneous catalysts require relatively high temperature and prolonged reaction time. However, an elevated temperature induces the aggregation of Pd NPs dispersed on solid supports and thereby damages the recyclability of the catalysts. In some cases, the reactant molecules are not readily accessible to the active sites on the porous solid supports. Thus, catalyst systems with high reactivity, easy recyclability, in combination with the use of environment friendly solvents under mild reaction conditions are still considered as an important objective for Suzuki-Miyaura cross-coupling reactions.

### 4.3.2 Scope of the present investigation

Visible light driven photocatalysis is an attractive and greener approach to chemical transformations in various bond formation, cleavage and degradation reactions because the common organic reagents rarely absorb visible light, leaving it all to the photocatalysts, leading to a high degree of reaction yield and selectivity.<sup>23-25</sup> Suzuki cross-coupling reactions can also be triggered by photocatalysis route in the presence of suitable photocatalysts under visible light.<sup>26-30</sup>

Besides, the reaction temperature for Suzuki-Miyaura cross-coupling can be lowered to room temperature by maintaining a high yield by using a light-harvesting catalyst or photocatalyst. The visible light generates excited electrons and holes in a photocatalyst, which can be transferred to a reactant molecule to initiate the C–C coupling reactions. Such photochemical reactions for C–C bond formation can be carried out by using inorganic semiconductors that absorb visible light and has good stability. Xiao et al. reported Au-Pd bimetallic nanostructured photocatalyst for the C-C coupling reaction and obtained a high yield.<sup>20</sup> In this Au–Pd system, Au nanoparticles absorb visible light through localized surface plasmon resonance (LSPR) and transfer energetic electrons to Pd, thereby an enhanced reaction yield. Many semiconductor photocatalysts such as ZrO<sub>2</sub>, SiC, WS<sub>2</sub>, CeO<sub>2</sub>, TiO<sub>2</sub> etc. were used as the support material for loading of Pd NPs.<sup>31-33</sup> However, metal free semiconductors are very limited and have not been used widely for the C-C coupling reactions.

Two-dimensional (2D) g-C<sub>3</sub>N<sub>4</sub> NSs have gained enormous attention in various fields, including catalysis, energy storage and conversion, electronic devices and sensing because of their outstanding physical and chemical properties and excellent stability.<sup>34-36</sup> 2D g-C<sub>3</sub>N<sub>4</sub> NSs are good candidates as photocatalysts for Suzuki coupling reaction because they have band gaps ranging from 2.5 to 2.7 eV, falling in the visible range.<sup>37-40</sup> Till now there is only one report where Pd NPs loaded g-C<sub>3</sub>N<sub>4</sub> nanorod composite was used for the Suzuki coupling reactions.<sup>29</sup> However, their Pd loading was done by chemical reduction method and the catalytic activity was also very low. Therefore, 2D g-C<sub>3</sub>N<sub>4</sub> NSs, owing to their higher surface area and better carrier mobility, could be a better candidate for the support photocatalyst materials for Suzuki coupling reaction.

We report an effective photocatalyst system (Pd/g-C<sub>3</sub>N<sub>4</sub> NSs) for the efficient Suzuki-Miyaura cross-coupling reactions under visible light irradiation. Pd NPs loaded onto g-C<sub>3</sub>N<sub>4</sub> NSs become electron-rich under visible light irradiation due to generation excited electrons which get transferred to the Pd NPs and thereby accelerates the rate-determining step by facilitating the oxidative addition of aryl halides. The Suzuki-Miyaura cross-coupling reaction was carried out in environmentally friendly aqueous media at room temperature. As synthesized Pd/g-C<sub>3</sub>N<sub>4</sub> NSs exhibited a very high turnover frequency of 1700 h<sup>-1</sup> for photocatalytic cross-coupling reactions as compared to the previously reported photocatalysts. This material also demonstrated high recyclability for Suzuki cross-coupling reactions. The findings provide an efficient photocatalytic

route for the preparation of biaryl compounds and a facile strategy to design novel photocatalysts for various organic transformation reactions driven by visible light.

### **4.3.3 Methods**

#### **4.3.3.1 Synthesis of g-C<sub>3</sub>N<sub>4</sub> nanosheets**

The synthesis of bulk g-C<sub>3</sub>N<sub>4</sub> has been done using melamine as precursor materials. Typically, 6 g of melamine was taken in a crucible and covered with a lid. The crucible was placed in a muffle furnace at 525 °C for 4 h. Yellow coloured powder sample of bulk g-C<sub>3</sub>N<sub>4</sub> was obtained. The solid sample was then ground using a mortar and pestle. The bulk g-C<sub>3</sub>N<sub>4</sub> powder was then exfoliated by adding conc. sulphuric acid (20 ml) and then stirred for 5 minutes at 400 rpm. 50 ml of water was added to the bulk g-C<sub>3</sub>N<sub>4</sub>-acid mixture. The temperature of the solution increases due to the exothermic process and the yellow-coloured solution turns into pale yellow. After 1 minute of water addition, 50 g of ice was added into the reaction mixture to stop further exfoliation. The sample was then washed several times with water followed by ethanol. The sample was dried in oven at 50 °C overnight.

#### **4.3.3.2 Synthesis of Pd (3 wt%)/g-C<sub>3</sub>N<sub>4</sub>NSs**

The deposition of Pd on g-C<sub>3</sub>N<sub>4</sub> NSs was done photo-chemically in a 100 ml round bottom flask using a 400 W Xenon lamp. Typically, 100 mg g-C<sub>3</sub>N<sub>4</sub> NSs was dispersed in 90 ml of water containing 8 ml methanol and sonicated for 5 minutes. The solution was first bubbled with N<sub>2</sub> for 45 minutes and then maintained an inert atmosphere during rest of the reaction. To deposit 3 wt% of Pd, palladium chloride solution was slowly added by a syringe and was illuminated under constant stirring at 600 rpm. After addition of the palladium solution, the colour of the g-C<sub>3</sub>N<sub>4</sub> powder changed from light yellow to brown, indicating the deposition of Pd on the g-C<sub>3</sub>N<sub>4</sub>. The solution was then washed two times with water followed by ethanol and then centrifuged at 10000 rpm. The product was then dried overnight at 55 °C. Similarly, 1, 2, 4 wt % of Pd loading were performed by adding the respective palladium chloride solution of suitable concentration.

### 4.3.3.3 Photocatalytic SuzukiMiyaura cross-coupling reaction

In a typical reaction, 1:1 (ethanol:water, 5 mL) mixture was chosen as reaction medium. The reaction was carried out in a 10 mL round bottomed flask with 1 mmol of aryl halides, 1.2 mmol of phenyl boronic acid, 2 mmol of potassium carbonate and 0.9 mg of Pd/g-C<sub>3</sub>N<sub>4</sub> NSs. The mixture was irradiated under sunlight for 130 minutes under magnetic stir. The temperature of the reactant aliquot was monitored during the reaction (27-30 °C). Thin Layer Chromatography (TLC) was used to analyze the reaction progress after every 5 min interval. After desired time of light irradiation, the resulting mixture was centrifuged to remove the photo-catalyst. The product was extracted with ethyl acetate and water mixture and then purified by silica column-chromatography. <sup>1</sup>H & <sup>13</sup>C NMR confirmed the products by comparing the spectral data of the pure compounds.

### 4.3.3.4 Characterization

All other characterization techniques except the ones noted above are discussed in chapter 2.

### 4.3.4 Results and Discussion

Powder X-ray diffraction (PXRD) was used to investigate the crystallinity and the phase purity of the samples. **Figure 4.3.1** shows the XRD pattern of the bare g-C<sub>3</sub>N<sub>4</sub> NSs and Pd NPs deposited

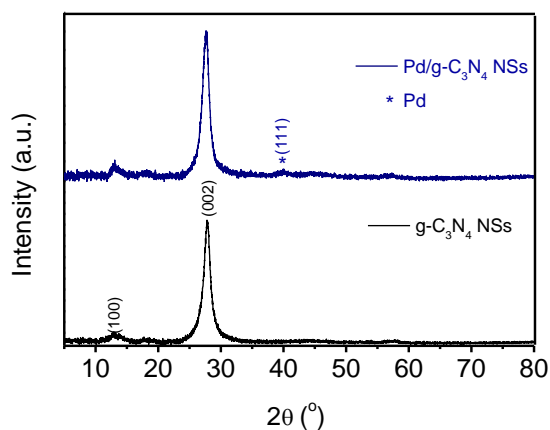


**Figure 4.3.1** PXRD patterns of the bare g-C<sub>3</sub>N<sub>4</sub> and Pd loaded g-C<sub>3</sub>N<sub>4</sub> NSs.

g- $C_3N_4$  NSs. The two typical peaks in the XRD pattern of bare g- $C_3N_4$ , located at 13.1 and 27.6, can be ascribed to the (100) and (002) planes of g- $C_3N_4$  respectively (180870-ICSD). The XRD pattern remained similar upon loading the sample with Au NPs (**Figure 4.3.1**). However, there were additional diffraction peaks with nearly low intensity at  $2\theta = 39.5^\circ$  corresponding to the (111) planes of Pd NPs (JCPDF#87-1526), suggesting that Pd NPs were successfully loaded on g- $C_3N_4$  NSs, as confirmed later transmission electron microscopy analysis.

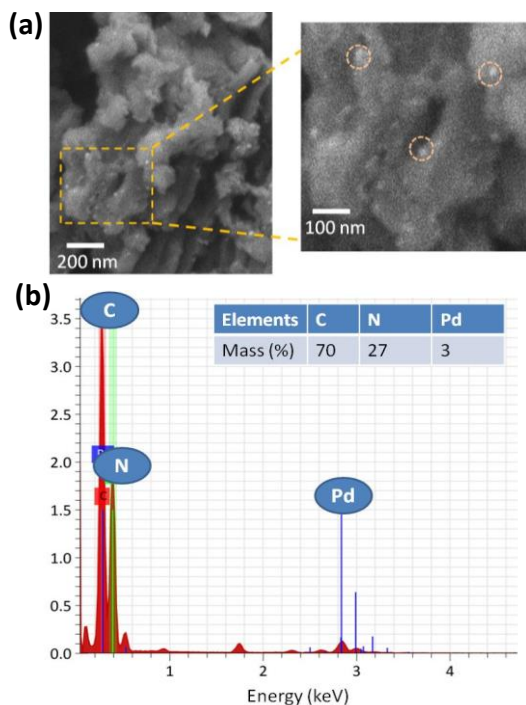


**Figure 4.3.2** (a) Typical FESEM images of the Pd loaded g- $C_3N_4$  NSs obtained after photo-deposition. (b) EDS spectra of the Pd/g- $C_3N_4$  nanosheets.

The morphologies of the as-synthesized samples were investigated by FESEM. As shown in **Figure 4.3.2a**, g- $C_3N_4$  possesses a sheet like structure and the Pd NPs were uniformly loaded on the g- $C_3N_4$  surface. Energy-dispersive X-ray spectroscopy (EDS) suggests the presence of 3 wt % Pd loading on the sample (**Figure 4.3.2b**). For better understanding of the nanostructures, the samples were characterized by TEM. The micrographs in **Figure 4.3.3a**, clearly shows the thin nanosheet morphology of the exfoliated g- $C_3N_4$  sample. Photo-deposition of the Pd(II) salt leads

to a uniform dispersion of Pd NPs with an average particle size of  $\sim 5.5$  nm on the surface of g-C<sub>3</sub>N<sub>4</sub> nanosheets as seen in **Figure 4.3.3a-d**. **Figure 4.3.3e** displayed a high-resolution TEM (HRTEM) image of a Pd NP deposited g-C<sub>3</sub>N<sub>4</sub>, confirming that the NPs are spherical and single-crystalline with an interplanar distance of 0.23 nm, which corresponds to the (111) plane of Pd. **Figure 4.3.3f** displays a typical selected area electron diffraction (SAED) pattern acquired on a Pd NPs loaded g-C<sub>3</sub>N<sub>4</sub> NSs.

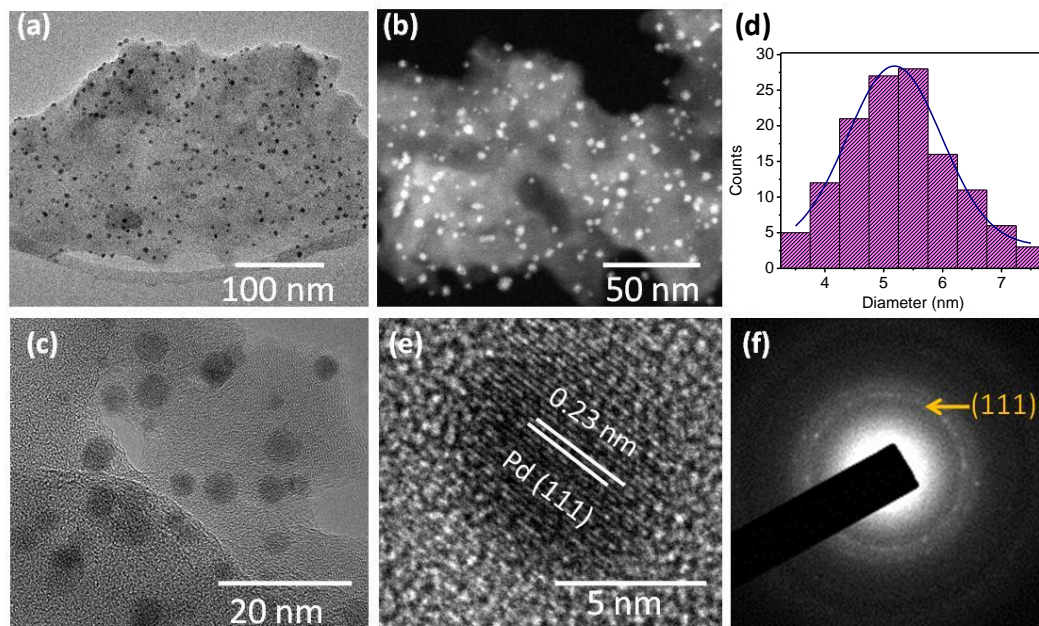


**Figure 4.3.3** (a,b,c) Typical TEM and STEM images of Pd NP loaded g-C<sub>3</sub>N<sub>4</sub> NSs. (d) the particle size distribution of the Pd NPs. (e) HRTEM image of a Pd NP on Pd/g-C<sub>3</sub>N<sub>4</sub> NSs showing the (111) planes of Pd NPs. (f) SAED pattern recorded on the Pd/g-C<sub>3</sub>N<sub>4</sub> NSs.

BET N<sub>2</sub> adsorption–desorption measurement was conducted to find out the specific surface area (SA) of the synthesized bulk and exfoliated g-C<sub>3</sub>N<sub>4</sub> NSs and Pd loaded g-C<sub>3</sub>N<sub>4</sub> NSs. The BET surface area of exfoliated g-C<sub>3</sub>N<sub>4</sub> NSs (40 m<sup>2</sup>/g) is nearly five times higher than that of bulk g-C<sub>3</sub>N<sub>4</sub>. The surface area of the Pd deposited g-C<sub>3</sub>N<sub>4</sub> NSs composite was found to be similar (38 m<sup>2</sup>/g) to the exfoliated g-C<sub>3</sub>N<sub>4</sub> NSs. A high SA of the catalyst is highly desirable for any chemical reaction (adsorption of organic substrates) and efficient deposition of Pd NPs.

The UV-visible diffuse reflectance spectra (DRS) and Tauc plot of the bare and Pd loaded g-C<sub>3</sub>N<sub>4</sub> NSs (**Figure 4.3.4a,b**) show that the band gap of Pd/g-C<sub>3</sub>N<sub>4</sub> NSs is marginally lower (2.57 eV) than the bare g-C<sub>3</sub>N<sub>4</sub> NSs (2.65 eV). Photoluminescence (PL) properties of the bare and Pd

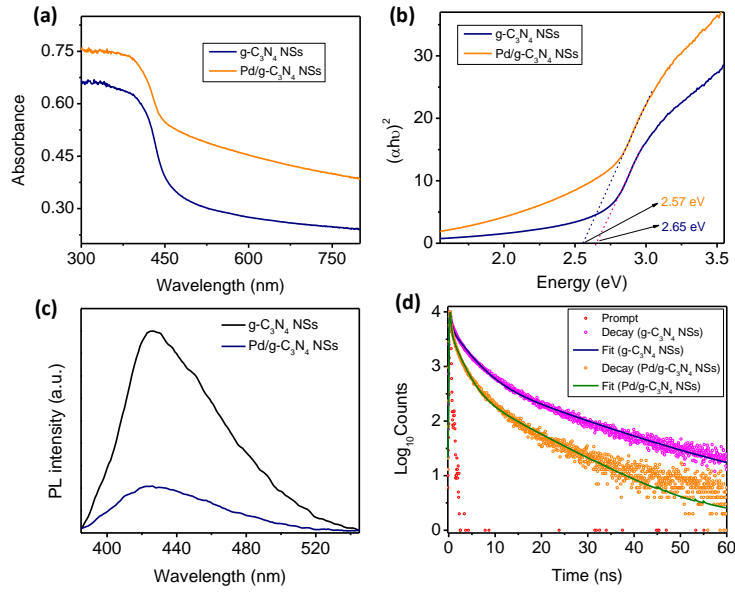


**Figure 4.3.4** (a) UV-Vis DRS of bare and Pd-loaded  $g\text{-C}_3\text{N}_4$  NSs. (b) Tauc plot of bare and Pd-loaded  $g\text{-C}_3\text{N}_4$  NSs. (c) PL emission intensities showing the intensity quenching in the case of Pd/ $g\text{-C}_3\text{N}_4$  NSs. (d) The PL decay plots for bare  $g\text{-C}_3\text{N}_4$  and Pd/ $g\text{-C}_3\text{N}_4$  NSs at 425 nm emission ( $\lambda_{ex}=375$  nm).

loaded  $g\text{-C}_3\text{N}_4$  NSs are displayed in **Figure 4.3.4c**, showing a significant decrease in the emission intensity in case of Pd/ $g\text{-C}_3\text{N}_4$  sample as compared to the bare  $g\text{-C}_3\text{N}_4$  NSs. The emission maximum is centred at 425 nm for both the samples. However, the decrease in the emission intensity corresponds to the decrease in the charge-recombination in Pd/ $g\text{-C}_3\text{N}_4$  NSs system due to presence of Pd. Further, we have analyzed average life-time of these two samples by using time-correlated single photon count (TCSPC) measurements. The sample was excited at 375 nm and emission decay kinetics were analyzed at 425 nm emission wavelength. Typical PL decay profiles of the bare and Pd loaded  $g\text{-C}_3\text{N}_4$  NSs are shown in **Figure 4.3.4d**. The data were fitted to a triple-exponential function (fitting parameters are given in the **Table 4.3.1**) and the average lifetime ( $\tau$ ), was calculated using the formula:

$$\text{Average lifetime } (\tau) = (\tau_1 A_1 + \tau_2 A_2 + \tau_3 A_3) / (A_1 + A_2 + A_3)$$



where,  $\tau_1$ ,  $\tau_2$ , and  $\tau_3$  represent emission lifetimes in three different time stages and  $A_1$ ,  $A_2$ , and  $A_3$  represent the amplitude of different emission lifetimes.

**Table 4.3.1:** PL decay lifetime analysis of bare and Pd NPs loaded g-C<sub>3</sub>N<sub>4</sub> NSs at an emission wavelength of 425 nm.

Triexponential emission (nm)	$\langle\tau\rangle$ ns	$\chi^2$	$\tau_1$ (ns)	$\tau_2$ (ns)	$\tau_3$ (ns)	$A_1$	$A_2$	$A_3$
425 nm (g-C <sub>3</sub> N <sub>4</sub> )	1.61	2.0	3.22	14.53	0.25	0.26	0.04	0.70
425 nm (Pd/g-C <sub>3</sub> N <sub>4</sub> )	0.71	1.67	1.80	8.77	0.16	0.17	0.02	0.81

The average emission lifetime of the g-C<sub>3</sub>N<sub>4</sub> (~1.61 ns) is longer than the Pd/g-C<sub>3</sub>N<sub>4</sub> (~0.71 ns). The decrease in  $\tau$  in presence of the Pd NPs is attributed to the transfer of the excited state electrons from g-C<sub>3</sub>N<sub>4</sub> to the Fermi level of Pd. In such a scenario, preferential transfer of long-lived excited electrons would result in lower  $\tau$  in the Pd loaded sample.

Electrochemical impedance spectroscopy (EIS) measurements were performed to investigate the charge transfer property of the materials. The Nyquist plots of Pd/g-C<sub>3</sub>N<sub>4</sub> and bare g-C<sub>3</sub>N<sub>4</sub> NSs are shown in **Figure 4.3.5**. The diameter of the semicircle in the high frequency region can be correlated to the charge transfer resistance ( $R_{ct}$ ) at the electrode and electrolyte interface. The Pd/g-C<sub>3</sub>N<sub>4</sub> NSs has a low  $R_{ct}$  (109 ohm) as compared to bare g-C<sub>3</sub>N<sub>4</sub> (123 ohm), suggesting that there was improved charge-transfer property in the Pd/g-C<sub>3</sub>N<sub>4</sub> nanocomposite system.

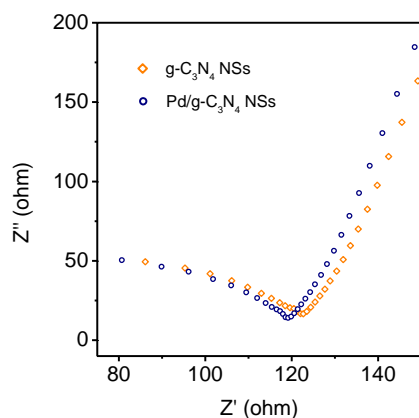
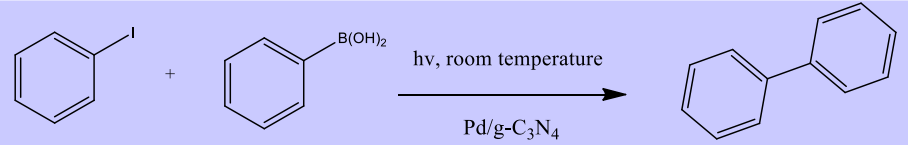


**Figure 4.3.5 (a)** EIS Nyquist plots of the bare g-C<sub>3</sub>N<sub>4</sub> and the Pd loaded g-C<sub>3</sub>N<sub>4</sub> nanosheets.

#### 4.3.4.1 Photocatalytic Suzuki cross-coupling reaction

The photocatalytic activity of the Pd/g-C<sub>3</sub>N<sub>4</sub> NSs was investigated using Suzuki-Miyaura cross-coupling reaction at room temperature under visible light irradiation (400-W Xenon lamp) as given in **Table 4.3.2**. The cross-coupling of 4-iodotoluene and phenylboronic acid were carried out in 4 ml solvent mixture using K<sub>2</sub>CO<sub>3</sub> as base in the presence of required amount of Pd/g-C<sub>3</sub>N<sub>4</sub> NSs. The reaction mixture was irradiated under visible light with continuous magnetic stirring for a necessary time period. The reactivity of Pd-based nanostructures for Suzuki-Miyaura cross coupling reaction has been shown to get influenced greatly by the solvent of the reaction mixture. We choose to carry out the reactions in aqueous media (water-ethanol mixture) as it is environmentally safe and industry-friendly. The ratio of the ethanol and water in the solvent mixture was found to significantly affect the catalysis rate as shown in **Figure 4.3.6a**. The reaction was relatively slower in either pure water or ethanol. The reaction rate increases when mixture of

**Table 4.3.2:** Photocatalytic Suzuki-coupling reaction under different conditions.



Entry	Changed parameters	hv	Yield (%)
1	No catalyst	+	—
2	g-C <sub>3</sub> N <sub>4</sub> NSs	+	—
3	Pd/g-C <sub>3</sub> N <sub>4</sub> NSs	+	94
4	Pd/g-C <sub>3</sub> N <sub>4</sub> NSs	—	35-38

water and ethanol were taken as solvent and reaches maximum with 1:1 volume mixture of water:ethanol as compared to the other ratios. The enhanced reaction kinetics in 1:1 volume mixture can be attributed to higher solubility of reactants as K<sub>2</sub>CO<sub>3</sub> is more soluble in water and phenylboronic acid and iodobenzene are better soluble in ethanol. Pd loading on g-C<sub>3</sub>N<sub>4</sub> NSs were optimized further to investigate the effect of surface coverage of Pd NPs on g-C<sub>3</sub>N<sub>4</sub> NSs for Suzuki-Miyaura cross coupling reaction. The Pd loading was varied from 0.5 to 5 wt% on g-C<sub>3</sub>N<sub>4</sub> NSs by varying the ratio of palladium salt and g-C<sub>3</sub>N<sub>4</sub> NSs. 3 wt % Pd loaded g-C<sub>3</sub>N<sub>4</sub> NSs yielded the highest activity after 120 min of light illumination under similar reaction conditions. The

reaction time decreases with increasing the Pd loading up to 3 wt%. With further increase of the Pd loading, the reaction took longer time (140 min) for completion. This could be due to higher surface coverage of Pd NPs at higher loading which reduces the light absorption capacity of g-C<sub>3</sub>N<sub>4</sub> NSs by shielding it. Further, we have optimized the Pd loading in the reaction mixture for 3 wt% Pd loaded g-C<sub>3</sub>N<sub>4</sub> NSs. With increasing the Pd content, the reaction time considerably reduced from 260 min (15 μg of Pd) to 75 min (57 μg of Pd). However, a maximum turnover frequency (TOF) of 1692 h<sup>-1</sup> was achieved using 0.9 mg of Pd/g-C<sub>3</sub>N<sub>4</sub> NSs (Pd loading ~27 μg). At this concentration, the cross-coupled product 4-phenyltoluene was isolated with a yield of 94% (**Figure 4.3.6b**). However, the reaction did not proceed using bare g-C<sub>3</sub>N<sub>4</sub> or in the absence of Pd/g-C<sub>3</sub>N<sub>4</sub> NSs even under visible light irradiation. The reaction yield was less than 40% in the absence of light irradiation (dark condition) using Pd/g-C<sub>3</sub>N<sub>4</sub> NSs in similar reaction condition (**Table 4.3.2**). The enhancement in the catalytic activity under visible light irradiation clearly indicates that the Suzuki coupling reaction was photo-sensitized by g-C<sub>3</sub>N<sub>4</sub> NSs.

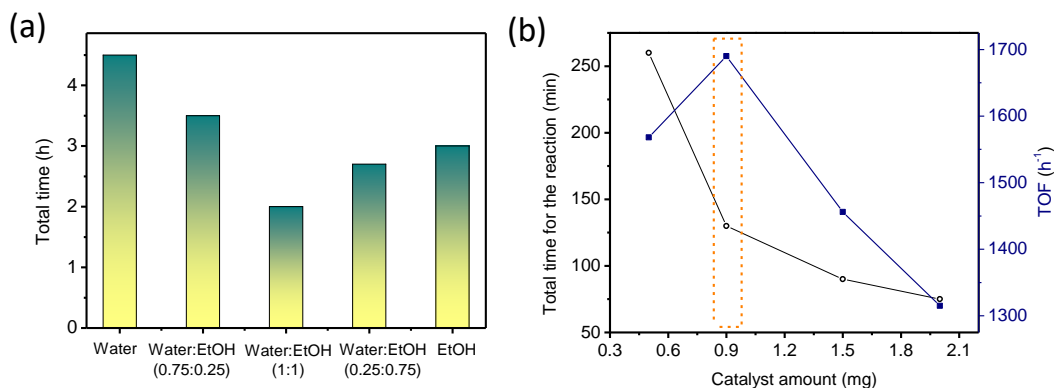


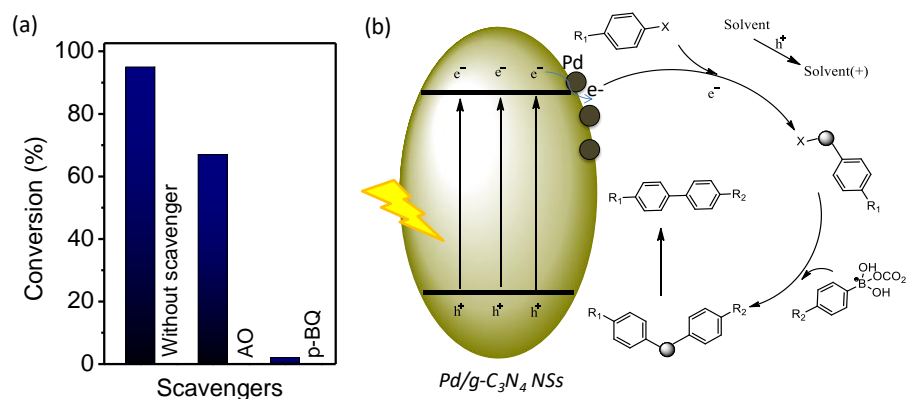
**Figure 4.3.6** (a) Conversion efficiency with different solvent ratios. (b) Optimization of the catalyst concentration for the Suzuki-coupling reaction.

In order to investigate the catalytic activity towards substituted aromatics, the coupling-reaction of various substituted aryl halide and arylboronic acid were performed under the optimized reaction condition. As given in **Table 4.3.3**, the aryl iodide containing electron donating groups showed the highest reactivity with TOF of 1692 h<sup>-1</sup> and 1620 h<sup>-1</sup> for 4-iodotoluene and 4-iodoanisole respectively as compared to the unsubstituted analogues. On the other hand, the aryl halide containing electron withdrawing group, 4-iodoacetophenone and 4-iodophenyl nitrile demonstrated slightly lower reactivity as compared to the methyl and methoxy substituents. The

coupling of 1-iodo-4-nitrobenzene with phenylboronic acid was the slowest (TOF  $\sim 500 \text{ h}^{-1}$ ). The photocatalytic Suzuki-coupling of aryl bromides in the presence of Pd/g-C<sub>3</sub>N<sub>4</sub> NSs were relatively slower (TOF  $\sim 300 \text{ h}^{-1}$ ) than that of the aryl iodides, as expected.

#### 4.3.4.2 Mechanistic investigation

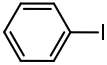
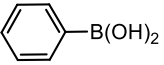
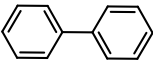
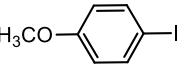
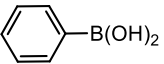
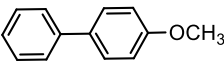
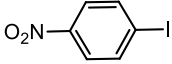
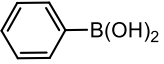
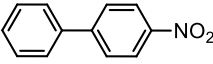
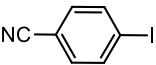
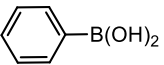
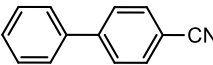
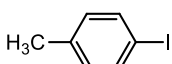
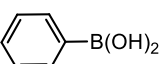
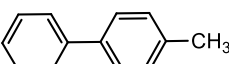
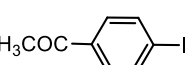
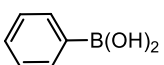
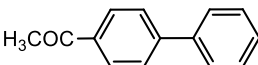
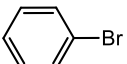
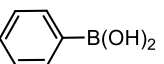
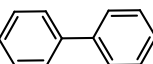
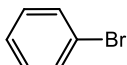
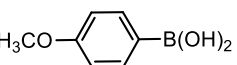
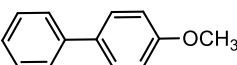
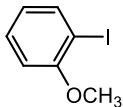
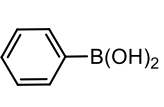
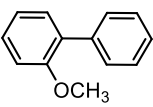
To elucidate the mechanism for the Suzuki-coupling reactions under photocatalytic condition by Pd/g-C<sub>3</sub>N<sub>4</sub> NSs, several controlled experiments using different scavenging reagents such as electron scavenger (p-benzoquinone) and hole scavenger (ammonium oxalate) were carried out during the photocatalytic reaction. When the reaction was performed by adding electron scavenger in the reaction aliquot of methyl iodobenzene and phenylboronic acid, negligible product ( $\sim 2\text{-}3\%$ ) was formed (**Figure 4.3.7a**), suggesting the restriction of the electron transfer from Pd to methyl iodobenzene. Moreover, when hole scavenger was added to the reaction aliquot to inhibit hole transfer to the borate salt, which generally suppresses the reaction in other reported literature, we still observed  $\sim 67\%$  conversion yield (**Figure 4.3.7a**). Hence, we hypothesize that the decreased yield might be due to the strong chemisorptions of AO on the active sites of Pd NPs loaded on g-C<sub>3</sub>N<sub>4</sub> NSs, hindering the oxidative addition of 4-iodobenzene during the photocatalytic reaction condition. The plausible mechanism for the photocatalytic Suzuki-coupling reaction on Pd/g-C<sub>3</sub>N<sub>4</sub> NSs is shown in **Figure 4.3.7b**.



**Figure 4.3.7** (a) Role of various scavengers during the photocatalytic Suzuki-coupling reaction. (b) A plausible reaction mechanism of Suzuki-coupling under photocatalytic condition using Pd/g-C<sub>3</sub>N<sub>4</sub> NSs photocatalyst.

The photo-stability and recyclability of the Pd/g-C<sub>3</sub>N<sub>4</sub> NSs were examined under similar reaction conditions to investigate the stability of the material. The Pd/g-C<sub>3</sub>N<sub>4</sub> NSs were separated from the reaction mixture by centrifugation after the completion of reaction, washed several times in water, ethyl acetate and ethanol in order to remove the reactant molecules from the surface of Pd/g-C<sub>3</sub>N<sub>4</sub> NSs and reused for the

**Table 4.3.3:** Photocatalytic performances of Pd/g-C<sub>3</sub>N<sub>4</sub> NSs for Suzuki coupling reaction of aryl halides with phenylboronic acids.

Entry	Aryl halide	Aryl Boronic Acid	Product	Time (min)	%Yield	TOF(h <sup>-1</sup> )
1.				150	>95%	1465
2.				140	>94%	1620
3.				510	>93%	500
4.				300	>94%	738
5.				120	>94%	1692
6.				250	>95%	978
7.				720	90%	300
8.				600	90%	360
9.				270	84%	801

**Reaction conditions:** 1 mmol of iodobenzene or one of its derivatives, 1.2 mmol of phenylboronic acid, 2 mmol of K<sub>2</sub>CO<sub>3</sub>, 4 mL of solvent (1:1 ethanol and water), 0.9 mg of 3 wt % Pd/g-C<sub>3</sub>N<sub>4</sub> NSs catalyst.

follow-up cycle. The reusability of Pd/g-C<sub>3</sub>N<sub>4</sub> NSs were studied using 4-iodotoluene and phenylboronic acid as substrates for a fixed time period (130 min). The Pd/g-C<sub>3</sub>N<sub>4</sub> NSs demonstrated remarkable stability with minimal loss catalytic performance in the successive 5 catalytic cycles (~12-14 % loss, **Figure 4.3.8a**). The PXRD pattern recorded for the used Pd/g-C<sub>3</sub>N<sub>4</sub> NSs further confirmed the stability of composite material (**Figure 4.3.8b**). The size of the Pd NPs on g-C<sub>3</sub>N<sub>4</sub> remains same (average size ~5.5 nm) even after photo-catalysis as observed from the TEM images (**Figure 4.3.8c**).

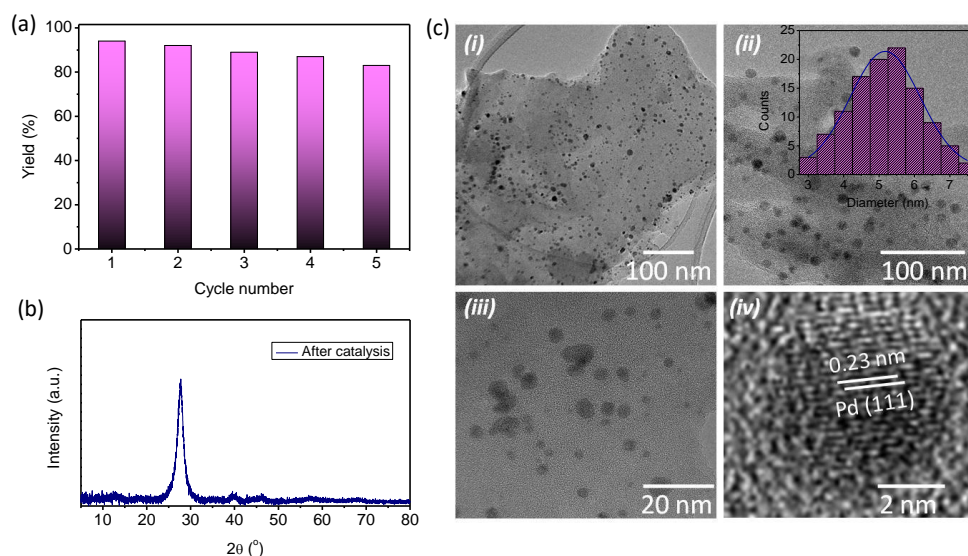


**Figure 4.3.8** (a) Reusability data showing the efficiency of Pd/g-C<sub>3</sub>N<sub>4</sub> nanosheets tested for five successive photocatalytic Suzuki-coupling reactions under natural sunlight. (b) PXRD pattern of used catalyst recovered after five cycles. (c) TEM image (i-iii), inset of 'ii' is the Pd particle size distribution plot. HR-TEM image (iv) of the Pd/g-C<sub>3</sub>N<sub>4</sub> nanosheets obtained after catalysis.

When the photo-catalytic performance of Pd/g-C<sub>3</sub>N<sub>4</sub> NSs was compared with the highly active photo-catalysts developed in the recent past for Suzuki-Miyaura cross-coupling reaction, the catalytic performance of Pd/g-C<sub>3</sub>N<sub>4</sub> NSs found to outperform most of the state-of-the-art catalyst as shown **Figure 4.3.9** (though the light source is different in all case). The TOF (1692 h<sup>-1</sup>) obtained for coupling of 4-iodotoluene and phenylboronic acid using Pd/g-C<sub>3</sub>N<sub>4</sub> NSs at room temperature is at least 5-10 times higher than most other carbon-based photo-catalyst reported at room temperature. The good performance of the Pd/g-C<sub>3</sub>N<sub>4</sub> NSs can be attributed to the photo-deposition techniques opted for the deposition of Pd NPs on g-C<sub>3</sub>N<sub>4</sub> NSs which provides a more

accessible surface area due to uniform decoration of Pd NPs and better contact between Pd and g-C<sub>3</sub>N<sub>4</sub> for facile electron transfer. The strongly bonding between Pd NPs and g-C<sub>3</sub>N<sub>4</sub> NSs prevents the agglomeration or leaching of the Pd species during catalytic cycles, leading to high stability.

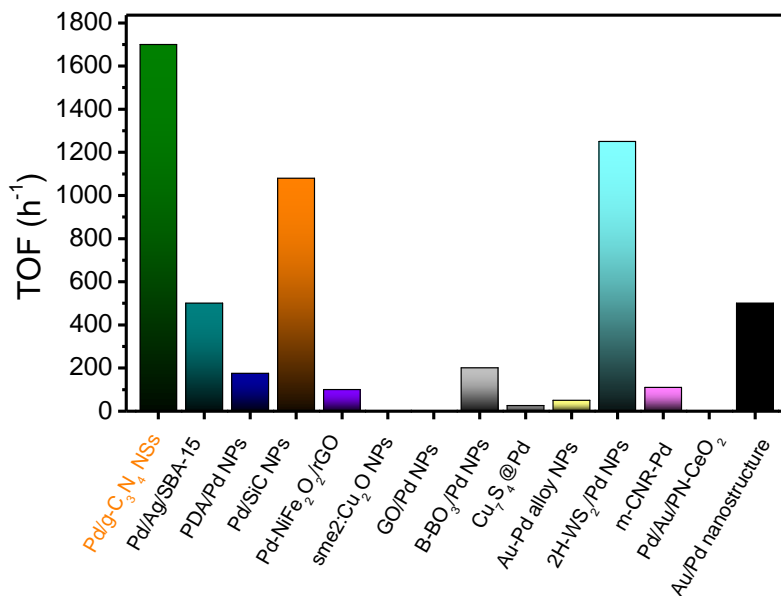


**Figure 4.3.9** Comparison of the TOF value of Pd/g-C<sub>3</sub>N<sub>4</sub> NSs with those of previously reported photocatalysts for Suzuki reactions.<sup>20,26-30,41-46</sup>

#### 4.3.5 Conclusions and further studies

In conclusion, we have designed an effective g-C<sub>3</sub>N<sub>4</sub> based photocatalyst system (Pd/g-C<sub>3</sub>N<sub>4</sub> NSs) for the efficient Suzuki-Miyaura cross-coupling reactions under visible light. Pd NPs loaded onto g-C<sub>3</sub>N<sub>4</sub> NSs via a photo-deposition method become electron-rich under visible-light irradiation due to the generation of excited electrons which get transferred to the Pd NPs and thereby accelerate the rate of the C-C coupling reaction. The Suzuki-Miyaura cross-coupling reaction was carried out in an environmentally friendly aqueous media at ambient condition. As synthesized Pd/g-C<sub>3</sub>N<sub>4</sub> NSs exhibited a very high turnover frequency of 1700 h<sup>-1</sup> for photocatalytic cross-coupling reactions when compared with previously reported photocatalysts. This material also demonstrated high recyclability for Suzuki cross-coupling reactions.

Even though the preliminary studies have demonstrated extremely high performance for Suzuki coupling reactions, a more careful comparison with other photocatalysts is needed as their

reaction conditions such as solvents, light source and intensity are different. It is also needed to perform light-intensity dependent catalytic study to find out the relation between intensity and reaction yield. Besides, atomic absorption spectroscopic (AAS) measurements need to be done to find out the leaching of Pd during the reaction under dark as well as photocatalytic condition. Finally, detailed X-ray photoelectron spectroscopy (XPS) studies on the catalyst-materials have to be performed to find out the oxidation states of various elements and catalyst-sensitizer interactions.

## Bibliography

1. K. M. Korch and D. A. Watson, *Chem. Rev.*, 2019, **119**, 8192–8228.
2. K. Kubota, T. Seo, K. Koide, Y. Hasegawa and H. Ito, *Nat. Commun.*, 2019, **10**, 111.
3. A. B. Pagett and G. C. Lloyd-Jones, *Org. React.*, 2019, 547–620.
4. T. Seo, N. Toyoshima, K. Kubota and H. Ito, *J. Am. Chem. Soc.*, DOI:10.1021/jacs.1c00906.
5. A. Suzuki, *J. Organomet. Chem.*, 2002, **653**, 83–90.
6. N. Miyaoura, K. Yamada and A. Suzuki, *Tetrahedron Lett.*, 1979, **20**, 3437–3440.
7. K. C. Nicolaou, P. G. Bulger and D. Sarlah, *Angew. Chemie Int. Ed.*, 2005, **44**, 4442–4489.
8. N. D. Patel, J. D. Sieber, S. Tcyrulnikov, B. J. Simmons, D. Rivalti, K. Duvvuri, Y. Zhang, D. A. Gao, K. R. Fandrick, N. Haddad, K. S. Lao, H. P. R. Mangunuru, S. Biswas, B. Qu, N. Grinberg, S. Pennino, H. Lee, J. J. Song, B. F. Gupton, N. K. Garg, M. C. Kozlowski and C. H. Senanayake, *ACS Catal.*, 2018, **8**, 10190–10209.
9. Yin and J. Liebscher, *Chem. Rev.*, 2007, **107**, 133–173.
10. Á. Molnár, *Chem. Rev.*, 2011, **111**, 2251–2320.
11. A. Buitrago Santanilla, M. Christensen, L.-C. Campeau, I. W. Davies and S. D. Dreher, *Org. Lett.*, 2015, **17**, 3370–3373.
12. L. Xue and Z. Lin, *Chem. Soc. Rev.*, 2010, **39**, 1692–1705.
13. A. B. Dounay and L. E. Overman, *Chem. Rev.*, 2003, **103**, 2945–2964.
14. A. Zapf and M. Beller, *Top. Catal.*, 2002, **19**, 101–109.
15. V. Polshettiwar, C. Len and A. Fihri, *Coord. Chem. Rev.*, 2009, **253**, 2599–2626.
16. N. T. S. Phan, M. Van Der Sluys and C. W. Jones, *Adv. Synth. Catal.*, 2006, **348**, 609–679.
17. M. Lamblin, L. Nassar-Hardy, J.-C. Hierso, E. Fouquet and F.-X. Felpin, *Adv. Synth. Catal.*, 2010, **352**, 33–79.
18. A. F. Littke and G. C. Fu, *Angew. Chemie Int. Ed.*, 2002, **41**, 4176–4211.
19. V. Polshettiwar, A. Decottignies, C. Len and A. Fihri, *ChemSusChem*, 2010, **3**, 502–522.
20. Q. Xiao, S. Sarina, E. Jaatinen, J. Jia, D. P. Arnold, H. Liu and H. Zhu, *Green Chem.*, 2014, **16**, 4272–4285.
21. L. Sahoo, S. Mondal, N. C. Beena, A. Gloskovskii, U. Manju, D. Topwal and U. K. Gautam, *ACS Appl. Mater. Interfaces*, 2021, **13**, 10120–10130.
22. L. Sahoo, S. Mondal, C. B. Nayana and U. K. Gautam, *J. Colloid Interface Sci.*, 2021, **590**, 175–185.

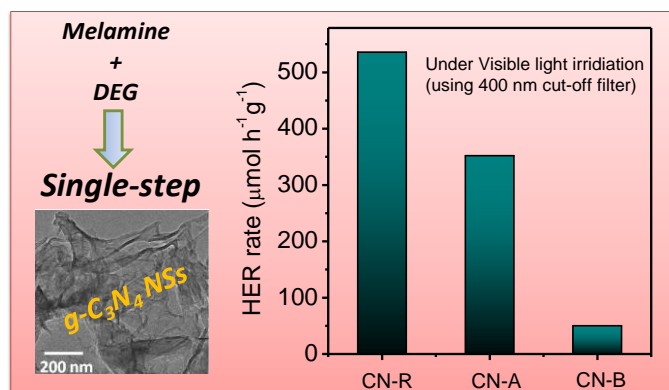


23. A. Kudo and Y. Miseki, *Chem. Soc. Rev.*, 2009, **38**, 253–278.
24. H. Li, F. Qin, Z. Yang, X. Cui, J. Wang and L. Zhang, *J. Am. Chem. Soc.*, 2017, **139**, 3513–3521.
25. Z. Wang, C. Li and K. Domen, *Chem. Soc. Rev.*, 2019, **48**, 2109–2125.
26. G. Singh, M. Kumar, K. Sharma and V. Bhalla, *Green Chem.*, 2016, **18**, 3278–3285.
27. Y. Li, Z. Zhang, L. Pei, X. Li, T. Fan, J. Ji, J. Shen and M. Ye, *Appl. Catal. B Environ.*, 2016, **190**, 1–11.
28. J. Cui, Y. Li, L. Liu, L. Chen, J. Xu, J. Ma, G. Fang, E. Zhu, H. Wu, L. Zhao, L. Wang and Y. Huang, *Nano Lett.*, 2015, **15**, 6295–6301.
29. X.-H. Li, M. Baar, S. Blechert and M. Antonietti, *Sci. Rep.*, 2013, **3**, 1743.
30. S. Zhang, C. Chang, Z. Huang, Y. Ma, W. Gao, J. Li and Y. Qu, *ACS Catal.*, 2015, **5**, 6481–6488.
31. Z. Jiao, Z. Zhai, X. Guo and X.-Y. Guo, *J. Phys. Chem. C*, 2015, **119**, 3238–3243.
32. D. Yim, F. Raza, J. H. Park, J.-H. Lee, H.-I. Kim, J.-K. Yang, I.-J. Hwang and J.-H. Kim, *ACS Appl. Mater. Interfaces*, 2019, **11**, 36960–36969.
33. M. Koohgard and M. Hosseini-Sarvari, *Catal. Commun.*, 2018, **111**, 10–15.
34. Y. Zhang, T. Mori, J. Ye and M. Antonietti, *J. Am. Chem. Soc.*, 2010, **132**, 6294–6295.
35. M. Ismael and Y. Wu, *Sustain. Energy Fuels*, 2019, **3**, 2907–2925.
36. X. Zhang, X. Xie, H. Wang, J. Zhang, B. Pan and Y. Xie, *J. Am. Chem. Soc.*, 2013, **135**, 18–21.
37. J. Fu, J. Yu, C. Jiang and B. Cheng, *Adv. Energy Mater.*, 2018, **8**, 1701503.
38. S. Yang, Y. Gong, J. Zhang, L. Zhan, L. Ma, Z. Fang, R. Vajtai, X. Wang and P. M. Ajayan, *Adv. Mater.*, 2013, **25**, 2452–2456.
39. X. Wang, K. Maeda, A. Thomas, K. Takanabe, G. Xin, J. M. Carlsson, K. Domen and M. Antonietti, *Nat. Mater.*, 2009, **8**, 76–80.
40. W.-J. Ong, L.-L. Tan, Y. H. Ng, S.-T. Yong and S.-P. Chai, *Chem. Rev.*, 2016, **116**, 7159–7329.
41. A. Xie, K. Zhang, F. Wu, N. Wang, Y. Wang and M. Wang, *Catal. Sci. Technol.*, 2016, **6**, 1764–1771.
42. K. Mori, M. Kawashima and H. Yamashita, *Chem. Commun.*, 2014, **50**, 14501–14503.
43. K. Sharma, M. Kumar and V. Bhalla, *Chem. Commun.*, 2015, **51**, 12529–12532.
44. F. Raza, D. Yim, J. H. Park, H.-I. Kim, S.-J. Jeon and J.-H. Kim, *J. Am. Chem. Soc.*, 2017, **139**, 14767–14774.
45. X. Zhao, J. Xie, X. Liu and X. Liu, *Appl. Organomet. Chem.*, 2019, **33**, e4623.
46. P. Verma, Y. Kuwahara, K. Mori and H. Yamashita, *J. Mater. Chem. A*, 2015, **3**, 18889–18897.



## CHAPTER 4.4

### One-step high-yield synthesis of high surface-area g-C<sub>3</sub>N<sub>4</sub> NSs for enhanced light absorption and solar H<sub>2</sub>-evolution



#### Summary

Visible-light driven hydrogen (H<sub>2</sub>) evolution from water (H<sub>2</sub>O) for renewable energy harvesting has triggered an extensive search for carbon-based semiconducting photocatalysts, as the traditional metal based semiconducting photocatalysts suffer from limited H<sub>2</sub> evolution efficiency due to low surface area and fast recombination of photogenerated excitons. 2D g-C<sub>3</sub>N<sub>4</sub> is a highly promising metal-free H<sub>2</sub>-evolution photocatalyst. However, due to its low surface area, they are further exfoliated using laborious, energy-consuming processes that gives high surface 2D nanosheets (NSs), but in low yields. Moreover, g-C<sub>3</sub>N<sub>4</sub> absorbs only part of the solar radiation due to a high band-gap of 2.7 eV. Herein, we report a strategy for one-step synthesis of high surface-area, red-shifted visible light active, high surface-area g-C<sub>3</sub>N<sub>4</sub>NSs. The NSs were synthesized by simple calcinations of melamine and diethyleneglycol mixture at 520°C for 4 h under N<sub>2</sub> atmosphere. The specific surface area of the synthesized sample was found to be ~3 times higher than the bulk g-C<sub>3</sub>N<sub>4</sub>, thereby offering more active sites for the catalytic reactions and eliminating the need for an extra, low-yield preparation step involving the high temperature or chemical exfoliation. The as-synthesized g-C<sub>3</sub>N<sub>4</sub> NSs showed an enhanced H<sub>2</sub> evolution rate (530  $\mu\text{mol h}^{-1} \text{g}^{-1}$ ) under visible light irradiation compare to the as-synthesized conventional g-C<sub>3</sub>N<sub>4</sub> (87  $\mu\text{mol h}^{-1} \text{g}^{-1}$ ).

‡ *Manuscript based on this work is under preparation.*

#### 4.4.1 Introduction

Avoidance of fossil fuels as an energy resource has been an urgent call in order to fight against not only energy environmental issues but also gradually increasing global energy crisis due to the depletion of conventional energy resources.<sup>1-3</sup> Hence, a search for an alternative to conventional energy resources has been of utmost importance in current time. Due to high energy capacity and being non-toxic, the utilization of hydrogen in fuel cell shows promising potential in this regard.<sup>4</sup> As the atmospheric content of hydrogen is very less, therefore solar energy-driven water-splitting has grown interest among researchers to build a sustainable way of producing hydrogen.<sup>5-9</sup> However, the existing catalysts are still not sufficient as good enough to realize the above-stated potential on an industrial scale because of their low durability under light irradiation and dependence on toxic metal-based systems.<sup>10-13</sup> Furthermore, nanostructuring of semiconducting materials bring more options in utilization in industries due to high surface area as compared to bulk.<sup>14,15</sup> Therefore, metal-free substitutes of present catalysts with enhanced energy conversion efficiency are highly desirable.<sup>16-18</sup> The photocatalytic activity has been realized using many metal-free materials like graphene oxide, carbon nanotubes, carbon quantum dots, hexagonal boron nitride, graphitic carbon nitride etc. as a component in photocatalyst system.<sup>13,19-24</sup>

Among the above metal-free semiconducting materials, graphitic carbon nitride (g-C<sub>3</sub>N<sub>4</sub>) has drawn immense attention to their application in various photocatalytic processes.<sup>25-29</sup> However, its bulk form limits high solar-to-hydrogen conversion efficiency because of its charge transport, restricted mass transfer to active sites due to multi-layered stacking, and low visible light absorption. In this broad context, significant improvement of g-C<sub>3</sub>N<sub>4</sub> efficiency can be achieved upon making nanosheets out of the layered structure to realize high surface-area and engineering some defect states in the intrinsic band structure either employing dopant or tuning its synthetic strategy.

#### 4.4.2 Scope for the present investigation

Several strategies have been adopted to reduce the rate of the electron-hole recombination and facilitate the transfer of photogenerated excitons to reactants such as loading of noble metal nanoparticles as plasmonic materials and co-catalysts,<sup>23,30-32</sup> non-metal elemental doping (e.g., N, O, B, C, S, P, F doping),<sup>33-38</sup> isotype heterojunction,<sup>39-42</sup> heterojunction/Z-scheme with other

semiconductors etc.<sup>43-46</sup> On the other hand, there are multiple approaches to make a facile mass transfer by using exfoliated g-C<sub>3</sub>N<sub>4</sub> nanosheets instead of multi-layered catalysts. Niu et al. showed a strategy for exfoliation by thermal oxidation etching of bulk g-C<sub>3</sub>N<sub>4</sub> at 500 °C for 2 hr at 5 °C/min in static air.<sup>47</sup> Yang et al. has demonstrated liquid exfoliation by treating dispersion of bulk g-C<sub>3</sub>N<sub>4</sub> in different solvents (IPA/NMP/Acetone) in sonication bath for 10 h.<sup>48</sup> High yield (60%) exfoliation strategy was achieved for the first time by Zhu and co-workers. 10 volume % aqueous solution of 98 wt% H<sub>2</sub>SO<sub>4</sub> was employed for chemical etching of layered bulk g-C<sub>3</sub>N<sub>4</sub> to get 60% nanosheets with large surface area (>200 m<sup>2</sup> g<sup>-1</sup>).<sup>49</sup> Zhang et al. employed another greener approach to yield g-C<sub>3</sub>N<sub>4</sub> nanosheets at large scale by sonicating aqueous dispersion of bulk g-C<sub>3</sub>N<sub>4</sub> for 16h.<sup>50</sup>

But those approaches mentioned above are multistep processes involving using long time and energy-consumption. Therefore, there is a high demand for a single-step synthesis procedure for making high surface-area g-C<sub>3</sub>N<sub>4</sub> nanosheets. A solution can potentially be achieved by finding out such a single-step synthetic method where after synthesis of g-C<sub>3</sub>N<sub>4</sub> layers, they don't get stacked too much so that nanosheets can be generated when dispersing the as-synthesized material in solvent/water without further processing. Vu et al. showed that under Ar atmosphere heat treatment leads to self-exfoliation of the layered structure into nanosheets after the polycondensation of precursors of g-C<sub>3</sub>N<sub>4</sub> (e.g. melamine, urea, thiourea etc.) to yield the thin carbon nitride structure.<sup>51</sup> Despite this work shows a single step synthetic strategy to get nanosheets but its low yield and low absorption in the visible still limit its application in visible light photocatalysis. Herein, we report a facile one-step synthesis of red-shifted g-C<sub>3</sub>N<sub>4</sub> nanosheets by a simple calcination of melamine and diethyleneglycol mixture under Ar-atmosphere.

### **4.4.3 Methods**

#### **4.4.3.1 Synthesis of bulk g-C<sub>3</sub>N<sub>4</sub>**

The synthesis of bulk g-C<sub>3</sub>N<sub>4</sub> has been done using melamine as precursor materials. Typically, 3 g of melamine was taken in an alumina boat. The boat was placed in a tube furnace at 520 °C for 4 h under Ar atmosphere. Yellow coloured powder sample of bulk g-C<sub>3</sub>N<sub>4</sub> was obtained. The solid sample was then ground using a mortar and pestle and washed with water and ethanol. The sample

synthesized under Ar atmosphere is termed as g-C<sub>3</sub>N<sub>4</sub>-A and bulk sample synthesized without purging any inert gas is termed as g-C<sub>3</sub>N<sub>4</sub>-B.

#### **4.4.3.2 One step synthesis of nanosheets of g-C<sub>3</sub>N<sub>4</sub>**

The nanosheets of g-C<sub>3</sub>N<sub>4</sub> were synthesized by a one-step calcinations route using a mixture of melamine and diethyleneglycol as starting materials. Typically, 3 g of melamine was mixed with 1 ml of diethyleneglycol by using a mortar and pestle. Next, the mixture was transferred in an alumina boat and placed in a tube furnace at 520 °C for 4 h under Ar atmosphere. Brown coloured powder sample was obtained. The solid brown sample was then ground using a mortar and pestle to get fine powder and washed with water and ethanol.

#### **4.4.3.3 Photocatalytic H<sub>2</sub>-evolution reaction**

Reactions were carried out in a glass top-irradiation reaction vessel. Photo-reduction of water to H<sub>2</sub> was performed in an aqueous dispersion of catalyst containing 10 volume% of triethanolamine (TEOA) as a sacrificial reagent. A typical photocatalytic hydrogen evolution reaction was performed by dispersing 10 mg of g-C<sub>3</sub>N<sub>4</sub> catalyst powder in a 30 ml aqueous solution containing TEOA. In the case of deposition of Pt, an appropriate amount of H<sub>2</sub>PtCl<sub>6</sub> was dissolved in the reactant solution. The reactant solution was purged with N<sub>2</sub> gas for 1 h to remove air completely prior to irradiation under a 400 W Xe-lamp. The wavelength of the incident light was controlled by using an appropriate cut-off filter attached with a water circulation to remove heat. The evolved gases were analyzed by gas chromatography. The experimental error in the rate of H<sub>2</sub> evolution was within 15 %. To study the stability of the material, after 1<sup>st</sup> cycle, the same solution was degassed and then performed the 2<sup>nd</sup> cycle of the reaction.

#### **4.4.3.3 Characterization**

All other characterization techniques except the ones noted above are discussed in chapter 2.

#### **4.4.4 Results and discussion**

The photographs of as-synthesized samples CN-B, CN-A and CN-R is displayed in **Figure 4.4.1a**, showing that CN-B, CN-A are light yellow, dark yellow coloured respectively whereas CN-R is brown coloured indicating absorption of a larger fraction of solar radiation. **Figure 4.4.1b** shows

X-ray diffraction (XRD) patterns of CN-B, CN-A and CN-R samples. CN-B and CN-A XRD pattern has two peaks at  $13.1^\circ$  and  $27.6^\circ$ , which are assigned to in-plane repeating units (100) of the tri-s-triazine matrix and the interlayer distances of parallel conjugated aromatics (002), respectively. The characteristic diffraction peaks of CN-R are located at  $13.1^\circ$  and  $27.6^\circ$ , indicating that CN-R has the same structure as CN-B and CN-A. The most intense peak of CN-R at  $27.6^\circ$  becomes less pronounced, indicating that the number of layers in the structure is reduced to form a thinner structure, which agrees with surface-area studies and TEM studies. Both the reduction in thickness and the nanosheet morphology are beneficial for mass transfer during photocatalysis to enhancing the activity.

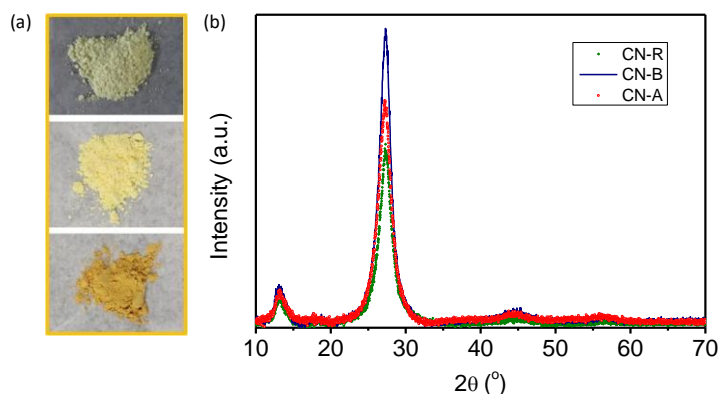


**Figure 4.4.1** (a) Photographic images of the samples after the synthesis showing the changes in colour in the three samples CN-B (a1), CN-A (a2) and CN-R (a3) respectively. (b) PXRD pattern of the as-synthesized samples CN-B, CN-A and CN-R.

The structure, morphology and texture of the synthesized materials were investigated by transmission electron microscopy (TEM). The TEM images of CN-B, CN-A, CN-R are displayed in **Figure 4.4.2**. CN-R shows translucent thin sheet like morphology with a folded edges surface, whereas CN-B and CN-A has thick sheet structure. The specific surface area of all synthesized samples was analyzed through BET measurements (**Figure 4.4.3**). CN-R has a BET specific surface area of  $27.0 \text{ m}^2\text{g}^{-1}$ , which is nearly 4 and 3 times higher than that of CN-B ( $7.1 \text{ m}^2\text{g}^{-1}$ ) and CN-A ( $10.1 \text{ m}^2\text{g}^{-1}$ ) respectively, suggesting that most CN-R samples should contain thin nanosheet morphology, thereby can provide more number of active sites for the photocatalytic reactions.

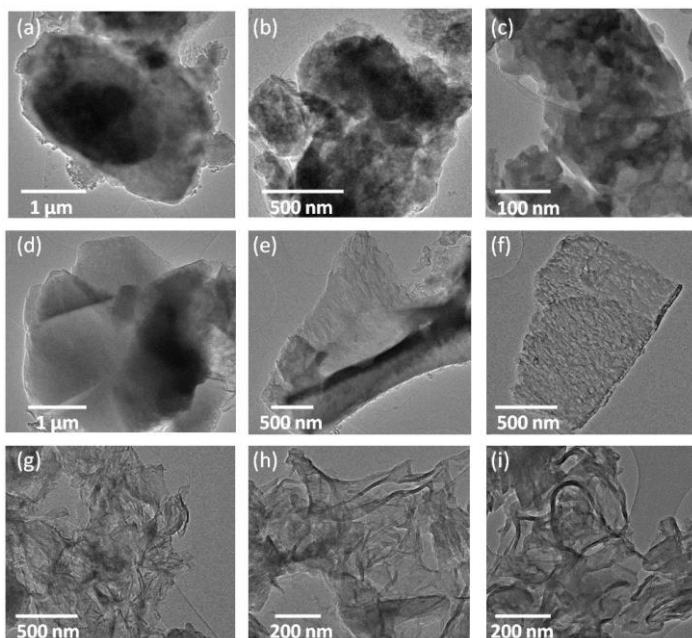


**Figure 4.4.2** (a,b,c) TEM images of bulk  $g\text{-C}_3\text{N}_4$  (CN-B). (d,e,f) TEM images of  $g\text{-C}_3\text{N}_4$  synthesized in Ar-purging (CN-A). (g,h,i) TEM images of red shifted  $g\text{-C}_3\text{N}_4$  synthesized by treating DEG with melamine precursor (CN-R).

The as-synthesized samples were characterized by FTIR spectroscopy. The FTIR spectra of CN-A and CN-R (**Figure 4.4.4**) revealed broad peaks between  $3000$  and  $3450\text{ cm}^{-1}$ , corresponding to the N-H bond of free amino groups, whereas the peaks in the range of  $1200\text{-}1700$

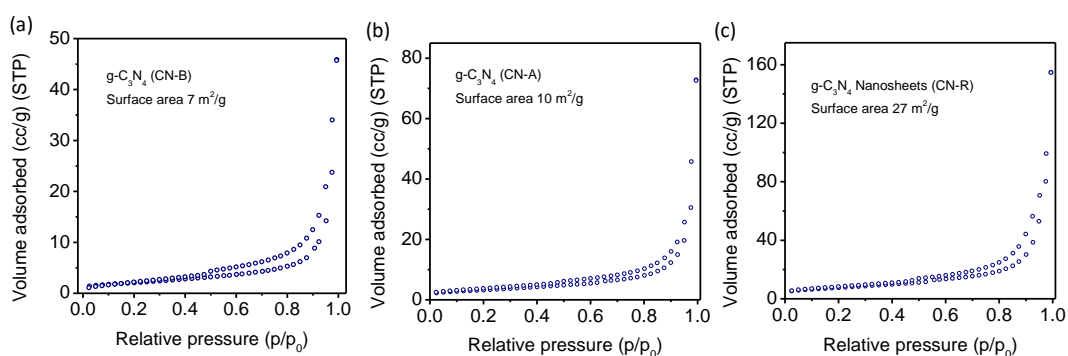


**Figure 4.4.3**  $\text{N}_2$  gas adsorption-desorption plots for CN-B (a), CN-A (b) and CN-R (c) samples respectively.



$\text{cm}^{-1}$  can be attributed to the vibration of the heptazine-derived repeating units, In addition, the peak at  $805 \text{ cm}^{-1}$  arises from the s-triazine-ring vibration. There are no significant differences in the FTIR spectra of CN-A and CN-R samples as well as that of CN-B, indicating the presence of similar bands in all the samples.

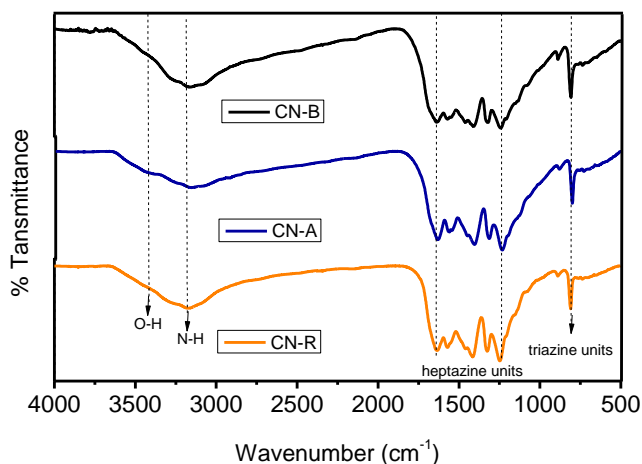


**Figure 4.4.4** Fourier-transform infrared (FT-IR) spectra of the CN-B, CN-A and CN-R samples.

The optical properties of the synthesized materials were investigated by UV-visible absorption and photoluminescence spectroscopy. **Figure 4.4.5a** is the UV-Visible DRS spectra of CN-A and CN-R. From the spectra it can be seen that onset of the absorbance for the CN-R is nearly 760 nm while CN-A has the onset  $\sim 500$  nm suggesting that the CN-R is highly red-shifted. The PL emission spectra of CN-A and CN-R are displayed in **Figure 4.4.5b**. The PL spectrum of CN-R showed an emission band centred at 465 nm, which is red-shifted in comparison to the CN-A ( $\lambda_{\text{em}}$  is 450 nm). The average life time of the excited electrons was analyzed by using time-correlated single photon count (TCSPC) measurements.

The sample was excited at 375 nm and emission decay kinetics was analyzed at 450 nm emission wavelength. Typical PL decay profiles of the CN-A and CN-R samples are shown in **Figure 4.4.5c**. The data were fitted to a triple-exponential function (fitting parameters are given in the **Table 4.4.1**) and the average lifetime ( $\tau$ ), was calculated using the formula:

$$\text{Average lifetime } (\tau) = (\tau_1 A_1 + \tau_2 A_2 + \tau_3 A_3) / (A_1 + A_2 + A_3)$$

where,  $\tau_1$ ,  $\tau_2$ , and  $\tau_3$  represent emission lifetimes in three different time stages and  $A_1$ ,  $A_2$ , and  $A_3$  represent the amplitude of different emission lifetimes. The average emission lifetime of the CN-A (2.68 ns) is longer than the CN-R (1.90 ns). The decrease of average life time value in case of CN-R might be due to the presence of defect states within the system.

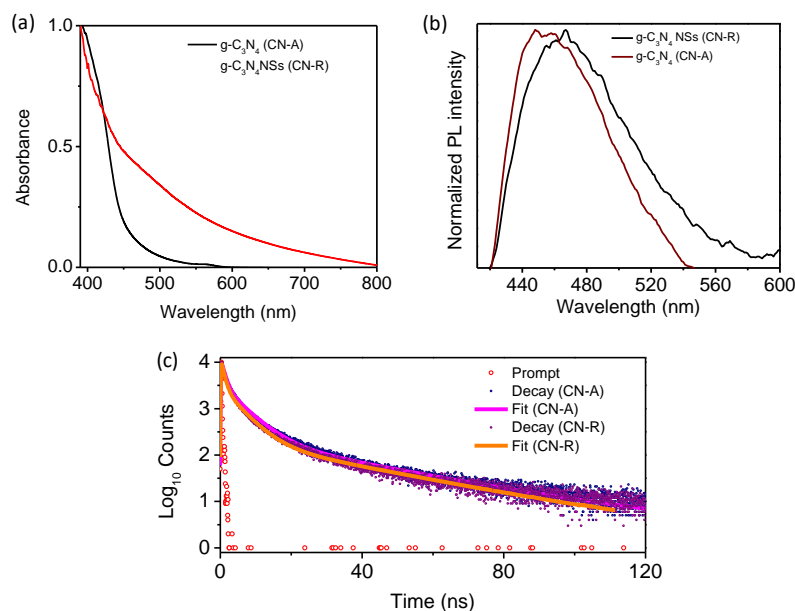


**Figure 4.4.5** (a) UV-visible diffuse reflectance spectra of CN-A and CN-R. (b) PL emission spectra of CN-A and CN-R samples showing the intensity quenching in the case of CN-R. (c) The PL decay plots for CN-A and CN-R at 425 nm emission ( $\lambda_{ex} = 375$  nm).

**Table 4.4.1:** PL decay lifetime analysis of CN-R and CN-A samples.

Triexponential emission (nm)	$\langle\tau\rangle$ ns	$\chi^2$	$\tau_1$ (ns)	$\tau_2$ (ns)	$\tau_3$ (ns)	$A_1$	$A_2$	$A_3$
(465 nm) CN-A	2.68	1.61	5.31	29.87	0.99	0.26	0.02	0.72
(465 nm) CN-R	1.90	1.72	4.42	0.78	27.49	0.21	0.78	0.01

The separation of photogenerated exciton of the as-prepared CN-A and CN-R samples were checked by performing transient photocurrent measurements. As displayed in **Figure 4.4.6**, the photocurrent of CN-R is the highest during six light on-off cycles under irradiation of a 400 W

Xe-lamp attached with 400 nm cut off filter, suggesting that the photogenerated electron-hole separation of CN-R is more efficient as compare to the CN-A sample.

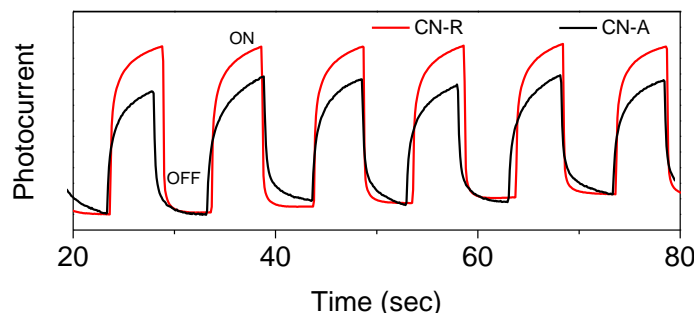


**Figure 4.4.6** Transient photocurrent recorded for CN-A and CN-R samples using 400-W Xe lamp (attached with a 400 nm cut-off filter).

## 4.4.5 Application

### 4.4.5.1 Photocatalytic performance for H<sub>2</sub>-evolution

The hydrogen evolution experiments were performed under irradiation of a 400 W Xe lamp to evaluate the photocatalytic performance of the CN-B, CN-A and CN-R samples as mentioned above. We have first checked the HER performance by loading different amounts (wt%) of Pt on the g-C<sub>3</sub>N<sub>4</sub> sample as shown in **Figure 4.4.7a**. From the experiment, the best activity was achieved when the Pt loading is 3 wt% and upon further increase with the loading amount the activity also decreases. Therefore, 3 wt% loading was taken for all the HER experiments. It was observed that both CN-A and CN-R show better photocatalytic H<sub>2</sub> evolution performance compared to the CN-B under the identical experimental conditions. **Figure 4.4.7b** indicates the hydrogen evolution rates of bulk (CN-B), bare g-C<sub>3</sub>N<sub>4</sub> nanosheets (CN-A) and red shifted g-C<sub>3</sub>N<sub>4</sub> nanosheets (CN-R). CN-R produces 530  $\mu\text{mol h}^{-1} \text{g}^{-1}$  hydrogen gas under 400 W Xenon light using a 400 nm cut off filter. It was calculated that CN-R and CN-A exhibits 6 times & 4 times higher photocatalytic H<sub>2</sub> production activity as compared to the bulk g-C<sub>3</sub>N<sub>4</sub> (CN-B). This suggests that CN-R structure features increased active sites, higher surface area, and low charge recombination, which responsible for enhanced photocatalytic performance.

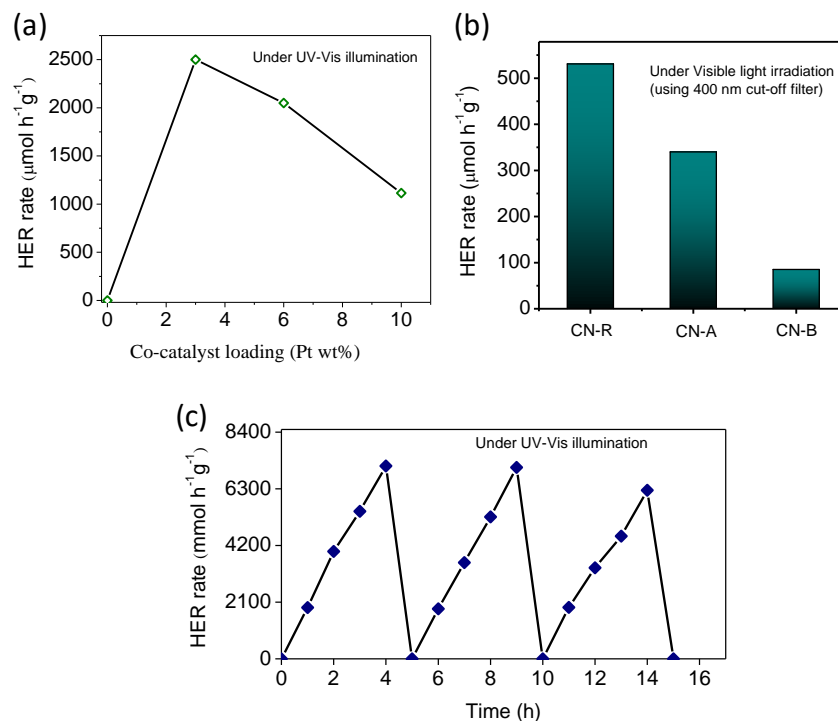


**Figure 4.4.7** (a) Photocatalytic H<sub>2</sub> production rate exhibited by with different co-catalyst loading.(b)Photocatalytic HER of CN-B, CN-A and CN-R samples under 400 W Xe-lamp attached with 400 nm cut off filter. (c) Recyclability test for H<sub>2</sub> production experiments using CN-R.

In addition, the CN-R also shows a relatively higher light absorbance in the visible light region as shown in DRS spectra, a lower exciton recombination rate as indicated with PL spectra and higher photocurrent in transient photocurrent measurement. All of these characterization data are consistent and supporting the improved HER performance of the CN-R sample. To investigate the stability of CN-R sample, cycling tests were performed under the identical reaction conditions. **Figure 4.4.7c** is the stability of the CN-R sample for three consecutive cycles and show slight decline after each cycle. Also, it was observed that the material shows a linear relationship between the H<sub>2</sub> production rate and time.

#### 4.4.5.2 Comparison of HER activity with state-of-art catalysts.

Under 400 W-Xe lampirradiations (using 400 nm cut-off filter), our synthesized CN-R produces H<sub>2</sub> from water at a steady rate of  $530 \mu\text{mol h}^{-1} \text{g}^{-1}$  whereas bare g-C<sub>3</sub>N<sub>4</sub> (CN-A) shows HER rate as  $340.08 \mu\text{mol h}^{-1} \text{g}^{-1}$  which is 4 times higher than HER activity shown by bulk g-C<sub>3</sub>N<sub>4</sub> ( $86 \mu\text{mol h}^{-1} \text{g}^{-1}$ ).

Although other exfoliated bare g-C<sub>3</sub>N<sub>4</sub> nanosheets show higher activity they limit their industrial utilization because of several reasons. For example, under 300 W Xenon Light using 400 nm cut-off filter Niu et al. could achieve a significantly higher (800  $\mu\text{mol h}^{-1} \text{g}^{-1}$ ) HER rate with 6wt % Pt loaded exfoliated g-C<sub>3</sub>N<sub>4</sub> nanosheets synthesized by thermal oxidation etching method with very low yield (6%).<sup>47</sup> Yang et al. observed a great enhancement in HER activity (1860  $\mu\text{mol h}^{-1} \text{g}^{-1}$  under 300 W Xe lamp (420 nm cut-off filter) using g-C<sub>3</sub>N<sub>4</sub> nanosheets obtained in a liquid exfoliation process. Any liquid exfoliation strategy takes 10-16 h of additional time for sonication (energy consuming) and also involves a large volume of solvents (IPA/Acetone/NMP/H<sub>2</sub>O).<sup>48</sup> In case of sonication of an aqueous dispersion of bulk g-C<sub>3</sub>N<sub>4</sub>, it can exfoliate only 0.15 mg/ml in H<sub>2</sub>O.<sup>50</sup> Because of this high solvent volume requirement, this exfoliation process has not been realized beyond the 100 mg scale. Although the chemical exfoliation pathway can yield 60% nanosheets from bulk g-C<sub>3</sub>N<sub>4</sub>, it shows only 230  $\mu\text{mol h}^{-1} \text{g}^{-1}$  HER rate (300 W Xe lamp, 420 nm cut-off filter).<sup>49</sup> Chemical exfoliation also limits its industrial application because it involves exothermic steps, the use of hazardous chemicals like H<sub>2</sub>SO<sub>4</sub>, HNO<sub>3</sub> and an additional cooling set-up to maintain 600 °C during the exfoliation. From the above discussion, it can be concluded that this work shows an optimum improvement in order to find a large scale facile synthetic strategy to get g-C<sub>3</sub>N<sub>4</sub> nanosheets as 4 times improvement in HER activity is observed by using bare g-C<sub>3</sub>N<sub>4</sub> nanosheets obtained in a single process with about 50% yield.

#### 4.4.6 Conclusions and further studies

In this preliminary study we have we designed a strategy for one-step synthesis of highly red-shifted visible light active, high surface-area g-C<sub>3</sub>N<sub>4</sub> NSs. The synthesized NSs have nearly 3 times higher specific surface area as compared to the bulk g-C<sub>3</sub>N<sub>4</sub>, thereby offering more number of active sites for the catalytic reactions. Along with high surface area, the prepared g-C<sub>3</sub>N<sub>4</sub> absorbs a higher fraction of the visible light. It was also observed that CN-R sample has high photocurrent response as compared to the bulk sample (CN-A) and showed an enhanced H<sub>2</sub> evolution rate under visible light irradiation compare to the conventional g-C<sub>3</sub>N<sub>4</sub>.

Even though the single-step synthesis of high surface area g-C<sub>3</sub>N<sub>4</sub> holds great promise for HER, further studies are needed for a complete understanding. I would like to propose that the origin of red-shift optical absorption spectrum of the as-synthesized sample (CN-R) is needed to

be examined thoroughly. XPS and CHN analysis of the CN-R sample need to be performed to find the composition and identify crystal-defects in the sample. Besides, the role of DEG in the synthesis process needs to be investigated. I believe that using other similar reagents and by changing the synthesis conditions, it will be possible to make further improvements in optical properties, surface area, synthesis yield and HER efficiency. The recyclability of CN-R for HER activity is needed to be checked.

## Bibliography

1. N. Armaroli and V. Balzani, *Angew. Chemie Int. Ed.*, 2007, **46**, 52–66.
2. J. Martinich and A. Crimmins, *Nat. Clim. Chang.*, 2019, **9**, 397–404.
3. J. Lelieveld, K. Klingmüller, A. Pozzer, R. T. Burnett, A. Haines and V. Ramanathan, *Proc. Natl. Acad. Sci.*, 2019, **116**, 7192 LP – 7197.
4. I. Staffell, D. Scamman, A. Velazquez Abad, P. Balcombe, P. E. Dodds, P. Ekins, N. Shah and K. R. Ward, *Energy Environ. Sci.*, 2019, **12**, 463–491.
5. A. FUJISHIMA and K. HONDA, *Nature*, 1972, **238**, 37–38.
6. J. Ran, T. Y. Ma, G. Gao, X.-W. Du and S. Z. Qiao, *Energy Environ. Sci.*, 2015, **8**, 3708–3717.
7. T. Takata, J. Jiang, Y. Sakata, M. Nakabayashi, N. Shibata, V. Nandal, K. Seki, T. Hisatomi and K. Domen, *Nature*, 2020, **581**, 411–414.
8. L. Zhang, G. Morello, S. B. Carr and F. A. Armstrong, *J. Am. Chem. Soc.*, 2020, **142**, 12699–12707.
9. P. Wang, S. Guo, H.-J. Wang, K.-K. Chen, N. Zhang, Z.-M. Zhang and T.-B. Lu, *Nat. Commun.*, 2019, **10**, 3155.
10. T. Hisatomi and K. Domen, *Nat. Catal.*, 2019, **2**, 387–399.
11. Z. Lian, M. Sakamoto, H. Matsunaga, J. J. M. Vequizo, A. Yamakata, M. Haruta, H. Kurata, W. Ota, T. Sato and T. Teranishi, *Nat. Commun.*, 2018, **9**, 2314.
12. S. Yu, X.-B. Fan, X. Wang, J. Li, Q. Zhang, A. Xia, S. Wei, L.-Z. Wu, Y. Zhou and G. R. Patzke, *Nat. Commun.*, 2018, **9**, 4009.
13. I. Shown, S. Samireddi, Y.-C. Chang, R. Putikam, P.-H. Chang, A. Sabbah, F.-Y. Fu, W.-F. Chen, C.-I. Wu, T.-Y. Yu, P.-W. Chung, M. C. Lin, L.-C. Chen and K.-H. Chen, *Nat. Commun.*, 2018, **9**, 169.
14. Y. Qu and X. Duan, *Chem. Soc. Rev.*, 2013, **42**, 2568–2580.
15. Z. Wang, C. Li and K. Domen, *Chem. Soc. Rev.*, 2019, **48**, 2109–2125.
16. M. Z. Rahman, M. G. Kibria and C. B. Mullins, *Chem. Soc. Rev.*, 2020, **49**, 1887–1931.
17. J. Liu, Y. Liu, N. Liu, Y. Han, X. Zhang, H. Huang, Y. Lifshitz, S.-T. Lee, J. Zhong and Z. Kang, *Science (80-. )*, 2015, **347**, 970 LP – 974.
18. A. Naseri, M. Samadi, A. Pourjavadi, A. Z. Moshfegh and S. Ramakrishna, *J. Mater. Chem. A*, 2017, **5**, 23406–23433.
19. A. Iwase, Y. H. Ng, Y. Ishiguro, A. Kudo and R. Amal, *J. Am. Chem. Soc.*, 2011, **133**, 11054–11057.
20. T.-F. Yeh, C.-Y. Teng, S.-J. Chen and H. Teng, *Adv. Mater.*, 2014, **26**, 3297–3303.
21. T.-F. Yeh, J. Cihlář, C.-Y. Chang, C. Cheng and H. Teng, *Mater. Today*, 2013, **16**, 78–84.
22. S. Cao and J. Yu, *J. Photochem. Photobiol. C Photochem. Rev.*, 2016, **27**, 72–99.

23. Z. Jin, X. Jiang, Q. Zhang, S. Huang, L. Zhang, L. Huang, T. He, H. Zhang, T. Ohno, S. Ruan and Y.-J. Zeng, *Commun. Mater.*, 2020, **1**, 90.
24. X. Li, J. Zhao and J. Yang, *Sci. Rep.*, 2013, **3**, 1858.
25. W.-J. Ong, L.-L. Tan, Y. H. Ng, S.-T. Yong and S.-P. Chai, *Chem. Rev.*, 2016, **116**, 7159–7329.
26. A. Mishra, A. Mehta, S. Basu, N. P. Shetti, K. R. Reddy and T. M. Aminabhavi, *Carbon N. Y.*, 2019, **149**, 693–721.
27. J. Fu, J. Yu, C. Jiang and B. Cheng, *Adv. Energy Mater.*, 2018, **8**, 1701503.
28. X. Wang, K. Maeda, A. Thomas, K. Takane, G. Xin, J. M. Carlsson, K. Domen and M. Antonietti, *Nat. Mater.*, 2009, **8**, 76–80.
29. Z. Wang, X. Hu, G. Zou, Z. Huang, Z. Tang, Q. Liu, G. Hu and D. Geng, *Sustain. Energy Fuels*, 2019, **3**, 611–655.
30. Q. Zhang, J. Deng, Z. Xu, M. Chaker and D. Ma, *ACS Catal.*, 2017, **7**, 6225–6234.
31. S. Samanta, S. Martha and K. Parida, *ChemCatChem*, 2014, **6**, 1453–1462.
32. J. Zeng, T. Song, M. Lv, T. Wang, J. Qin and H. Zeng, *RSC Adv.*, 2016, **6**, 54964–54975.
33. Y. Wang, H. Li, J. Yao, X. Wang and M. Antonietti, *Chem. Sci.*, 2011, **2**, 446–450.
34. G. Liu, P. Niu, C. Sun, S. C. Smith, Z. Chen, G. Q. (Max) Lu and H.-M. Cheng, *J. Am. Chem. Soc.*, 2010, **132**, 11642–11648.
35. Y. Zhang, T. Mori, J. Ye and M. Antonietti, *J. Am. Chem. Soc.*, 2010, **132**, 6294–6295.
36. Y. Zhou, L. Zhang, W. Huang, Q. Kong, X. Fan, M. Wang and J. Shi, *Carbon N. Y.*, 2016, **99**, 111–117.
37. G. Dong, K. Zhao and L. Zhang, *Chem. Commun.*, 2012, **48**, 6178–6180.
38. L. Zhou, H. Zhang, H. Sun, S. Liu, M. O. Tade, S. Wang and W. Jin, *Catal. Sci. Technol.*, 2016, **6**, 7002–7023.
39. G. Liu, G. Zhao, W. Zhou, Y. Liu, H. Pang, H. Zhang, D. Hao, X. Meng, P. Li, T. Kako and J. Ye, *Adv. Funct. Mater.*, 2016, **26**, 6822–6829.
40. Y. Bai, Y. Zhou, J. Zhang, X. Chen, Y. Zhang, J. Liu, J. Wang, F. Wang, C. Chen, C. Li, R. Li and C. Li, *ACS Catal.*, 2019, **9**, 3242–3252.
41. F. Dong, Z. Zhao, T. Xiong, Z. Ni, W. Zhang, Y. Sun and W.-K. Ho, *ACS Appl. Mater. Interfaces*, 2013, **5**, 11392–11401.
42. D. Vidyasagar, S. G. Ghugal, S. S. Umare and M. Banavoth, *Sci. Rep.*, 2019, **9**, 7186.
43. K. Maeda, *ACS Catal.*, 2013, **3**, 1486–1503.
44. P. Zhou, J. Yu and M. Jaroniec, *Adv. Mater.*, 2014, **26**, 4920–4935.
45. X. Zhou, B. Jin, L. Li, F. Peng, H. Wang, H. Yu and Y. Fang, *J. Mater. Chem.*, 2012, **22**, 17900–17905.
46. F. Yan, Y. Wu, L. Jiang, X. Xue, J. Lv, L. Lin, Y. Yu, J. Zhang, F. Yang and Y. Qiu, *ChemSusChem*, 2020, **13**, 876–881.
47. P. Niu, L. Zhang, G. Liu and H.-M. Cheng, *Adv. Funct. Mater.*, 2012, **22**, 4763–4770.
48. S. Yang, Y. Gong, J. Zhang, L. Zhan, L. Ma, Z. Fang, R. Vajtai, X. Wang and P. M. Ajayan, *Adv. Mater.*, 2013, **25**, 2452–2456.
49. J. Xu, L. Zhang, R. Shi and Y. Zhu, *J. Mater. Chem. A*, 2013, **1**, 14766–14772.
50. X. Zhang, X. Xie, H. Wang, J. Zhang, B. Pan and Y. Xie, *J. Am. Chem. Soc.*, 2013, **135**, 18–21.
51. N.-N. Vu, C.-C. Nguyen, S. Kaliaguine and T.-O. Do, *ChemSusChem*, 2019, **12**, 291–302.





## CHAPTER 4.5

### Conclusions of part 2 & future directions

#### Conclusions

Recently, g-C<sub>3</sub>N<sub>4</sub> has been realized as a desirable and efficient photocatalyst to drive diverse chemical reactions due to their non-toxicity, earth-abundant nature, excellent chemical and thermal stability, relative ease of synthesis, visible-light absorption, high surface area, high charge mobility, improvable exciton separation, appropriate band structure and electronic properties. g-C<sub>3</sub>N<sub>4</sub> based materials have been widely used in solar energy conversion (H<sub>2</sub>-production and reduction of CO<sub>2</sub>) and environmental remediation (degradation of organic pollutants). Conversion of nanosheets from bulk g-C<sub>3</sub>N<sub>4</sub> is highly required to get better activity. Chapter 4.2 describes a greener synthesis route for the quantum confined g-C<sub>3</sub>N<sub>4</sub> nanosheets and their enhanced photocatalytic oxidation performance upon coupling with plasmonic Au NPs. Chapter 4.3 is focused on the enhanced catalytic activity of Pd NPs by the photo-sensitization of g-C<sub>3</sub>N<sub>4</sub> nanosheets. A strategy to one-step synthesis of high surface area g-C<sub>3</sub>N<sub>4</sub> nanosheets for enhanced photocatalytic H<sub>2</sub>-evolution has been discussed in Chapter 4.4. The key findings discussed in chapter 3 of the thesis are summarized below:

Chapter 4.2 describes the development of novel g-C<sub>3</sub>N<sub>4</sub> nanosheets exhibiting highly blue-shifted, excitation-energy independent photoluminescence (PL) centered at ~425 nm. When the g-C<sub>3</sub>N<sub>4</sub> nanosheets are loaded with Au nanoparticles (NPs), the composite retains the PL characteristics but results in alteration of its exciton decay kinetics due to transfer of the long-lived photoexcited electrons in g-C<sub>3</sub>N<sub>4</sub> to the adjacent the Au NPs. The Au/g-C<sub>3</sub>N<sub>4</sub> nanosheets exhibited excellent light-harvesting in the extended solar spectrum and photocatalytic efficiency for benzylamine oxidation, emanating not only from a typical Surface Plasmon induced ‘hot-electron injection’ mechanism but also from a less-cared-for, pronounced co-catalytic effect by the Au NPs. The surface plasmon resonance of the Au NPs are responsible for the high visible-light response and assisting the reaction by the ‘hot-electron injection’ mechanism, while an uncharacteristic, pronounced co-catalytic effect by them further improves the efficiency.

Chapter 4.3 demonstrates the engineering of an effective strategy to improve the efficiency of traditional Pd catalysts for the Suzuki-Miyaura cross-coupling reactions by visible light irradiation using g-C<sub>3</sub>N<sub>4</sub> nanosheets as a sensitizer. Pd NPs loaded onto g-C<sub>3</sub>N<sub>4</sub> NSs become electron-rich under visible light irradiation due to the generation of excited electrons which get transferred to the Pd NPs and thereby accelerates the rate-determining step by facilitating the oxidative addition of aryl halides. The Suzuki-Miyaura cross-coupling reaction was carried out in environmentally friendly aqueous media at room temperature and exhibited a very high turnover frequency of 1700 h<sup>-1</sup> for photocatalytic cross-coupling reactions as compared to the previously reported photocatalysts. The catalyst also demonstrated high recyclability for Suzuki cross-coupling reactions.

Chapter 4.4 describes a simple strategy for one-step synthesis of high yield, high surface-area, red-shifted visible-light active, high surface-area g-C<sub>3</sub>N<sub>4</sub> NSs, unlike the multistep literature methods to get them in low yields. The NSs were synthesized by simple calcination of melamine and diethylene glycol mixture at 520 °C for 4 h under Ar atmosphere. The specific surface area of the synthesized sample was found to be ~3 times higher than the bulk g-C<sub>3</sub>N<sub>4</sub>, thereby offering more active sites for the catalytic reactions and eliminating the need for an extra, low-yield preparation step involving the high temperature or chemical exfoliation. The synthesized g-C<sub>3</sub>N<sub>4</sub> NSs showed a significantly enhanced H<sub>2</sub> evolution rate (530 μmol h<sup>-1</sup> g<sup>-1</sup>) under visible light irradiation compare to the as-synthesized conventional g-C<sub>3</sub>N<sub>4</sub> (87 μmol h<sup>-1</sup> g<sup>-1</sup>), which is comparable to those observed using low-yield synthesis processes in the literature.

## **Future directions**

The new findings on the semiconductor exciton dynamics in the vicinity of plasmonic NPs and the dual role offered by the NPs towards realizing high photocatalytic activity are expected to inspire the design of many other superior photocatalyst systems for a wide range of solar-driven organic transformation reactions.<sup>1</sup> The strategy to make high-yield g-C<sub>3</sub>N<sub>4</sub> nanosheets through the single-step route using alcohol with a high specific surface-area provides a green synthesis methodology. A lot is yet to be understood in this process such as (i) the role of alcohol in inducing high surface area, (ii) scope for using other similar reagents, (iii) the origin of redshift in the light absorption

spectrum, (iv) the changes in the PL spectra, (v) charge-separation dynamics, (vi) carrier-diffusion characteristics, etc. to fully exploit the new findings.

The same single-step method should also be useful for the synthesis of other 2D semiconductor materials such as boron nitride. Besides, the doping of P, B by using suitable precursor during the single-step synthesis of g-C<sub>3</sub>N<sub>4</sub> may be implemented.<sup>2-5</sup> The synthesized novel g-C<sub>3</sub>N<sub>4</sub> based heterostructures in conjugation with other semiconductor nanostructures or even molecular catalysts can be envisioned to improve their photocatalytic performance significantly for several organic transformation and energy conversion reactions.<sup>6,7</sup>

## Bibliography

1. J. Xiao, X. Liu, L. Pan, C. Shi, X. Zhang and J.-J. Zou, *ACS Catal.*, 2020, **10**, 12256–12283.
2. S. Zhang, L. Gao, D. Fan, X. Lv, Y. Li and Z. Yan, *Chem. Phys. Lett.*, 2017, **672**, 26–30.
3. N. Sagara, S. Kamimura, T. Tsubota and T. Ohno, *Appl. Catal. B Environ.*, 2016, **192**, 193–198.
4. Y.-P. Zhu, T.-Z. Ren and Z.-Y. Yuan, *ACS Appl. Mater. Interfaces*, 2015, **7**, 16850–16856.
5. M. Bellardita, E. I. García-López, G. Marci, I. Krivtsov, J. R. García and L. Palmisano, *Appl. Catal. B Environ.*, 2018, **220**, 222–233.
6. Y. He, L. Zhang, B. Teng and M. Fan, *Environ. Sci. Technol.*, 2015, **49**, 649–656.
7. Z. Jiang, W. Wan, H. Li, S. Yuan, H. Zhao and P. K. Wong, *Adv. Mater.*, 2018, **30**, 1706108.